Université Fédérale

Toulouse Midi-Pyrénées

THÈSE

En vue de l'obtention du

DOCTORAT DE L'UNIVERSITÉ DE TOULOUSE

Délivré par :

Institut Supérieur de l'Aéronautique et de l'Espace

Présentée et soutenue par :
Lucien CANUET

le lundi 16 avril 2018

Titre :

Fiabilisation des transmissions optiques satellite-sol

Reliability of satellite-to-ground optical communication

École doctorale et discipline ou spécialité :

ED MITT : Réseaux, télécom, système et architecture

Unité de recherche :

Équipe d'accueil ISAE-ONERA MOIS

Directeur(s) de Thèse :

M. Jérôme LACAN (directeur de thèse)
Mme Angélique RISSONS (co-directrice de thèse)

Jury :

M. Joseph KAHN Professeur Stanford University - Président
M. Aniceto BELMONTE Professeur Technical University of Catalonia, BarcelonaTech
M. Jérôme LACAN Professeur ISAE-SUPAERO - Directeur de thèse
M. Nicolas PERLOT Directeur de Recherche Fraunhofer Institute for Telecommunications
M. Christophe PEUCHERET Professeur ENSSAT Université Rennes 1 - Rapporteur
Mme Angélique RISSONS Professeure ISAE-SUPAERO - Co-directrice de thèse
M. Nicolas VEDRENNE Ingénieur de Recherche ONERA
M. Zoran SODNIK Directeur de Recherche European Space Agency

Acknowledgements/Remerciements

I am deeply grateful to all the members of my defense committee – Géraldine Artaud, Pr. Joseph Kahn, Pr. Aniceto Belmonte, Pr. Christophe Peucheret, Dr. Nicolas Perlot and Dr. Zoran Sodnik – for having done me the honor of their presence and for their interest in my work. I appreciated the discussions we had on the different topics of this thesis.

J'ai eu la chance au cours de cette thèse d'avoir trois encadrants exceptionnels. Je leur dois d'avoir fait de ces trois années une expérience inoubliable. Ils sont en très grande partie responsables de la peine que je ressens à la voir s'achever par la rédaction de ce manuscrit.

Mes débuts à l'ONERA ont été marqués par l'enthousiasme sans limites (et contagieux) de Nicolas, probable détenteur du record au sprint des couloirs du centre de Châtillon. Merci de m'avoir (gentiment) introduit à l'optique adaptative et surtout de m'avoir fait comprendre dès le commencement de mon travail de recherche que le plus important était tout simplement d'en tirer le maximum de plaisir. Je dois également énormément à Jérôme qui, à l'ISAE, a fait preuve d'une extrême patience pour m'initier à la théorie de l'information. Merci pour ta grande gentillesse, ta pédagogie et ta disponibilité toujours sans faille. Un grand merci aussi à Angélique qui a su partager son expertise expérimentale opto-hyper, me sensibilisant par là même à l'importance de toujours évaluer la pertinence de mes développements théoriques à la lumière de la pratique. Je vous remercie sincèrement tous les trois pour vos conseils tout au long de cette thèse.

Je souhaite également adresser mes remerciements les plus chaleureux à Jean-Marc Conan et Cyril Petit pour leur soutien et aide dans la rédaction de mon premier article. Vous avez toujours pris le temps de précisément répondre à mes questions et je vous en suis très reconnaissant. J'en profite pour saluer également l'accueil chaleureux de toute l'équipe HRA.

Je n'oublie pas bien sûr Géraldine Artaud qui a suivi mes travaux pour le compte du CNES durant ces trois années. Merci également de m'avoir convié au tout début de ma thèse, à la première démo d'un lien optique satellite-sol en France à l'OCA... un moment inoubliable qui a bien "boosté" ma motivation pour toute la suite de mon travail.

Acknowledgements

Je remercie également les co-financeurs, avec le CNES, que furent Airbus Defense and Space et Thales Alenia Space; mais surtout les personnes au sein de ces deux entités qui ont régulièrement suivi l'avancement de mon travail. Je pense en particulier à Sylvain Poulenard, Arnaud Le Kernec et Michel Sotom.

J'ai une pensée pour tous mes compagnons d'infortune, anciens collègues thésards à l'ONERA et à l'ISAE. Une pensée particulière pour mon co-bureau Parisien super Kassem. Un clin d'œil à Adrien (le lien montant) qui fut de quelques virées Toulousaines mémorables. Et un grand merci à tous les autres, à Paris et à Toulouse, Pédro, Elena, Sébastien, Joël, Karim, Selma, Bastien, Henrick, Doriane...

Enfin, je remercie bien évidemment ma famille qui m'a soutenu tout au long des ces trois années; ma soeur et mon frère qui se demandent probablement toujours en quoi a consisté mon travail (c'est pas faute d'avoir essayé de vous l'expliquer ;)) et mes parents qui ont toujours fait en sorte de me donner toutes les chances pour réussir.

A mes parents,

Abstract

Optical wavelengths are an alternative to radio-frequency links for future satellite-to-ground transmissions. They are envisioned in the framework of payload/telemetry data transfer (optical downlinks from LEO satellites) or communication (bi-directional optical links with GEO satellites). However, as it propagates through the atmosphere, the optical wave can be deeply affected by atmospheric turbulence which induces random spatial and temporal variations of its amplitude and phase. Variations in amplitude translate into fluctuations of the collected power (scintillation). The phase distortions affect the spatial distribution of the power at the focal plane of the telescope causing deleterious losses when the incident flux needs to be coupled to an optoelectronic detector or to a single-mode optical fiber. Such losses result in dynamical attenuations of the received signal -called fading- and hence potentially to the loss of information. The most recent feasibility studies highlight the use of two types of fading mitigation techniques: adaptive optics systems and digital techniques (coding and interleaving). To limit the complexity and cost of such systems, the optimization of these mitigation techniques should be conducted jointly. The main objective of this thesis is therefore the investigation of the complementarity of physical (adaptive optics) and digital data reliability mechanisms (interleaving, correcting and erasure codes in a cross-layer approach).

Résumé

Les longueurs d'onde optiques sont une alternative aux liens radio-fréquences pour les transmissions satellite-sol du futur. Elles sont envisagées pour les futurs systèmes de télémesure satellitaires (liens optiques descendants en provenance de satellites LEO) ou de communication (liens optiques bi-directionnels avec des satellites GEO). A sa traversée de l'atmosphère l'onde optique peut être profondément affectée par la turbulence atmosphérique. Elle subit des variations spatiales et temporelles d'amplitude et de phase. Les variations d'amplitudes se traduisent par des variations de la puissance lumineuse collectée (scintillations). Les perturbations de la phase affectent la distribution spatiale de la puissance au foyer du système de détection, qui n'est alors plus limitée par la diffraction. Des pertes peuvent en découler lors du couplage du flux incident à un détecteur optronique ou à une fibre optique monomode. Ces pertes se traduisent par des atténuations du signal reçu et donc par la perte d'informations. Pour s'en abstraire, les études de faisabilité les plus récentes mettent en avant l'utilisation de systèmes d'optique adaptative et de techniques numériques adaptées (codage/entrelacement). Pour limiter la complexité et le coût des systèmes de liens optiques, la définition des techniques de compensation des atténuations peut être menée conjointement. C'est l'objectif principal de cette thèse. Il s'agit d'investiguer les complémentarités des techniques de compensation physiques (optique adaptative) et numériques (entrelacement, codes correcteurs) pour disposer des éléments permettant de définir les systèmes de correction les mieux adaptés.

Contents

List of Figures

List of Tables

List of Symbols and Acronyms

a_{FS}	Free-space link loss
a_{p}	Pointing losses
a_{t}	Tracking losses
a_{SMF}	Identical to f_{SMF}
a_{Tx}, a_{Rx}	Losses due to imperfections of the optical components constituting the transmitter and the receiver
$B_{\Psi}(\rho)$	Spatial coherence function of the field
B_e	3-dB Electrical filter bandwidth
B_o	3-dB Optical filter bandwidth
$C_{\mathrm{n}}^2(h)$	Index of refraction structure constant
$D_{\Delta_{\mathrm{n}}}(\rho,h)$	Structure function of the refractive index fluctuations
D_{Sat}	Distance between the optical ground station and satellite
D_{Trop}	Thickness of the tropopause layer
$\boldsymbol{D}_{\mathrm{Z}}$	Matrix characterizing the wavefront sensor and expressed in the Zernikes basis
$E_{\mathrm{Tx}}(t)$	output optical field from the transmitter
$E_s(t)$	modulated signal
$E_{\mathrm{ASE}_{\mathrm{Tx}}}(t)$	amplified spontaneous emission noise field at the optical booster's output
$E_{\mathrm{back}}(t))$	parasitic field due to background light sources
$E_{\mathrm{Rx}}(t)$	signal coupled into the fiber at the receiver
f_{samp}	Adaptive optics loop sampling frequency
f_{SMF}	Instantaneous coupled flux attenuation into a single mode fiber
$f_{\Phi_{\mathrm{res}}}^{\mathrm{APPROX}}$	Analytic approximation of the instantaneous coupled flux into a single mode fiber
$f_{\Phi_{\mathrm{res}}}^{\mathrm{SAOST}}$	Analytic expression (exact) of the instantaneous coupled into a single mode fiber
G_{Tx}	On-axis transmit antenna gain
G_{boost}	Optical booster gain
$\boldsymbol{g}$	Integrator gain associated to the command of each actuator of the deformable mirror

$G_1(s)$	Transfer function representing the wave-front sensor averaging process
$G_2(s)$	Transfer function characterizing the wavefront reconstruction
G_{Rx}	Gain of the receiving aperture
$G_{\text{pre-amp}}$	Pre-amplifier gain
h_{Trop}	Altitude of the tropopause
h	Planck's constant
$H(X)$	Information entropy
$H(X\|Y)$	Conditional information entropy
$H_{\text{Opt}}(f)$	Bandpass optical filter transfer function
$H_{\text{El}}(f)$	Low-pass electrical filter transfer function
$H_1(f)$, $H_2(f)$	Transfer functions for each arm of a delay-line interferometer
$I(X;Y)$	Mutual information
k_{B}	Boltzmann constant
l_0	Turbulence inner scale
L_0	Turbulence outer scale
L_g	Fiber Bragg grating length
Link margin	Link (or power) margin
$\boldsymbol{M}_{\text{inf}}$	Influence matrix
$\boldsymbol{M}_{\text{inter}}$	Interaction matrix
$\boldsymbol{M}_{\text{com}}$	Command (reconstruction) matrix
M_0	Single mode fiber mode (in the pupil plane) approximated by a Gaussian mode
$n(\boldsymbol{r},t)$	Refractive index of the atmosphere
N_{ph}	Number of photons received per sub-pupil of a Shack-Hartmann wavefront sensor
N_{corr}	Number of corrected radial orders
N_{boost}	Power spectral density of amplified spontaneous emission generated by the booster amplifier
$N_{\text{pre-amp}}$	pre-amplifier ASE noise power spectral density
$n_{\text{sp}_{\text{rx}}}$	Pre-amplifier spontaneous-emission factor
$n_{\text{sp}_{\text{tx}}}$	Optical booster spontaneous-emission factor
P_{Outage}	Channel outage probability
$P_{\text{Rx}}(t)$	Instantaneous received optical power
P_{S}	Targeted receiver sensitivity
$p_Z(z)$	Probability density function of the sum of independent and non identical Gamma random variables
$P_Z(z)$	Cumulative distribution function of the sum of independent and non identical Gamma random variables

$p_{F_{\mathrm{SMF}}}(f_{\mathrm{SMF}})$	Probability density function of the partially corrected coupled flux into a single mode fiber
$P_{F_{\mathrm{SMF}}}(f_{\mathrm{SMF}})$	Cumulative distribution function of the partially corrected coupled flux into a single mode fiber
$P_{\mathrm{CW}}(t)$	Instantaneous intensity (power) of the optical field emitted by a laser source under continuous wave condition
$\mathrm{PER}^{\mathrm{dec.}}(t)$	Instantaneous decoded packet-error rate at the higher layers output
$\mathrm{PER}(t)$	Instantaneous packet-error rate at the output of the physical layer
R_{load}	load resistor of photodiode module
R_0^{GLOBAL}	System global code rate
R_{PIN}	Photodiode responsivity
R_0^{PHY}	Physical layer error correcting coding rate
R_0^{HL}	Higher layers erasure code coding rate
$R_{\rho_\Phi}(\tau)$	Approximation of the auto-covariance of the partially corrected coupling efficiency
$R_{f_{\mathrm{SMF}}}(\tau)$	Approximation of the auto-covariance of the partially corrected coupled flux
r_0	Fried parameter
$S_{\dot{\phi}_L}(f)$	Two-sided power spectral density of the Wiener process describing the laser phase noise
$T_{\mathrm{Field}}(V_1, V_2)$	optical field transfer function of a Mach-Zehnder modulator
T_b	Bit duration
$\boldsymbol{u}_n$	Command applied at discrete instant n to the actuators
V_{Grnd}	Ground wind speed
$V_{\mathrm{Layer}}(h)$	Contribution (speed) of both natural wind and the satellite's speed at altitude h
$V_\perp(\boldsymbol{r})$	Average transverse wind speed
V_{Sat}	Orthoradial component of the satellite's instantaneous velocity
V_{Trop}	Wind speed at the tropopause
$V_{\mathrm{Wind}}(h)$	Transverse wind speed at altitude h
$V_1(t)$, $V_2(t)$	driving voltages in each arm of a Mach-Zehnder modulator
$V_{\pi 1}$, $V_{\pi 2}$	Required voltages in order to obtain a phase shift of π in each arm of a Mach-Zehnder modulator
$W_{\Delta_{\mathrm{n,h}}}(\boldsymbol{f})$	Power spectrum density of refractive index fluctuations
$W_\chi(\boldsymbol{f})$	Log-amplitude power spectral density
$W_\phi(\boldsymbol{f})$	Phase power spectral density

$W_{a_i}(\nu)$	Temporal power spectrum corresponding to the Zernike coefficient a_i
X_{S}	Number of pixels taken into account in the calculation of the center of gravity (wavefront sensor sub-pupil)
X_{T}	FWHM of the image formed in the focal plane of a sub-pupil of a Shack-Hartmann wavefront sensor
X_{D}	FWHM of the diffraction limited image by a sub-pupil of a Shack-Hartmann wavefront sensor
$Z_i(\boldsymbol{r})$, a_i	Zernike polynomial and its associated coefficient
(α_x^k, α_y^k)	Local slope of the phase on the sub-pupil k of a Shack-Hartmann wavefront sensor
$\beta(f)$	Fiber Bragg grating coupling coefficient
δ	Mach-Zehnder modulator extinction ratio
ω_{Sat}	Satellite's angular velocity
$\chi(\boldsymbol{r})$	Log-amplitude of the propagating wave
$\phi(\boldsymbol{r})$	Phase of the propagating wave
$\phi_{\mathrm{corr}}(\boldsymbol{r}, t)$	Corrected phase
$\phi_{\mathrm{res}}(\boldsymbol{r}, t)$	Residual phase
$\phi_{\mathrm{turb}}(\boldsymbol{r}, t)$	Turbulent phase
$\phi(V_1)$, $\phi(V_2)$	voltage-modulated optical phases in each arm of a Mach-Zehnder modulator
$\mu_{f_{\mathrm{SMF}}^{\mathrm{Scint}}}$	Average coupled flux into a single mode fiber that neglects phase aberrations of the turbulent wavefront
σ_χ^2	Log-amplitude variance
$\sigma_{\chi R}^2$	Rytov variance
σ_ϕ^2	Phase variance
σ_I^2	Scintillation index
σ_{phot}^2	Shack-Hartmann wavefront sensor photon noise
$\sigma_{\mathrm{detect}}^2$	Shack-Hartmann wavefront sensor detection noise
σ_{e^-}	Standard deviation of the noise per pixel (wavefront sensor)
σ_{Noll}^2	Noll's statistical variance of the residual phase
σ_{res}^2	Residual phase variance
$\sigma_{\mathrm{Fitting}}^2$	Fitting error (adaptive optics system)
$\sigma_{\mathrm{Tempo}}^2$	Temporal error (adaptive optics system)
$\sigma_{\mathrm{Alias}}^2$	Aliasing error (adaptive optics system)
$\sigma_{\mathrm{turb}}^2(n)$	Approximation of the variance of a turbulent mode (Zernike) of radial order n
$\sigma_{\phi_L}^2$	Variance characterizing the Wiener process describing the laser phase noise

σ^2_{therm}	Variance of thermal noise generated by the photodiode module circuitry
$\Omega(t)$	Matching between the electromagnetic field's complex amplitude of incident beam and the single mode fiber mode (in pupil plane)
$\rho(t)$	Instantaneous coupling efficiency of a perturbed incident beam
$\rho^{\text{APPROX}}_{\Phi_{\text{res}}}$	Analytic approximation of the instantaneous normalized coupling efficiency into a single mode fiber
$\rho^{\text{SAOST}}_{\Phi_{\text{res}}}$	Analytic expression (exact) of the instantaneous normalized coupling efficiency into a single mode fiber
$\bar{\tau}_{\text{fade}}(f^0_{\text{SMF}})$	Average fade duration under the threshold f^0_{SMF}

ADC	Analog-to-digital converter
AIFD	Average inter-fading time
AFD	Average fade time
AO	Adaptive optics
AOST	Adaptive optics simulation tool
APD	Avalanche photo-diode
ASE	Amplified spontaneous emission
ASIC	Application-specific integrated circuit
BER	Bit-error rate
CDF	Cumulative distribution function
CNES	Centre national d'études spatiales
COTS	Commertial off-the-shelf
CW	Continuous-wave (laser)
DBPSK	Differential binary phase shift keying
DLI	Delay-line interferometer
DM	Deformable mirror
DREAM	Data Reliability Evaluation Module
EC	Erasure code
ECC	Error-correction code
EDFA	Erbium-doped fiber amplifiers
EDRS	European data relay system
ESA	European space agency
FBG	Fiber Bragg gratings
FDD	Fade duration distribution
FFD	Fractional fade time
FPF	Fabry-Perot filter
FSO	Free-space optical
GEO	Geosynchronous orbit
HL	Higher layers
IFDD	Inter-fade duration distribution
ISAE	Institut supérieur de l'aéronautique et de l'espace
ISI	Inter-symbol interference
ISS	International space station
JDRS	Japan's Data Relay System
JPL	Jet propulsion laboratory
LADEE	Lunar Atmospheric Dust and Environment Explorer
LCE	Laser Communication Experiment
LCRD	Laser Communications Relay Demonstration
LEO	Low-Earth orbit
LIDAR	Light detection and ranging

LLCD	Lunar Laser Communication Demonstrator
LUCE	Laser Utilizing Communications Equipment
MI	Mutual information
MZM	Mach-Zehnder Modulator
NASA	National aeronautics and space administration
NRZ	Non-return to zero
OCA	Observatoire de la Côte d'Azur
OCTL	Optical Communications Telescope Laboratory
OICETS	Optical Inter-orbit Communication Engineering Test Satellite
OGS	Optical ground station
ONERA	Office national d'études et de recherches aérospatiales
OOK	On-off keying
OPALE	Optical PAyload for Inter Satellite Link Experiment
OPALS	Optical Payload for Lasercom Science
OSIRIS	Optical Space Infrared Downlink System
OSNR	Optical signal to noise ratio
PAM	Pulse amplitude modulation
PDF	Probability density function
PER	Packet-error rate
PHY	Physical layer
PPM	Pulse position modulation
PSF	Point-spread function
PSK	Phase-shift keying
QAM	Quadrature amplitude modulation
QKD	Quantum key distribution
RIN	Relative intensity noise
RZ	Return to zero
SAOST	Simplified adaptive optics simulation tool
SAR	Synthetic aperture radar
SCIDAR	Scintillation detection and ranging
SIMCOP	Simulateur Couche Physique Optique
SH WFS	Shack-Hartmann wavefront sensor
SILEX	Semi-conductor laser inter-satellite link experiment
SLODAR	Slope detection and ranging
SOCRATES	Space Optical Communications Research Advanced Technology Satellite
SODAR	Sonic detection and ranging
SOTA	Small Optical Transponder
SMF	Single-mode fiber
SNR	Signal to noise ratio
SR	Strehl ratio

SWaP	Size, weight and power
TURANDOT	Turbulence simulator for space-ground optical telecommunication
WDM	Wavelength-division multiplexing
WFS	Wavefront sensor

1 INTRODUCTION AND CONTEXT

Contents

1.1 Satellite-to-ground optical links

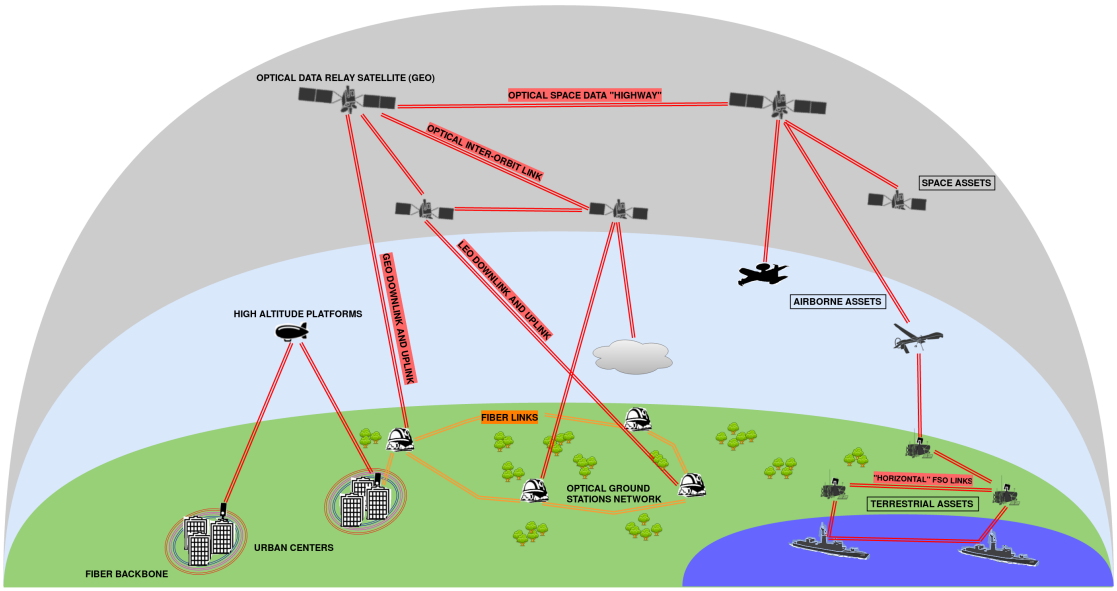

Figure 1.1: Hypothesized free-space optical network including satellite-to-ground optical links

In the recent decades, information and communication technologies have witnessed a tremendous expansion. Correspondingly, the capacity and bandwidth requirements of wireless systems' end-users have drastically increased. In meeting the needs of such a bandwidth increasingly hungry world, conventional wireless systems based upon radio-frequency (RF) technologies will soon appear to reach their fundamental limits. As a consequence, the wish to shift from RF to optical frequencies naturally arose several years ago.

Nowadays, wireless optical communication is considered a viable technology for the next generation of broadband communication systems. Due to several of their inherent advantages over RF telecommunication systems, they are envisioned in a variety of applications. Their extensive range, from a few meters to over thousands of kilometers, potentially offers the adoption of optical links in the framework of various scenarios as shown in Fig. 1.1. Theoretically, several wireless optical networks involving satellite, terrestrial, and even indoors links could be integrated and operated as a whole by connecting them to the fiber backbone. In doing so, wireless optical links could geographically extend the high capacity characteristics of the latter to remote areas otherwise difficult to reach.

In the context of data transmission from scientific or defense satellite payloads, free space optical links offer as well promising expectations. As shown in Fig. 1.2, spaceborne platforms equipped with earth-observing sensors are facing an exponential growth in the amount of data they are able to gather and that need to be transmitted to ground stations.

This is mainly due to the development and deployment of high spatial and spectral resolution

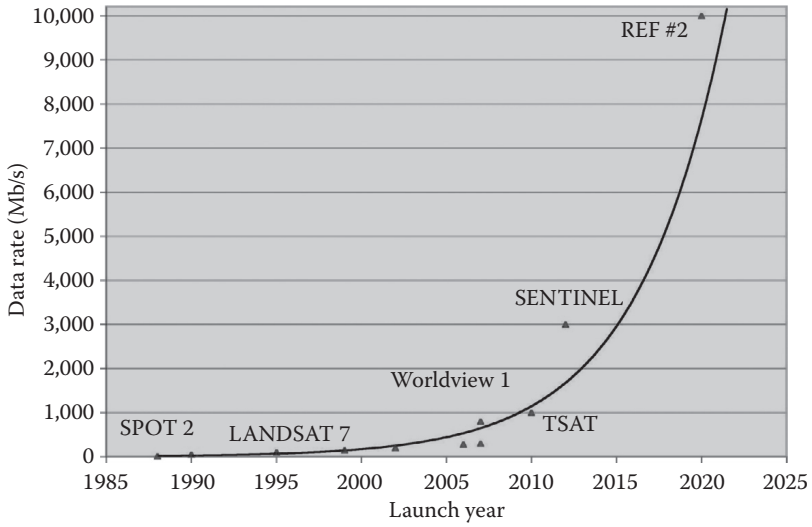

Figure 1.2: Data-rate trends for earth-orbiting spacecrafts . From [Hemmati, 2009a]

instruments such as Synthetic Aperture Radars (SAR) and hyperspectral imagers on board such spacecrafts. Typically, these instruments provide scientists with information on Earth's dynamic processes (ocean dynamics, desertification, deforestation...) and high resolution images of surface features, such as soil and vegetation that enables geologists, agriculturalists and others to identify mineral deposits and to monitor crop health [Lansing et al., 2002]. Enormous amounts of generated data thus need to be delivered at the earliest occasion to such investigators. Table 1.1 shows the expected evolution of the quantity of information generated by the aforementioned imaging systems in 2020. Hence, it highlights the demand in very high rate transmission from Earth orbiting satellites to ground stations in the near future.

Table 1.1: Past and projected required data rates for selected instruments [Lansing et al., 2002]

Year	2010	2020
Hyperspectral	10 Gbps	100 Gbps
SAR	10 Gbps	60 Gbps
LIDAR	150 Mbps	1 Gbps

Another scenario expected to benefit from optical communication is related to deep-space science and exploration. The communication infrastructure is a critical component of any spacecraft system design as it impacts the return of the mission. The spacecrafts, or probes, involved in such missions have generally highly constrained resources as the size, weight and power (SWaP) of onboard equipment is severely restricted. Laser-based transmission from such probes could significantly reduce the communication system SWaP. Furthermore, it is interesting to note that, in the U.S., the potential use of optical links for deep space application has been one of the major financial supports for the development of satellite-ground optical

links [Boroson and Robinson, 2015, Cesarone et al., 2011].

1.1.1 Advantages of satellite-to-ground optical links

The advantages offered by wireless optical communication stem from the narrow transmit beam width (high directivity) and large carrier frequency. Among these advantages are:

- **Reduced overall SWaP:** Roughly one half of the mass and power consumption of typical RF systems, as well as roughly on tenth of the diameter of a typical RF antenna.
- **High modulation bandwidth:** the amount of information transmitted by a communication system is directly related to the bandwidth of the modulated carrier. It is usually some fraction of the carrier frequency itself. In the C-band the carrier frequency is around 192 THz [Yoichi Maeda, 2009]
- **Unlicensed spectrum:** RF transmission suffers from interference of adjacent carriers leading to the congestion of the corresponding spectra. It is therefore regulated.The high directivity of optical transmission precludes signal interference. Hence, there are no regulatory restrictions for frequency use and bandwidths in the optical spectrum.
- **Increased security:** Given their high directivity and immunity to electromagnetic interference, optical links have a low probability of being intercepted or jammed.

1.1.2 Challenges faced by satellite-to-ground optical links

To offer the significant potential for improvement over RF previously described, satellite optical downlinks have to overcome several drawbacks. The large carrier frequency -or smaller wavelength- typically used in free-space optical communication also induces several impediments that can impact the reliability and availability of such links. Among those, three major issues are:

- The impact of **atmospheric phenomena**, such as haze, fog and turbulence that greatly affect the propagation of the optical wave through the atmosphere
- The high directivity of the transmitted beam which makes **acquisition and pointing more complicated**
- The potential system's unavailability caused by **cloud coverage**

To counter cloud related attenuation, weather statistics can be exploited to implement site diversity (optimized geographical network of optical ground stations). Typically, multiple ground

stations within the field of view of the flight terminal are required to provide such a weather diversity [Lacoste et al., 2011]. By extracting cloud motion vector field from weather forecast as in [Poulenard et al., 2014] link availability optimization can be performed by both selecting the station localization with lowest probability of clouds and minimizing the weather correlation between stations [Fuchs et al., 2017, Poulenard et al., 2017]. The use of data buffers onboard the spacecraft, in conjunction with data communication protocols [Clare and Miles, 2016], can improve as well the transmission availability.

The mitigation of pointing errors is decomposed into the stabilization of the optical line-of-sight and providing the appropriate pointing reference to the receiver location [Kaushal et al., 2017]. At the receiver location, by using a beacon, stabilization is achieved. When necessary, the sensing and correction of the platform jitter is done by using a high bandwidth control loop.

Atmospheric phenomena limit the system's performance by causing distortions of the carrier. The constituent gases and particulates of the atmosphere cause absorption and scattering that give rise primarily to the attenuation of the optical wave (see Section 2.2.1.1).

Temperature and humidity variations along the line of sight towards the satellite cause spatio-temporal variations of the refractive index of air. These variations are called atmospheric optical turbulence. Such fluctuations of the refractive index are at the origin of fluctuations in the amplitude and phase of the incident beam (see Section 2.2.2). Fiber-optic communication technologies, such as Single Mode Fiber (SMF) Erbium-Doped Fiber Amplifiers (EDFAs), may be leveraged by free-space optical communications systems in order to reach the expected very high data rates and potentially integrate them to the existing infrastructures and networks [Arimoto et al., 2012]. In that case, optical turbulence will cause fading of the received signal due to fluctuations affecting both the power collected by the receiving aperture and the coupling efficiency of the incident beam into such fiber components (see Section 2.4). To mitigate such fading, current systems typically employ two types of mitigation techniques:

- Physical mitigation techniques such as adaptive optics that act on the received optical beam

- An ensemble of digital techniques including interleavers and channel coding that acts on the digital/telecom signal

In this thesis, the emphasis is put on the effects related to atmospheric turbulence and the mitigation of the induced signal fading by jointly investigating two types of techniques: adaptive optics (AO) and data reliability mechanisms (coding and interleaving).

1.2 State-of-the-art of satellite-to-ground optical links

1.2.1 Technological trends evolution

During the past decade, several experimental programs have been commissioned with satellites and payloads developed in order to demonstrate and investigate near-Earth optical communication techniques [Toyoshima, 2006, Hemmati and Caplan, 2013, Toyoshima et al., 2015]. A quick chronological review of the landmarks of such investigations follows. While the first successful optical communication downlink demonstration occurred in 1994, a fair increase in the number of systems development started in the last five to seven years.

GEO-to-ground links

- **Laser Communication Experiment (LCE) - 1994.** Developed by the Japanese Communications Research Laboratory in Japan was **the first system developed for demonstrating space-to-ground laser communications**. It flew onboard the ETS-VI satellite that failed to reach its intended GEO orbit and therefore the experiment was carried out from an elliptical orbit [Arimoto et al., 1995]. It demonstrated a 1.024 Mbps link.

- **SILEX/ARTEMIS - 2001.** The SILEX (semi-conductor laser inter-satellite link experiment) system comprised two optical terminals: PASTEL, on board the French Earth observation satellite SPOT-4, and OPALE (Optical PAyload for Inter Satellite Link Experiment) embarked on the European communications satellite ARTEMIS. **The first bidirectional optical link between ARTEMIS in GEO orbit and the European Space Agency (ESA) Optical Ground Station (OGS) in Spain (Teneriffa) was established in November 2001** [Alonso et al., 2004]. The GEO orbit allowing for several successive measurements of link parameters over many days, it provided the community with a better understanding of the atmospheric impairments at low zenith angle.

- **GEOLite - 2001.** This program was sponsored by the U.S. Department of Defense. Not many details have been made publicly available about GEOLite. The payload, developed by the Massachusetts Institute of Technology's Lincoln Laboratory supposedly allowed successful **transmission at data rates greater than 1 Gbps** [Hemmati, 2009a].

- **EDRS/Alphasat - 2014.** The European Data Relay System (EDRS) aims at becoming world's first commercial optical data relay system. To circumvent the need of future Earth observation satellites for high capacity and availability satellite-to-ground links, as mentioned in Section 1.1, EDRS will rely on GEO relay links, i.e. communication links from LEO satellites to a geostationary relay satellite which transmits the data to the ground [Bohmer et al., 2012]. As a precursor to the EDRS GEO satellites equipped with Tesat Spacecom's Laser Communication Terminals (LCT) [Gregory et al., 2017], an LCT

was embarked on Alphasat, a GEO spacecraft developed by Airbus Defense and Space on behalf of Inmarsat and ESA. **Since 2014, Alphasat has enabled several GEO-to-ground links tests with ESA OGS and a Tesat's transportable adaptive optical ground station (T-AOGS)**. [Heine et al., 2018, Saucke et al., 2017, Fischer et al., 2017b]

LEO-to-ground links

- **OICETS/LUCE - 2006.** The Japanese Optical Inter-orbit Communication Engineering Test Satellite (OICETS) carried the Laser Utilizing Communications Equipment (LUCE) in order to **demonstrate inter-orbit communications between OICETS and ARTEMIS**. It also aimed at demonstrating LEO-to-ground communication using the optical ground stations in Japan and Europe including a transportable OGS [Jono et al., 2007].

- **TerraSAR X - 2008.** The Laser Communication Terminal (LCT) on the German satellite TerraSAR-X, developed by Tesat Spacecom under contract of the German Space Agency (DLR) was used to perform a downlink to DLR's OGS in Oberpfaffenhofen. Although TerraSAR-X is equipped with a coherent BPSK transmission laser terminal, downlink trials did not included coherent signal reception. **Instead, the received power and wavefront-quality were measured in the framework of assessing performance required by adaptive optics system.** [Giggenbach et al., 2009] Note that another LCT payload was launched on the U.S. satellite NFIRE which allowed to carry out the first experimental trials of LEO-to-LEO links.

- **OPALS - 2014.** The Optical Payload for Lasercom Science (OPALS) is an experimental terminal that was developed by the NASA Jet Propulsion Laboratory for use on the International Space Station (ISS). It allowed the demonstration of a 50 Mbps downlink by transferring a video from the ISS to JPL's Optical Communications Telescope Laboratory (OCTL) in California. Later in 2015, it allowed for the first time, **the demonstration of AO correction of an optical communication signal from a LEO platform coupled into a single-mode fiber** [Wright et al., 2015].

- **SOCRATES/SOTA - 2015.** The Small Optical Transponder (SOTA) terminal on the Japanese Space Optical Communications Research Advanced Technology Satellite (SOCRATES) was developed by NICT (National Institute of Information and Communications Technology) foster application of free-space optical communication using microsatellites. One of its scientific goal is to experiment with QKD (Quantum Key Distribution). It also demonstrated (classical) LEO-to-ground links to stations in Japan, Germany, and France. **It has been used to establish the second to date downlink including AO correction at the receiver in order to couple the signal into a single-mode fiber [Petit et al., 2016]**. The AO system developed by ONERA (*Office national d'études et de recherches aérospatiales*) equipped the OGS of the *Observatoire de la Côte d'Azur* (OCA) in collaborative

project funded by CNES (*Centre National d'Études Spatiales*), Airbus Defense and Space, Thales Alenia Space and ONERA.

Table 1.2 synthesizes the general characteristics of the aforementioned systems. In addition to those, it includes NASA's Lunar Laser Communication Demonstrator (LLCD), a milestone for future deep-space optical links, LLCD demonstrated in 2014 a broadband link between several ground stations and a payload on the Lunar Atmospheric Dust and Environment Explorer (LADEE) spacecraft achieving 622 Mbps in downlink [Boroson et al., 2009, Boroson and Robinson, 2015]. For the sake of completeness, Table 1.2 includes as well China's first optical communication experiment HY-2 in 2011 and Russia's BTLS (Onboard Terminal of a Laser Communication System) on RS (Russian Segment) of the ISS downlink [Grigoryev et al., 2014], carried out as well in 2011. Near-future systems and programs are also reported. They include Japan's Data Relay System (JDRS), NASA's Laser Communications Relay Demonstration (LCRD) and DLR's Optical Space Infrared Downlink System (OSIRIS). Moreover, information about the modulation formats and coding schemes of the most recent systems is given.

Analyzing the chronological evolution of the systems described above, as well as the information reported in Table 1.2, several trends concerning some of their fundamental features can be inferred. The latter concern their **communication sub-system** (detection technique, modulation format), the use of **adaptive optics**, and their **data reliability techniques** (coding scheme):

- **Communication sub-system.** Over the experiments and demonstrators, the carrier wavelength has clearly increased. The wavelength of operation of the vast majority of recent and planned systems is situated in the 1550 nm band. The advantages of using the latter in the context of free space optical communication are detailed in 2.2.1.3. This choice stems probably as well from the vast number of existing electro-optic components developed for fiber communication in this specific band. Overall, another striking characteristic feature that is the preponderance of direct detection systems combined with the simple modulation formats that are On-Off Keying (OOK) and Pulse-Amplitude Modulation (PPM). This overwhelming choice in using simpler direct detection techniques with respect to coherent detection is discussed in more details in Section 1.2.2. It motivated the emphasis put on the former techniques in this thesis.
- **Use of adaptive optics.** The most recent and planned demonstrations include the use or testing of an AO system on the ground in order to mitigate the deleterious effects of atmospheric turbulence as stated in Section 1.1.2. This trend is consistent with the aim of leveraging fiber-optic communication technologies such as optical pre-amplifiers which will enable the ambitioned data rates. Current AO systems used in the framework

of satellite downlinks are presented and discussed in Section 1.2.3.1.

- **Data reliability techniques.** Fading on the free-space optical channel usually occur in bursts that limit the performances of existing coding techniques. To counter this kind of fading efficiently, the use of interleavers that spread the data stream burst errors are considered beneficial. Such a fact is confirmed by number of recent systems using interleaving as reported in Table 1.2. Some reported coding schemes have the particularity of being concatenated. They combine two types of error-correcting codes (ECC) ("internal" and "external") in parallel or in series and an interleaving layer is actually often added between the two. Conventionally, the decoding in this case is done by the decoding of the internal code followed by that of the external code. In the case of LLCD's SCPPM (serially-concatenated PPM), turbocodes' principle is used [Sklar, 1997]. For OPALS, the ECCs are also associated with an external repetition code: the output of the ECC is re-injected directly to its input an arbitrary number of times. This variability of techniques revealed in such an non-exhaustive list suggests that finding the optimal coding for satellite laser communication is a very active field of investigation. It is discussed in further details in 1.2.4.

Table 1.2: Overview of several past and planned space-to-ground optical links and their associated programs in Japan (blue), the U.S. (red), Europe (green), China (orange) and Russia (cyan).

Year	Program	Scenario	Wavelength [µm]	Detection	Max Data rate	Modulation	Coding
1994	LCE	GEO-ground	0.8/0.5	DD	1 Mbps		
2006	OICETS	LEO-GEO LEO-ground	0.8	DD	50 Mbps		
2015	SOTA	LEO-ground	0.98/1.5	DD	10 Mbps	OOK	Reed-Solomon or LDGM + interleaving [Inoue et al., 2014]
2019	JDRS	GEO-ground	1.5	DD	1.8 Gbps	DPSK	
1995	GOLD	GEO-ground	0.8/0.5	DD	1 Mbps		
2001	GeoLITE	GEO-ground	1.5	DD	1 Gbps		
2013	LLCD	Lunar-ground	1.5	DD	622 Mbps	16-PPM	SCPPM [Boroson et al., 2014, Arnold, 2014] [Moision and Hamkins, 2005, Roth, 2013]
2014	OPALS	ISS-ground	1.5	DD	50 Mbps	OOK	Reed-Solomon(255,223) with 8-bit symbols (CCSDS-131.0-B-2)[CCSDS, 2011] + external code 2-3 repetitions [Oaida et al., 2014]
2018	LCRD	GEO-LEO GEO-ground	1.5	DD	2.8 Gbps	16-PPM/DPSK	PPM: Idem to LLCD DPSK: Rate 1/2 DVB-S2 standard: LDPC + convolutional interleaving (1 s) [Edwards et al., 2012]
2001	SILEX	GEO-LEO GEO-ground GEO-Air	0.8	DD	50 Mbps		
2008	TerraSAR-X	LEO-LEO LEO-ground	1.06	Coherent	5.6 Gbps		
2014	EDRS	GEO-LEO GEO-ground	1.06	Coherent	1.8 Gbps	BPSK	Reed Solomon+interleaving
2018	OSIRISv1-3	LEO-ground	1.5	DD	10 Gbps		
2018-20	Optelμ/D	Deep Space-Ground LEO-ground	1.5	DD	2 Gbps	OOK/8-PPM	CCSDS 101.0-B-6 [CCSDS, 2002] Concatenated Code: External: RS Internal: convolutional code (1/2,3/4,7/8) [Dreischer et al., 2014, Arnold et al., 2014]
2011	HY-2	LEO-ground	1.5	DD	504 Mbps		
2011	BTLS	ISS-ground	1.5/0.85	DD	125 Mbps		

1.2.2 Communication sub-system trade-offs

During this thesis, the emphasis was put on the investigation of direct detection (using OOK) and differentially coherent detection systems (using DBPSK). The underlying motivation behind such a choice was influenced by the trade-offs detailed in the remainder of the present subsection.

1.2.2.1 Detection technique: complexity against performance

Traditionally in (fiber) optical communication and in the case of digitally modulated optical signals, there exist three main categories of detection method [Kahn, 2006]:

- **Direct detection** or non-coherent detection where only the presence or absence of energy is exploited and any phase information is lost. The most commonly used modulation formats in that case are referred to as M-ary pulse-amplitude modulation (M-PAM). The special case of 2-PAM, also named on-off keying (OOK), will be considered in the remainder.
- **Differentially coherent detection** where the phase corresponding to a given symbol is compared to the previous symbol's phase. M-ary differential phase-shift keying (M-DPSK) is associated with this detection. The special case of 2-DPSK (referred to as DBPSK in this manuscript) implemented with interferometric detection will be considered in the remainder as well.
- **Coherent detection** where the optical signal is detected using a carrier phase reference generated at the receiver (local oscillator). Coherent detection typically yields more complex and efficient modulation schemes such as M-ary phase-shift keying (M-PSK) or M-ary quadrature-amplitude modulation (M-QAM).

Direct detection, although often outperformed by coherent detection systems, has the advantage of offering lower implementation complexity and cost. Furthermore, with the advent of the Erbium Doped Fiber Amplifier (EDFA) the typical sensitivity of direct detection systems have been drastically improved. Hence, under the assumption that the detection noise is dominated by the EDFA's amplified-spontaneous emission (ASE), these simpler direct detection systems achieve in theory the same performance as heterodyne or homodyne coherent based systems [Tonguz and Wagner, 1991].

As a consequence, fiber-based optical communication at 1550 nm have in general been performed thanks to direct detection receivers [Winzer, 2002]. The required components are widely available off-the-shelf and have been proven reliable during the last decades. The majority of space based systems logically aim at leveraging the benefits of using such

components while keeping implementation complexity and costs at a minimum for the near future. Therefore, the acute complexity presented by coherent transceivers designs preclude, for now, their wide spread use in space-to-Earth links.

In that regard, differentially coherent detection (with a DBPSK modulation format) provides an interesting overall efficiency-complexity trade-off. It has received significant interest [Gnauck et al., 2002, Sinsky et al., 2004] due to its theoretical 3 dB sensitivity improvement over OOK modulation [Winzer, 2002, Gnauck and Winzer, 2005]. It is therefore unsurprising that it is considered in both the U.S. and Japanese future relay systems (LCRD and JDRS respectively). Its increase in implementation complexity compared to direct detection stems mainly from the fact that a phase-to-amplitude converting element such as a delay-line interferometer (DLI) has to be inserted in the optical path at the receiver and two balanced photodectors are required.

1.2.2.2 Modulation formats: spectral efficiency against energy efficiency

Choices made in terms of modulation formats are motivated by the potential application of the distinct systems reported in 1.2. They have been made on the basis of how energy and/or spectrally efficient such formats are.

The former refers to the maximum achievable data rate at a target BER for a given transmit energy irrespective of the occupied bandwidth while the later refers to the information transmission rate for a given bandwidth without taking the required transmit energy into account.

Therefore, for mission scenarios and applications where energy efficiency is paramount, such as deep-space links, better energy efficient solutions are envisioned. Associated to photon counting detectors, PPM has been proven to be a promising solution [Gagliardi and Karp, 1995, Wilson et al., 2005]. NASA is distinctly invested in carrying future deep space exploration activities, hence investing consequent resources towards developing the related technologies. The past LLCD and current DSOC (Deep Space Optical Communications) programs attest of such ambitions. PPM is therefore predominately considered in U.S. demonstrators.

PPM is generally however less bandwidth efficient than OOK [Caplan, 2007, Mahdiraji and Zahedi, 2006]. It is worth noting as well that PPM presents a certain increase in complexity compared to OOK. Because PPM maps the input bits on a symbol of fixed duration, it requires slot and symbol-level synchronization. On the other hand, the complexity in implementing OOK lies in the dynamic thesholding required at the receiver for optimal detection [Personick, 1973, Webb and Marino, 1975, Brown, 1997, Alexander, 1997]. The latter necessitates a certain knowledge about the instantaneous channel fading state, which is usually circumvented in practice using pilot symbols [Xiaoming Zhu, 2002, Xu et al., 2009]. As a conclusion, for near-Earth ap-

plications, which are less stringent on energy efficiency than deep-space applications, OOK is seen to be the favored modulation format.

1.2.3 Fading Mitigation techniques

After providing a brief overview of the specific challenges encountered by physical and digital mitigation techniques separately, **this subsection highlights the interests in jointly optimizing AO systems and coding/interleaving schemes from an overall system-level point of view.**

1.2.3.1 Physical mitigation: adaptive optics and aperture averaging

This work emphasized on adaptive optics as a physical mitigation system. It should be noted however that it is not only mean of physically mitigating turbulence induced fading in a downlink path. Systems based on multi-apertures receivers -exploiting receive diversity- have been widely considered as well. Multi-aperture receivers combine signals detected by several subapertures. The optical signals corresponding to each subaperture are downconverted separately and can be processed digitally [Belmonte and Kahn, 2016]. The performance of such receivers has been studied for instance in [Geisler et al., 2016, Belmonte and Kahn, 2011, Aghajanzadeh and Uysal, 2010]. Such a system was demonstrated by the aforementioned LLCD program. Conventionally, multi-aperture receivers require a detection chain per subaperture. Hence, such systems are put to a disadvantage if one intends to multiply the number of channels (by implementing wavelength-division multiplexing) as the number of required amplifiers, detectors and processing chains scales accordingly. In that regard, the use of AO offers an "economy of scale".

Signal fading and channel impairments related to the degradation of the injection efficiency of the incoming signal into a SMF can be specifically mitigated by using AO. The operating principle of AO is detailed in 3.2. It allows to compensate in real-time the phase fluctuations of the incoming wave due to atmospheric turbulence.

Table 1.3 gives characteristic parameters of AO systems used or planned to be used in the framework of optical downlinks. Globally, satellite-to-ground links, especially from LEO satellites, represent a challenging framework for AO due to difficult operational conditions involving scintillation and fast evolving turbulence. Therefore it is only until recently, that the first demonstrations of ground-based AO for optical downlinks were reported (see Section 1.2.1). Consequently, from an experimental point of view much still needs to be done to understand the practical performance limitations of AO, and specifically its impact on the coupling efficiency into SMFs. As such, it should be noted that the systems presented in Table 1.3 might in fact not be representative of future operational systems.

Fundamentally, the characteristic parameters of an AO correction are conditioned by the distance to the satellite and its apparent speed. For instance, in the case of a GEO downlink, the telescope's aperture diameter is expected to be larger -several tens of centimeters to compensate the link loss and close the link budget (see 2.4.3.8)- than in the LEO case. On the other hand, the control-loop frequency of the correction depends on the apparent speed of the satellite and therefore generally is higher in the case of LEO downlinks.

Table 1.3: Overview of several adaptive optics systems used in recent satellite-to-ground demonstrations

System/OGS	Wave-front sensing	Drx	DM	Loop frequency	Application
CARO/ESA OGS [Fischer et al., 2017b] [Fischer et al., 2017a]	Conventional (SH WFS)	100 cm	24x24 actuators	4kHz	LEO/GEO-Ground
OCTL [Wright et al., 2015] [Roberts et al., 2016]	Conventional (SH WFS)	100 cm	Two DMs: LODM 12x12 actuators HODM 34x34 actuators	20kHz	LEO/GEO-Ground
TAOGS [Heine et al., 2018]	Conventional (SH WFS)	27 cm	12x12 actuators	10 kHz	GEO-Ground
ODISSEE and LISA/OCA [Petit et al., 2016]	Conventional (SH WFS)	100 cm	8x8 actuators	1.5 kHz	LEO-Ground

In addition to phase distortions, atmospheric turbulence causes irradiance fluctuations, that is fluctuations in the power impinging the receiving aperture. Those are commonly referred to as scintillation. The impact of scintillation is more important as the propagation distance through the atmosphere increases (see for instance Eq. 2.38). Hence, it potentially severely affects downlinks from LEO satellites whose path changes quickly and elevation angle can become quite low. Scintillation can be mitigated by increasing the aperture of the receiving telescope. This effect is known as aperture averaging and is used in practice to reduce the impact of scintillation on the communication system.

However, since the turbulent wavefront variance increases as $\left(\frac{D_{Rx}}{r_0}\right)^{5/3}$, with r_0 denoting Fried parameter (see Eq. 2.16) and D_{Rx} the diameter of the telescope, increasing the amount of aperture averaging without improving the AO system can intensify the injection losses. Conversely, assuming a fixed diameter aperture, residual scintillation is imposed upon the detector and the AO performance leads to two limiting cases:

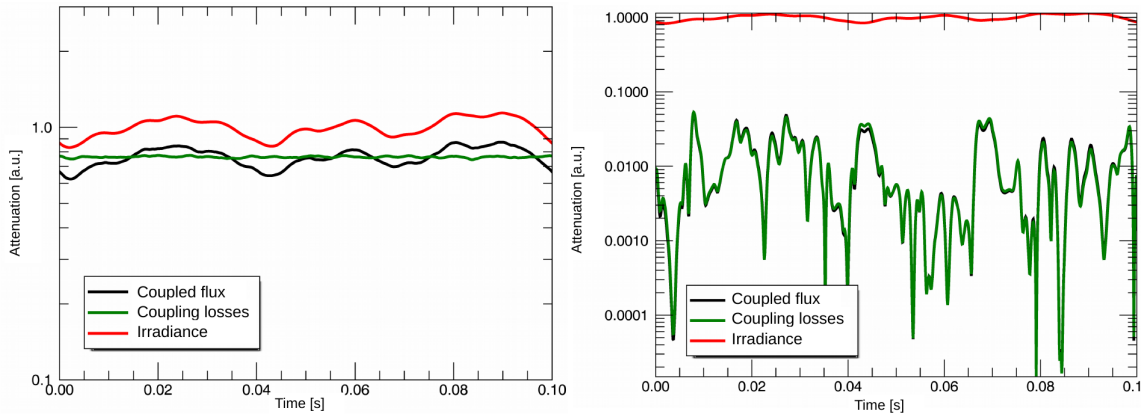

(a) (b)

Figure 1.3: Illustration of two limiting cases related to the performance level of AO for a fixed diameter. (A) The coupling flux fluctuations are dominated by irradiance fluctuations in the case of a very high performance AO. (B) The coupling flux fluctuations are dominated by coupling losses in the case of a poor performance AO.

- A poor AO correction yields fading induced mainly by injection losses
- A very good AO system allows scintillation induced fading

This is illustrated in Fig. 1.3. As mentioned, the latter limiting case might not be achievable for a large aperture -such as required by GEO-to-ground links- if not at the cost of a more complex AO system including non-COTS components.

Such trade-offs analyses are made possible thanks to analytic tools developed and validated during the course of this thesis.

1.2.4 Data reliability mechanisms

In addition to the trade-offs related to aperture averaging and AO, digital mitigation techniques need to be considered as they might relax the specifications and cost of AO systems when very high injection stability is required. The aforementioned channel coding allows the transmitted data to be correctly interpreted at reception despite the loss of a significant fraction of the individual codeword elements when a fading event occurs.

In practice these codewords cannot be made arbitrarily long and are usually adapted to combat randomly distributed errors rather than bursty errors that are characteristic of the free-space optical channel. To overcome this bursty distribution of errors, symbol time-interleaving is mandatory. Typically, these interleavers, after disassembling every codeword will spread their individual elements with a temporal interval comparable to a characteristic duration of the

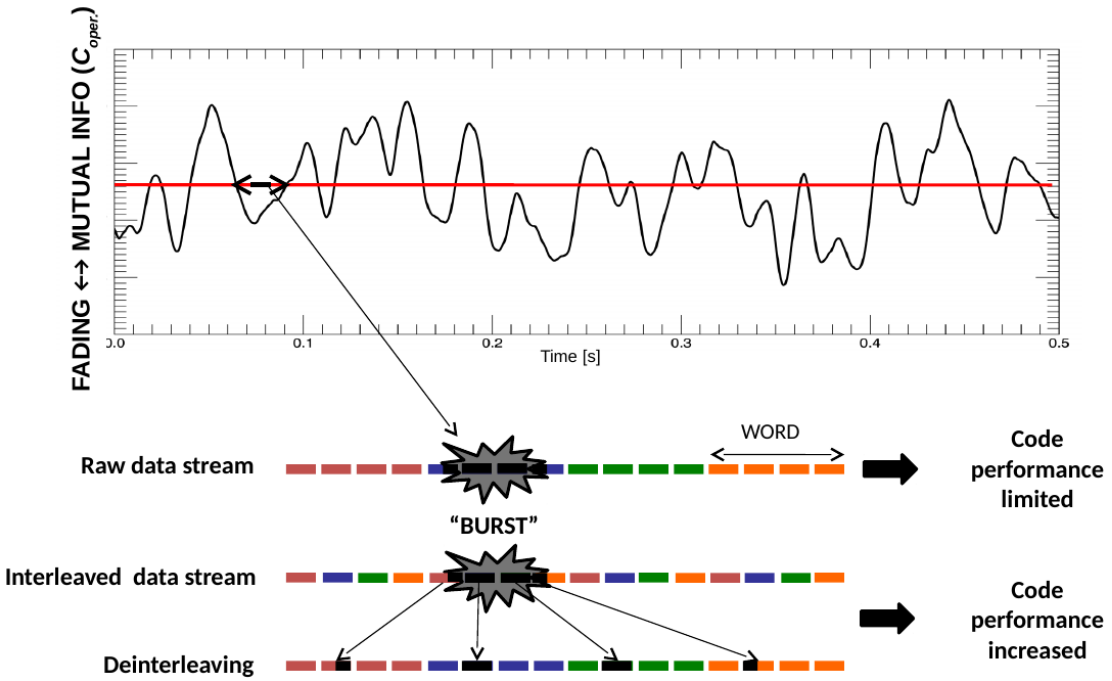

Figure 1.4: Illustration of the impact of the bursty nature of the FSO communication channel on the design of data reliability mechanisms such as interleaving and error coding codes.

channel fades, as illustrated in Fig. 1.4. In addition to the latency inherently introduced by such a fading mitigation technique, the interleaving process may simply lead to potentially high memory sizes due to the typical fading coherence time (see Section 2.4.1).

To alleviate the drawbacks induced by interleavers, reliability mechanisms at the different layers of the communication stack need to be considered. On any correlated channel, by studying the interactions between these reliability mechanisms at different layers, cross-layering strategies that allow for better overall performances may be found. In the framework of satellite optical communication such an approach was considered in [Henniger and Gonzalez, 2006, Henniger, 2006, Fuchs et al., 2007, Henniger, 2007].

In this thesis a similar layered coding scheme is proposed where error correcting codes at the physical layer combined with symbol interleaving is associated to erasure codes combined with packet interleaving at the higher layers.

The benefits related to such a strategy are discussed in details in Section 4.4.

1.2.5 Joint optimization: problem statement

Data reliability techniques are efficient when tailored to fading channel. The optimization of the overall system hence requires an accurate knowledge of the fading statistical and temporal properties. The latter are obviously related to the instantaneous variations of the AO corrected coupled flux into the SMF.

If not by experiments, these statistics can usually be obtained by means of wave-optics simulations that are nonetheless very time consuming or complex to implement when a good depiction of the involved physical phenomena is required.

During this thesis several modeling options and tools have been developed, validated and used. They rely on either simpler digital methods (with respect to wave-optics) for the generation of correlated time series describing the fading channel of interest or on analytic statistical results characterizing the latter (Section 3.3). Accurate modeling of the optical communication subsystem was also undertaken to rigorously investigate the benefits of both time-interleaving and coding (Section 4.2.4).

1.3 Summary of contributions and main results

The global objective of this thesis was to study the reliability of satellite-to-ground optical communication links jointly considering adaptive optics and data reliability mechanisms.

Figure 1.5 presents an overview of the different simulation modules implemented, enhanced and used for that purpose. They can be organized in four groups with respect to:

- the modeling of optical wave propagation in the atmosphere
- the modeling of partial adaptive optics
- the modeling of the communication/detection layer
- the modeling of data reliability mechanisms

At ONERA, several options considering the former two groups are highlighted. They consist of end-to-end simulation tools such as TURANDOT mentioned in 2.3.2 and AOST (Adaptive Optics Simulation Tool) as well as a simplified model named SAOST (Simplified Adaptive Optics Simulation Tool) detailed in Section 3.3.

At ISAE, SIMCOP ("Simulateur Couche Physique Optique" translated as Optical Physical Layer Simulator) was enhanced in order to accurately take into account the characteristics of the communication subsystems (link budget, modulation, impact of noises sources at the

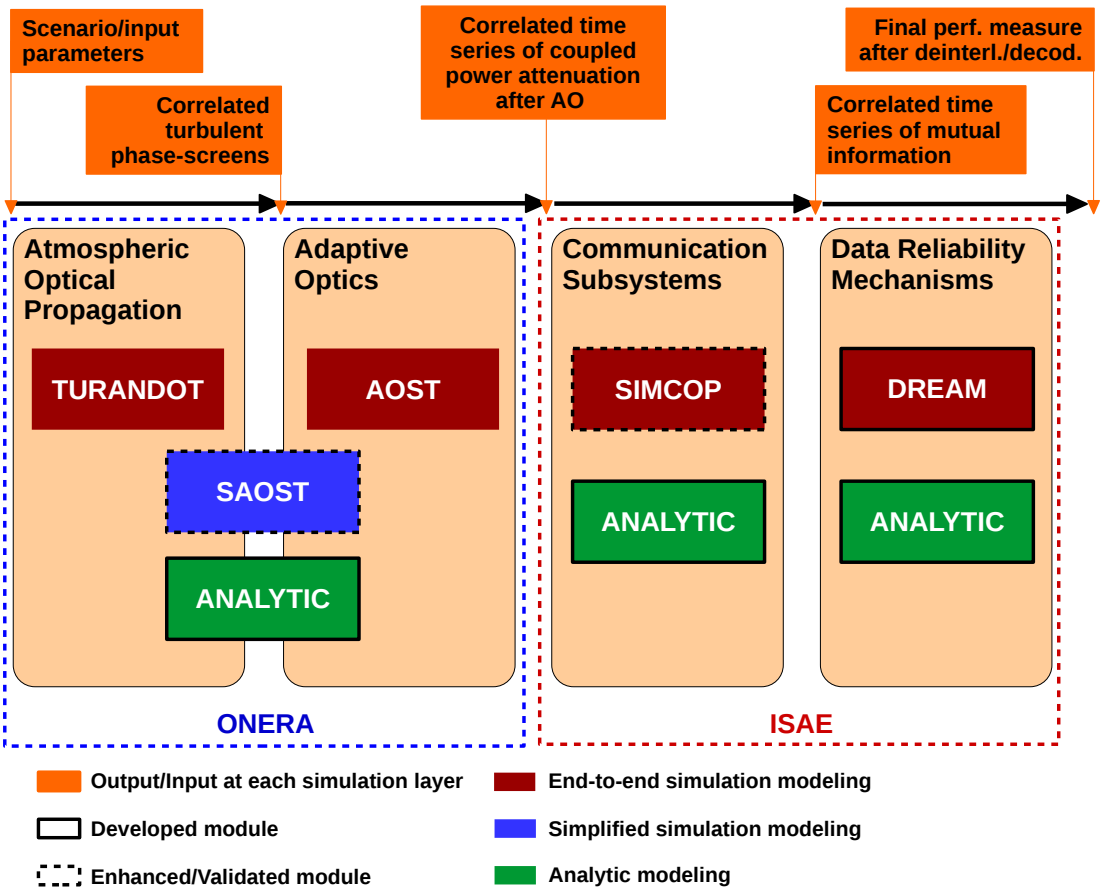

Figure 1.5: Overview of the various domains addressed during the thesis and the contributions made in terms of development or enhancement of existing models. The overall layout allows to compute the decoded packet-error rate at the input of the application layer by taking as input general scenario and system parameters (see Fig. 1.6).

transmitter and receiver sides, filtering). It will be described in further details in Section 4.2. It takes as inputs temporally correlated normalized times series of power attenuation generated by AOST or SAOST and outputs computed time series of instantaneous channel capacity.

The latter are exploited by the last simulation module developed at ISAE, named DREAM (Data Reliability EvAluation Module), in order to study the impact of interleaving and coding at both the physical and higher layers of communication.

As shown in Fig. 1.6 a wide range of input parameters defining several application-cases of interest need to be considered. Future efficient optimization of the overall system including physical mitigation techniques as well as data reliability mechanisms is therefore a complex problem. End-to-end simulation tools such as TURANDOT combined with AOST can render this process very time-consuming and ineffective. Simplified simulation software as well as specific analytic developments presented in the remainder of this manuscript aim to render

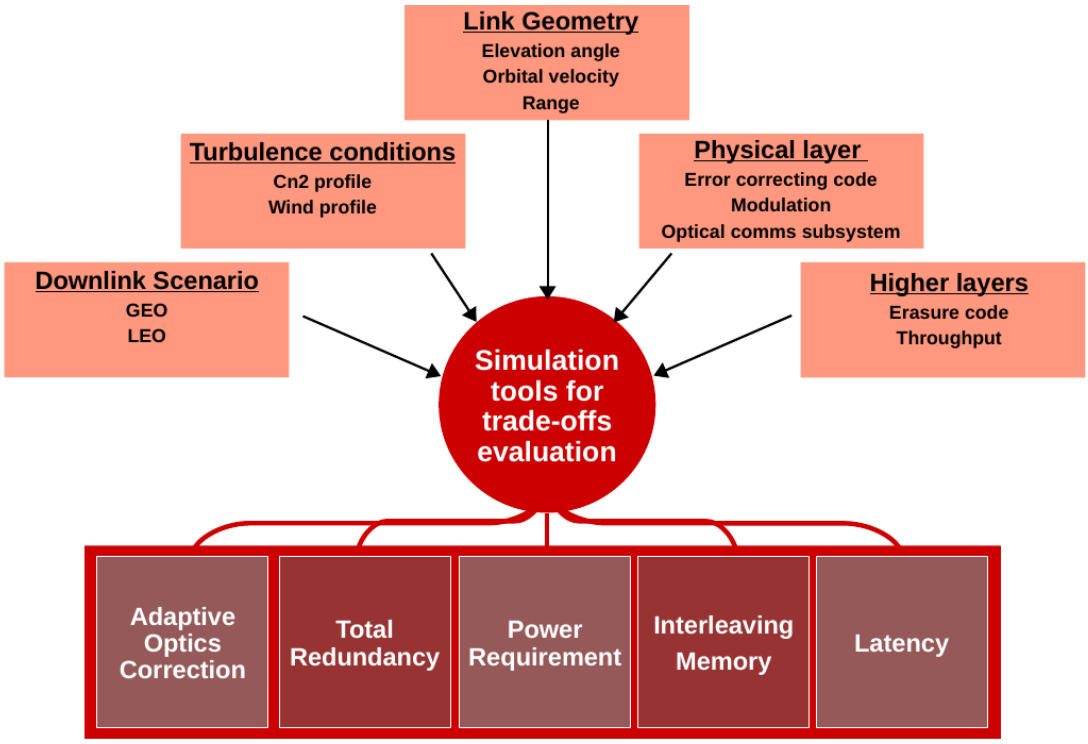

Figure 1.6: Overview of the various input parameters accounted for by the distinct simulation tools in order to investigate trade-offs for the overall system.

this task practical while fairly accurate in the prospect of efficient overall system dimensioning.

Therefore, the main contributions of this work are related to the developments of the various software and models previously mentioned. Their exploitation allowed the in-depth study of the specific characteristics and the various trade-offs of reliable satellite optical donwlinks. The following original results should be underlined:

- An analytic framework for the description of the statistics of the coupled signal into SMFs after partial AO correction has been laid down. This model takes into account the impact of an ensemble of intrinsic errors on the residual wavefront characteristic of real AO systems. It accounts for the impact of both scintillation and phase fluctuations in the computation of SMF coupled flux temporally correlated fluctuations. This model has been compared in details to end-to-end simulations results and validated for both LEO and GEO downlinks at elevations above 20 deg.

- The aforementioned model takes into account the temporal correlation of the satellite-to-ground optical channel. Therefore, in addition to providing relevant statistical results, it allows to easily compute relevant temporal properties (e.g. mean, maximum and minimum duration of fade) of the channel necessary to optimize interleaver and codes

on the physical layer. Novel analytic expressions for these statistical and temporal properties have been developed and validated by simulations. Using those, the impact of distinct AO performances on the distribution of fading duration has been studied for both LEO and GEO downlinks.

- The performance investigation of several physical layer architectures including OOK and DBPSK receivers with distinct AO systems has been conducted. Combining these architectures with interleaving and error correcting codes on the physical layer, trade-offs have been studied. An application case concerning a LEO downlink is presented in this thesis.

- The study of a cross-layered coding scheme and its performances has been conducted. Given a targeted performance level, the optimal combination of the strengths of error and erasure-correction coding and the depths of interleavers was investigated. Such an optimization is done while considering the global system resources (required power, total memory) utilization efficiency. Jointly investigating such a coding scheme with AO leads to interesting results that could influence future system designs.

1.4 Thesis structure

This chapter briefly underlined the motivation for satellite-to-ground optical transmission in general while introducing the work accomplished during this thesis. Due to the various fields of study addressed in this work, it was chosen to not completely disconnect some required fundamentals from the findings in the organization of this manuscript. The remainder of this thesis is organized as follows:

Chapter 2 recalls and summarizes fundamentals of atmospheric propagation theory and information theory. The first parts of Chapter 2 describe the characteristics and properties of the satellite-to-ground optical channel. They recall important concepts as well as the fundamentals of atmospheric optical wave propagation theory. The last section of Chapter 2 is dedicated to recalling important information theory results and relates them to the communication performance measures that will be subsequently studied.

Chapter 3 is dedicated to the investigation of the impact of AO on the fluctuations of coupled flux into SMFs. The fist part of Chapter 3 constitutes a detailed introduction to AO and its principles. End-to-end and simplified modeling options of partial AO are reviewed. The second part of this chapter presents the analytic developments related to the statistical properties of the fluctuations of coupled flux after partial AO correction. The results obtained are validated by end-to-end simulations in the case of LEO and GEO downlink scenarios. Moreover, this part sheds light upon the impact of AO on the channel fade and inter-fade durations through

a case study for the same scenarios.

Chapter 4 presents the data reliability mechanisms studied in this work and investigates their performance. Firstly, it details the communication sub-system modeling. In a second part, it explains in further details the cross-layer approach considered by emphasizing the modeling of the physical and high layer interleaving and coding techniques. To illustrate the scope of the various models developed, the performance of the overall system (including AO and data reliability mechanisms) is investigated through a case study for the LEO downlink. Results from the optimization of the global system are presented. Several features and trends highlighted by these results are explained in further details.

Chapter 5 summarizes and concludes this thesis. Moreover, after discussing the limitations of the presented results, it identifies potential future work.

2 THE SATELLITE-TO-GROUND OPTICAL TRANSMISSION CHANNEL

Contents

2.1 Introduction

This chapter is dedicated to the description of the transmission channel typically characterizing satellite optical downlinks.

The Earth's atmosphere affects the propagation of electromagnetic waves that propagate trough it. Firstly, the purpose of this chapter is to briefly recall the physical mechanisms of atmospheric turbulence. With regard to stochastic phenomena, the tools and statistical models commonly used in the literature to describe the effects of turbulence on a propagating optical wave are recalled. Key parameters and models commonly used in the domain of optical atmospheric propagation and throughout this manuscript are introduced.

In the last part of this chapter the emphasis is put on the impairments experienced by the communication system itself. The turbulent wave-front distortions causes the signal received by the optical ground station to fluctuate. Such fluctuations, called fading can lead to important information losses. In order to understand to what extent the performance of a coded communication system is potentially affected, basic principles and results from information theory are briefly recalled.

2.2 Atmospheric optical propagation

2.2.1 The atmosphere

The atmosphere extends to several hundred kilometers above Earth's surface. Four primary subdivisions of the atmosphere are usually done based on the average temperature variations with altitude as depicted in Fig. 2.1. Most of earth's atmospheric mass is contained in the lower layers (troposphere and stratosphere) which predominantly affects the propagation of electromagnetic radiation [Andrews and Phillips, 2005].

Specifically in the case of optical waves, such a propagation is mostly affected by three phenomena: absorption, scattering and refraction. Absorption and scattering by the constituent gases and particulates of the atmosphere give rise primarily to attenuation of the optical wave. Refraction effects, i.e. fluctuations in the air index of refraction, lead to irradiance fluctuations, beam spreading, beam wander and loss of spatial coherence of the optical wave. These phenomena, over time, lead to power losses at the receiver end that might results in link failures (outages).

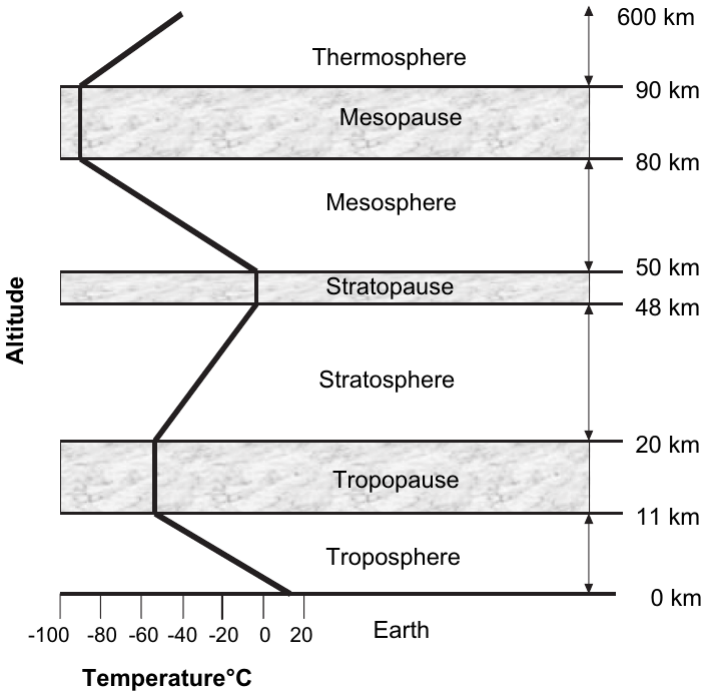

Figure 2.1: Diagram depicting various atmospheric layers and air temperature. From [Andrews and Phillips, 2005]

2.2.1.1 Absorption and scattering

Absorption occurs when a photon of radiation is absorbed by a gaseous molecule of the atmosphere that converts the photon into the molecule's kinetic energy. This process depends strongly on the wavelength of the incoming photons.

In the visible and infra-red bands, scattering occurs when the radiation propagates through certain air molecules and particles. Light scattering is strongly wavelength dependent, however in contrary to absorption, there is no loss of energy. Two types of scattering processes exist, determined by the physical size of the scatterers:

- **Rayleigh scattering** (or molecular scattering) caused by air molecules and haze that are small in comparison with the wavelength of the radiation.
- **Mie scattering** (or aerosol scattering) by particles comparable in size to the radiation wavelength.

Absorption and scattering lead to losses in the power received from the satellite that depend on the transmission wavelength. It is quantified in terms of atmospheric transmittance. Obviously, since the composition of the Earth atmosphere varies with location on Earth and altitude over sea level so does the transmittance as shown by the spectra in Fig. 2.2. Taken

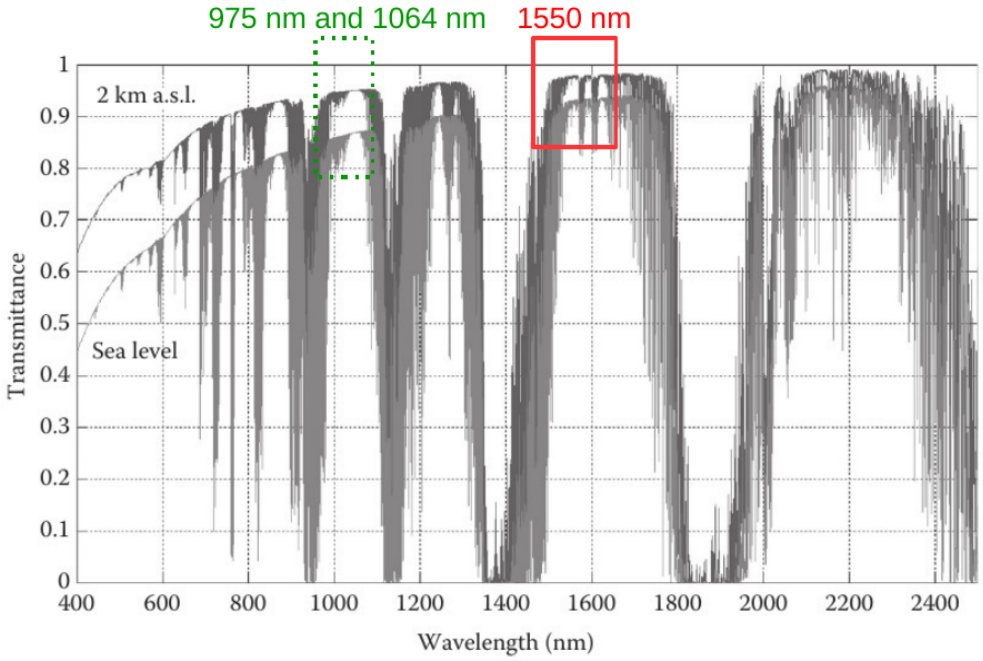

Figure 2.2: Simulated atmospheric transmittance for an Earth-to-space path at zenith. Two scenarios are illustrated: one at sea level and another at 2 km above sea level. Typical transmission windows are highlighted including the one coinciding woth 1550 nm transmitter technologies. From [Hemmati, 2009a]

form [Hemmati, 2009a], this figure depicts such a behavior for a simulated Earth-to-space path at zenith, in a rural aerosol composition for two scenarios where the observer is located at sea level (lower transmittance) and 2 km above sea level.

2.2.1.2 Refraction

The refractive index of the atmosphere, $n(\boldsymbol{r},t)$, is a function of the atmospheric pressure, temperature, and humidity. For optical and infrared wavelengths, it is given by [Owens, 1967, Smith, 1993]:

$$n(\boldsymbol{r},t) = 1 + \alpha_d(\lambda)\frac{P_d(\boldsymbol{r},t)}{T(\boldsymbol{r},t)} + \alpha_w(\lambda)\frac{P_w(\boldsymbol{r},t)}{T(\boldsymbol{r},t)}, \tag{2.1}$$

where $P_d(\boldsymbol{r},t)$ is the partial pressure of the dry air (in mbar), and $P_w(\boldsymbol{r},t)$ the partial pressure of water vapor. The temperature $T(\boldsymbol{r},t)$ is in kelvins. The parameters $\alpha_d(\lambda)$ and $\alpha_w(\lambda)$ are wavelength dependent functions that characterize respectively the atmosphere dry air and water vapor contents. The random variations of $n(\boldsymbol{r},t)$, created by wind shears in the presence of a temperature gradient, induce optical atmospheric turbulence that will greatly affect the propagation of an optical wave. Such fluctuations have important consequences on applications such as astronomical imaging, optical communications, remote sensing, and laser radar for example. Their characteristics are briefly recalled in the next sections of this

chapter.

2.2.1.3 Wavelength selection

Figure 2.2 shows two highlighted transmission windows typically available for optical communication through the atmosphere. However in the recent years, the fiber/telecom industry has developed a selection of inexpensive and reliable electro-optic components working in the 1550 nm band such as vertical-cavity surface-emitting lasers offering very high bandwidth modulation capabilities, erbium-doped fiber amplifiers (EDFA) as well as Avalanche-photodiodes (APDs) or PIN detectors with low noise levels [Agrawal, 2011, Kaminow et al., 2013] that should be leveraged by free-space optical communication in order to reach very high throughput. In addition, the 1550 nm window is known to be more eye-safe than the near-infrared wavelengths [Arnon et al., 2012]. Moreover, it is to some extent less impacted by atmospheric turbulence as turbulence effects are greater for shorter wavelengths. For these primary reasons, transmission at 1550 nm is typically favored over other typical communication wavelengths such as 1064 nm or 975 nm for which there exist favorable atmospheric transmission windows as well. In the remainder of this thesis a transmission wavelength of 1550 nm is assumed.

2.2.2 Atmospheric turbulence

Atmospheric turbulence is produced by the kinetic energy induced by the movement of air masses that is by convection or wind shear. This energy, in a first step, allows for the creation of eddies with a characteristic size called the turbulence outer scale or L_0. It is then transmitted to eddies of decreasing sizes until it is dissipated when reaching the viscosity regime characterized by the turbulence inner scale or l_0. This process is known in the literature as the energy cascade theory (due to Richardson [Richardson and Lynch, 2007]) and is depicted in Fig. 2.3. The outer scale is conditioned by the strength of the phenomena at the origin of the motions of air masses such as the scale of ground temperature variations (at the origin of differences in temperature of air masses close to the ground), humidity (which facilitates heat transfer), viscosity, and even the topography. Near the ground (in the first ten meters), L_0 is strongly influenced by the proximity of the ground. Its order of magnitude is fixed by the distance to the ground. At higher altitude, L_0 can also be influenced by radiative transfers between the atmosphere and solar radiation and can vary from a few meters to several tens of meters. The value of the external scale conditions the amplitude of the low spatial frequencies of the phase disturbances due to turbulence.

The inner scale l_0, on the other hand, is strongly dependent on the density of the atmosphere. From a few millimeters near the ground, it can reach the centimeter in the tropopause.

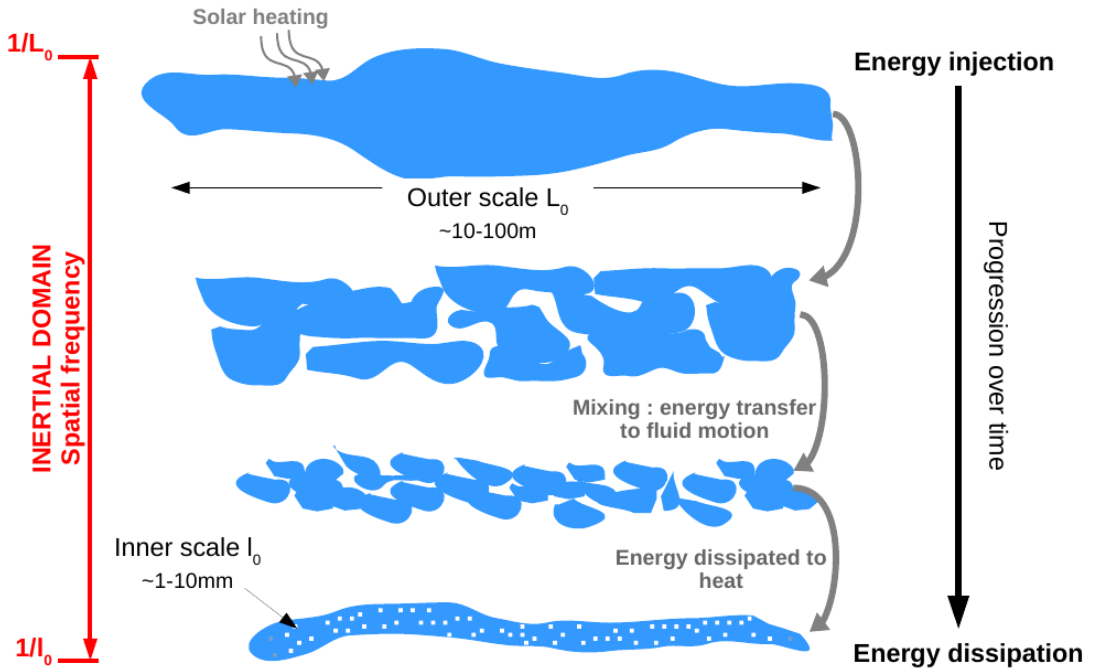

Figure 2.3: Illustration of the energy cascade process and division turbulent eddies in the atmosphere. Kinetic energy is transmitted from large masses of heated air characterized by the outer scale L_0 to smaller scales. Eventually, energy is dissipated as heat when reaching the viscosity regime characterized by the inner scale l_0. Adapted from [Tyson and Frazier, 2012].

The domain lying between these two characteristic scales is called the inertial domain and corresponds to the regime where the turbulence is said to be fully developed. In this domain, the mixing of distinct air masses induces air temperature and humidity fluctuations that in turn leads to fluctuations of the refractive index of air. The latter are at the origin of the perturbations encountered by an optical beam propagating through the atmosphere. It is therefore mandatory to recall relevant properties and characteristics of atmospheric turbulence in order to completely understand the channel impairments experienced by the telecommunication signal and the scope of the mitigation systems considered further.

2.2.3 Statistical properties of the refractive index fluctuations

2.2.3.1 Structure function of the refractive index

At a given altitude h, let us consider the variance of the difference between the index of refraction fluctuations at two points separated by the distance $\boldsymbol{\rho}$:

$$D_{\Delta_n}(\rho, h) = \left\langle \left(\Delta_n(\boldsymbol{r}, h) - \Delta_n(\boldsymbol{r}+\boldsymbol{\rho}, h)\right)^2 \right\rangle \tag{2.2}$$

The function $D_{\Delta_n}(\rho, h)$ is called the structure function of the refractive index fluctuations and the operator $\langle\cdot\rangle$ represents the ensemble average. In the inertial domain, where the turbulence is temporally and spatially stationary, it is shown in [Obukhov, 1949, Corrsin, 1951] that this structure function depends only on $\rho = |\boldsymbol{\rho}|$ and is given by:

$$D_{\Delta_n}(\rho, h) = C_n^2(h)\rho^{\frac{2}{3}}, \quad l_0 < \rho < L_0. \tag{2.3}$$

The term $C_n^2(h)$ is called the index of refraction structure constant which indicates the strength of the turbulence at the altitude h. Its dimensions are measured in $m^{-2/3}$. The inner scale of turbulence, l_0, and the outer scale of turbulence, L_0 limits the inertial domain.

2.2.3.2 Power spectral density of the refractive index

The structure function of the refractive index fluctuations gives access, thanks to a simple Fourier transform and to the Wiener-Khinchine theorem [Tatarski, 1961], to a very convenient mathematical tool commonly used in the characterization of random processes: the power spectrum density of said fluctuations. In the inertial domain such a spectrum -named Kolmogorov's spectrum- is defined by:

$$W_{\Delta_{n,h}}(\boldsymbol{f}) = 0.033(2\pi)^{-\frac{2}{3}} C_n^2(h) f^{-\frac{11}{3}}, \quad \frac{1}{L_0} < f < \frac{1}{l_0}. \tag{2.4}$$

In this equation $\boldsymbol{f}$ is the spatial frequency and $f = |\boldsymbol{f}|$ is given in m^{-1}. A singularity exists when $f = 0$, where this spectrum does not converge. In order to be representative of the whole range of spatial frequencies, this model has to be modified so that it is valid outside the inertial domain as well. It was proposed by Von Karman to take into account the impact of both the inner and outer scales of turbulence:

$$W_{\Delta_{n,h}}(\boldsymbol{f}) = 0.033(2\pi)^{-\frac{2}{3}} C_n^2(h) \left(\frac{1}{L_0^2} + f^2\right)^{-\frac{11}{6}} \exp\left(-\left(\frac{2\pi l_0}{5.91} f\right)^2\right), \quad 0 \leq f < \infty. \tag{2.5}$$

The spectrum given by Eq. (2.5) saturates when $f < L_0^{-1}$ and cuts when $f = l_0^{-1}$. This, in contrary to the simpler model corresponding to Eq. (2.4), ensures that the spectrum does not include any singularity at the price however of providing realistic values for the inner and outer scales. Fortunately, the influence of the external scale and its evaluation have been the subject of much work. In practice, different techniques exist today to estimate it either by direct measurement [Abahamid et al., 2004], as in the case of the Generalized Seeing Monitor [Martin et al., 1994], or by exploiting interferometric data [Ziad et al., 2004, Maire et al., 2006] or Adaptive Optics systems [Rigaut et al., 1991, Fusco et al., 2004]. Altitude-based external scale profiles have been obtained from wavefront slope correlations measured on lunar edge

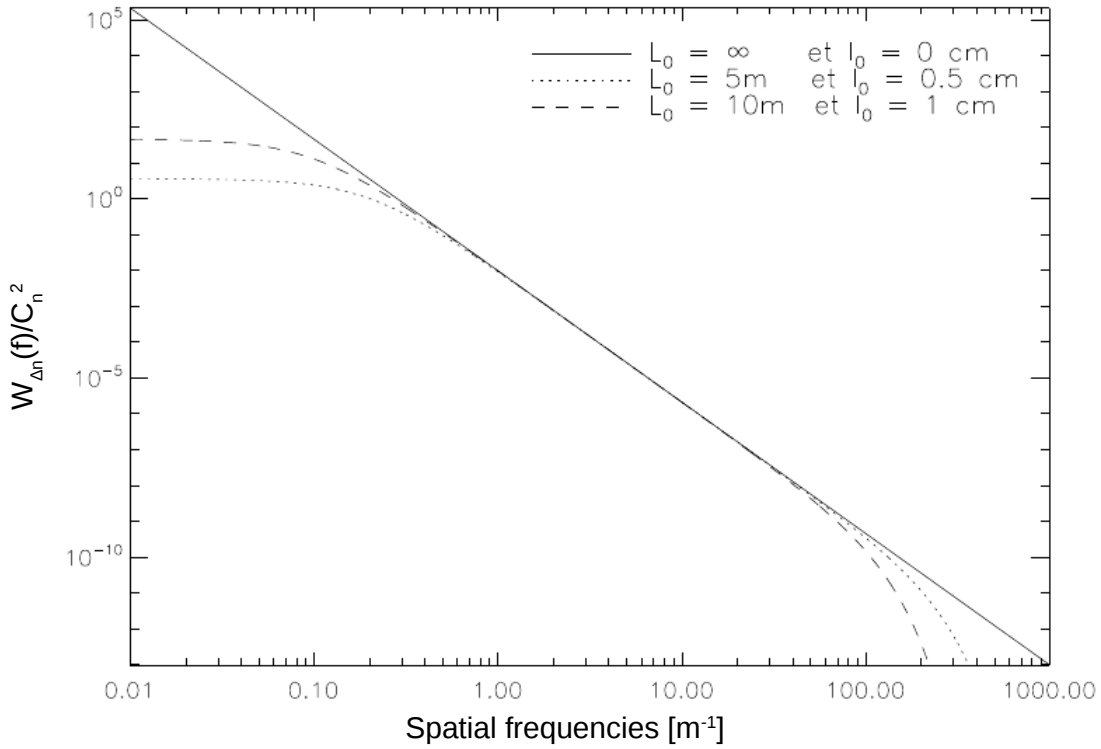

Figure 2.4: Spectral density of refractive index fluctuations for $C_n^2(h) = 1$ and different values of (l_0, L_0)

images [Maire et al., 2007].

The Von Karman spectrum was used for deriving the results presented in this thesis. Figure 2.4 shows the impact of different inner and outer scales of turbulence on the Von Karman spectrum.

2.2.3.3 Refractive index structure constant profile

The refractive index structure constant $C_n^2(h)$ is a measure of the intensity of optical turbulence. Models of this parameter exist at many levels of complexity. They can be based upon empirical and/or theoretical developments and be presented under a purely analytic form (closed or not) or a numerical one requiring input empirical parameters. The refractive index structure constant depends (among different meteorological variables) on the geographical location, altitude, and time of day. Different locations can present distinct characteristics in terms of temperature distribution and humidity that are reflected on the values taken by $C_n^2(h)$. Below the tropopause, the largest gradients of temperature, associated with the largest values of atmospheric pressure and air density are close to ground, at sea level, where therefore one should expect the largest values of $C_n^2(h)$. As the altitude increases the temperature gradient as

well as the atmospheric pressure and air density decrease resulting in smaller values of $C_n^2(h)$ until the tropopause where strong wind shear occurs producing an increase in $C_n^2(h)$ anew.

Moreover, considering the temperature dynamics during the day closer to the ground, one should expect turbulence to be stronger around noon. Conversely, at sunset and dawn, due to a form of thermal equilibrium along the atmosphere vertical profile, one should expect $C_n^2(h)$ to have lower values [Smith, 1993, R.E Good and Dewan, 1988, Jennifer C. Ricklin and Lachinova, 2008, Walters and Kunkel, 1981].

Whereas $C_n^2(h)$ along a horizontal path can be considered "constant", slant path implies that it varies due to the different temperature gradient, air pressure, and density along the altitude. Determining the profile of $C_n^2(h)$ with altitude is a difficult task in the sense that generally, experimental data are not readily available and it is not easy to capture properly its variations measured usually with radiosondes, SCIDAR (SCIntillation Detection And Ranging), SLODAR (SLOpe Detection And Ranging) and SODAR (SOnic Detection And Ranging) [Wilson et al., 2003, Wilson, 2002, Drobinski et al., 1998, Miller et al., 2001].

However, a number of models have been formulated to describe such profiles since the 70s. Most of these original models [R.E Good and Dewan, 1988] were developed for specific places or (micro-)climates complicating their generalization. They are usually referred as non-parametric models i.e. they depend only on the altitude and represent average profiles (without stratification) that are usually highly site-dependent. On the other hand, parametric models have been developed in an attempt to include the dependence on sitehumidity, soil roughness, solar radiation, peculiar wind profile etc.), the stratification (typical profiles show $C_n^2(h)$ varying in layers of thickness of hundred of meters) as well as meteorological parameters. Due to different atmospheric dynamical regimes, $C_n^2(h)$ ranges from $10^{-13}\mathrm{m}^{-2/3}$ near the surface to $10^{-20}\mathrm{m}^{-2/3}$ in the upper atmosphere. The most commonly used profile in the literature is probably the Hufnagel-Valley profile [Valley, 1980]. In the framework of this thesis, the following generic $C_n^2(h)$ profile -derived from a Hufnagel-Valley profile following the International Telecommunication Union recommendation ITU-RP.1621-1- has been used:

$$C_n^2(h) = 8.148\times10^{-56} v_{\mathrm{RMS}}^2 h^{10} \exp\left(\frac{-h}{1000}\right) + 2.7\times10^{-16}\exp\left(\frac{-h}{1500}\right) + C_0\exp\left(\frac{-h}{100}\right). \tag{2.6}$$

This profile depends on two input parameters, v_{RMS} the altitude average wind velocity and C_0 the value of $C_n^2(h)$ at the optical ground station level.

2.3 Optical wave propagation theory

2.3.1 Propagation equation

The refractive index fluctuations due to atmospheric turbulence described in the previous section distort the wavefront of a visible or infrared optical wave propagating through the atmosphere. This causes random fluctuations of the wave's amplitude and phase.

Theoretically, several approaches exist for statistically describing these fluctuations. Some rely on solving the wave propagation equation analytically in the case where small fluctuations are assumed. However this cannot be done for all the propagation regimes. When considering the case of strong turbulence conditions, heuristics and numerical models based on the decomposition of the turbulent volume in phase screens are usually used (e.g. split-step wave propagation simulations).

2.3.1.1 Helmholtz Equation

The developments hereafter apply mainly to the case of a monochromatic plane wave. One intends to characterize the propagated wave in terms of the statistical moments of the random optical field $\boldsymbol{E}(\boldsymbol{r})$. As any other electro-magnetic wave propagating in a dielectric (such as the air), this random optical field follows Maxwell's equations. Assuming that the turbulent atmosphere is isotropic and that the characteristic evolution time of the refractive index fluctuations is smaller than the optical wave period ($2\pi/\omega$), one can show that evolution of $\boldsymbol{E}(\boldsymbol{r},t)$ obeys to Helmholtz's propagation equation:

$$\nabla^2\boldsymbol{E}(\boldsymbol{r}) + k_0^2 n(\boldsymbol{r})^2\boldsymbol{E}(\boldsymbol{r}) + 2\nabla(\boldsymbol{E}(\boldsymbol{r}).\nabla(\log(n(\boldsymbol{r})))) = 0, \tag{2.7}$$

where $\boldsymbol{r}$ represent the coordinates of a point in space, $n(\boldsymbol{r})$ is the refractive index at this point, $k_0 = 2\pi/\lambda$ is the wave number with λ the wavelength of the propagating optical wave. The term $2\nabla(\boldsymbol{E}(\boldsymbol{r}).\nabla(\log(n(\boldsymbol{r}))))$ is related to the variations of polarization of the wave. For the visible and infrared wavelengths typically considered for free-space optical transmissions, this effect can be neglected since λ is very small compared to the variation scale of the refractive index [Tatarskii, 1971]. A reduced wave equation is therefore considered:

$$\nabla^2\boldsymbol{E}(\boldsymbol{r}) + k_0^2 n(\boldsymbol{r})^2\boldsymbol{E}(\boldsymbol{r}) = 0. \tag{2.8}$$

2.3.1.2 Parabolic equation method

In solving the Helmholtz equation, the parabolic equation methods has the advantage that it is applicable under all turbulence conditions. Assuming that an almost plane wave is

propagating in the direction $\vec{e}_z$, the amplitude of the scalar field $E(\boldsymbol{r})$ is:

$$E(\boldsymbol{r}) = A_0 \Psi(\boldsymbol{r}) \exp(ikz). \tag{2.9}$$

Here, $\Psi(\boldsymbol{r})$ is the complex amplitude of the deviation from the perfectly plane wave $\exp(ikz)$ and, A_0 is the unperturbed amplitude. The temporal average of the refractive index characterizing the propagation medium is noted $\langle n(\boldsymbol{r})\rangle$. The wave number is hence given by $k = \langle n(\boldsymbol{r})\rangle k_0$. The complex amplitude $\Psi(\boldsymbol{r})$ is therefore solution of the reduced wave equation:

$$\nabla^2 \Psi(\boldsymbol{r}) + 2ik\frac{\partial \Psi(\boldsymbol{r})}{\partial z} + k_0(n(\boldsymbol{r})^2 - \langle n(\boldsymbol{r})\rangle^2)\Psi(\boldsymbol{r}) = 0. \tag{2.10}$$

The parabolic approximation consists in assuming that $|\frac{\partial^2 \Psi(\boldsymbol{r})}{\partial^2 z}| \ll |k\frac{\partial \Psi(\boldsymbol{r})}{\partial z}|$. This is true as long as the diffraction effects affecting $\Psi(\boldsymbol{r})$ vary slowly with respect to z. Furthermore, if the refraction index fluctuations are small, that is $n_1(\boldsymbol{r}) \ll 1$ where $n(\boldsymbol{r}) = \langle n\rangle + n_1(\boldsymbol{r})$, Eq. (2.10) becomes Helmholtz parabolic equation:

$$\nabla_{\mathrm{T}}^2 \Psi(\boldsymbol{r}) + 2ik\frac{\partial \Psi(\boldsymbol{r})}{\partial z} + 2k_0^2 n_1(\boldsymbol{r})\langle n(\boldsymbol{r})\rangle \Psi(\boldsymbol{r}) = 0, \tag{2.11}$$

where ∇_{T}^2 denotes the transverse Laplacian operator $\left(\frac{\partial^2}{\partial^2 x} + \frac{\partial^2}{\partial^2 y}\right)$. All the aforementioned hypotheses hold in the case of an optical wave (in the visible or the infrared) propagating in the atmosphere hence the parabolic approximation (also called the paraxial approximation in the literature) provides a general method that is theoretically applicable under all atmospheric conditions.

2.3.2 Phase-screen propagation modeling: TURANDOT

Helmholtz equation, whose coefficients evolve spatially and temporally, can be solved analytically only when the turbulence is limited to the regime of weak fluctuations. However, relying on the Markov approximation [Tatarski, 1961], it is locally solvable even in strong turbulence conditions considering a perturbative approach [Lee and Harp, 1969]. It should be noted however that the latter allows to compute certain statistical properties of the propagated field but not a rigorous expression of the propagated field itself.

2.3.2.1 Principle

The phase-screen propagation method is based upon two principles: the discretization of the turbulent volume in several turbulent layers and the separation of the turbulence's impact on the optical wave from its very propagation. This is illustrated in Fig. 2.5. The layers' -or phase-screens'- thickness δh must be sufficiently small in order to ensure that diffraction

effects within them can be neglected, and large enough in order to make sure that they are successively uncorrelated. While the propagation between the phase screens is simulated as if it occurs in perfect vacuum, the diffraction effects inside a layer are modeled as if the latter were an homogeneous medium by assuming $n_1(\boldsymbol{r}) = 0$.
In this framework, using the parabolic approximation for describing the propagation of the perturbation $\Psi(\boldsymbol{\rho}, z = h)$ -where $\boldsymbol{\rho}$ now denotes the coordinates (x, y) in the plan $z = h$- through one layer of thickness δh, is described thanks to a Fresnel propagation:

$$\Psi(\boldsymbol{\rho}, h+\delta h) = \Psi(\boldsymbol{\rho}, h) * \mathscr{F}_{\delta h}(\boldsymbol{\rho}), \tag{2.12}$$

where the symbol $*$ denotes the convolution operator and $\mathscr{F}_{\delta h}$ is Fresnel's propagator defined as:

$$\Psi(\boldsymbol{\rho}, h) * \mathscr{F}_{\delta h}(\boldsymbol{\rho}) = \frac{k \exp[ik\delta h]}{i2\pi\delta h} \int_{-\infty}^{+\infty} d\boldsymbol{\rho'} \Psi(\boldsymbol{\rho'}, h) \exp\left(ik \frac{|\boldsymbol{\rho} - \boldsymbol{\rho'}|^2}{2\delta h}\right). \tag{2.13}$$

Within a layer, the refractive index heterogeneity is modeled by multiplying the field by a simple phase shift term, ϕ, corresponding to the path difference experienced by the optical wave through δh. This phase shift term is computed assuming the near-field approximation as:

$$\phi(\boldsymbol{\rho}, h+\delta h) = k_0 \int_h^{h+\delta h} dh n_1(\boldsymbol{\rho}, h). \tag{2.14}$$

Eventually, the perturbed field emerging from a single layer of thickness δh can then be expressed in function of the input field as:

$$\Psi(\boldsymbol{\rho}, h+\delta h) = \left(\Psi(\boldsymbol{\rho}, h) * \mathscr{F}_{\delta h}(\boldsymbol{\rho})\right) \exp\left[i\phi(\boldsymbol{\rho}, h+\delta h)\right]. \tag{2.15}$$

As represented in Fig. 2.5 this process can be generalized to an arbitrary number of phase screens. The propagated field is therefore modeled as a succession of phase perturbations induced by the phase screens as well as phase and amplitude perturbations induced by the diffraction between the layers [Flatté et al., 1993, Flatté et al., 1994, Martin and Flatté, 1988].

Such a modeling principle is implemented in the propagation code named PILOT ("Propagation et Imagerie Laser ou Optique à travers la Turbulence") [Mahé, 2000] developed by ONERA. Atmospheric turbulence is sampled by a finite number of independent phase-screens. Each of these screens is generated thanks to the Fourier approach [McGlamery, 1976]. More precisely, one generates white noise that is subsequently colored in the Fourier domain by the corresponding turbulent Von Karman spatial spectrum and Fourier inverted to obtain the turbulent phase.

Wave-optics results used during this thesis were obtained thanks to an upgraded version of this code called TURANDOT(TUrbulence simulatoR for spAce-grouND Optical Telecommunication) [Védrenne et al., 2012] that allows for an efficient use of PILOT through the automation of

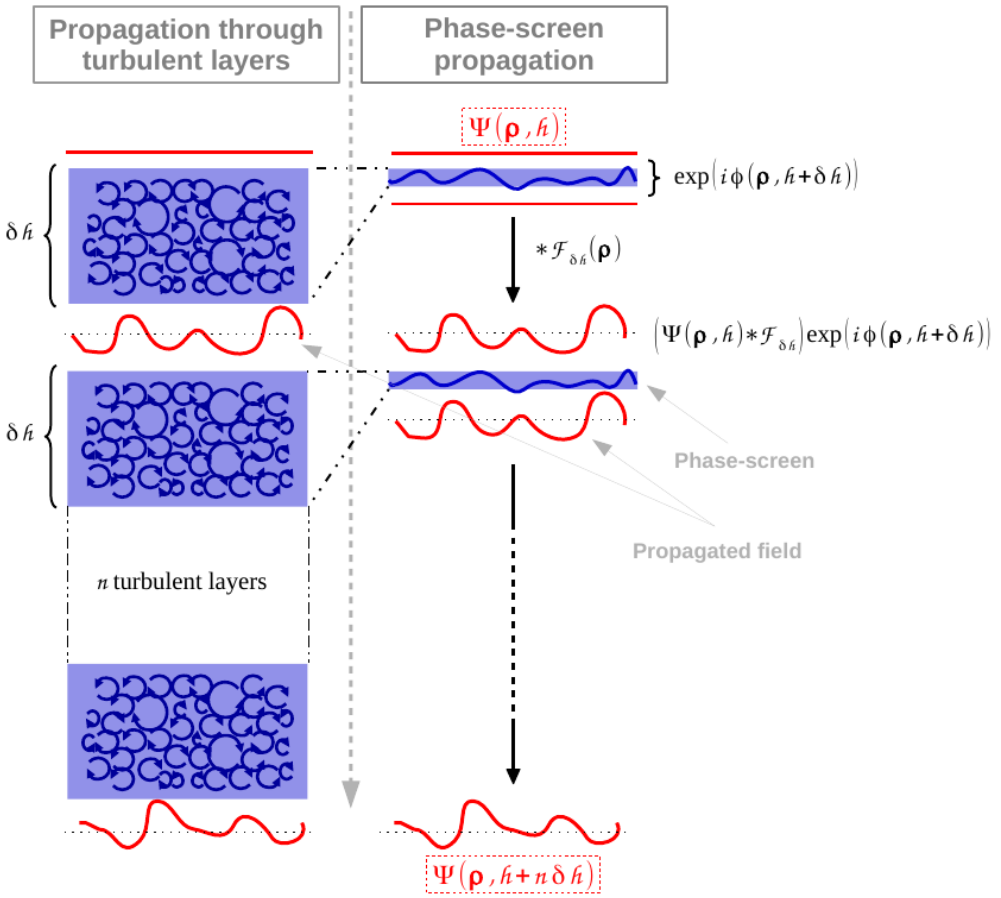

Figure 2.5: Diagram depicting the principle of phase screen propagation.

input parameters relevant to satellite-to-ground links (turbulence and wind profiles, satellite range and velocity etc.), and of an optimization of the phase-screen sampling of the turbulence volume. In the case of a LEO satellite downlink, it has been confronted to experimental data presented in [Védrenne et al., 2012].

2.3.2.2 Spatial Coherence of the Field

An essential parameter when dealing with the effects of atmospheric turbulence on the propagation of an optical beam is Fried parameter r_0. It is defined as an equivalent aperture diameter setting the telescope resolution limit (i.e. in the focal plane) in the presence of turbulence. It accounts for the total strength of turbulence due to the different atmospheric layers along the line-of-sight. For a plane wave and considering a Kolmogorov spectrum it is given by:

$$r_0 = \left[0.42\left(\frac{2\pi}{\lambda}\right)^2 \sec(\Theta)\int_0^L C_n^2(h)\,dh\right]^{-\frac{3}{5}}, \tag{2.16}$$

where Θ is the satellite zenith angle. It can be related to the spatial coherence function of the field (a quantity defined in the pupil plane). The latter is defined in the pupil plane as:

$$B_\Psi(\boldsymbol{\rho}', \boldsymbol{\rho}, L) = \langle \Psi(\boldsymbol{\rho}', L, t)\Psi^*(\boldsymbol{\rho}' + \boldsymbol{\rho}, L, t)\rangle. \tag{2.17}$$

Assuming stationary refractive index fluctuations and a unitary average refractive index, relying on the phase-screen propagation principle, Roddier has shown:

$$B_\Psi(\rho) = \exp\left(\frac{\rho}{\rho_0}\right)^{\frac{5}{3}}, \tag{2.18}$$

where $\rho = |\boldsymbol{\rho}|$ and ρ_0 denotes the coherence length of the field. This quantity corresponds to the distance between two points for which the spatial correlation equals $1/e$. It is related to r_0 by:

$$r_0 = 2.11\rho_0. \tag{2.19}$$

2.3.2.3 Temporal effects modeling

Assuming that the characteristic evolution time of the wavefront is negligible compared to its translation -due to wind- in front of the telescope aperture, spatial statistics can be converted to temporal statistics by knowledge of the average transverse wind speed $V_\perp(\boldsymbol{r})$. This is known as Taylor's frozen turbulence hypothesis. The refractive index at time t can therefore be computed as:

$$n(t) \simeq n(\boldsymbol{r} - V_\perp(\boldsymbol{r})\, t). \tag{2.20}$$

In practice, modeling the temporal evolution of turbulence is equivalent to translating the phase screens transversely to the propagation direction. As in the case of the refractive index structure constant, the wind strength depends on altitude. The well-known Bufton wind profile [Bufton, 1973] is considered here. The transverse wind speed $V_{\text{wind}}(h)$ at altitude h is:

$$V_{\text{Wind}}(h) = V_{\text{Grnd}} + V_{\text{Trop}} \exp\left(-\frac{h - h_{\text{Trop}}}{D_{\text{Trop}}}\right)^2, \tag{2.21}$$

where V_{Grnd} is the ground wind speed, V_{Trop} is the wind speed at the tropopause, h_{Trop} is the height of the tropopause, and D_{Trop} its thickness.

In addition to the wind speed, the translation of a given turbulent layer (phase screen) at altitude h must account for the beam slew rate related to the velocity of the satellite. Consider the diagram represented in Fig. 2.6. In a Cartesian coordinate system centered on the OGS, the satellite line-of-sight is referenced by its elevation angle Θ and azimuth angle ϕ. The intersection of the line-of-sight with a given turbulent layer situated at an altitude h from ground defines the point S_r which is at a distance r from the OGS. It defines as well the

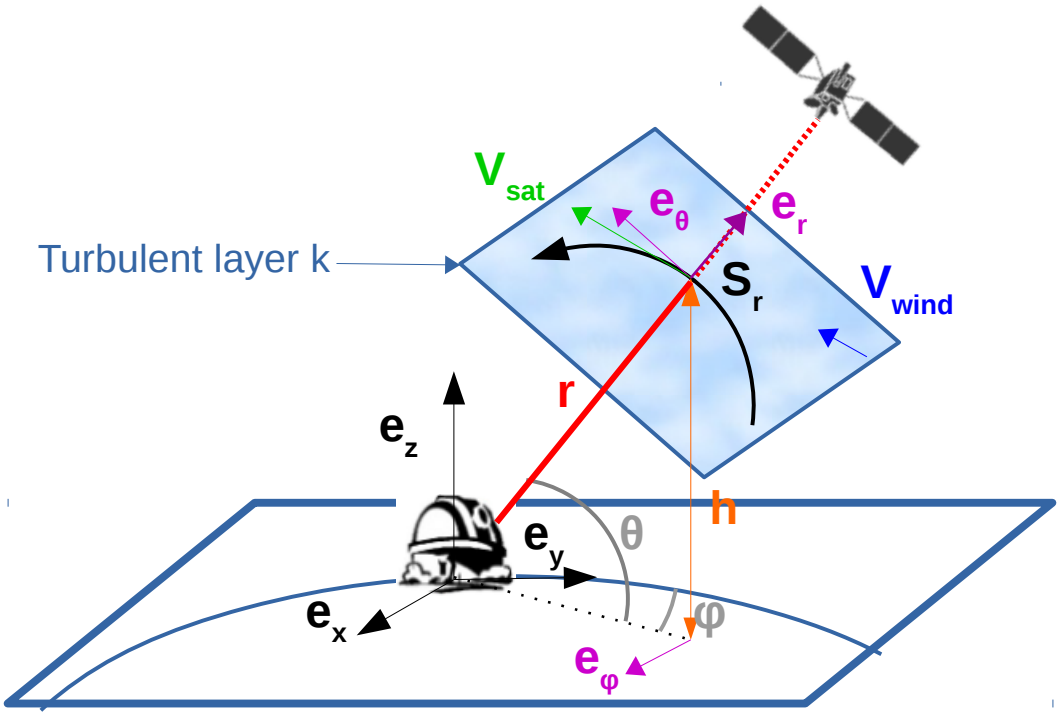

Figure 2.6: Notation conventions for the translation of a given turbulent layer (phase screen) at altitude h between two instants.

spherical coordinates system $(S_r, e_r, e_\Theta, e_\phi)$. The orthoradial component of the instantaneous velocity of the point S_r, in the turbulent layer referential, is equal to:

$$V_{\text{Sat}} = r\dot{\Theta}e_\Theta + r\cos(\Theta)\dot{\phi}e_\phi. \tag{2.22}$$

Between two following simulated samples, the temporal evolution due to both natural wind and the satellite's speed is therefore modeled by translating each turbulent layer along the line-of-sight at a speed:

$$V_{\text{Layer}}(h) = h\omega_{\text{Sat}} + V_{\text{Wind}}(h), \tag{2.23}$$

where, again h denotes the height of one particular layer and ω_{Sat} the satellite's angular velocity given by

$$\omega_{\text{Sat}} = \frac{V_{\text{Sat}}}{D_{\text{Sat}}}, \tag{2.24}$$

with D_{Sat} the distance between the OGS and satellite. Note that this model assumes that both the speed of the satellite and of the wind are oriented in the same direction.

2.3.3 Weak fluctuations regime

As stated in the previous section, Helmholtz's equation admits an analytic solution assuming that the amplitude of the perturbations induced by atmospheric turbulence are small. Historically, two approaches based on this weak fluctuations assumption have been developed: the Rytov approximation [Tatarski, 1961] and the Born approximation [Clifford,]. Both are based on a linearization of the wave equation, however they differ by certain assumptions underlying this linearization. In this manuscript we will only recall the treatment related to the Rytov approximation. Using the latter one can find an expression of the complex amplitude of the perturbed field and thus of its statistical properties.

2.3.3.1 Rytov approximation

Let $E_0(\boldsymbol{r}) = \exp(\psi_0(\boldsymbol{r}))$ denotes the amplitude of the field of a monochromatic wave. As it propagates through a turbulent volume, it is affected by random fluctuations of the refractive index according to Eq. (2.8). In the Rytov approximation, this propagating field is written as:

$$E(\boldsymbol{r}) = \exp(\psi_0(\boldsymbol{r}) + \psi(\boldsymbol{r})). \tag{2.25}$$

Applying the reduced wave equation (2.8) to it yields:

$$\nabla^2(\psi_0(\boldsymbol{r}) + \psi(\boldsymbol{r})) + \big(\nabla(\psi_0(\boldsymbol{r}) + \psi(\boldsymbol{r}))\big)^2 + k_0^2 n(\boldsymbol{r})^2 = 0. \tag{2.26}$$

Moreover, the unperturbed field $E_0(\boldsymbol{r})$ follows Helmholtz's equation as well:

$$\nabla^2\psi_0(\boldsymbol{r}) + \big(\nabla\psi_0(\boldsymbol{r})\big)^2 + k_0^2\langle n(\boldsymbol{r})\rangle = 0. \tag{2.27}$$

By expanding $n^2(\boldsymbol{r})$ as $n^2(\boldsymbol{r}) = \langle n(\boldsymbol{r})\rangle^2(1 + 2\delta n(\boldsymbol{r}) + \delta n^2(\boldsymbol{r}))$, where $\delta n(\boldsymbol{r}) = \frac{n_1(\boldsymbol{r})}{\langle n(\boldsymbol{r})\rangle}$ corresponds to the fluctuations of $n(\boldsymbol{r})$, and by inserting Eq. (2.27) into Eq. (2.26) yields:

$$\nabla^2\psi(\boldsymbol{r}) + \nabla\psi(\boldsymbol{r}).(\nabla\psi(\boldsymbol{r}) + 2\nabla\psi_0(\boldsymbol{r})) + k_0^2\delta n^2(\boldsymbol{r}) + 2k_0^2\langle n(\boldsymbol{r})\rangle\delta n(\boldsymbol{r}) = 0. \tag{2.28}$$

Equation (2.28) can be solved analytically assuming that the terms $(\nabla\psi(\boldsymbol{r}))^2$ and $k_0^2\delta_n^2$ can be neglected. The Rytov approximation consists in considering that these assumptions are verified when the following conditions are satisfied [Tatarski, 1961, Brown, 1966, Fante, 1975]:

- $\delta n(\boldsymbol{r}) \ll 1$.
- $|\nabla\psi(\boldsymbol{r})| \ll |\nabla\psi_0(\boldsymbol{r})| = k_0$.

The first condition imposes that refractive index fluctuations are small, which is always verified in the atmosphere. The second condition imposes an important constraint on the

strength of the perturbations that affect $E(\boldsymbol{r})$ that limits the validity of the Rytov approximation [Fante, 1975] to the so-called weak fluctuations regime of turbulence. When both these conditions are satisfied, Eq. (2.28) becomes:

$$\nabla^2\psi(\boldsymbol{r}) + 2\nabla\psi_0(\boldsymbol{r})\nabla\psi(\boldsymbol{r}) + 2k_0^2\langle n(\boldsymbol{r})\rangle\delta n(\boldsymbol{r}), \tag{2.29}$$

to which a solution is:

$$\psi(\boldsymbol{r}) = \frac{k^2}{2\pi E_0(\boldsymbol{r})}\int_{\mathcal{V}} d\boldsymbol{r'}\delta n(\boldsymbol{r'})E_0(\boldsymbol{r'})\frac{\exp(ik|\boldsymbol{r}-\boldsymbol{r'}|)}{|\boldsymbol{r}-\boldsymbol{r'}|} \tag{2.30}$$

2.3.3.2 Statistical properties of the field

In the framework of the Rytov approximation the perturbation induced by refractive index fluctuations, $\exp(\psi(\boldsymbol{r}))$, can be decomposed into two terms related to different contributions:

$$\psi(\boldsymbol{r}) = \chi(\boldsymbol{r}) + i\phi(\boldsymbol{r}). \tag{2.31}$$

The terms $\chi(\boldsymbol{r})$ and $\phi(\boldsymbol{r})$ are respectively the amplitude (usually called log-amplitude) and the phase associated to the perturbation. Applying the parabolic approximation to Eq. (2.31) yields [Tatarski, 1961, Sasiela, 1994]:

$$\chi = \frac{k^2}{2\pi}\int_0^L \frac{dh}{L-h}\int_{-\infty}^{+\infty} d\boldsymbol{\rho'}n_1(\rho',h)cos\left(k\frac{|\boldsymbol{\rho}-\boldsymbol{\rho'}|^2}{2(L-h)}\right), \tag{2.32}$$

$$\phi = \frac{k^2}{2\pi}\int_0^L \frac{dh}{L-h}\int_{-\infty}^{+\infty} d\boldsymbol{\rho'}n_1(\rho',h)sin\left(k\frac{|\boldsymbol{\rho}-\boldsymbol{\rho'}|^2}{2(L-h)}\right) \tag{2.33}$$

2.3.3.2.1 Power spectrum densities

As a first statistical characterization of these quantities one can consider their power spectrum densities:

$$W_\chi(\boldsymbol{f}) = k^2\int_0^L W_{\Delta_{n,h}}\sin^2(\pi h\lambda f^2)dh, \tag{2.34}$$

$$W_\phi(\boldsymbol{f}) = k^2\int_0^L W_{\Delta_{n,h}}\cos^2(\pi h\lambda f^2)dh, \tag{2.35}$$

where $W_{\Delta_{n,h}}$ is given by Eq. (2.5) for the Von Karman spectrum of refractive index fluctuations and with the propagation occurring from $h = L$ to $h = 0$. These expressions for the power spectrum densities of χ and ϕ are obtained thanks to Eq. (2.30) and to the application of the phase-screens decomposition of the turbulent volume as in [Roddier, 1981]. One notes that in the weak fluctuations regime the impact of the turbulence corresponds in fact to filtering the electromagnetic field. Hence it provides a simple way to take into account the effects related

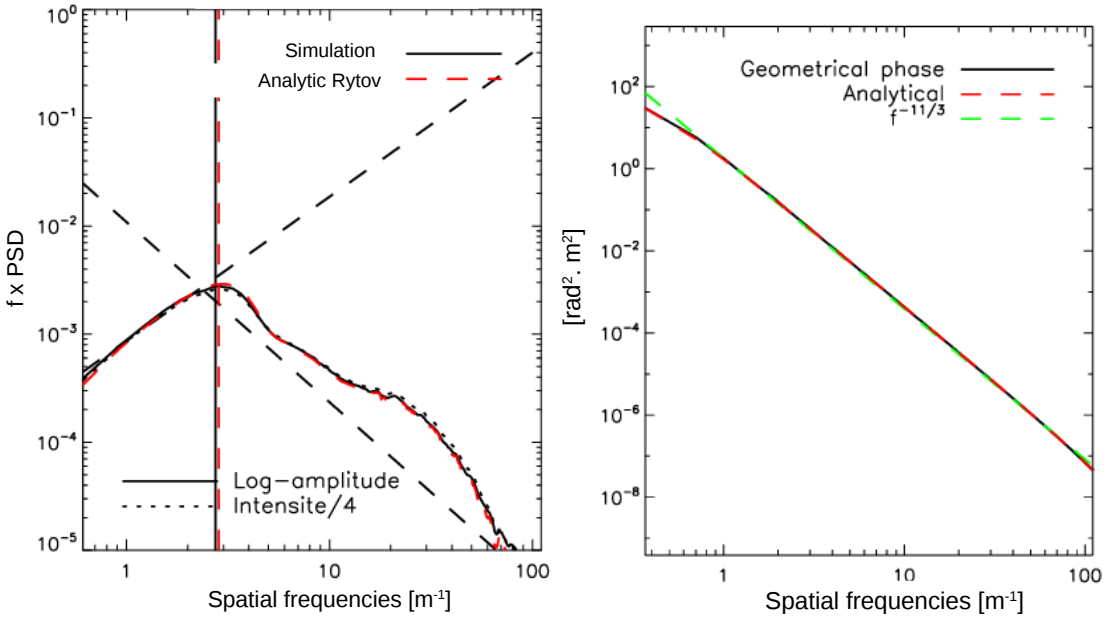

(a) (b)

Figure 2.7: Simulated spectra of log-amplitude (A) and plane-wave phase fluctuations (B) in the plane of the receiver after a 20 km propagation and for a Von Karman spectrum of refractive index fluctuations. Analytic spectra are reported as well (dashed red lines) using Rytov approximation for the log-amplitude and the Von Karman spectra for the phase.

to the geometry of the optical system [Sasiela, 1994]. Figure 2.7 shows the simulated spectra of χ and ϕ for a GEO-downlink using the $C_n^2(h)$ profile given in 2.6. The spectrum $W_\chi(\boldsymbol{f})$ presents a maximum that characterizes the intensity fluctuations (scintillation speckle). In the case of a single turbulent layer as presented here, this maximum occurs at $f = \frac{1}{\sqrt{\lambda L}}$, where λL is commonly referred to as the Fresnel distance.

The variances of χ and ϕ are given by the integrals of the corresponding power spectrum densities:

$$\sigma_\chi^2 = k_0^2 \int_0^L \int_0^\infty 2\pi f W_{\Delta_{n,h}} \sin^2(\pi h \lambda f^2) df dh, \tag{2.36}$$

$$\sigma_\phi^2 = k_0^2 \int_0^L \int_0^\infty 2\pi f W_{\Delta_{n,h}} \cos^2(\pi h \lambda f^2) df dh. \tag{2.37}$$

Equation (2.36) converges even when one considers Kolmogorov's spectrum (that diverges in $f = 0$, see Eq. (2.4)) due to the weighting by the term $\sin^2(\pi h \lambda f^2)$. The log-amplitude variance is therefore not very affected by the outer scale of turbulence and hence a simpler, analytic expression exists for σ_χ^2:

$$\sigma_{\chi R}^2 = 0.5631 k^{7/6} \sec^{11/6}(\Theta) \int_0^L C_n^2(h) h^{5/6} dh. \tag{2.38}$$

Empirically, it has been shown that $\sigma_{\chi R}$ is accurate as long as it is less than 0.3 [Fante, 1975, Clifford et al., 1974] and as such, provides a parameter delimiting the weak fluctuations regime. This analytic expression emphasizes that, for plane waves, the turbulent layers farther away from the receiver contribute to scintillation.

2.3.3.2.2 Probability density functions

In weak fluctuations, ϕ is the sum of independent and centered Gaussian random variables (see Eq. (2.32)). Therefore it follows a Gaussian probability density function centered in 0 with a full width at half maximum of $2\sqrt{2\log 2}\sigma_\phi$.

In weak fluctuations, χ is also a Gaussian random variable. However, the optical wave irradiance (sometimes called intensity), denoted I in the following, is a parameter of greater interest especially in the regime of moderate to strong turbulence. It is given by the squared magnitude of the field: $I = \Psi\Psi^* = I_0 \exp(2\chi)$ and therefore follows a log-normal probability density function [Goodman, 1985]:

$$p(I) = \frac{1}{2\sqrt{2\pi} I \sigma_\chi} \exp\left[-\frac{\left(\log\left(\frac{I}{I_0}\right) - 2\langle\chi\rangle\right)^2}{8\sigma_\chi^2} \right], I > 0. \tag{2.39}$$

In Eq. (2.39), $\langle\chi\rangle = -\sigma_\chi^2$ to ensure energy conservation [Fried, 1966]. Commonly, to quantify the amount of scintillation affecting a system, one defines the scintillation index σ_I^2 as the normalized variance of the field intensity. It is related to the variance of the log-amplitude as follows:

$$\sigma_I^2 = \frac{\langle I^2\rangle}{\langle I\rangle^2} - 1 = \exp\left(4\sigma_\chi^2 - 1\right). \tag{2.40}$$

An expansion to the first order of the intensity in terms of χ, hence valid for weak fluctuations, yields:

$$\sigma_I^2 = 4\sigma_\chi^2. \tag{2.41}$$

2.3.3.3 Limits of validity

Throughout this thesis, the presented original developments were made assuming the regime of weak fluctuations. It is however important to keep in mind potential difficulties that might limit the scope of such results in practice.

The Rytov approximation leads to a simple analytic characterization of the properties of the propagated field. It is however no longer valid when the strength of the fluctuations increases. Strong fluctuations induce the emergence of a saturation of intensity fluctuations [Gracheva and Gurvich, 1965] that the approximation of weak fluctuations is incapable of

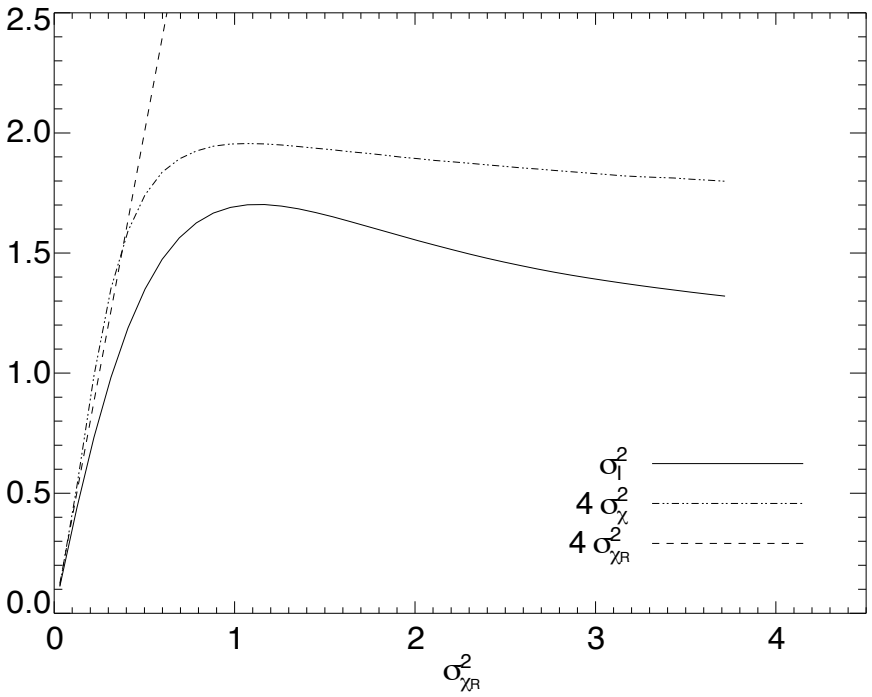

Figure 2.8: The emergence of the saturation of the fluctuations of intensity as the strength of the fluctuations increases.

reproducing. There is no longer any analytic solution to the Helmholtz equation. However, the Markov approximation is still valid and therefore the statistical properties of the perturbed field can still be studied by a phase-screen propagation approach. The ability to reproduce by numerical simulation the properties of the perturbed field in the case of strong perturbations has been confirmed by numerous measurements [Flatté et al., 1993, Flatté et al., 1994, Martin and Flatté, 1988].

The saturation regime is illustrated in Figure 2.8 which represents the evolution of such intensity fluctuations characterized by their variance (σ_I^2 for intensity as well as σ_χ^2 for the log-amplitude) against Rytov variance $\sigma_{\chi R}^2$ defined by Eq.(2.38). The evolution of σ_I^2 and $4\sigma_{\chi R}^2$ are close as long as $\sigma_{\chi R}^2 \leq 0.15$. This zone delimits the very weak fluctuations regime. However the evaluation of σ_χ^2 by Rytov's expression is satisfying up to roughly $\sigma_{\chi R}^2 \leq 0.3$. The statistical properties of the intensity fluctuations in the strong fluctuation regime have been investigated in [Wang and Strohbehn, 1974, Gazzi et al., 1976, Churnside and Clifford, 1987, Gochelashvily and Shishov, 1971]. For instance, in the saturated regime, it is possible to show that the probability density function of the intensity tends towards an exponential distribution [Gochelashvily and Shishov, 1971]. Other heuristic models have been proposed to describe the properties of the intensity in the moderate to strong regime [Hill and Frehlich, 1997, Andrews et al., 1999].

Strong fluctuations will affect the statistical description of phase fluctuations as well. This is due to the apparition of "branch points" (discontinuities) associated with nulls in the intensity pattern of the propagated field [Fried and Vaughn, 1992, Voitsekhovich et al., 1998]. Such discontinuities affect the phase measurements required by adaptive optics systems and hence their performance. While somewhat complex, practical solutions have been proposed to estimate the phase while minimizing the impact of branch points [Roggemann and Koivunen, 2000b, Roggemann and Koivunen, 2000a, Fried, 2001] in the framework of AO.

2.3.4 Modal decomposition of the phase

It is usually convenient to decompose the turbulent phase onto a discrete number of modes (or basis) in order to model its evolution. Several bases exist, the most commonly used one being the Zernike polynomials that will be described in further details. Other bases traditionally used include for instance the deformable mirror modes of an adaptive optics system.

2.3.4.1 Zernike polynomials

The Zernike polynomials have the advantage to constitute an orthonormal basis over a circular pupil of surface $\mathscr{S}$ [Noll, 1976] :

$$\frac{1}{\mathscr{S}}\int_{\mathscr{S}} Z_i^*(\boldsymbol{r})Z_j(\boldsymbol{r})d\boldsymbol{r} = \delta_{ij}. \tag{2.42}$$

In Eq. (2.42), δ_{ij} represents the Kronecker symbol. Each polynomial of this basis has an analytic expression that is the product of radial function $R_n^m(\boldsymbol{r})$ and an azimuthal function $\Theta_n^m(\theta)$ where the parameters n and m are respectively their radial and azimuthal degrees:

$$Z_i(\boldsymbol{r}) = R_n^m(\boldsymbol{r})\Theta_n^m(\theta), \tag{2.43}$$

with

$$R_n^m(r) = \sum_{s=0}^{(n-m)/2} \frac{(-1)^s(n-s)!}{s![(n+m)/2-s]![(n-m)/2-s]!}\boldsymbol{r}^{n-2s}, \tag{2.44}$$

and

$$\Theta_n^m(\theta) = \begin{cases} \sqrt{n+1} & \text{if} \quad m=0 \\ \sqrt{2(n+1)}\cos(m\theta) & \text{if} \quad m\neq 0 \quad \text{and} \quad i \quad \text{even} \\ \sqrt{2(n+1)}\sin(m\theta) & \text{if} \quad m\neq 0 \quad \text{and} \quad i \quad \text{odd} \end{cases} \tag{2.45}$$

The first 21 polynomials are represented in Fig. 2.9. They are usually classified by increasing radial and azimuthal orders. This classification corresponds to the ordering of the turbulence's spatial frequencies: the higher the polynomial order, the higher is the spatial frequency. It corresponds as well to the energy content of turbulence: the higher the polynomial orders, the

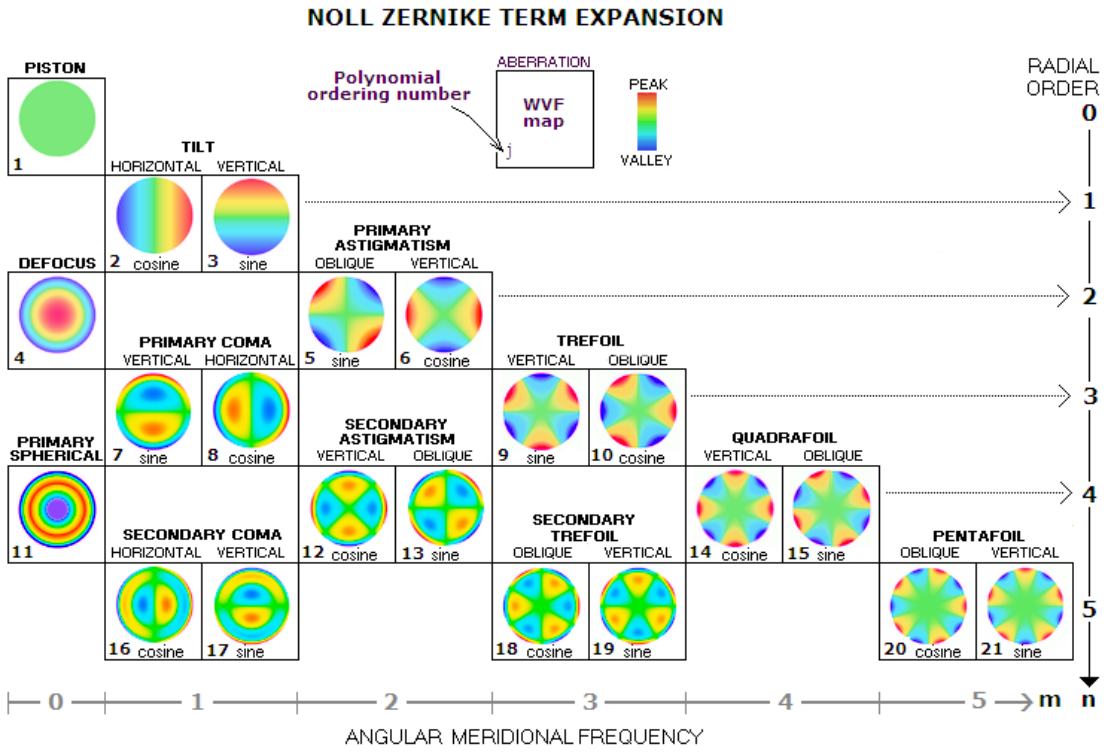

Figure 2.9: The first 21 Zernike polynomials and their corresponding radial and azimuthal orders. From [Sacek,]

lower is their energy content [Wang et al., 1978].

2.3.4.2 General properties of the turbulent phase decomposed onto Zernike polynomials

The Zernike basis being a complete set, the turbulent phase is expressed as:

$$\phi(\boldsymbol{r}) = \sum_{i=1}^{\infty} a_i Z_i(\boldsymbol{r}), \tag{2.46}$$

where a_i is the coefficient corresponding to $Z_i(\boldsymbol{r})$ and is given by:

$$a_i = \frac{1}{\mathscr{S}} \int_{\mathscr{S}} \phi(\boldsymbol{r}) Z_i(\boldsymbol{r}) d\boldsymbol{r}. \tag{2.47}$$

These coefficients allow a simple statistical characterization of the turbulent phase. For instance, Noll [Noll, 1976] has developed an expression of the covariance between two turbulent

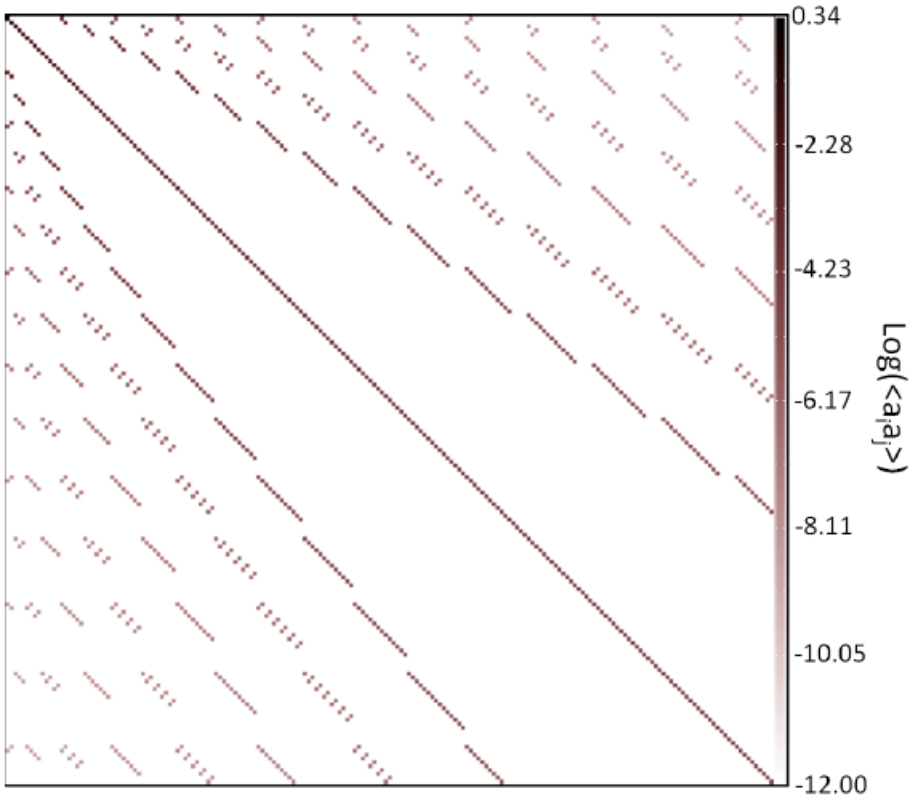

Figure 2.10: Covariance matrix of Zernike modes assuming Kolmogorov like turbulence. Note the logarithmic scale in order to distinguish the weak non-diagonal terms.

modes i and j expressed for a Kolmogorov spectrum:

$$\begin{aligned}\left\langle a_i a_j \right\rangle = 3.9\sqrt{(n_i+1)(n_j+1)}(-1)^{(n_i+n_j-2m_i)/2}\delta_{m_i m_j}\left(\frac{D}{r_0}\right)^{5/3} \\ \times \frac{2^{-14/3}\Gamma(14/3)\Gamma\left((n_i+n_j-5/3)/2\right)}{\Gamma\left((-n_i+n_j+17/3)/2\right)\Gamma\left((n_i-n_j+17/3)/2\right)\Gamma\left((n_i+n_j+23/3)/2\right)},\end{aligned} \tag{2.48}$$

where n_i, m_i (respectively n_j, m_j) denotes the radial and azimuthal order of mode i (respectively j). The pupil diameter is D, and $\Gamma(\cdot)$ denotes the Gamma function. These covariances are shown in Fig. 2.10. It is seen that this covariance matrix is not diagonal. This means that the Zernike modes are not statistically independent from each other. Such a statistical dependence complexifies the process of generating random draws of Zernike coefficient when modeling the turbulent phase. Therefore another basis, commonly used as well is the Karhunen-Loëve basis. For the latter however there exists no analytic modal expressions describing the atmospheric turbulence. Considering the fact that the Zernike basis does not differ greatly from the Karhunen-Loëve basis for the lower modes of turbulence (that is the modes that contain most of its energy content as explained above) Zernikes were used to

describe the turbulent phase corrected by adaptive optics in a simplified simulation tool described later in Section 3.2.3.

Furthermore, the Zernike basis being orthonormal, the statistical variance of the turbulent phase ϕ is equal to the sum of the variances of every polynomial coefficient:

$$\sigma_\phi^2 = \frac{1}{\mathscr{S}} \int_{\mathscr{S}} \langle \phi(\boldsymbol{r}) \rangle \, d\boldsymbol{r} = \sum_{i=1}^{\infty} \langle a_i^2 \rangle. \tag{2.49}$$

In the near field approximation and considering a Kolmogorov spectrum, the theoretical variances of every $\langle a_i^2 \rangle$ (i.e. the values of the diagonal of the covariance matrix shown in Fig. 2.10) are obtainable thanks to Eq (2.48). Conan [Conan, 1994] has developed the latter in order to obtain a simple approximation of the variance of a mode of radial order n, when n is large:

$$\sigma_{\text{turb}}^2(n) = 2.698(n+1) \frac{\Gamma(n-5/6)(D/r_0)^{5/3}}{(\Gamma(17/6))^2 \Gamma(n+23/6)}. \tag{2.50}$$

Given a pupil of diameter D, $\sigma_{\text{turb}}^2(n)$ follows the well-know law in $(n-1)^{-11/3} \left(\frac{D}{r_0}\right)^{\frac{5}{3}}$, and are represented in Fig. 2.11. Finally, given these expressions for the variance of each a_i, an expression for the variance of the turbulent phase, over a circular pupil, without the variance of the piston term (the coefficient a_1 associated to the first mode) is:

$$\sum_{i=2}^{\infty} \langle a_i^2 \rangle \simeq 1.03 \left(\frac{D}{r_0}\right)^{\frac{5}{3}} \tag{2.51}$$

2.4 Communication channel impairments induced by atmospheric turbulence

The previous sections explained how atmospheric turbulence causes random fluctuations of the phase and the amplitude of the optical wave propagating from the satellite to the optical ground station. These random fluctuations cause considerable degradation of the performances of the telecommunication system. This section aims to rigorously define performance measures relevant to free-space optical communication links that will be amply used in subsequent chapters. Techniques and systems able to mitigate these fluctuations that were studied in this thesis are also briefly introduced. They will be described, and their performances analyzed in further details later.

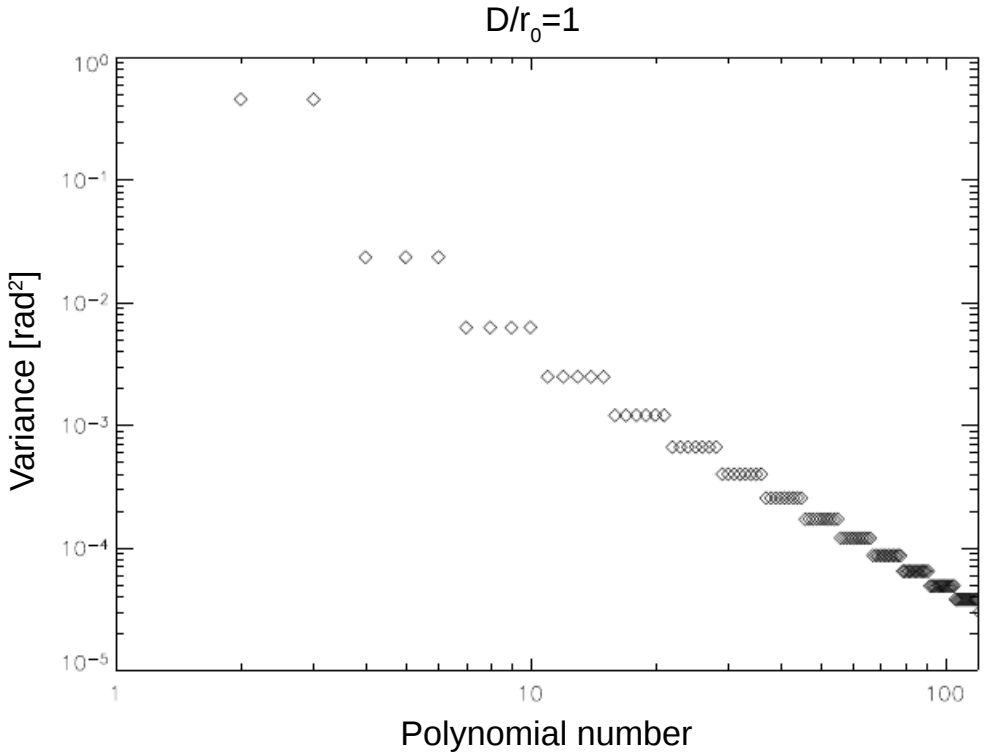

Figure 2.11: Variances of the coefficients of the first 200 Zernike modes of the decomposition of a turbulent phase for $D/r_0 = 1$

2.4.1 Signal fading: origin and general characteristics

As it is conditioned by turbulent wave-front distortions, the signal received by the optical ground station fluctuates. Such fluctuations, called fading, can lead to link failures or outages when, for instance, the instantaneous signal intensity drops below the detection threshold of the receiver.

Due to the characteristic times of evolution of the turbulence induced fading and the typical data rates aimed by such transmission the atmospheric optical channel is a slow-fading channel. As it impacts the performance evaluation of the communication systems operating over it, this is an important notion. It is related to the coherence time of the channel -measuring the period over which the fading process is correlated- and the data rate (or equivalently the symbol time duration). The former is of the order of 1 ms and 10 ms in the respectively LEO and GEO downlinks while data rates usually aimed by such transmission is at least about several Gbps. Hence a given fade level can affect many successive symbols, which leads to numerous successive errors called error bursts.

Another important characteristic of such fading channels is their frequency selectivity. If all the spectral components of the transmitted signal are affected in a similar manner, the fading is

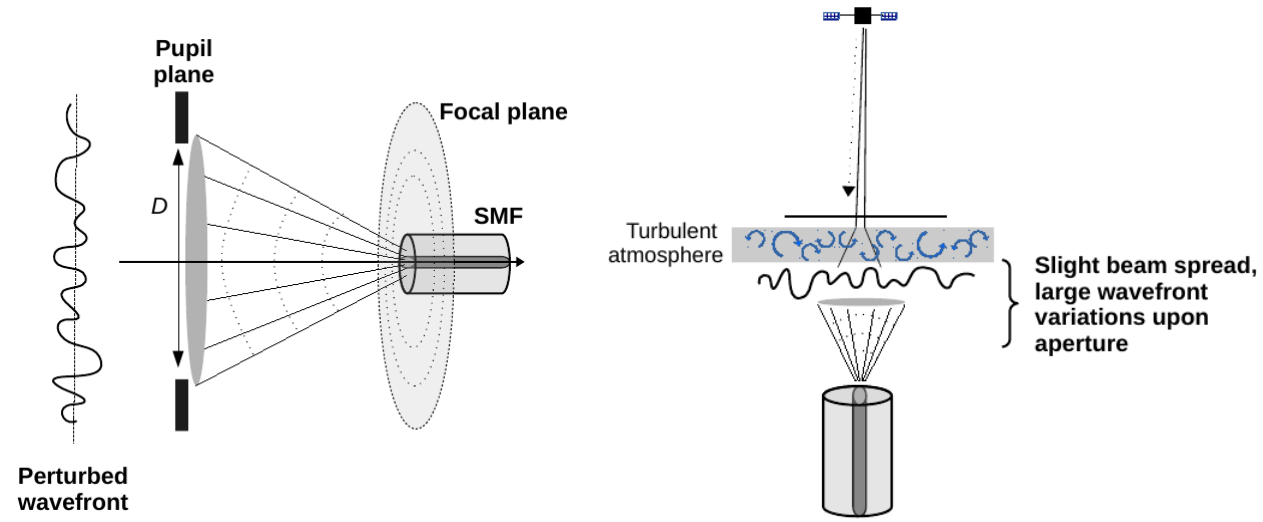

(a) (b)

Figure 2.12: (A) Diagram illustrating the coupling of the perturbed wavefront with a single-mode fiber. (B) An optical downlink is characteristic of large phasefront perturbation over the receiving aperture.

said to be frequency-nonselective or equivalently frequency-flat. In clear-sky conditions the atmospheric optical channel can be considered frequency-nonselective [Khalighi and Uysal, 2014]. This is potentially not the case when considering links impacted by fog, moderate cloud, and rain that can result in temporal broadening of the transmitted optical pulses. Such effects were neglected in this thesis.

2.4.2 Coupling efficiency into single-mode-fibers

In the near future, very high data-rates downlinks -several hundreds of Gbps to several Tbps- might be achieved only by leveraging the benefits of existing single mode components developed for fiber telecommunication such as Single Mode Fiber (SMF) Erbium-Doped Fiber Amplifiers (EDFAs), used at the receiver as a pre-amplifier in order to significantly amplify the signal prior to detection with PIN detectors. However, as sketched in Fig. 2.12, in the downlink case phase-front distortions in the receiving aperture may dramatically degrade the coupling efficiency of the incoming wave with the SMF.

Mathematically, one can consider an incoming perturbed wave before it reaches the telescope pupil of diameter D. Its electromagnetic field's complex amplitude is:

$$\Psi(\mathbf{r},t) = A_0 \exp(\chi(\mathbf{r},t) + j\phi(\mathbf{r},t)), \tag{2.52}$$

where A_0 denotes the complex field amplitude without perturbation, and as before $\chi(\mathbf{r},t)$ corresponds to the turbulence-induced log-amplitude fluctuations and $\phi(\mathbf{r},t)$ represents the phase variations (aberrations). In the pupil plane, its matching with the SMF Gaussian mode $M_0(\boldsymbol{r})$ is given by the following overlap integral [Shaklan and Roddier, 1988]:

$$\Omega(t) = \frac{\iint P(\boldsymbol{r}) \cdot \Psi(\boldsymbol{r},t) \cdot M_0^*(\boldsymbol{r}) d^2\boldsymbol{r}}{\left(\iint P(\boldsymbol{r}) \cdot \Psi(\boldsymbol{r},t) \cdot \Psi^*(\boldsymbol{r},t) d^2\boldsymbol{r} \iint P(\boldsymbol{r}) \cdot M_0(\boldsymbol{r}) \cdot M_0^*(\boldsymbol{r}) d^2\boldsymbol{r}\right)^{\frac{1}{2}}}, \tag{2.53}$$

where $P(\boldsymbol{r})$ represents the pupil transmittance:

$$P(\boldsymbol{r}) = \begin{cases} 1 & \text{if} \quad 0 \leq \frac{2|r|}{D} \leq 1 \\ 0 & \text{otherwise} \end{cases} \tag{2.54}$$

The SMF mode M_0 expressed in the pupil plane is approximated by a Gaussian mode whose waist is set in order to maximize its matching with an unperturbed incident beam [Ruilier, 1998]. The squared modulus of the aforementioned overlap integral corresponds to the instantaneous coupling efficiency of the perturbed incident beam:

$$\rho(t) = |\Omega(t)|^2. \tag{2.55}$$

2.4.3 Transmission performance assessment

2.4.3.1 Communication subsystems overview

When designing a communication system that operates in a fading environment, it is mandatory to be able to statistically describe the communication channel -i.e. the propagation medium- as well as the properties of the communication subsystem to be implemented. These properties include the selected modulation format, the transmitter and receiver setup and their noise characteristics. The communication subsystems that were studied during this thesis will be described in details in Section 4.2 as well as with a Monte-Carlo based simulation tool developed to emulate the performance of distinct receiver and transmitter configurations. Non-coherent receivers were considered only, with two types of binary modulation: On-Off Keying (OOK) and Differential Binary Phase-Shift Keying (2-DPSK or DBPSK). This choice is discussed in Section 1.2.2. Figure 2.13 gives a simplified overview of the corresponding receiver structures, and of the overall physical layer of the studied communication system.

These two receiver architectures present noise characteristics and statistics that are affected differently by their setup and environment. They will be described in details in Section 4.2. Nevertheless, prior to understanding how they affect or improve the quality of a communication link when facing turbulence-induced fading, it is important to recall what are useful and relevant performance measures typically used in such cases.

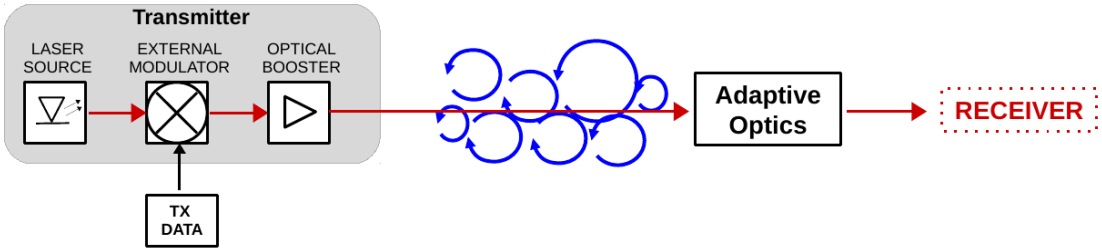

(a)

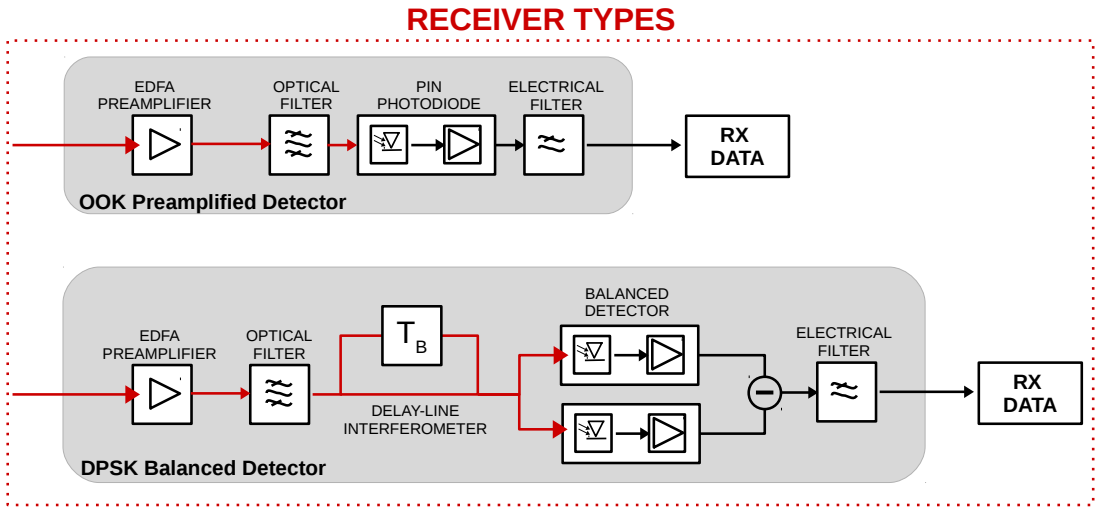

(b)

Figure 2.13: Diagram giving an overview of the physical layer and the two detection architectures investigated in this manuscript. (A) The transmitter consist essentially in an externally modulated continuous wave laser and a booster amplifier. (B) After partial AO correction the cases of an OOK preamplified and a DBPSK balanced receivers are considered

2.4.3.2 Error probability

The repetitive use of the term "performance" thus far begs for a succinct definition and enumeration of the measures that will be used in the remainder of this manuscript. The probability of error is mandatory to compute measures such as the bit-error rate (BER) and the channel capacity. Figure 2.14 illustrate the computation of such an error probability with respect to a given detection threshold. Due to the inherent noisiness of any given detection setup -induced by intrinsic limitations and/or the transmission environment- there exist a certain probability of detecting either a ZERO or a ONE. Such noises create two types of errors:

- The detection of a ONE whereas a ZERO was transmitted with probability denoted Pr(ONE|ZERO)
- The detection of a ZERO whereas a ONE was transmitted with probability denoted

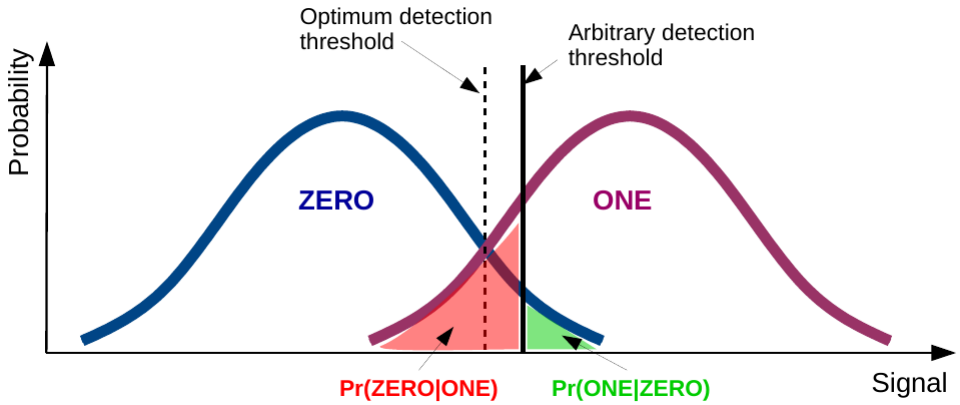

Figure 2.14: Illustration associated to the computation of the error probability with respect to a given detection threshold.

Pr (ZERO|ONE)

2.4.3.3 Bit error rate

The bit error rate (or analogously symbol error rate) is a measure that is very often illustrated in documents containing system performance evaluations because it is unambiguously revealing about the nature of the system's behavior. It is defined, after reception, as the proportion of erroneous bits:

$$\mathrm{BER} = \frac{\text{number of errors}}{\text{number of transmitted bits}}. \tag{2.56}$$

Assuming that the probability of sending a ONE is p_{ONE} and the probability of sending a ZERO is p_{ZERO}, the BER depends on the conditional probability of errors previously defined:

$$\mathrm{BER} = p_{\mathrm{ZERO}}\Pr(\mathrm{ONE}|\mathrm{ZERO}) + p_{\mathrm{ONE}}\Pr(\mathrm{ONE}|\mathrm{ZERO}). \tag{2.57}$$

Considering for instance an OOK modulation and in the elementary case where Gaussian statistics is accurately applicable for all noise sources affecting the detector and for an optimum detection threshold, the BER is given by the widely known analytic formula:

$$\mathrm{BER} = \frac{1}{2}\mathrm{erfc}\left(\frac{\mathrm{SNR}_0}{2\sqrt{2}}\right), \tag{2.58}$$

where it has been assumed that $p_{\mathrm{ZERO}} = p_{\mathrm{ONE}} = \frac{1}{2}$ and where SNR_0 corresponds to the post-detection (i.e. electrical) signal-to-noise ratio. However, in most cases this expression is not useful since noises in optical communication systems, especially preamplified architectures, can rarely be accurately modeled as Gaussian [Humblet and Azizoglu, 1991, Chan and Conradi, 1997, Jacobsen, 1994]. More details on how to accurately compute these probability of errors will be given in Section 4.2.4. At a given data rate, the evaluation of the

BER gives access to the assessment of the system performance in terms of its sensitivity, which is the average optical input power required to achieve a certain error probability.

Over time, turbulence-induced fading affects the proportion of energy from the incident beam impinging the receiver and hence the SNR as well as the BER. In slow-fading channel, a communication performance measure often found in the literature is the average of the "instantaneous" (i.e. conditioned on the instantaneous fading) BER defined by Eq.(2.57) over all the fading events. It is called the ergodic BER [Tse and Viswanath, 2005, Simon and Alouini, 2005, Cover and Thomas, 2006]

$$\mathrm{BER}_{\mathrm{Ergodic}} = \int_0^\infty \mathrm{BER}(s(t))\, f_S(s)\, ds, \tag{2.59}$$

where s represents the fading and f_S their probability density function (PDF). The ergodic BER provides a fundamental measure of the average performance of the communication subsystem. It does not however allow for an assessment of data reliability mechanisms such as coding and interleaving. These are important and very often mandatory mitigation techniques for the inevitable loss of information that occurs in slow-fading channels.

2.4.3.4 Measures of information: entropy and mutual information

Defining succinctly but rigorously a concept as broad as *information* as well as simple measures of it is a challenging task. However there exist a quantity, coined in the pioneering work of Shannon [Shannon, 1948] that founded *information theory* itself, called *entropy* and that presents properties that one can consider closely related to the intuitive notion of what a measure of information should be. In the context of *information generation*, consider a discrete information source emitting during every signaling interval a symbol x_i from a finite given alphabet $\mathscr{X}$:

$$\mathscr{X} = \{x_i \dots x_n\}, \quad n \in \mathbb{N} \tag{2.60}$$

The output of such a source can be modeled as a stochastic process for which a sample is denoted by the random variable X, that is:

$$\Pr(X = x_i) = p_i. \tag{2.61}$$

Assuming that the symbols emitted during successive intervals are statistically independent, it can be shown [Cover and Thomas, 2006] that mathematically, the average amount of information per symbol produced by the source is given by the entropy of the associated random variable:

$$H(X) = \sum_{\mathscr{X}} p_i \log_2\left(\frac{1}{p_i}\right), \tag{2.62}$$

where the use of a logarithm to base 2 allows to associate such a definition to binary signaling and its resulting unit of information the *bit* used in telecommunication engineering. In the case of a binary source emitting equally likely symbols (bits) $H(X) = 1$. In other words, one bit is the amount of information that we gain when one of two possible and equiprobable events occurs.

The concept of entropy defined by Eq. (2.62) can be extended to two random variables X and Y in order to relate it to the issue of *information transmission*. In that case, X represents the input to a discrete memoryless channel and Y its output which is a "noisy" version of X since it has been "corrupted" by the channel. Note that the term channel used here does not characterize the fading channel introduced earlier. Rather, it characterizes now the noise realization related to the detection process (as if no fading were present). The channel is said to be memoryless because the output (received) symbol depends only on the current input (sent) symbol. Because of its noisy nature, at the receiver when a symbol y is observed, there exists an uncertainty about the corresponding sent symbol x. In this context the average amount of uncertainty remaining about the channel input after the channel output has been observed is called the conditional entropy [Cover and Thomas, 2006]:

$$H(X|Y) = \sum_{\mathscr{X}} \sum_{\mathscr{Y}} p(x_i, y_j) \log_2 \left(\frac{1}{p(x_i|y_j)} \right). \tag{2.63}$$

Given $H(X)$ and $H(X|Y)$, the mutual information of the channel is:

$$I(X;Y) = H(X) - H(X|Y). \tag{2.64}$$

The entropy $H(X)$ can be seen as corresponding to the uncertainty surrounding the channel input before receiving the channel output. The conditional entropy $H(X|Y)$ accounts for the uncertainty about the channel input after observing the channel output. Equation (2.64) can therefore be interpreted as a measure of the uncertainty about the channel input, which is resolved by observing the channel output. These concepts and the relationship between entropy and mutual information are described by the Venn diagram presented in Fig. 2.15.

2.4.3.5 Channel capacity

The mutual information defined by Eq. (2.64) can be developed into:

$$I(X;Y) = \sum_{\mathscr{X}} \sum_{\mathscr{Y}} p(y_j|x_i) p(x_i) \log_2 \left(\frac{p(y_j|x_i)}{\sum_{\mathscr{X}} p(y_j|x_i) p(x_i)} \right), \tag{2.65}$$

where the following relationships have been used:

$$p(x_i, y_j) = p(y_j|x_i) p(x_i), \tag{2.66}$$

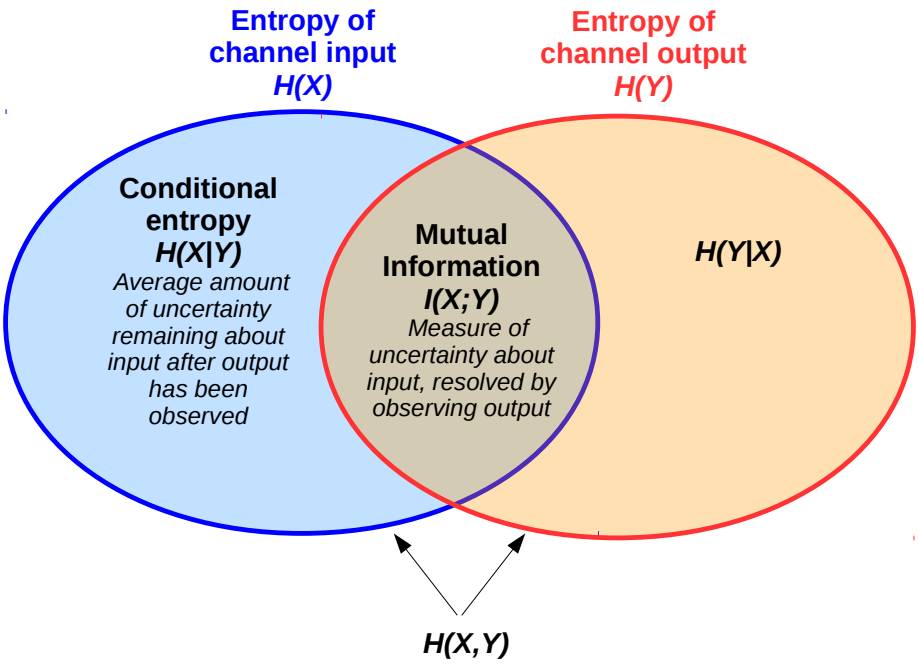

Figure 2.15: Venn diagram illustrating the relation between entropy and mutual information.

and

$$p(y_j) = \sum_{\mathcal{X}} p(y_j|x_i)\,p(x_i). \tag{2.67}$$

Hence, the mutual information depends on two different probabilities that are independent of each other. The probability distribution $\{p(x_i)\}$ characterizing the channel input and the conditional probability distribution $\{p(y_j|x_i)\}$ characterizing the channel i.e. the noise statistics of the detection system itself. The channel capacity, measured in bits per channel use, is defined as the maximum mutual information in any single use of the channel (i.e., signaling interval), where the maximization is over all possible input probability distributions [Cover and Thomas, 2006]:

$$C = \max_{\{p(x_i)\}} I(X;Y). \tag{2.68}$$

Thus far, only the case of discrete inputs and outputs has been considered. The definitions of entropy, mutual information and capacity can easily be extended to the continuous case. In that regard, the most commonly used result concerns the case of an additive white Gaussian noise (AWGN) channel leading to the well-known Shannon's capacity which is proportional to $\log_2(1+\mathrm{SNR})$. This expression is widely used in the literature however it should be noted that it corresponds to the case where the inputs follow a Gaussian distribution which maximizes the mutual information of AWGN channels. It is therefore approached in practice only for very dense constellations. In the framework of this thesis, the case of a binary (discrete) input and continuous output has been considered. Only second order modulation schemes

(OOK and DBPSK) have been considered, hence the input alphabet is composed of two symbols $\mathscr{X} = \{\text{ZERO}, \text{ONE}\}$. Furthermore, the case of ideal soft-decoding has been assumed hence the continuous channel decoder output alphabet $\mathscr{Y} = \{\mathscr{R}\}$. In practice soft-decoding requires a sophisticated decision circuit that allows to measure how reliable the decision about a received output is thereby increasing system performance [Couch, 2000]. The mutual information given by Eq. (2.65) in that case becomes:

$$I(X;Y) = \int_{\mathscr{Y}} \sum_{\mathscr{X}} f_{y|x}(y|x)\Pr(x)\log_2\left(\frac{f_{y|x}(y|x)}{\sum_{\mathscr{X}} f_{y|x}(y|x)\Pr(x)}\right) dy. \tag{2.69}$$

Only equally likely binary sources have been considered, i.e. $\Pr(x = \text{ONE}) = \Pr(x = \text{ZERO}) = \frac{1}{2}$ although they do not maximize the mutual information in the case of asymmetric channels such as when a preamplified receiver is used. Theoretically the gain from optimizing the input distribution (or in other words the difference between the mutual information and the capacity) can be shown to be very small [Li, 2003] at the cost, in practice, of greatly complexifying the transmitter. Hence, in the remainder, the terms mutual information and capacity are interchangeable.

2.4.3.6 Noisy channel coding

The consequence of noisy transmission is the manifestation of errors at the receiver end. For many applications it induces a level of reliability that is unsatisfactory. To achieve a higher level of performance, one resorts to the use of channel coding. It consists in mapping the transmitted data into a channel input sequence and inverse mapping the channel output sequence into an output data sequence in order to minimize the effect of channel noise [Couch, 2000]. Figure 2.16 shows a block diagram overview of a typical digital communication system where the operation of channel encoding and decoding can be situated. Channel coding is based upon the arbitrary introduction of a certain redundancy by the channel encoder, so as to reconstruct the original source sequence as accurately as possible at the receiver. The generic channel encoder is characterized by its code rate R. The latter is defined as the ratio:

$$R = \frac{k}{n}, \tag{2.70}$$

where k is the number of symbols (bits) in the input message and n the number of coded symbols in the output sequence. The *Noisy Channel Coding Theorem*, presented by Shannon [Shannon, 1948], essentially states that there exist channel codes that allow to achieve reliable communications with an error probability as small as desired, provided that the transmission rate of information is lower than the channel capacity. More precisely, if a channel has capacity C, all rates such that $R < C$ are achievable, that is, there exists a coding scheme such that the output of the source can be transmitted over the channel with an arbitrarily small error

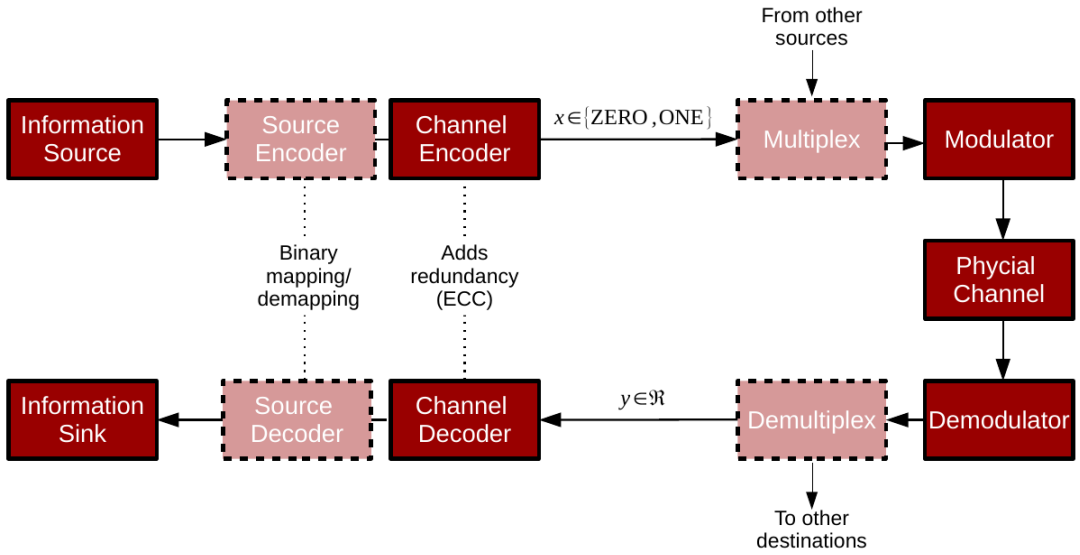

Figure 2.16: Block diagram of a communication system including channel encoder, decoder and modulator, demodulator

probability (which is a sufficient condition). Conversely, any coding scheme such that the output of the source can be transmitted over the channel with an arbitrarily small error probability must have $R \leq C$ (which is a necessary condition).

This channel-coding theorem is one of the most important results of information theory. However, it has two limitations. It does not provide any form of insight on how to construct such coding schemes and it does not provide a precise result for the probability of symbol error after decoding the channel output (only that such probability tends to zero as the length n of the code increases).

2.4.3.7 Capacity of fading channels

Let us now consider anew the case of a fading channel such as the optical atmospheric channel. Analogously to how it impacts BER, time varying fading will impact as well channel capacity. In the case of slow-fading, several code words can be affected by a single fading event. There exists therefore a nonzero probability the channel would not support the code rate ($R > C$). As represented in Fig. 2.17, this is in contrary to fast-fading channels, where a code word spans several fading states. In that case, a relevant performance measure is the average of the capacity over the different fading states, often called ergodic capacity. Intuitively, the transformation from a slow-fading to such a fast-fading channel could be obtained by increasing the code word length. In the case of the optical atmospheric channel, that is hardly implementable in practice as it would require unmanageable long code words. Therefore to characterize the performance of optical satellite-to-ground link the notion of outage, that will

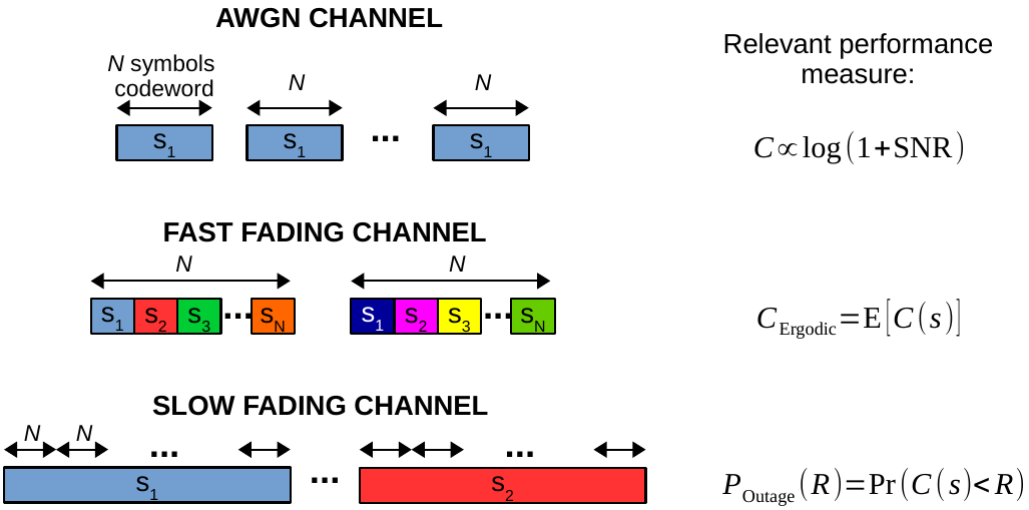

Figure 2.17: Illustration of the relevant performance measure over distinct types of wireless fading channel.

be defined shortly, is used.

In the case of slow-fading channel, instantaneous realizations -with respect to the fading evolution- of the mutual information can be considered. This is justified theoretically when the receiver has perfect channel state information, which is the assumption made throughout this thesis. In practice, the instantaneous channel state information is commonly estimated on a short-term basis by using training sequences (or pilot sequences) [Xu et al., 2009].

In these conditions, the instantaneous mutual information (or capacity) is itself a random variable that is in fact a bijection of the corresponding fading [Guo et al., 2005]. It is given by Eq. (2.69) conditioned by the value of the fading $s(t)$ at a given instant:

$$C(t) = I(X;Y|s(t)). \tag{2.71}$$

For a fixed code rate R the probability of outage of the channel is defined as:

$$P_{\mathrm{Outage}} = \Pr(C(t) < R). \tag{2.72}$$

Intuitively, the outage probability corresponds to the transmission's packet error rate (PER), since data (i.e. packets of encoded symbols) are only correctly received in proportion $1-P_{\mathrm{Outage}}$ times.

2.4.3.8 Link budget

In order to assess the performance of the transmission, in addition to the fading induced by turbulence, power losses and gains related to the transmitter, the receiver and the atmosphere have to be considered when computing the link budget. The instantaneous received optical power $P_{\mathrm{Rx}}(t)$ depends on the transmitted power P_{Tx} as:

$$P_{\mathrm{Rx}}(t) = a_{\mathrm{Total}}\, s(t) P_{\mathrm{Tx}}, \tag{2.73}$$

where $s(t)$ denotes, as before, (power) fading induced by turbulence. The parameter a_{Total} relates to several other static (i.e. not time varying) power losses related to phenomena such as atmospheric absorption and scattering a_{atmo}, the optical transmissions of optical components, free-space path losses among others. They are succinctly described in the subsequent paragraphs. Link budget calculations allow to determine the overall system power margin which is defined as the difference between the selected (or available) transmitted power and the minimum signal power needed to achieve a given performance level such as the sensitivity of the selected receiver. Typical values of the aforementioned losses for a satellite-to-ground link are given in [Hemmati, 2009b]. The free-space link loss and the gains provided by the transmitter and receiver apertures predominately affect the link budget.

2.4.3.8.1 Antennas gain

Considering equal transmitter size and power, the divergence of a laser beam is fundamentally smaller than that of a beam produced by a microwave source. Consequently the gain of an optical antenna is greater, and can easily be well over 100 dB for moderate telescope diameters. The on-axis transmit antenna gain in dB is given by [Klein and Degnan, 1974]:

$$G_{\mathrm{Tx}} = 10\log_{10}\left(\frac{4\pi A_{\mathrm{Tx}}}{\lambda^2}\eta_{\mathrm{Tx}}\right), \tag{2.74}$$

where $A_{\mathrm{Tx}} = D_{\mathrm{Tx}}^2\pi/4$ with D_{Tx} the diameter of the transmitting telescope, and η_{Tx} is an efficiency factor accounting for the loss due to truncation of the beam by the telescope. At the receiver, given the plane wave assumption the gain of the receiving aperture is:

$$G_{\mathrm{Rx}} = 10\log_{10}\left(\frac{4\pi A_{\mathrm{Rx}}}{\lambda^2}\right), \tag{2.75}$$

where $A_{\mathrm{Rx}} = D_{\mathrm{Rx}}^2\pi/4$ with D_{Rx} the diameter of the receiving telescope.

2.4.3.8.2 Free-space link loss

The loss in power of any electromagnetic wave propagating in free-space over a range L is

given in dB by [Friis, 1946]:

$$a_{\mathrm{FS}} = 20\log_{10}\left(\frac{4\pi L}{\lambda}\right). \tag{2.76}$$

2.4.3.8.3 Transmitter and Receiver losses

Losses due to imperfections such as aberrations and reflections of the optical components constituting the transmitter and the receiver have to be taken into account. Imperfect assembly of these components can cause losses as well. These are denoted a_{Tx} and a_{Rx} for the transmitter and receiver respectively. Pointing losses a_{p} due to miss-pointing of the transmitted beam toward the optical ground station as well as tracking losses due to missponiting of the receiving telescope a_{t} might be non-negligible.

2.4.3.8.4 Link margin

The link (or power) margin is given in dB by the difference between the allocated signal power and the power required to achieve a targeted receiver sensitivity P_{S}:

$$\text{Link margin} = (P_{\mathrm{Tx}} + G_{\mathrm{Tx}} - a_{\mathrm{FS}} - a_{\mathrm{Tx}} - a_{\mathrm{Rx}} - a_{\mathrm{p}} - a_{\mathrm{t}} - a_{\mathrm{atmo}} + G_{\mathrm{Rx}}) - P_{\mathrm{S}}. \tag{2.77}$$

In order to provide orders of magnitude consider a transmitter with an aperture of 0.135 m in diameter on a LEO satellite that is, at a given instant, 1500 km away from a 0.25 m receiver on Earth. Given the transmission wavelength of 1550 nm, the link loss amounts to 262 dB while the transmit and receive gains are about 108 and 114 dB respectively. The combined transmitter, receiver, pointing, tracking and atmospheric transmission losses amounts to roughly 10 dB [Hemmati, 2009b]. With a 20 dBm transmit power the average receive power is about -30 dBm.

3 ADAPTIVE OPTICS FOR OPTICAL SATELLITE TO GROUND COMMUNICATION

Contents

3.1 Introduction

The concept of adaptive optics was first proposed in 1953 by Babcock [Babcock, 1953]. Despite its early implementation dedicated to defense applications, its use in astronomy was enable only after some advancements in computer technology and civilian detectors in 1990 [Rousset et al., 1990]. Nowadays, adaptive optics is of interest in several fields such as retinal imaging and obviously free-space optical communication.

The first part of this chapter introduces the principle of operation of an adaptive optics system by providing a global vision of such a system and its limitations. Simulation tools required to study the performance of such a system are then introduced. A detailed description about the theoretical performance modeling of adaptive optics, taking into account not only the atmospheric turbulence, but also each of the characteristics of its components is given.

The second part of this chapter is an adaptation of a paper published during this thesis [Canuet et al., 2018]. It describes several analytic developments regarding the statistical properties of the coupled flux into single-mode fibers after partial adaptive optics correction and their confrontation to end-to-end wave optics simulations.

3.2 Introduction to adaptive optics

3.2.1 General Principle and components

An adaptive optics (AO) system is an opto-mechanical system that corrects, in real time, phase fluctuations induced by propagation of the optical field through atmospheric turbulence. It is constituted of three key components: a wavefront sensor (WFS), a real-time computer (RTC) and a deformable mirror (DM). The operational principle of such a system, as illustrated in Fig. 3.1, is the following: the data provided by the WFS are processed by RTC to control the DM which will adapt to the wavefront deformations in order to correct them. Assuming a perfect correction, this results in a planar wavefront and hence, in the focal plane, a maximum amount of energy can be coupled into the SMF/detector.

Only closed-loop AO systems are considered in the remainder. In this configuration, as depicted in Fig. 2.1, the WFS is located downstream of the DM and hence measures a residual wavefront instead of the turbulent wavefront itself (precise definitions are given subsequently). The characteristic time evolution of turbulence (a few milliseconds) requires fast and optimized control loops [Gendron and Lena, 1994, Gendron and Lena, 1995, Dessenne, 1998, Dessenne et al., 1998], able to drive the DM with bandwidths corresponding to the evolution of turbulence [Greenwood, 1977].

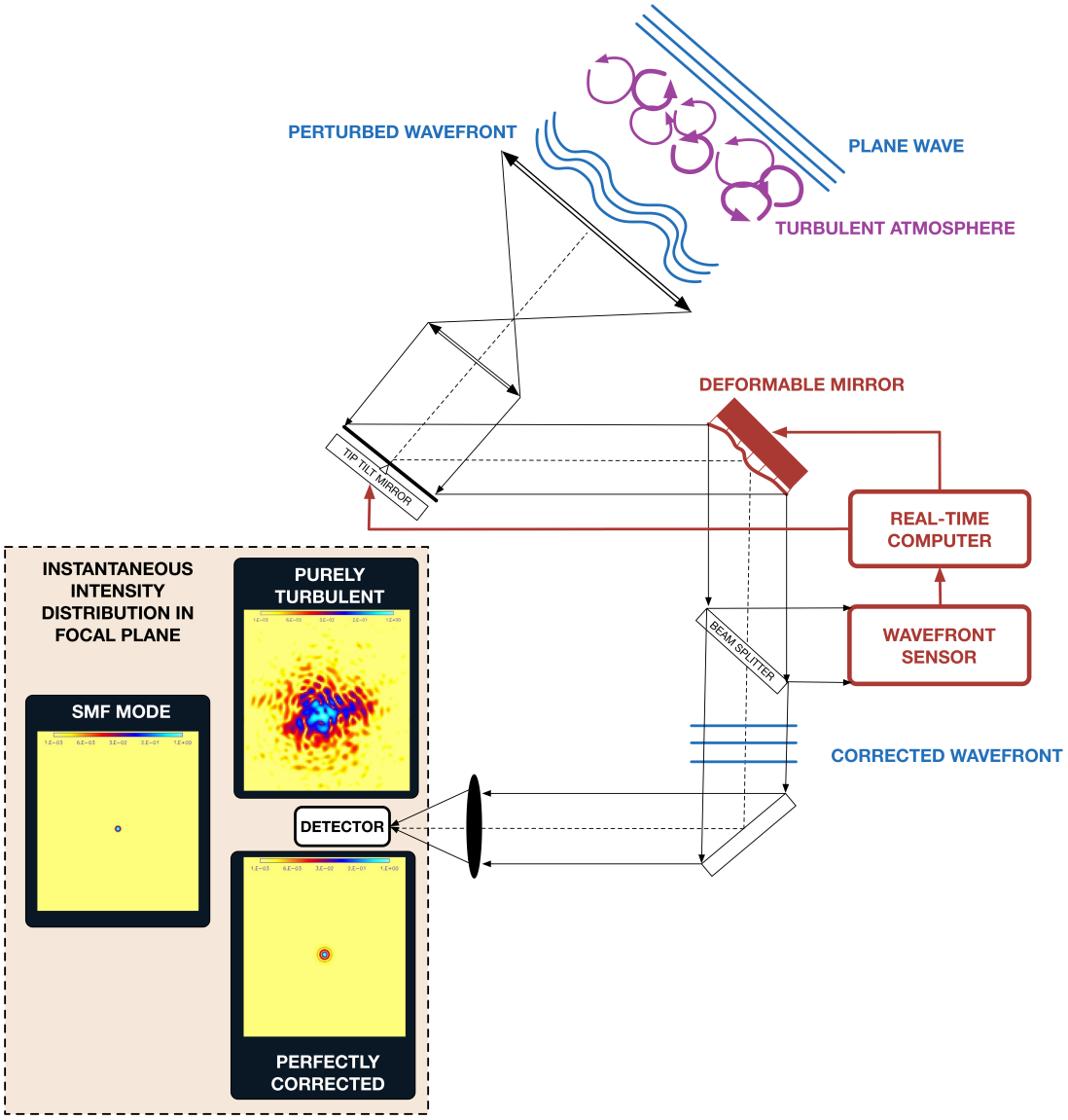

Figure 3.1: Diagram depicting the general principle of a closed-loop AO system. The main components are reported. Snapshots of the instantaneous intensity distribution in the focal plane are shown considering no correction at all (purely turbulent) and in the case of an ideal perfect correction. For comparison the SMF mode is depicted as well.

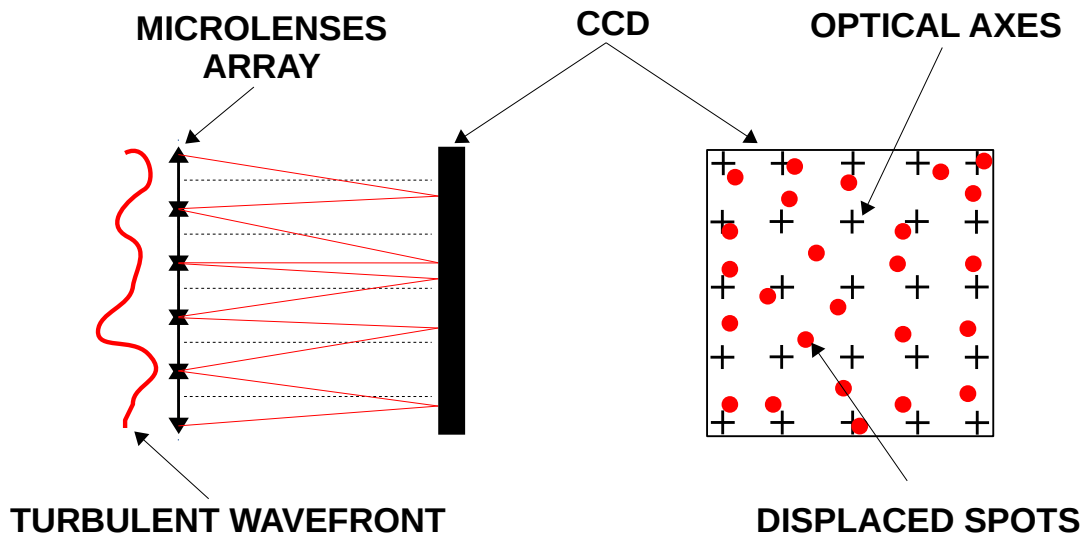

Figure 3.2: Schematic diagram of the Shack-Hartmann analyzer

3.2.1.1 Wave-front sensing

3.2.1.1.1 Principle

In the context of AO, two types of wavefront analyzers are conventionally used. The Shack-Hartmann WFS [Shack and Platt, 1971] and the curvature WFS [Roddier, 1988]. Both are pupil plane analyzers. They consist of sampling the pupil by sub-pupils, each of them giving local information on the wavefront. The Shack-Hartmann measures the local slope of the wavefront while the curvature WFS measures a local curvature by analyzing intensity on both sides of the pupil plane. [Rousset-l-99] provides a very complete description of analyzers for adaptive optics. Another type of WFS typically used is the pyramidal WFS [Ragazzoni, 1996, Esposito et al., 2000], that like the SH WFS measures the local slope of the wavefront. Hereafter, the emphasis is put on the Shack-Hartmann WFS as it is the analyzer most commonly used in AO and, its limitations are representative of those of most pupil plane analyzers.

The Shack-Hartmann WFS principle is based on the formalism of optics geometric. Each image formed at the focal plane of a sub-pupil yields information about the mean slope of the wavefront through the measurement of a center of gravity as presented in Fig. 3.2. The local slope (α_x^k, α_y^k) of the phase ϕ_k on the sub-pupil k is related to the displacement (x_c, y_c) of the center of gravity of the spot at the focus of the sub-pupil (of focal distance f_L) by the following relation, respectively in the x and y axes:

$$\alpha_x^k = \frac{x_c}{f_L} = \frac{\iint_{sp} \frac{\partial \phi_k(\boldsymbol{r})}{\partial x} |\Psi_k(\boldsymbol{r})|^2 d\boldsymbol{r}}{\iint_{sp} |\Psi_k(\boldsymbol{r})|^2 d\boldsymbol{r}}. \tag{3.1}$$

$$\alpha_y^k = \frac{y_c}{f_L} = \frac{\iint_{\text{sp}} \frac{\partial \phi_k(\boldsymbol{r})}{\partial y} |\Psi_k(\boldsymbol{r})|^2 d\boldsymbol{r}}{\iint_{\text{sp}} |\Psi_k(\boldsymbol{r})|^2 d\boldsymbol{r}}. \tag{3.2}$$

where the integration is carried out over the k^{th} sub-pupil surface and $|\Psi_k(\boldsymbol{r})|$ is the complex filed amplitude. Note that when the impact of scintillation upon the sub-pupils is negligible the intensity $|\Psi_k(\boldsymbol{r})|^2$ over the latter are constant.

3.2.1.1.2 Measurement noise

In addition to scintillation effects, measurement noise can have an impact on the precision of WFS. Two types of noise exist:

- **Photon noise** that depends on the number of photons received per sub-pupil N_{ph} , respectively the FWHM of the image formed in the focal plane and of the diffraction limited image X_{T} and X_{D} (both in pixels):

$$\sigma^2_{\text{phot}} = \left(\frac{\pi}{\sqrt{2}}\right)^2 \frac{1}{N_{\text{ph}}} \left(\frac{X_{\text{T}}}{X_{\text{D}}}\right)^2. \tag{3.3}$$

- **Detection noise** that depends on the standard deviation of the noise per pixel σ_{e^-} (in number of electrons) and X_{S} the number of pixels taken into account in the calculation of the center of gravity:

$$\sigma^2_{\text{detect}} = \left(\frac{\pi \sigma_{e^-} X_{\text{S}}^2}{\sqrt{3} N_{\text{ph}} X_{\text{D}}}\right)^2. \tag{3.4}$$

The WFS does not provide a direct measurement of the phase. However the latter is the physical quantity to be corrected. Hence, phase reconstruction from the data provided by the analyzer, is required. When the phase perturbation is small, the Shack-Hartmann WFS is characterized by the following linear system of equations:

$$\boldsymbol{y} = \boldsymbol{D}\phi + \boldsymbol{b}, \tag{3.5}$$

where $\boldsymbol{y}$ is the vector of local slopes in each sub-pupil, $\boldsymbol{D}$ is a linear operator characterizing the WFS, and $\boldsymbol{b}$ is associated to measurement noise.

Measurement noise will be neglected in the following developments. This is soundly justified as a first order approximation considering the typical optical power requested for high data rates transmission that are significantly larger than those required by the WFS. For instance, consider the power required to ensure a 10^{-3} BER in the ideal case of a photon limited detector transmitting 10 Gbps using On-Off Keying modulation. The required number of

photon per bit is equal to:

$$N_{\text{ph}} = -2\log(2 * \text{BER}). \tag{3.6}$$

At a transmission wavelength of 1550 nm and considering a quantum efficiency of 0.7 it corresponds to roughly 23 nw. In comparison, considering the characteristics of a WFS measuring 12 radial orders (169 sub-pupil) at 2 kHz while using a typical infra-red camera (such as a C-RED2 from *First Light* characterized by 50 noise electrons per pixel), the power required is approximately 1.8 nw.

3.2.1.2 Deformable mirror

The deformable mirror allows the correction of the wavefront. A thorough review of the different types of correction systems can be found in [Madec, 2012]. The general correction principle of such mirrors is as follows: the perturbed wavefront arrives on the DM while the reflecting surface of the latter is deformed so that it adapts to the wavefront, thus correcting the phase defects introduced by turbulence. The following basic equation defines the residual phase in function of the corrected and turbulent phases, $\phi_{\text{corr}}(\boldsymbol{r}, t)$ and $\phi_{\text{res}}(\boldsymbol{r}, t)$ respectively:

$$\phi_{\text{res}}(\boldsymbol{r}, t) = \phi_{\text{turb}}(\boldsymbol{r}, t) - \phi_{\text{corr}}(\boldsymbol{r}, t). \tag{3.7}$$

The corrected phase $\phi_{\text{corr}}(\boldsymbol{r}, t)$ is conventionally obtained by using the piezo-electric effect by means of actuators that push or pull on the reflecting surface of the mirror (in the case of stacked actuators mirrors). At a given instant, since the response of each engine of such a DM can be considered as linear in the general case, the corrected phase generated by the DM is defined by the linear relationship:

$$\phi_{\text{corr}} = \boldsymbol{M}_{\text{inf}}\boldsymbol{u}, \tag{3.8}$$

where $\boldsymbol{u}$ denotes the vector of commands applied to the DM actuators. The operator $\boldsymbol{M}_{\text{inf}}$, called the influence matrix, is formed by the actuators individual influence functions. The influence matrix can be expressed directly in a pixellic basis or decomposed upon any other modal basis such as the Zernike polynomials. This will be explained in Section 3.2.2.5 as it constitutes the method used for modeling AO systems in the framework of the simulation tools used in this thesis.

3.2.1.3 Command and reconstruction

In order to correct the turbulent wavefront, the latter has to be properly reconstructed by applying the (voltage) commands to the DM actuators while considering the measurements provided by the WFS of the residual wavefront $\phi_{\text{res}}(\boldsymbol{r}, t)$. This is characteristic of a closed-loop AO configuration for which a block diagram is given in Fig. 3.3. In practice, the reconstruction

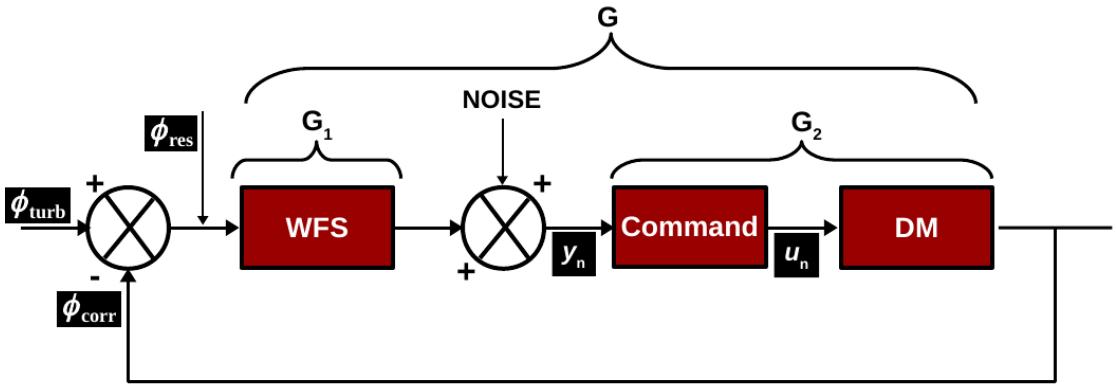

Figure 3.3: Simplified diagram of the servo-loop of an AO system. The transfer functions detailed in 3.2.1.4 are reported. The wavefront analyzer is downstream of the DM, therefore it measures a residual wavefront. Note that the noise is in fact neglected in the subsequent developments as explained in 3.2.1.1.2.

of the corrected wavefront is performed on the basis of the modes of the DM, allowing the computation of the control voltages applicable directly to the DM. Consider the relationship between the WFS measurements and the command voltages:

$$\boldsymbol{y} = \boldsymbol{M}_{\text{inter}}\boldsymbol{u}, \tag{3.9}$$

where $\boldsymbol{M}_{\text{inter}}$ is called the interaction matrix. Practically the latter is obtainable thanks to a calibration step consisting of arbitrarily driving (pushing) each actuator while measuring the WFS output. Once such a calibration is done, the command $\boldsymbol{u}_{\text{corr}}$ providing the turbulent wavefront correction ϕ_{corr} is given by:

$$\boldsymbol{u}_{\text{corr}} = -\boldsymbol{M}_{\text{com}}\boldsymbol{y}_{\text{res}}, \tag{3.10}$$

where $\boldsymbol{y}_{\text{res}}$ is the WFS measurement corresponding to the residual turbulent phase ϕ_{res} , and $\boldsymbol{M}_{\text{com}}$, called the command (or reconstruction) matrix, is the generalized inverse of the interaction matrix:

$$\boldsymbol{M}_{\text{com}} = \left(\boldsymbol{M}_{\text{inter}}^{T}\boldsymbol{M}_{\text{inter}}\right)^{\dagger}\boldsymbol{M}_{\text{inter}}^{T}. \tag{3.11}$$

Whatever the basis used for the reconstruction, it is of finite dimension since the number of sub-pupils of the WFS and hence the number of measurements that it gives is finite. Conversely, the phase is described by a decomposition onto an infinite number of modes. Therefore, the modes not taken into account in the reconstruction process are projected onto the reconstruction basis and tamper with the measurements. This error is called the aliasing error [Rousset, 1993] In addition to such spatial reconstruction of the wavefront, dynamical aspects of the closed-loop system need to be considered. The dynamics of the AO system

must be sufficient to follow the temporal evolution of the turbulent phase. They depend on the characteristics of the primary components of the AO loop. For instance, due to the time required by WFS measurements, their treatment by the RTC and the computation of the command, there exist delays between the AO frames implying that the command continuously chasing the turbulent signal in order to ensure a minimal residual wave-front. This behavior is represented by the chronogram in Fig. 3.4. The WFS integrate the residual phase over a time interval noted T to which corresponds the sampling frequency $f_{\text{samp}} = 1/T$. The read-out of the WFS measurement, its treatment and the computation of the command by the RTC is assumed to take another T seconds. The delay related to the correction of the turbulent phase by the DM itself is assumed negligible. This AO servo-loop is therefore said to have a delay of two frames. Since it is typically used in practice, the servo command considered here consists of a simple integrator. Hence, in the discrete time domain (computations are done digitally by the RTC) the DM command voltages obey the following relation:

$$\boldsymbol{u}_{n+1} = \boldsymbol{u}_n + \boldsymbol{g}\delta\boldsymbol{u}_n, \tag{3.12}$$

where $\boldsymbol{g}$ is a diagonal matrix whose elements correspond to the integrator gain associated to the command of each actuator. It takes into account the servo-loop delay as described in the next subsection. The parameter $\boldsymbol{u}_n$ is the command applied at discrete instant n and $\delta\boldsymbol{u}_n$, given by Eq. (3.10), is the corrective term allowing for the computation of a proper command at the instant $n+1$. The stability of the control loop depends on the delay, which imposes a range of values for the choice of $\boldsymbol{g}$. There exists a trade-off between performance and robustness [Petit, 2006]: taking a unitary gain allows for the highest bandwidth possible however at the expense of stability. Such an optimization between delay, gain and bandwidth of the AO loop is beyond the scope of the work presented here. If not otherwise mentioned, a delay of 2 frames and a gain for all corrected actuators (or mode) $g = 0.5$ will be considered in the remainder.

3.2.1.4 Dynamical analysis of the servo-loop

As depicted in Fig. 3.3, such a delay is characterized in terms of transfer functions G_1 and G_2 that stem from two main components of the loop:

- The WFS that integrates during T seconds the continuous signal $a_i^{\text{res}}(t)$, which is the coefficient corresponding to the i^{th} mode of the residual phase. This operation may be characterized by a time transfer function in the Laplace space (i.e. $s = i\omega$ is the Laplace transform variable where $\omega = 2\pi\nu$):

$$G_1(s) = \frac{1-\exp(-sT)}{sT}. \tag{3.13}$$

  Such a transfer function corresponds to the convolution by a boxcar window represent-

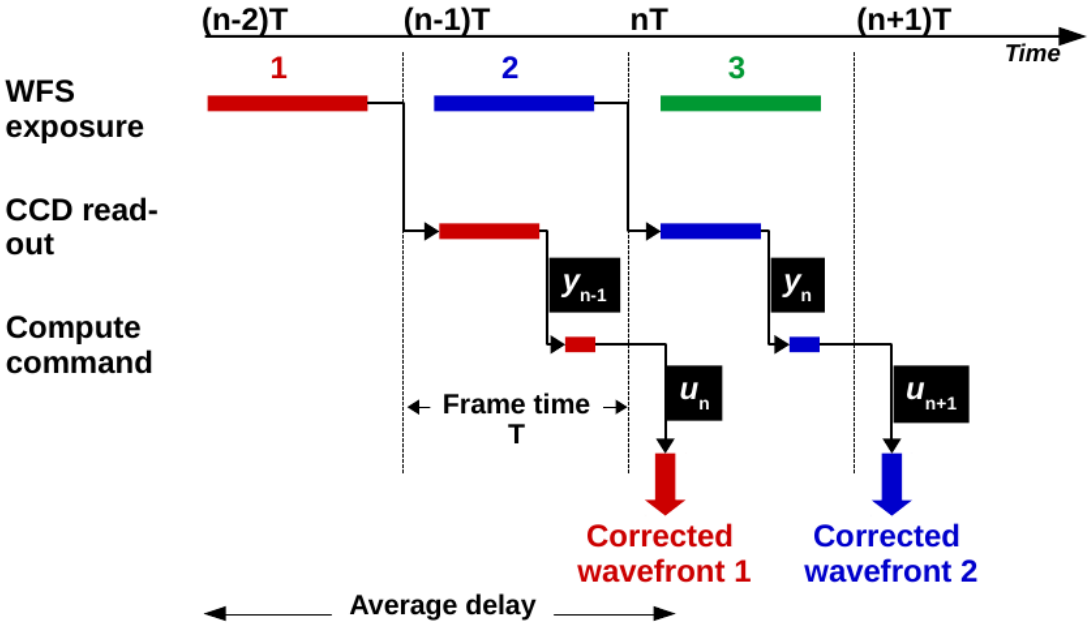

Figure 3.4: Typical chronogram of a closed-loop AO system presenting a delay corresponding to two frames.

ing the WFS averaging process during the time T.

- The wavefront reconstruction characterized by a time transfer function G_2, which takes into account the delay related to the read-out of the WFS measurement, its treatment and the computation of the command (an integrator characterized by its gain g_i, the latter being the gain corresponding to each corrected mode) by the RTC (assumed to take another T seconds) is given by:

$$G_2(s) = \underbrace{\exp(-sT)}_{\text{RTC}} \; \underbrace{g_i/(sT)}_{\text{INTEGRATOR}} \; . \tag{3.14}$$

As previously explained, the typical bandwidth of the type of DM considered here allows to neglect the delay related to the correction of the turbulent phase by the DM itself. The latter is therefore simply modeled by a subtractor of unit transfer function.

3.2.2 End-to-end simulation: AOST

3.2.2.1 Turbulent propagation

The end-to-end AO simulator considered here consists in a software implementing the theoretical features described in the previous sections. It takes as inputs the turbulent phase-screens generated by TURANDOT (see Section 2.3.2) and models each component of the AO system, as

well as their effects on the propagated wavefront. It outputs correlated times series of coupled flux attenuation into a SMF.

3.2.2.2 Wavefront sensing

Following Section 3.2.1.1, a natural way to simulate the Shack-Hartmann WFS is to straightforwardly consider the subdivision of the incoming phase screens subsequently averaged over each sub-pupil and include the impact of measurement noise analytically using Eqs. (3.3) and (3.4). However, in this end-to-end simulation of an AO loop, the Shack-Hartmann modeling differs from this geometrical description as it is based on a diffractive approach in describing the image formation on the sensor after crossing the microlenses. This allows to accurately model the image formation, thus taking into account the pupil amplitude distribution in the presence of strong turbulence as well as a under-sampling effects. The local slope measurements of the wavefront on each sub-pupil is accurately simulated by setting the number of photo-electrons on the detector, before calculating a center of gravity.

3.2.2.3 Temporal dynamics

The simulation is iterative and assumes a discretized description of the AO loop. To each iteration is associated a frame, of duration $1/f_{\text{samp}}$, of the wavefront analyzer. Akin to the description of the temporal modeling introduced in Section 2.3.2.3, the phase screens are translated by the quantity V/f_{samp} -where V is the wind speed- converted into a pixels number. The turbulence projected in the pupil at a given iteration is therefore considered to be the averaged turbulence during the WFS integration time and in other words it is assumed that the loop frequency is sufficient and the turbulence supposed frozen during a frame.

3.2.2.4 Command

The modal description of the system allows to easily incorporate a state-space approach to the modeling of optimal commands [Petit, 2006, Petit et al., 2009]. In the simple case of an integrator, the closed-loop delay is modeled by shifting the application of the correction voltages by the desired number of iterations with respect to the iteration where they are calculated.

3.2.2.5 Reconstruction

The phase reconstruction performed in this simulator is different from the principle introduced in Section 3.2.1.3 where it was assumed it is performed on the basis of the modes of the DM, allowing the computation of the control voltages applicable directly to the DM. Here

a modal reconstruction of the phase is implemented where the latter is decomposed onto Zernike polynomials. This approach is fundamentally more general since the notion of phase reconstruction is merged with the notion of control of the DM. Choosing the Zernike polynomials as a basis for reconstruction and correction implicitly assumes that the mirror is capable of generating such surfaces. In doing so, the effect related for instance to the mechanical characteristics of the deformable mirror are neglected however this representation allows to easily relate analytic expressions characterizing turbulence with AO performances. In this framework, the measurements vector of the WFS are given by:

$$\boldsymbol{y} = \boldsymbol{D}_Z \boldsymbol{a}, \tag{3.15}$$

where $\boldsymbol{D}_Z$ is the matrix characterizing the WFS expressed in the Zernikes basis: each column is the measurement given by the WFS where the phase corresponds to one of the Zernike polynomials. The vector $\boldsymbol{a}$ contains the coefficients associated with the modal decomposition of the phase:

$$\phi = \sum_{i=2}^{N_{\max}} a_i Z_i. \tag{3.16}$$

Similarly to 3.2.1.3, the problem lies in the inversion of Eq. (3.15). One wants to find a knowing the vector of measurement y. Obviously, the number of Zernike coefficients, denoted $N_{\max}$, must be less than the number of measures given by the WFS in order to ensure that the problem is well defined. There is therefore no exact solution, however, commonly, the vector a (and thus the phase) is estimated using maximum of likelihood procedures. The latter can include some a priori statistical knowledge about the phase and the noise [Sasiela and Mooney, 1986]. In the absence of such knowledge, this method corresponds to a least squares solution [Herrmann, 1980]:

$$\boldsymbol{a} = \left(\boldsymbol{D}_Z^T \boldsymbol{D}_Z\right)^{\dagger} \boldsymbol{D}_Z^T \boldsymbol{y}, \tag{3.17}$$

where † denotes the generalized inverse. In practice, to avoid noise amplification the number of reconstructed modes is fixed in order to ensure that the problem is well-conditioned.

3.2.3 Simplified AO modeling

The analytic modeling of a partial adaptive optics system consists in describing the impact of the ensemble of intrinsic errors on the residual wavefront using simple analytic expressions. The latter are detailed in the following subsections. There exist several approaches yielding such analytic results. They differ primarily by the basis chosen to describe the phase in the pupil. For instance a Fourier approach is used in [Rigaut et al., 1998, Neichel, 2008, Jolissaint et al., 2006]. Here we will consider the Zernike polynomials, as the Fourier approach is usually not suitable for small systems and finite supports. In this framework, the models

detailed in [Conan, 1994, Conan et al., 1995] have been used during this thesis. These models have enabled several practical dimensioning studies [Rousset et al., 1998, Fusco et al., 2006] and post system-integration performance analyses [Fusco et al., 2004].

3.2.3.1 Equivalence between spatial frequencies and Zernike modes

The developments made in [Conan, 1994] rely upon existing similarities between the basis of Zernike polynomials and the spatial frequencies of atmospheric turbulence. These similarities are important for physically understanding the relationship between the characteristics of the main components of an AO system and the correction quality of the turbulent wavefront. A Zernike polynomial cannot be directly associated with a pure spatial frequency. However, Conan has studied the frequency components of each Zernike polynomials in order to determine their energy content. The polynomial $Z_i(n,m)$ of radial order n and azimuthal degree m is characterized by the power spectrum [Noll, 1976]:

$$\left|\mathscr{F}\left[Z_i\right](\boldsymbol{f})\right|^2 = 4(n+1)\left[\frac{J_{n+1}(\pi D f)}{\pi D f}\right]^2 \begin{cases} 2\cos^2(m\Theta) & \text{for} \quad m \neq 0 \quad \text{and even} \\ 2\sin^2(m\Theta) & \text{for} \quad m \neq 0 \quad \text{and odd} \\ 1 & \text{for} \quad m = 0 \end{cases} \tag{3.18}$$

In Eq. (3.18), the operator $\mathscr{F}[\cdot]$ denotes the Fourier transform, $J_{n+1}(\cdot)$ denotes the Bessel function of first kind, D the diameter of receiver circular aperture and (f,Θ) are polar coordinates in the plane of spatial frequencies. The spectrum averaged over all polynomials corresponding to the same radial order n are characterized by a symmetrical revolution centered about a cutting frequency denoted $F_c(n)$. These spectra are all the more peaked as the radial order increases. Hence, the larger the latter, the more it is comparable to a pure spatial frequency. After asymptotically developing $J_{n+1}(\cdot)$, an approximation of $F_c(n)$ is given by:

$$F_c(n) \simeq 0.37\frac{n+1}{D}. \tag{3.19}$$

3.2.3.2 Temporal properties

Given such a characterization of the spatial properties of the turbulent phase, its temporal properties are easily determined. Each polynomial is associated with an ensemble of Fourier modes corresponding to the spatial frequency $F_c(n)$. Using Taylor hypothesis 2.3.2.3, an equivalent temporal frequency is simply given by[Conan et al., 1995]:

$$\nu_c(n) = V F_c(n) \simeq 0.37\frac{V(n+1)}{D}, \tag{3.20}$$

where V is the wind speed in a single layer. Moreover, the temporal power spectrum corresponding to the Zernike coefficient a_i is related to the phase power spectrum $W_\phi(\boldsymbol{f})$ (given by

Eq. (2.35)) by:

$$W_{a_i}(\nu) = \int_0^L \int_{-\infty}^{\infty} \frac{1}{V(h)} \left| \mathscr{F}[Z_i]\left(\frac{\nu}{V(h)}, f_y\right)\right|^2 W_\phi\left(\frac{\nu}{V(h)}, f_y\right) dh df_y. \tag{3.21}$$

This expression assumes that the wind at altitude h is co-linear with the x-axis, the y-axis component of spatial frequencies is given by f_y. Considering a single turbulent layer, the cutting frequency $\nu_c(n)$ defines the limit between two regimes:

- At frequencies greater than $\nu_c(n)$, the power spectrum asymptotic behavior characterizing any radial order n follows a $f^{-17/3}$ power law and is proportional to V/D.
- At frequencies lower than $\nu_c(n)$, this asymptotic behavior is notably dependent on the wind direction which introduces disparities according to the radial and azimuthal orders.

Figure 3.5 shows temporal power spectral densities of the turbulent phase as well as its properties for some of the Zernike polynomials obtained by end-to-end simulations.

When several turbulent layers are considered, these effects are averaged. The various cutoff frequencies accumulate to form a composite spectrum, the high frequency asymptotic behavior remains in $f^{-17/3}$, the low frequency asymptotic behavior is in f^0 for $n > 1$ and $f^{-2/3}$ for $n = 1$.

3.2.3.3 Noll residual variance

As a starting point to the analytic modeling of a partial AO system, consider the case of a perfect correction of the first N_{corr} radial orders. In that case Noll [Noll, 1976] has shown that the statistical variance of the residual phase is given by:

$$\sigma^2_{\text{Noll}} = \sum_{n=N_{\text{corr}}+1}^{\infty} (n+1)\sigma^2_{\text{turb}}(n), \tag{3.22}$$

where $\sigma^2_{\text{turb}}(n)$ is given by Eq. (2.50). The partial AO model extends this fundamental result by discriminating the residual correction at low frequencies from the residual correction at high frequencies. The similarities relating frequencies to Zernike polynomials (radial orders) allows for a characterization of AO correction residuals as follows:

- High orders residuals when $n > N_{\text{corr}}$: the AO system does not correct the wave-front aberrations. It corresponds to the residual error given by Eq. (3.22), called the fitting error.

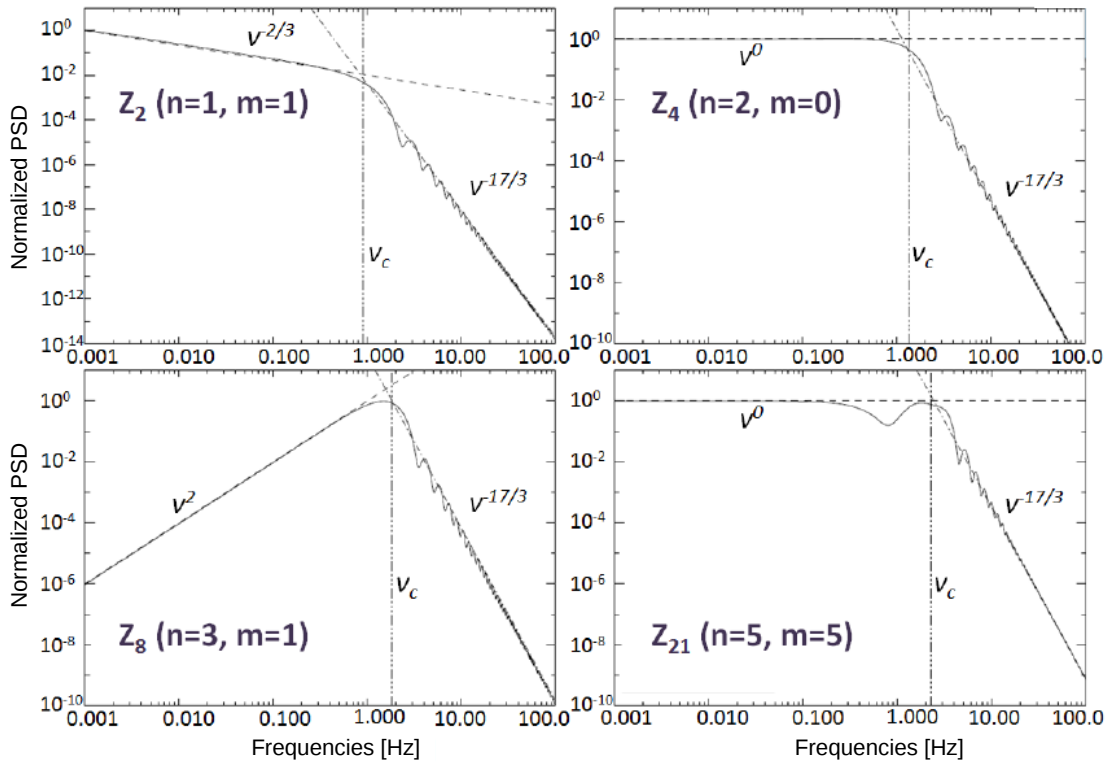

Figure 3.5: Turbulence normalized power spectral densities decomposed on Zernike modes, in the case of a single turbulent layer ($V/D = 8$ Hz). Four polynomials are presented. Low and high frequency asymptotes are indicated. The vertical lines $\nu_c(n)$ identify the cutoff frequencies.

- Low orders residuals when $n < N_{\text{corr}}$: the residual error corresponds to the sum of the contribution of the temporal, aliasing and noise errors. It is assumed in the following that they are not correlated, which is a good approximation in the case of small phase fluctuations and high signal-to-noise ratio, as shown in [Véran, 1998].

Assuming such an independence between the low order residuals, the total residual variance is simply given by the sum of each error:

$$\sigma^2_{\text{res}} \simeq \underbrace{\sigma^2_{\text{Fitting}}}_{\text{High orders}} + \underbrace{\sigma^2_{\text{Tempo}} + \sigma^2_{\text{Alias}} + (\sigma^2_{\text{Other}})^{\text{neglected}}}_{\text{Low orders}}. \tag{3.23}$$

This discrimination between high and low residual frequencies is depicted in Fig. 3.6b. Figure 3.6a, on the other hand, illustrates the spectrum corresponding to a perfect AO correction only composed of the fitting error. The number of corrected radial orders is related to the cutting spatial frequency $F_c(N_{\text{corr}})$ by replacing n by N_{corr} in Eq. (3.19). The frequency $F_c(N_{\text{corr}})$ thus defines the sampling frequency of the pupil by the actuators array. For instance, in the case of actuators separated by intervals of length d , it is given by $F_c = 1/(2d)$. In the following

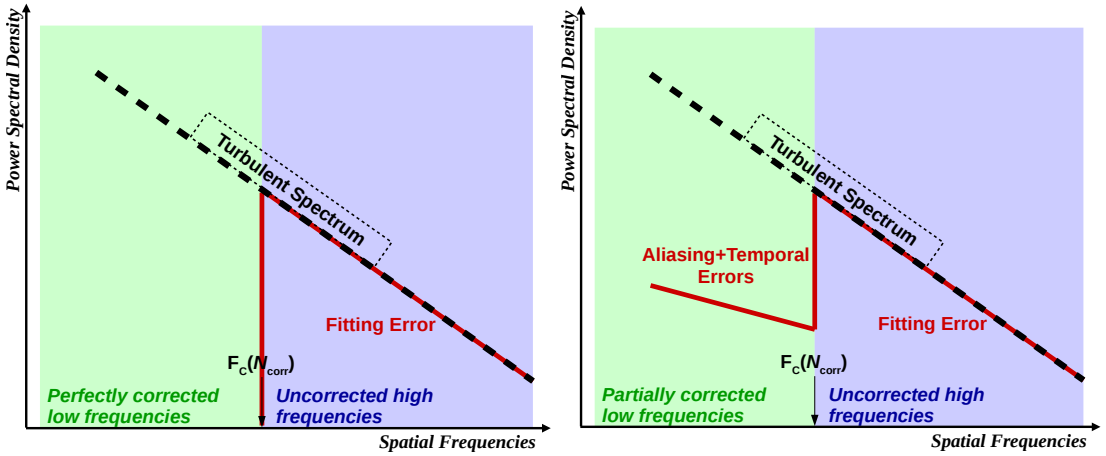

(a) (b)

Figure 3.6: Power spectral densities of the residual error after (A) perfect AO correction composed only by the high orders error (fitting) and (B) including both low orders (temporal and aliasing) and high orders residuals.

subsections, analytic expressions characterizing the aforementioned residual error terms are given.

3.2.3.4 Fitting error

It is implicitly supposed in the framework of such an AO modeling tool that the optical surfaces generated by the DM are obtained by linear combination of low order Zernike polynomials. While this might seem unrepresentative of a real mirror, the results obtained by Conan and summarized in the previous paragraphs imply that low-order Zernike polynomials correspond to low spatial frequencies. A DM, composed of a finite number of actuators, can only reproduce spatial frequencies lower than the inverse of the distance between the actuators, hence a certain analogy. The fitting error is related to this intrinsic limitation. It corresponds to the turbulence projected onto the space that is orthogonal to DM's modes and hence constituting a high order residual error. An asymptotic development of Eq. (3.22) when N_{corr} is large yields the following expression:

$$\sigma^2_{\text{Fitting}} \simeq 0.458\,(N_{\text{corr}}+1)^{-\frac{5}{3}} \left(\frac{D}{r_0}\right)^{\frac{5}{3}}. \tag{3.24}$$

Equation (3.24) can be written in terms of the last corrected Zernike mode:

$$\sigma^2_{\text{Fitting}} \simeq 0.257 Z_{\text{corr}}^{-\frac{5}{6}} \left(\frac{D}{r_0}\right)^{\frac{5}{3}}, \tag{3.25}$$

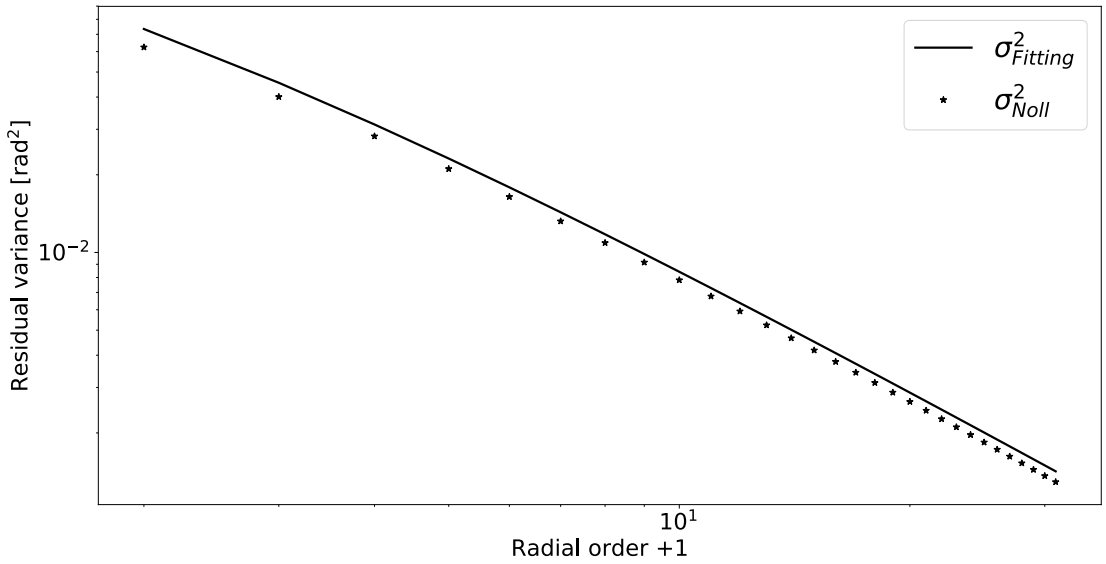

Figure 3.7: Residual variance after a perfect correction of all the modes up to a given radial order (x-axis). Comparison of the analytic expressions given (3.24) and (3.27)

with Z_{corr} given by:

$$Z_{\text{corr}} = \frac{(N_{\text{corr}}+1)(N_{\text{corr}}+2)}{2}. \tag{3.26}$$

As shown in Fig. 3.7, Eq. (3.25) is very close to the analytic expression originally found by Noll [Noll, 1976]:

$$\sigma^2_{\text{Noll}} \simeq 0.2944 Z_{\text{corr}}^{-\frac{\sqrt{3}}{2}} \left(\frac{D}{r_0}\right)^{\frac{5}{3}}. \tag{3.27}$$

3.2.3.5 Aliasing error

Due to the sampling of the wavefront by the finite number of sub-pupils composing the Shack-Hartmann WFS, part of the turbulence, of high spatial frequency, is poorly sampled and partially folds upon the measured lower frequencies. This induces a bias that propagates in the AO loop, creating an aliasing residual error. The latter is commonly modeled as a fraction of the error associated to the fitting error:

$$\sigma^2_{\text{Alias}} = \alpha \sigma^2_{\text{Fitting}}. \tag{3.28}$$

According to asymptotic developments presented in [Neichel, 2008], one can consider values of α ranging from 0.3 to 0.4. If not explicitly stated, $\alpha = 0.35$ is assumed in the remainder. Moreover, adapting further developments conducted by Neichel in his thesis, led to us to consider an analytic form for the aliasing residual power spectral density proportional to

$f^{-8/3}$. The latter was corroborated by end-to-end simulations. It should be noted that such developments were initially based on a Fourier modes approach that might no be accurate in the case of small systems. As such, the selection of α for instance merits further studies that were not treated in the present thesis.

3.2.3.6 Temporal error

The temporal error corresponds to an imperfect correction of the dynamic aberrations of the turbulence, due to the delay between measurement and correction. Assuming perfectly uncorrelated error terms, the average temporal residual error corresponding to the radial order $n < N_{\text{corr}}$ results in the imperfect rejection of the frequency content of the turbulent temporal spectrum by the servo loop.

Neglecting the propagation of WFS measurement noise inside the loop yields the following relation between the residual, $a_i^{\text{res}}(t)$, and turbulent, $a_i^{\text{turb}}(t)$, Zernike coefficients:

$$W_{a_i^{\text{res}}}(\nu) = \left| \frac{1}{1+G(\nu)} \right|^2 W_{a_i^{\text{turb}}}(\nu), \tag{3.29}$$

where $G = G_1 G_2$ is called the open-loop transfer function and G_1, G_2 are respectively given by Eqs (3.13) and (3.14). The cutting frequency of this function taken at 0 dB defines the bandwidth of the AO loop. The function $\left| \frac{1}{1+G(\nu)} \right|^2$ is called the rejection transfer function (RTF). This function accounts for the correction efficiency of the AO system as a function of the evolution frequency of the aberration to be mitigated. In other words it filters the spectrum of the turbulent coefficient. Typically, the system attenuates the low frequencies approximately up to the value of its bandwidth. It somewhat amplifies the frequencies slightly higher than this value and transmits, with a unit gain, the very high frequencies. Frequencies that are greater than the bandwidth of the AO loop are therefore not corrected. Such an overall behavior of the AO rejection transfer function is shown in Fig. 3.8, where the aforementioned analytic modeling is compared to end-to-end simulation. The temporal residual variance characterizing a mode corresponding to the radial order $n < N_{\text{corr}}$ is therefore given by the integral of Eq. (3.29):

$$\sigma^2_{\text{Tempo}}(n) = \int_0^\infty \left| \frac{1}{1+G(\nu)} \right|^2 W_n(\nu) d\nu. \tag{3.30}$$

3.2.3.7 Other sources of error

As suggested by Eq. (3.23), in addition to the preponderant temporal, fitting and aliasing terms other sources of errors, which can be neglected in a first order approximation, may impact the practical implementation of an AO system [Gousset, 2015]. Some stem from static aberrations and the close environment of the AO bench. The former are characterized by constant or

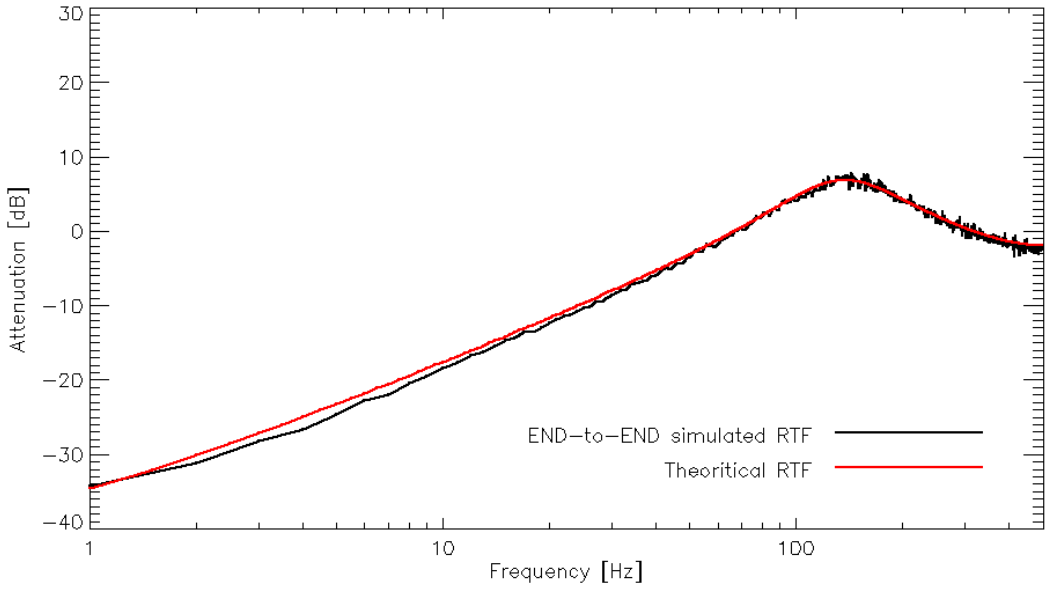

Figure 3.8: Comparison of analytic and simulated AO rejection transfer functions (RTF).

slowly variable terms, the evolution of which are for instance related to temperature change and precision and stability of the opto-mechanical structures. They typically comprise:

- A calibration error of the interaction matrix and subsequent errors in the computation of the command. It has in practice three main origins. A measurement bias in the acquisition of the interaction matrix due to noise and local turbulence. A poorly conjugated DM with the WFS sub-pupils, causing a loss of overall sensitivity of the system. A poor treatment of the modes not taken into account during the inversion of the interaction matrix.

- An error related to static aberrations that are not measured by the WFS and hence not compensated. They are induced by the intrinsic defects of the distinct optical components of the system.

- An exogenous error term that include the residual errors related to the experimental environment of the bench. It usually specifically refers to the impact of mechanical vibrations potentially affecting the system that can be filtered out using predictive control laws [Petit et al., 2008].

As mentioned in Section 3.2.1.1, due to scintillation two other contributors to the total residual error are worth mentioning. They can be characterized by the relative size of the induced spatial structures with respect to the size of the sub-pupils:

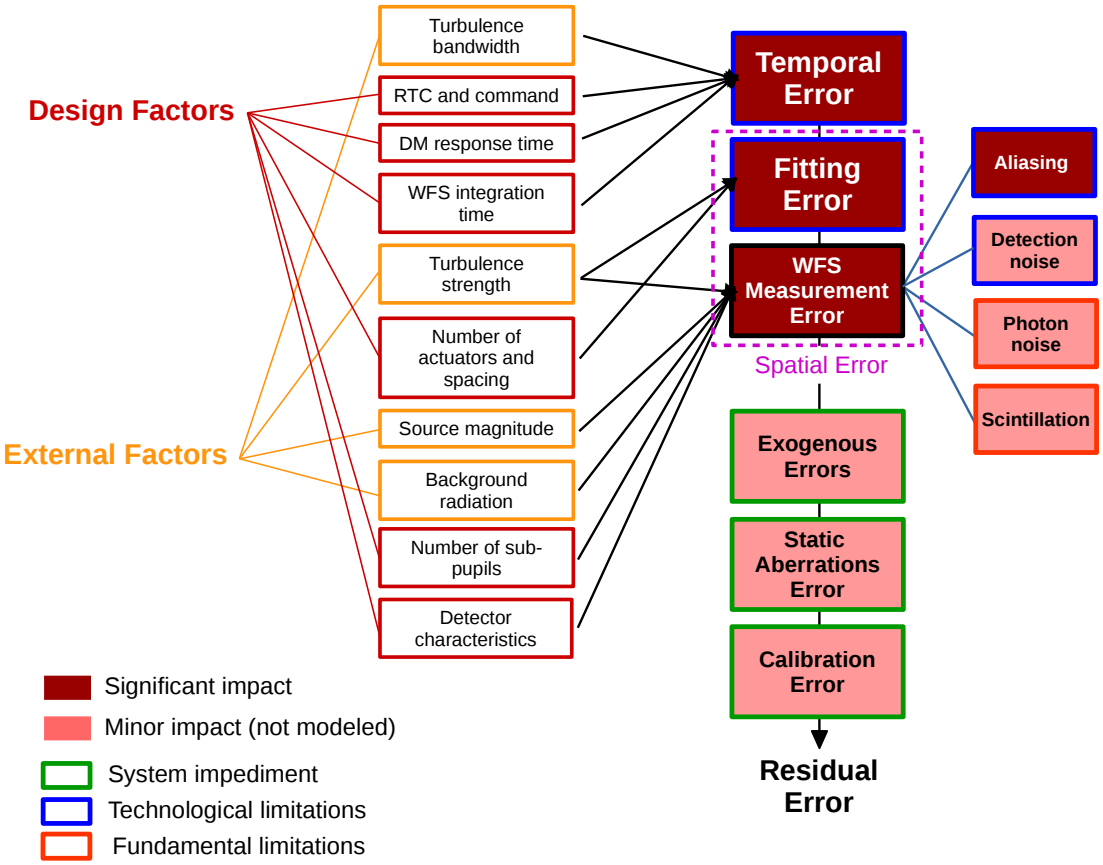

Figure 3.9: Main limitations impacted by design and external factors that affect an AO system performances in the framework of satellite downlinks. The most significant limitations are highlighted.

- Spatial structures greater than the sub-pupils size induce variations in the signal-to-noise ratio per sub-pupil.

- Spatial structures that are internal to each sub-pupil limit the measurement precision potentially affecting the computation of the corresponding centers of gravity [Mahé, 2000].

The impact of scintillation on wavefront-sensing was not taken into account during the development of the simplified AO model as it occurs under conditions of severe turbulence. This may impose a certain limitation regarding the validity of such a model in challenging conditions characterizing for instance very low elevation (LEO) downlinks.

Figure 3.9 synthesizes the limitations discussed thus far of an AO system as well as their origins: technological (often related to the components cost, complexity or development time), fundamental (related to the impact of turbulence on the propagation and magnitude of the signal source) and system or instrumental impediments.

3.2.4 Partial adaptive optics average performance assessment

The residual phase variance is by definition a good performance estimator for any closed-loop AO system since it is the quantity that is minimized. However, depending on the intended application, various additional performance measures of interest have been derived.

Among those, one finds the Strehl ratio (SR), which is widely used experimentally for estimating the quality of a correction. It is defined as the ratio of the on-axis intensities of the corrected Point-Spread Function (PSF) and the diffraction pattern of the telescope (Airy disk), that is:

$$\mathrm{SR} = \frac{\mathrm{PSF}(\alpha)}{\mathrm{Airy}(\alpha)}, \tag{3.31}$$

where α denotes the off-axis angle. Assuming small residual phase fluctuations the SR can be approximately expressed in terms of the residual phase variance as the coherent energy [Maréchal, 1947]:

$$\mathrm{SR} \simeq \exp(-\sigma_{\mathrm{res}}). \tag{3.32}$$

The SR and associated performance measures such as the coherent energy are particularly adapted to application related to image processing such as for instance image deconvolution.

In the context of communication applications, the relevant quantity is the amount of energy that is coupled into a single-mode fiber (SMF) or a mono-detector. In that case, the SR does not provide an accurate estimation of the latter. Hence, a natural AO performance measure proposed in this thesis is the average attenuation (i.e. compared to the transmitted power in non-turbulent conditions), given in dB, of the coupled power into the a SMF. It will be widely used in the remainder to describe the average performance of distinct receiver systems. Note that this average attenuation characterizes the losses induced by both residual phase and log-amplitude (scintillation) fluctuations. It is therefore related to the overall physical mitigation system performance including the telescope aperture (aperture averaging of scintillation) and AO (phase fluctuations mitigation).

Obviously, contrary to typical imaging application, data transmission performance assessment requires not only average efficiency estimators but also a precise statistical characterization of the instantaneous fluctuations of the coupled power. Such statistics are presented in the following Section 3.3 which constitutes a adaptation of a previously published paper [Canuet et al., 2018].

3.3 Analytic modeling of instantaneous power attenuations into single-mode fibers

3.3.1 Mathematical definitions and notations

3.3.1.1 Notations

Bold lower case and upper case variables will denote respectively vectors and matrices. When not used as a subscript the letter j will denote the imaginary unit. In the following, the operator $\langle\cdot|\cdot\rangle_Z$ denotes a scalar product with weight Z defined as:

$$\langle X|Y\rangle_Z \triangleq \iint Z(\boldsymbol{r})\cdot X(\boldsymbol{r})\cdot Y^*(\boldsymbol{r})d^2\boldsymbol{r}, \tag{3.33}$$

where $X(\boldsymbol{r})$, $Y(\boldsymbol{r})$, $Z(\boldsymbol{r})\in\mathbb{C}$ are functions of the spatial coordinates $\boldsymbol{r}$ and $Y^*(\boldsymbol{r})$ denotes the complex conjugate of $Y(\boldsymbol{r})$. Following this notation, instantaneous "spatial" normalized averages and variances are defined as:

$$\langle X\rangle_Z \triangleq \frac{\langle X|1\rangle_Z}{\langle 1|1\rangle_Z}, \tag{3.34}$$

$$\sigma_Z^2(X) \triangleq \langle X^2\rangle_Z - \langle X\rangle_Z^2. \tag{3.35}$$

This normalization ensures that $\langle 1\rangle_Z = 1$. The usual statistical average (or time average when time occurrences are considered) as well as statistical variance of the random variable $X(t)$ will be denoted respectively as μ_X and σ_X^2. The auto-covariance of the wide-sense stationary temporal process $V(t)$ is defined as:

$$R_V(\tau) \triangleq \mathrm{COV}(V(t),V(t)) = E[V(t)V(t+\tau)] - \mu_V^2. \tag{3.36}$$

3.3.1.2 Definitions

Let us consider an incident beam (unbounded plane wave) after propagation through turbulence and before reaching the telescope pupil of diameter D. Its electromagnetic field's complex amplitude is characterized by:

$$\Psi(\boldsymbol{r},t) = A_0\exp(\chi(\boldsymbol{r},t) + j\phi_{\mathrm{turb}}(\boldsymbol{r},t)), \tag{3.37}$$

where A_0 denotes the complex field amplitude without perturbation, $\chi(\boldsymbol{r},t)$ corresponds to the log-amplitude fluctuations and $\phi_{\mathrm{turb}}(\boldsymbol{r},t)$ represents the phase variations (aberrations). For a perfect plane wave in the absence of turbulence the incident field would simply be given

by $\Psi_0(\boldsymbol{r},t) = A_0$ and, without loss of generality the normalization of A_0 is chosen to ensure $\langle A_0|A_0\rangle_P = 1$ where P represents the pupil transmittance $P(\boldsymbol{r})$ defined as:

$$P(\boldsymbol{r}) = \begin{cases} 1 & \text{if} \quad 0 \leq \frac{2|r|}{D} \leq 1 \\ 0 & \text{otherwise} \end{cases} \tag{3.38}$$

The SMF mode expressed in the pupil plane, denoted as M_0 in the following, is a Gaussian mode whose waist is set in order to maximize its instantaneous matching with the unperturbed incident beam $\Psi_0(\boldsymbol{r},t)$ [Ruilier, 1998]. This matching is characterized in the pupil plane by the following normalized overlap integral [Shaklan and Roddier, 1988]:

$$\Omega_0 = \frac{\langle \Psi_0|M_0\rangle_P}{[\langle \Psi_0|\Psi_0\rangle_P \times \langle M_0|M_0\rangle_P]^{1/2}}, \tag{3.39}$$

where, for notational convenience, the time dependence of $\Psi_0(\boldsymbol{r},t)$ and hence $\Omega_0(t)$ have been omitted. In the absence of turbulence the instantaneous coupling efficiency is therefore given by:

$$\rho_0 = |\Omega_0|^2 \tag{3.40}$$

Similarly, the matching between the perturbed incident wave $\Psi(\boldsymbol{r},t)$ and the SMF mode is given by:

$$\Omega = \frac{\langle \Psi|M_0\rangle_P}{[\langle \Psi|\Psi\rangle_P \times \langle M_0|M_0\rangle_P]^{1/2}}. \tag{3.41}$$

The squared modulus of the aforementioned overlap integral corresponds to the instantaneous coupling efficiency of the perturbed incident beam:

$$\rho = |\Omega|^2, \tag{3.42}$$

and hence the instantaneous coupled flux into the SMF is:

$$f_{\text{SMF}} = |\Omega|^2 \times \langle \Psi|\Psi\rangle_P \tag{3.43}$$

3.3.2 Coupling efficiency estimator neglecting log-amplitude fluctuations

3.3.2.1 An approximation to the instantaneous normalized coupling efficiency

Neglecting turbulence-induced log-amplitude fluctuations, after partial AO correction, the electromagnetic field's complex amplitude of the incident wave is given by:

$$\Psi_{\Phi_{\text{res}}}(\boldsymbol{r},t) = A_0 \exp(j\phi_{\text{res}}(\boldsymbol{r},t)). \tag{3.44}$$

After defining $W_0 = PM_0$, the matching between $\Psi_{\Phi_{\text{res}}}(\boldsymbol{r}, t)$ and the SMF mode can be expressed as the following spatial normalized average:

$$\frac{\Omega_{\Phi_{\text{res}}}}{\Omega_0} = \frac{\langle \Psi_{\Phi_{\text{res}}} | M_0 \rangle_P}{\langle \Psi_0 | M_0 \rangle_P} = \langle \exp(j\phi_{\text{res}}) \rangle_{W_0}. \tag{3.45}$$

The right-hand term of Eq. (3.45) can always be written as:

$$\langle \exp(j\phi_{\text{res}}) \rangle_{W_0} = \exp(j\langle \phi_{\text{res}} \rangle_{W_0}) \langle \exp[j(\phi_{\text{res}} - \langle \phi_{\text{res}} \rangle_{W_0})] \rangle_{W_0}. \tag{3.46}$$

Taking the second multiplicative term of the right-hand side of Eq. (3.46) in the form of its power series expansion yields

$$\langle \exp(j\phi_{\text{res}}) \rangle_{W_0} = \exp(j\langle \phi_{\text{res}} \rangle_{W_0}) \sum_{l=0}^{\infty} \frac{\left\langle \left[j(\phi_{\text{res}} - \langle \phi_{\text{res}} \rangle_{W_0}) \right]^l \right\rangle_{W_0}}{l!}. \tag{3.47}$$

By invoking the ergodic hypothesis of the phase, one could assume that it is normally distributed over the pupil. Hence, the moment of order l of $\phi_{\text{res}} - \langle \phi_{\text{res}} \rangle_{W_0}$ would be given by:

$$\left\langle (\phi_{\text{res}} - \langle \phi_{\text{res}} \rangle_{W_0})^l \right\rangle_{W_0} = \begin{cases} 0 \text{ if } l \text{ odd} \\ \sigma^l_{W_0}(\phi_{\text{res}})(l-1)!! \text{ if } l \text{ even} \end{cases} \tag{3.48}$$

and one could write

$$\langle \exp(j\phi_{\text{res}}) \rangle_{W_0} = \exp(j\langle \phi_{\text{res}} \rangle_{W_0}) \exp\left(-\frac{\sigma^2_{W_0}(\phi_{\text{res}})}{2} \right). \tag{3.49}$$

However, when the normality of the spatial distribution of the phase over the pupil cannot be justified Eq. (3.49) is not exact. Nevertheless, when $\phi_{\text{res}} - \langle \phi_{\text{res}} \rangle_{W_0} \ll 1$, Ruilier and Cassaing have shown that it could still be a good approximation [Ruilier and Cassaing, 2001] and, Meimon et. al. experimentally confirmed it [Meimon et al., 2013]. Therefore an approximation of the instantaneous normalized coupling efficiency is given by:

$$\rho^{\text{APPROX}}_{\Phi_{\text{res}}} \simeq \rho_0 \exp\left[-\sigma^2_{W_0}(\phi_{\text{res}}) \right]. \tag{3.50}$$

3.3.2.2 Decomposition onto an orthonormal basis

In theory, over a circular pupil, at a given instant t, the residual phase $\phi_{\text{res}}(\boldsymbol{r}, t)$ can always be expanded on the set constitued by the Zernike polynomials (see Eq. (3.16)).

However, in practice, the phase is expanded on a truncated Zernike decomposition constituted of a finite number N_{Max} polynomials that should be chosen large enough in order to minimize the turbulent wavefront aberrations not taken into account by such a truncation.

Moreover, when one considers the coupling of the incident field with a SMF, the set of Zernike polynomials over the weighted pupil does not constitute an orthonormal basis anymore [Mahajan, 2013]. In that case, by working with Zernike polynomials one would not be able to take advantage of the properties of a set of polynomials in their orthonormal form. More precisely, the spatial variance of the turbulent phase over the pupil would not be equal to the sum of the squares of the Zernike coefficients (without the piston term) anymore. Dai and Mahajan [Dai and Mahajan, 2007, Dai and Mahajan, 2008] have derived a simple and convenient method that permits the computation of a conversion matrix linking the decomposition coefficients of the Zernikes polynomials to the coefficients of a new basis of orthonormal polynomials.

Such an efficient yet simple method derived in [Dai and Mahajan, 2007, Dai and Mahajan, 2008] for computing a conversion matrix linking the decomposition coefficients of the Zernikes polynomials to the coefficients of a new basis of orthonormal polynomials is summarized hereafter.

Let us first write the complete set of Zernike polynomials as $\{Z_i\}$ over the intensity domain Σ comprising a circular pupil and the back-propagated Gaussian SMF on the pupil as well. Because of the completeness of $\{Z_i\}$, one can represent any other set of polynomials as a linear combination of $\{Z_i\}$ including a set $\{F_i\}$ that is indeed orthonormal over Σ. These two sets are related to each other according to:

$$F_i = \sum_{j=1}^{N} M_{ij} Z_j \tag{3.51}$$

where $\boldsymbol{M}$ is a conversion matrix and N is the number of polynomials arbitrarily determined in order to represent a given aberration. One can always write:

$$\langle F_i | Z_k \rangle_{W_0} = \sum_{j=1}^{N} M_{ij} \langle Z_j | Z_k \rangle_{W_0} \tag{3.52}$$

or

$$\langle Z_k | F_i \rangle_{W_0} = \sum_{j=1}^{N} \left[M_{ij} \langle Z_j | Z_k \rangle_{W_0} \right]^T = \sum_{j=1}^{N} \langle Z_k | Z_j \rangle_{W_0} \left[M_{ij} \right]^T \tag{3.53}$$

written in matrix form as:

$$\boldsymbol{C}^{ZF} = \boldsymbol{C}^{ZZ} \boldsymbol{M}^T \tag{3.54}$$

where $\boldsymbol{C}^{ZF}$ is a $N \times N$ matrix of the inner products between the first N polynomials of Z_k and the first N polynomials of F_i and, $\boldsymbol{C}^{ZZ}$ is a $N \times N$ matrix of the inner products between the

first N polynomials of Z_k with themselves. Similarly, one can write:

$$\langle F_i|F_k\rangle_{W_0} = \sum_{j=1}^{N} M_{ij}\langle Z_j|Z_k\rangle_{W_0} = \delta_{ik} \tag{3.55}$$

where δ_{ik} is the Kronecker symbol and which can be written in matrix form as well:

$$\boldsymbol{M}\boldsymbol{C}^{ZF} = \mathbf{1} \tag{3.56}$$

Substituting Eq. (3.54) in Eq. (3.56) yields

$$\boldsymbol{M}\boldsymbol{C}^{ZZ}\boldsymbol{M}^T = \mathbf{1} \tag{3.57}$$

Now, let

$$\boldsymbol{M} = (\boldsymbol{Q}^T)^{-1} \tag{3.58}$$

Then Eq. (3.57) can be written as:

$$\boldsymbol{Q}^T\boldsymbol{Q} = \boldsymbol{C}^{ZZ} \tag{3.59}$$

The inner product matrix $\boldsymbol{C}^{ZZ}$ is symmetric positive definite. Therefore Eq. (3.59) can be solved for $\boldsymbol{Q}$ uniquely with a simple Cholesky decomposition and eventually the conversion matrix $\boldsymbol{M}$ can be obtained from Eq. (3.58). The inverse of the transposed of this conversion matrix, $\left(\boldsymbol{M}^T\right)^{-1}$, is required to express the orthonormal coefficients in terms of the original Zernike coefficients (see Eq. (3.60)). This matrix (the absolute values of its elements) is represented in Figure 3.10 for the first 50 modes (piston included). One can see that it is nearly diagonal, but terms with the same azimuthal frequency such as tip–tilt and comas or piston, defocus, and spherical aberration, are not completely null and hence induce some correlation among the orthonormal coefficients. The latter is nevertheless relatively weak and can be neglected in a first approximation. Eventually, the orthonormal polynomials' coefficients $\boldsymbol{b}^{\text{res}}$ can be obtained from the initial Zernike coefficients $\boldsymbol{a}^{\text{res}}$ given the lower triangular conversion matrix $\boldsymbol{M}$:

$$\boldsymbol{b}^{\text{res}} = \left(\boldsymbol{M}^T\right)^{-1}\boldsymbol{a}^{\text{res}}, \tag{3.60}$$

and the coupling efficiency given by Eq. (3.50) can be expressed directly in terms of these coefficients:

$$\rho_{\Phi_{\text{res}}}^{\text{APPROX}} \simeq \rho_0 \exp\left[-\sum_{i=2}^{N}(b_i^{\text{res}})^2\right]. \tag{3.61}$$

3.3.2.3 Difference between SAOST and the analytic approximation model

The simplified partial AO modeling tool SAOST, introduced in Section 3.2.3 relies on the computation of random occurrences of centered normally distributed Zernike coefficients

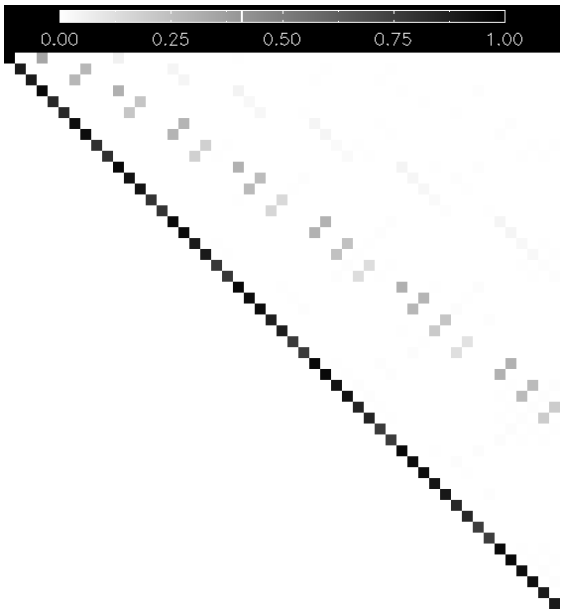

Figure 3.10: Absolute values of the inverse of the transposed of conversion matrix, $|\left(\boldsymbol{M}^{T}\right)^{-1}|$

for describing the corrected phase. This is done by following an analogous version of the algorithm described in [Roddier, 1990], however without taking into account the non-diagonal terms of the covariance matrix between the Zernike modes. The temporal correlation of the residual phase is induced by filtering the temporal power spectra densities of the corrected phase. The residual phase variance characterizing the performance of the simulated AO system comprises terms related to the finite number of actuators (fitting error), wave-front sensing precision (aliasing error) and control-loop frequency (temporal error).

Therefore, although SAOST assumes a simplified (analytic) AO modeling (see Section 3.2.3), it does compute time-correlated random samples of injection losses according to the exact expression:

$$\rho_{\Phi_{\text{res}}}^{\text{SAOST}} = \left| \frac{\langle \Psi | M_0 \rangle_P}{[\langle \Psi | \Psi \rangle_P \times \langle M_0 | M_0 \rangle_P]^{1/2}} \right|^2 . \tag{3.62}$$

3.3.2.4 Accuracy of the analytic approximation

To infer on the accuracy of the distinct approximations made so far concerning the injection losses into the SMF, one may compare simulation results that correspond to Eq. (3.62) (SAOST outputs), Eq. (3.50) (pre-reorthonormalisation approximation) and Eq. (3.61) (post-reorthonormalisation approximation).

Histograms of Monte-Carlo computations of these expressions are presented in Figures 3.11a and 3.11b for a GEO as well as a LEO downlink scenario. The link parameters corresponding

to both scenarios are detailed in Table 3.1. They include as well the approximations given by the squarred modulus of Eq. (3.47). The difference with the output from SAOST is measured through the computation of their respective Jensen-Shannon (JS) distances [Cha, 2007] with the histogram of $\rho_{\Phi_{\text{res}}}^{\text{SAOST}}$.

The results corresponding to Eq. (3.50) and Eq. (3.61) are perfectly equivalent and hence validate the re-orthonormalization process of the Zernike's polynomials weighted by the Gaussian mode of the SMF. For comparison, the expansion in Eq. (3.47) is carried up to the fourth and sixth orders as well by computing the corresponding l-th central moment of the phase using the orthonormal polynomial decomposition approach:

$$\langle \left[j(\phi - \langle \phi \rangle_{W_0}) \right]^l \rangle_{W_0} = j \sum_{j=2}^{N} \cdots \sum_{k=2}^{N} b_j \cdots b_k \langle F_j \cdots F_k \rangle_{W_0} \tag{3.63}$$

This requires the expensive calculation of l nested sums of the products of l polynomials and their expansion coefficients and quickly leads to intractable analytic statistical results. Owing to the non-normality of the phase distribution over the pupil, carrying the expansion in Eq. (3.47) up to the sixth order yield more accurate results than Eq. (3.50). On the other hand, while providing a simpler expression Eq. (3.61) yields results as precise as a fourth order expansion hence justifying the choice made in the following analytic developments to use the former instead of a slightly more precise expression related to Eq. (3.63). This is true at least for the two cases presented here. Note as well, that this choice leads to a pessimistic approximation of the coupling efficiency.

Finally, note that the accuracy of SAOST simulations depends on the finite number of modes representing the turbulent wavefront, which as it gets larger, requires for proper sampling a higher number of pixels describing the pupil. Accurate results, depending on the scenario and turbulent conditions under consideration, hence may come at the expense of computing time that can be comparable to those related to end-to-end wave-optics based simulations thus motivating the recourse to precise statistical analytic expressions that will be described 3.3.5.

3.3.3 Coupled flux: taking into account the impact of scintillation

Consider the ideal case where the phase fluctuations induced by the atmosphere are completely corrected (or otherwise neglected). Using the results related to the average of the long-exposure images' modulation transfer function presented in [Fried, 1966], an expression for the average coupled flux into a SMF while neglecting phase aberrations of the turbulent

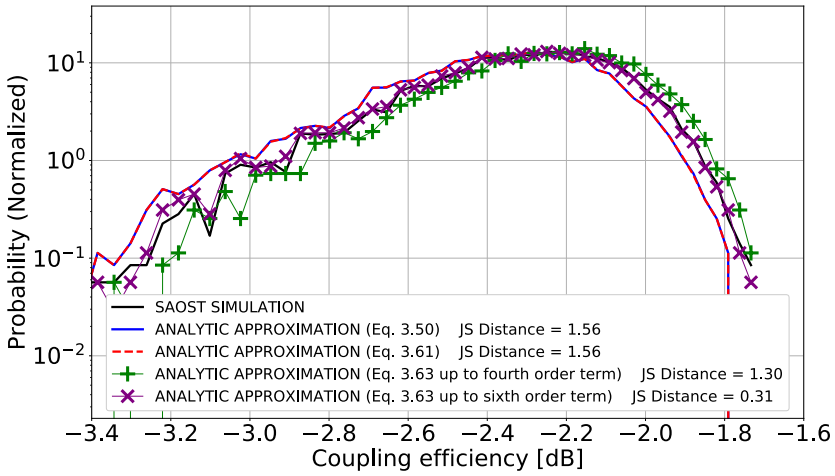

(a)

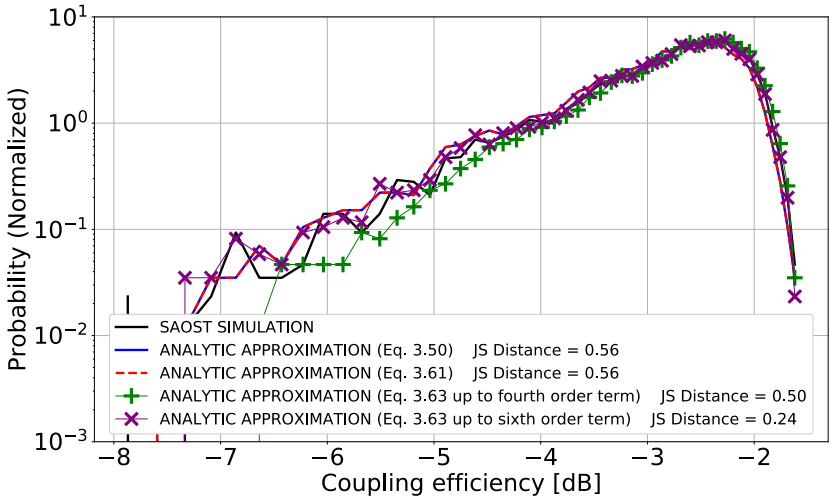

(b)

Figure 3.11: Histograms of Monte-Carlo simulated coupling efficiency for (A) GEO-to-ground downlink scenario (B) LEO-to-ground downlink scenario

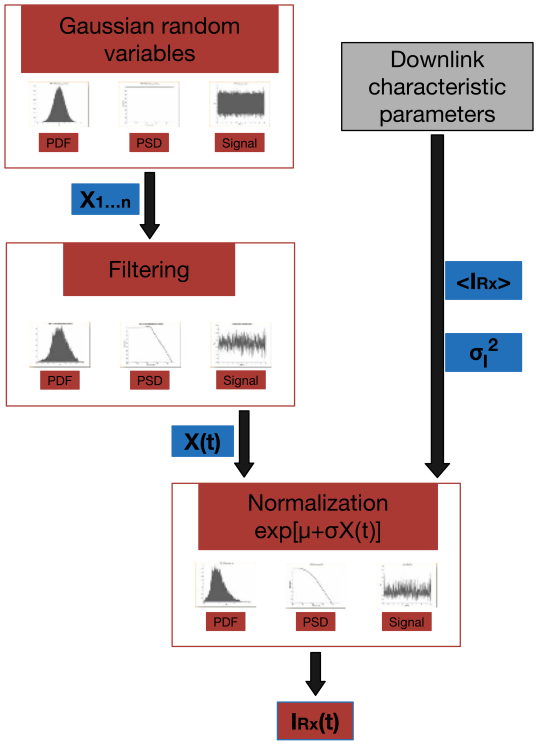

Figure 3.12: Diagram representing the algorithm for generating irradiance time series. Adapted from [Epple, 2010].

wavefront is given by:

$$\mu_{f_{\text{SMF}}^{\text{Scint}}} = \frac{A_0^2}{\rho_0} \exp(-C_\chi(0)) \iint W_0(\boldsymbol{r}) W_0(\boldsymbol{r}+\boldsymbol{s}) \exp(C_\chi(\boldsymbol{s})) d^2\boldsymbol{r} d^2\boldsymbol{s}. \tag{3.64}$$

where $C_\chi(\boldsymbol{r})$ is the log-amplitude spatial covariance function. This equation can always be written as:

$$\mu_{f_{\text{SMF}}^{\text{Scint}}} = \frac{A_0^2}{\rho_0} \exp(-C_\chi(0)) \int \exp(C_\chi(\boldsymbol{s}))(W_0 * W_0)(\boldsymbol{s}) d^2\boldsymbol{s}, \tag{3.65}$$

where the symbol $*$ denotes convolution. The term $(W_0 * W_0)(\boldsymbol{s})$ corresponds to the autocorrelation of the apodized pupil (i.e. weighted by the Gaussian mode of the SMF), which is in fact the transfer function of the instrument (i.e. telescope and SMF). Approximating $\exp(C_\chi(\boldsymbol{s}))$ by its first two series terms yields:

$$\begin{aligned} \mu_{f_{\text{SMF}}^{\text{Scint}}} \simeq \frac{A_0^2}{\rho_0} \exp(-C_\chi(0)) \Bigg(\int (W_0 * W_0)(\boldsymbol{s}) d^2\boldsymbol{s} + \\ \int C_\chi(\boldsymbol{s})(W_0 * W_0)(\boldsymbol{s}) d^2\boldsymbol{s} \Bigg). \end{aligned} \tag{3.66}$$

This approximation tends to be less accurate as the log-amplitude fluctuation regime is stronger. Using the generalized Parseval theorem and remembering that $\langle A_0|A_0\rangle_P = 1$, yields:

$$\mu_{f_{\text{SMF}}^{\text{Scint}}} \simeq \exp(-C_\chi(0))\left(1+\frac{\int \mathscr{F}\left[C_\chi(\boldsymbol{r})\right](\boldsymbol{\omega})\left[\mathscr{F}\left[W_0(\boldsymbol{r})\right](\boldsymbol{\omega})\right]^2 d^2\boldsymbol{\omega}}{\rho_0 \times \langle 1|1\rangle_P}\right), \tag{3.67}$$

where the symbol $\mathscr{F}$ denotes the Fourier transform operator. In Eq. (3.67), the numerator of the last term in the right-hand side corresponds to the spectral power density of the log-amplitude fluctuations in the pupil filtered by the instrument (that is the pupil and the SMF). It represents the influence of the spatial correlation of the speckles in the pupil on the mean coupled flux attenuation. Since the difference has been verified numerically to be negligible for the downlink scenarios studied here, it is approximated by the spectral power density of the log-amplitude fluctuations filtered by the pupil only.

Furthermore, as long as one does not consider strong fluctuation regimes of $\chi(\boldsymbol{r},t)$, it is widely accepted that the aperture averaged irradiance fluctuations are log-normally distributed [Tatarski, 1961, Strohbehn, 1978]. The random generation of the latter is done using an algorithm analogous to the one described in [Epple, 2010]. The general principle of such an algorithm is represented in Fig 3.12. The irradiance fluctuations, denoted $\exp(2\chi_{\text{Ap}}(t))$ in the following, depends on the Gaussian random variable $\chi_{\text{Ap}}(t)$ representing the aperture averaged log-amplitude fluctuations that are characterized by their variance $\sigma^2_{\chi_{\text{Ap}}}$. The analytic model describing this variable, including its temporal power spectrum, can be found in [Robert et al., 2008].

The log-normality assumption of the aperture averaged irradiance stems from arguments presented in Section 2.3.3.2. It can be used to state that in this regime the completely corrected coupled flux into the SMF can be described as well by a log-normal random variable. By setting the mean of the aperture averaged log-amplitude fluctuations equal to $-\sigma^2_{\chi_{\text{Ap}}}$ it is ensured that $\mu_{\exp(2\chi_{\text{Ap}})} = 1$. Thence, the random variable $\mu_{f_{\text{SMF}}^{\text{Scint}}} \times \exp(2\chi_{\text{Ap}}(t))$ represents the scintillation-only induced variations of the coupled flux whose mean is fixed by Eq. (3.67). By considering the different origins of the fluctuations of the log-amplitude and the phase that is, the former are mostly caused by distant turbulence, whereas the latter are mostly introduced close to ground [Perlot, 2007], one can assume statistical independence of scintillation and phase effects. Therefore, after combining the results characterizing the completely corrected case described above and those of Section 3.3.2 the instantaneous coupled flux in a SMF after partial AO correction is approximated by:

$$f_{\text{SMF}}^{\text{APPROX}}(t) \simeq \rho_0 \mu_{f_{\text{SMF}}^{\text{Scint}}} \exp(2\chi_{\text{Ap}}(t)) \exp\left[-\sum_{i=2}^{N} b_i(t)^2\right]. \tag{3.68}$$

3.3.4 Synthesis of the distinct modeling options

For the sake of clarity, hereafter are recalled the difference between AOST (end-to-end), SAOST and the analytic approximation to the instantaneous power coupled into a SMF after partial AO correction.

AOST

The generation of time series by AOST relies in fact on two different softwares. For simulating the atmospheric propagation of an optical wave, AOST uses the phase-screen approach described in Section 2.3.2. This is a highly time-consuming computation done by TURANDOT (an optimized version of the wave-optics software developed by ONERA). The correlated phase-screen generated by the latter are fed to a partial AO end-to-end modeling software (AOST) that outputs correlated time series of the attenuation of the power coupled into the SMF. AOST relies on accurate modeling of the WFS, command and wavefront reconstruction as detailed in 3.2.2.

SAOST

The generation of time series by SAOST is based upon the assumption that log-amplitude and phase variations are independent. The computation of the residual phase is done by modeling the impact of a partial AO system as detailed in Section 3.2.3. A filtering approach is applied to the well-known spectra (spatial and temporal) of the turbulent phase in order to simulate the residual phase.

The impact of scintillation is taken into account similarly to the description given in Section 3.3.3. The random generation of aperture-averaged irradiance fluctuations is implemented as in [Epple, 2010] and assumes weak to moderate turbulence conditions. These fluctuations are temporally correlated by filtering them by the spectrum described in [Robert et al., 2008]. The impact of scintillation on the coupled flux is statistically taken into account on average thanks to Eq. (3.67).

Using SAOST, the coupled flux fluctuations are hence obtained by considering the product between the term related to such an instantaneous aperture-averaged irradiance and the term related to the exact injection efficiency $\rho_{\Phi_{\text{res}}}^{\text{SAOST}}$ given by Eq. (3.62):

$$f_{\text{SMF}}^{\text{SAOST}}(t) = \mu_{f_{\text{SMF}}^{\text{Scint}}} \exp(2\chi_{\text{Ap}}(t)) \rho_{\Phi_{\text{res}}}^{\text{SAOST}}. \tag{3.69}$$

Analytic approximation

In terms of the treatment of scintillation and the partial AO modeling, the analytic approxima-

tion relies on assumptions that are identical to those made for SAOST. The difference lies in the computation of the instantaneous injection efficiency. Here, the analytic approximation counterpart of the latter is obtained after converting the correlated Zernike coefficients into orthonormal polynomials coefficients and using the approximation given by Eq. (3.61). This yields Eq. (3.68) that has the advantage of being analytically statistically characterizable. Such statistical laws are derived and compared to end-to-end simulation in the remainder of the present chapter. Note that for the results presented subsequently, the parameters required by these statistical law have been evaluated empirically from the outputs of SAOST, themselves based on the analytic models described throughout Section 3.2.3.

3.3.5 Analytic statistical results

3.3.5.1 Statistical distribution functions: PDF and CDF

Let us first derive the PDF and CDF of the quantity $\sum_{i=2}^{N} b_i^2(t)$. Since the Zernike coefficients $\{a_i\}$ are Gaussian random variables [Roddier, 1981], in light of Eq. (3.60) it is clear that the coefficients $\{b_i\}$ are Gaussian as well. Therefore, the square of each one of the latter is Gamma distributed with constant shape parameter $\alpha = 0.5$ and scale parameter $\beta_i = 2\sigma_{b_i}$ where σ_{b_i} is the statistical variance of the coefficient corresponding to mode i, obtained empirically. In consequence, the sum of these coefficients $\sum_{i=2}^{N} b_i^2(t)$ is characterized by a sum of independent and non identical Gamma random variables. Note that in light of Eq. (3.60), it might be argued that the coefficients $\{b_i\}$ are not completely independent. However, it was verified numerically that $\left(\boldsymbol{M}^T\right)^{-1}$ is nearly diagonal and hence the dependence between the aforementioned coefficients is negligible as shown in Fig. 3.10. The marginal characteristic function of such a process can be written as:

$$\varphi(u) = \prod_{i=2}^{N} \left(1 - \frac{ju}{\beta_i}\right)^{-\alpha}. \tag{3.70}$$

By performing the inverse Laplace transform of this characteristic function, the probability density function of $z(t) = \sum_{i=2}^{N} b_i^2(t)$ can be obtained using Gil-Pelaez's result [Gil-Pelaez, 1951]:

$$p_Z(z) = \frac{1}{\pi} \int_0^{\infty} \frac{\cos\left(\sum_{i=2}^{N} \alpha \arctan(\beta_i u) - zu\right)}{\prod_{i=2}^{N} \left(1 + u^2 \beta_i^2\right)^{\frac{\alpha}{2}}} du. \tag{3.71}$$

The cumulative distribution function can be determined as well:

$$P_Z(z) = \frac{1}{2} - \frac{1}{\pi} \int_0^{\infty} \frac{\mathrm{Im}\left\{\prod_{i=2}^{N} (1 - \beta_i ju)^{-\alpha} \exp[-juz]\right\}}{u} du. \tag{3.72}$$

To the best of our knowledge this result was first published by G. Efthymoglou and V. Aalo [Efthymoglou and Aalo, 2008]. More recently, several authors have presented alternative forms

characterizing the distribution of such random variables [Ansari et al., 2012, Aalo et al., 2005]. However, although they may seem more tractable, these solutions can be more difficult to compute numerically. Using a simple change of variable the PDF and CDF of the normalized coupling efficiency given by Eq. (3.61) are respectively:

$$p_{P_\Phi}(\rho_\Phi) = \frac{1}{\rho_\Phi} p_Z\left(\log\left(\frac{\rho_0}{\rho_\Phi}\right)\right), \tag{3.73}$$

and

$$P_{P_\Phi}(\rho_\Phi) = 1 - P_Z\left(\frac{\rho_\Phi}{\rho_0}\right). \tag{3.74}$$

On the basis of the assumption of the independence of log-amplitude and phase fluctuations, the probability density function and the cumulative distribution function of the random variable defined by Eq. (3.68) are given respectively by Eq. (3.75) and Eq. (3.76), in which σ_I^2 is the aperture-averaged log-irradiance variance (approximated by the scintillation index in the weak fluctuation regime) and $\mu_I = \mu_{\exp(2\chi_{\mathrm{Ap}})} = 1$ (see subsection 3.3.3).

$$p_{F_{\mathrm{SMF}}}(f_{\mathrm{SMF}}) = \frac{1}{\pi\sqrt{2\pi}\sigma_I f_{\mathrm{SMF}}} \int_{-\infty}^{\infty} \left[\int_0^{\infty} \frac{\cos\left(\sum_{i=2}^{N} \alpha \arctan(\beta_i v) - \ln(\frac{\rho_0 \mu_{f_{\mathrm{SMF}}^{\mathrm{Scint}}}}{u}) v\right)}{\prod_{i=2}^{N} \left(1 + v^2 \beta_i^2\right)^{\frac{\alpha}{2}}} dv \right] \frac{1}{|u|} \exp\left(- \frac{\left[\ln(\frac{f_{\mathrm{SMF}}}{u\mu_i}) + \frac{\sigma_I^2}{2}\right]^2}{2\sigma_I^2} \right) du. \tag{3.75}$$

$$P_{F_{\mathrm{SMF}}}(f_{\mathrm{SMF}}) = \int_0^{\infty} \left[\frac{1}{2} + \frac{1}{2} \mathrm{erf}\left(\frac{\ln(\frac{f_{\mathrm{SMF}}}{u\mu_I} + \frac{\sigma_I^2}{2})}{\sqrt{2}\sigma_I} \right) \right] \frac{1}{u\pi} \left[\int_0^{\infty} \frac{\cos\left(\sum_{i=2}^{N} \alpha \arctan(\beta_i v) - \ln(\frac{\rho_0 \mu_{f_{\mathrm{SMF}}^{\mathrm{Scint}}}}{u}) v\right)}{\prod_{i=2}^{N} \left(1 + v^2 \beta_i^2\right)^{\frac{\alpha}{2}}} dv \right] du. \tag{3.76}$$

These analytic PDF and CDF of the instantaneous coupled flux attenuation are per se useful results in deriving the channel capacity and probability of outages of FSO transmissions [Canuet et al., 2016].

3.3.5.2 Temporal Autocovariance

Let us first derive an approximation of the auto-covariance of the coupling efficiency $\rho_{\Phi_{\text{res}}}^{\text{APPROX}}$ given by Eq. (3.61) that will be denoted $\rho_\Phi(t)$ in the following. It is by definition a wide-sense stationary random process. The first-order expansion of its auto-covariance is hence given by:

$$R_{\rho_\Phi}(\tau) \simeq \rho_0^2 \left(E\left[\sum_{i=2}^{N} b_i^2(t) \sum_{i=2}^{N} b_i^2(t+\tau) \right] - \mu^2_{\sum_{i=2}^{N} b_i^2} \right). \tag{3.77}$$

Since every $\{b_i\}$ is a centered normal random variable, $\mu^2_{\sum_{i=2}^{N} b_i^2} = \left(\sum_{i=2}^{N} \sigma^2_{b_i}\right)^2$. By assuming that inter-modal covariances are negligible when compared to the modal covariances and by subsequently using the theorem of Isserlis [Isserlis, 1916, Isserlis, 1918] allowing to express higher-order moments of Gaussian random variables in terms of their covariances, it comes:

$$R_{\rho_\Phi}(\tau) \simeq 2\rho_0^2 \sum_{i=2}^{N} E\left[(b_i(t) b_i(t+\tau)\right]^2. \tag{3.78}$$

A simple approximation of the auto-covariance of the coupling efficiency $\rho_\Phi(t)$ is therefore obtained since the analytic models describing the Zernike coefficients temporal spectra are well-known (see Sections 3.2.3.2, 3.2.3.6 and [Conan et al., 1995]) whereas Zernikes' inter-spectrum can be obtained as in [Whiteley et al., 1998]. Figure 3.13 compares the auto-correlation functions corresponding to the approximations given by Eq. (3.77) and Eq. (3.78) and SAOST simulations. Bartlett's 95% confidence intervals are shown as well [Bartlett, 1946]. For both LEO and GEO links the first order approximation of the instantaneous coupling efficiency yields fairly accurate results. Neglecting intermodal correlations provides a less accurate approximation that is nevertheless still inside the confidence bands. The errors on the correlation time (width at half-maximum) are inferior to 3%. Using the result of [Wecker, 1978] dealing with the autocovariance of the product of two stationary time series, the auto-covariance of the coupled flux after partial AO correction is given by:

$$\begin{aligned} R_{f_{\text{SMF}}}(\tau) = \mu^2_{f_{\text{SMF}}^{\text{Scint}}} \big[& R_{\rho_\Phi}(\tau) R_{\exp(2\chi_{Ap})}(\tau) + \\ & + \mu^2_{\rho_\Phi} R_{\exp(2\chi_{Ap})}(\tau) + R_{\rho_\Phi}(\tau) \big]. \end{aligned} \tag{3.79}$$

As mentionned in subsection 3.3.3, the aperture-averaged irradiance's temporal characteristics are modeled as in [Robert et al., 2008] and μ_{ρ_Φ} can be obtained thanks to the PDF given by Eq. (3.73).

3.3.5.3 Average fading duration

For an arbitrary stationary differentiable random process such as $f_{\text{SMF}}(t)$ with a given probability density function $p_{F_{\text{SMF}}}(f_{\text{SMF}})$, it is possible to compute an approximation of the average

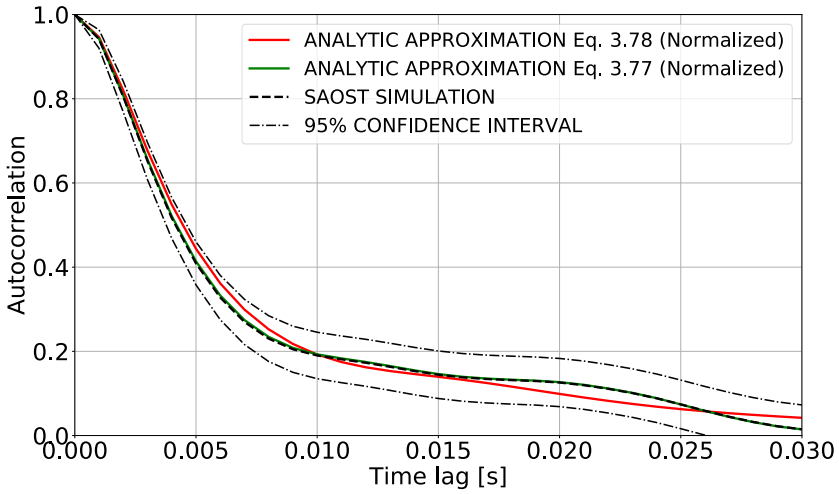

(a)

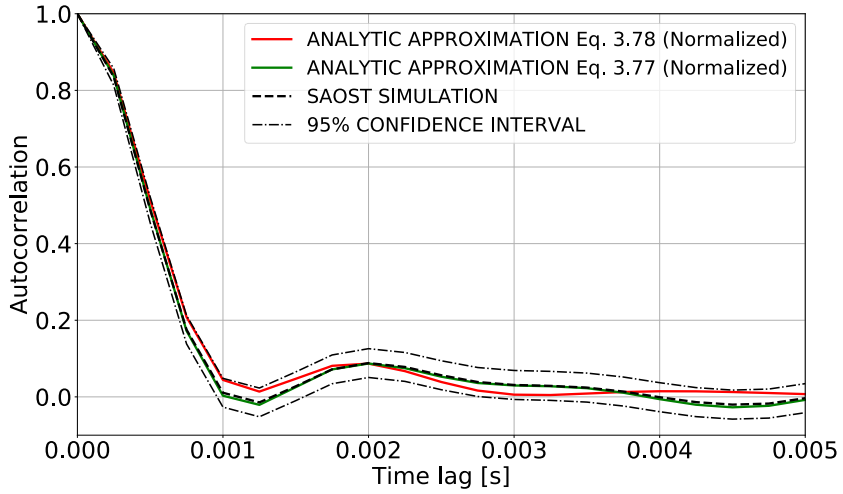

(b)

Figure 3.13: Numerically computed auto-correlation functions of Monte-Carlo (SAOST) simulation results for (A) GEO-to-ground downlink scenario (B) LEO-to-ground downlink scenario

unidirectional (upward or downward) level-crossing rate $\nu(f^0_{\mathrm{SMF}})$ at a given threshold f^0_{SMF} by using the result of [Yura and Hanson, 2010]:

$$\nu(f^0_{\mathrm{SMF}}) = \frac{1}{2}\frac{\sigma_{\dot{f}_{\mathrm{SMF}}}}{\pi\sqrt{\gamma}} \exp -\frac{h^2(f^0_{\mathrm{SMF}})}{2}, \tag{3.80}$$

where $\sigma_{\dot{f}_{\mathrm{SMF}}}$ is the standard deviation of the time derivative of $f_{\mathrm{SMF}}(t)$ which is by definition [Bendat and Piersol, 2012] given by the second time derivative of the autocovariance function in the vicinity of 0:

$$\sigma^2_{\dot{f}_{\mathrm{SMF}}} = -\ddot{R}_{f_{\mathrm{SMF}}}(\tau)|_{\tau=0}. \tag{3.81}$$

The function $h(\cdot)$ depends on the CDF of $f_{\mathrm{SMF}}(t)$ i.e. $P_{F_{\mathrm{SMF}}}(f_{\mathrm{SMF}})$ given by Eq. (3.76):

$$h(f^0_{\mathrm{SMF}}) = \sqrt{2}\,\mathrm{erf}^{-1}\left(2P_{F_{\mathrm{SMF}}}(f^0_{\mathrm{SMF}}) - 1\right), \tag{3.82}$$

whereas γ depends on the PDF of $f_{\mathrm{SMF}}(t)$ i.e. $p_{F_{\mathrm{SMF}}}(f_{\mathrm{SMF}})$ given by 3.75:

$$\gamma = \int_{F_{\mathrm{SMF}}} \frac{p_{F_{\mathrm{SMF}}}(f_{\mathrm{SMF}})}{\left[\frac{dh}{df_{\mathrm{SMF}}}\right]^2} df_{\mathrm{SMF}}. \tag{3.83}$$

The average fade duration (AFD) under the threshold f^0_{SMF} is finally equal to:

$$\bar{\tau}_{\mathrm{fade}}(f^0_{\mathrm{SMF}}) = \frac{P_{F_{\mathrm{SMF}}}(f^0_{\mathrm{SMF}})}{\nu(f^0_{\mathrm{SMF}})}. \tag{3.84}$$

The average inter-fade duration (AIFD) corresponding to threshold f^0_{SMF} is obtained by replacing the CDF $P_{F_{\mathrm{SMF}}}(f^0_{\mathrm{SMF}})$ in the previous equation by the complementary cumulative distribution $1 - P_{F_{\mathrm{SMF}}}(f^0_{\mathrm{SMF}})$.

3.3.5.4 Fades duration distributions

The AFD is an important parameter for the design of efficient numerical fading-mitigation techniques such as interleaving and forward error correction codes on bursty channels. The AFD can be used to infer on the fades' duration distribution (FDD), the latter being essential to the evaluation of coded error probability on correlated fading channels without interleaving or with imperfect interleaving [Adoul, 1974, Wilhelmsson and Milstein, 1999, Liva et al., 2009]. In [Henniger, 2012], these distributions were obtained from experimental links data and compared to those generated by a two-state Markov (Gilbert-Erasure) model. This kind of model was also validated through experimentation for the atmospheric channel in [Puryear et al., 2011, Lee and Chan, 2005]. Assuming the Markovian nature of the fading process as well, a similar two-state discrete time Markov model is used here to analytically

compute the exceedance probability of fades' duration (i.e.the probability of facing a fade duration greater than the one considered) of the SMF-coupled flux after partial AO correction:

$$\Pr\left(\tau_{\text{fade}} > \tau^0_{\text{fade}}\right) = \left(1 - \frac{1}{\bar{\tau}_{\text{fade}}\left(f^0_{SMF}\right)}\right)^{\tau^0_{\text{fade}}}. \tag{3.85}$$

Inter-fade duration distribution (IFDD) are computed by replacing the AFD $\bar{\tau}_{\text{fade}}\left(f^0_{SMF}\right)$ by the AIFD corresponding to the same threshold f^0_{SMF}.

3.3.6 Comparison to end-to-end simulations (AOST)

The analytic results described in Section 3.3.5 are hereafter compared to end-to-end wave-optics simulation (i.e. using TURANDOT and AOST introduced respectively in Sections 2.3.2 and 3.2.2).

Results for a GEO-to-ground as well as a LEO-to-ground link are presented. The transmission wavelength is 1.55 µm. The turbulence and wind profiles used here are given in [Vedrenne et al., 2016]. The parameters characterizing the simulated AO systems such as the number of corrected radial orders, N_{r} the control loop frequency f_{s} and the residual phase variance σ^2_{res} as well as other link parameters are given in Table 3.1. Both links are representative of an AO performance level corresponding to a mean coupled flux attenuation of roughly 3 dB. These parameters ensure as well that the amount of temporal error in the AO loop is equal to the amount of spatial errors (i.e. fitting plus aliasing).

Table 3.1: Characteristic link, turbulent and AO parameters for the GEO-to-ground and LEO-to-ground downlink scenarios

Downlink Scenario		GEO	LEO
Elevation		30 deg	20 deg
Range		38000 km	1584 km
Orbital Velocity		0 km s^{-1}	7.5 km s^{-1}
Rx Aperture Diameter		50 cm	25 cm
Fried Parameter r_0		0.069 m	0.056 m
Log-amplitude Variance σ^2_χ		0.067	0.135
AO Parameters	N_{r}	9	6
	f_{s}	1 kHz	2 kHz
	σ^2_{res}	0.4	0.5
	$\mu_{f_{\text{SMF}}}$	-2.7 dB	-3.2 dB

Figures 3.14a and 3.14b show the residual phase spectra respectively for the GEO and LEO links. In both figures a good agreement between the predicted analytic residual variances and

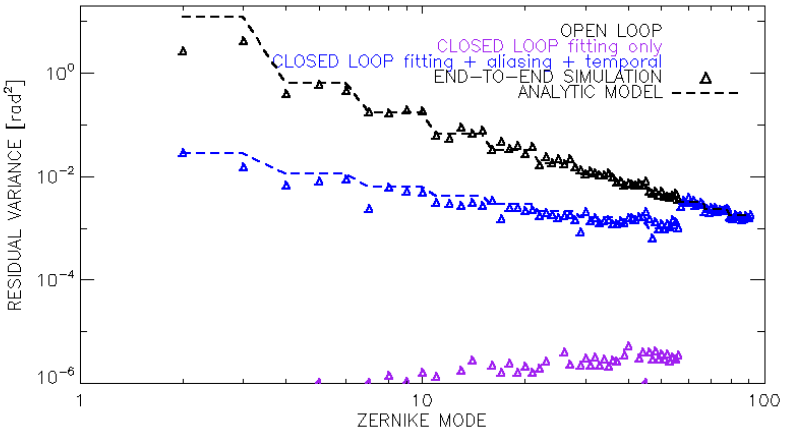

(a)

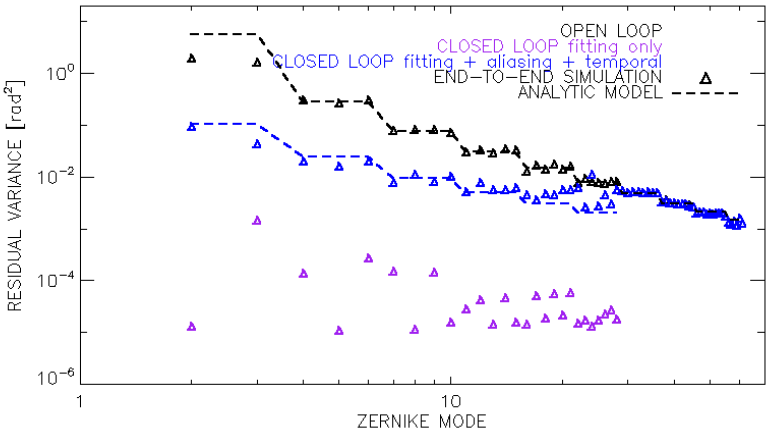

(b)

Figure 3.14: Residual modal variances obtained by end-to-end wave-optics simulations as well as analytic models for (A) GEO-to-ground downlink scenario (B) LEO-to-ground downlink scenario

the end-to-end simulations can be observed.

It should be noted however that in both end-to-end simulation and analytic results, the influence of noise and scintillation on wavefront sensing has been neglected. In the end-to-end simulation, the wavefront sensor noise is ignored but the impact of scintillation is taken into account in the modeling process of the images in the focal plane of the wavefront sensor. As evidenced by the point-specific log-amplitude variances in Table 3.1, scintillation under these weak-turbulence conditions negligibly affects the accuracy of wavefront measurement [Roddier, 1981, Voitsekhovich, V. V. et al., 2001]. This is especially true since the influence of noise on the wavefront sensor is neglected. In the presence of significant noise -for cases of low signal-to-noise ratio- this analysis should be reconsidered. However, given the typical optical power required for high data-rate satellite-to-ground communication [Fidler et al., 2010], the signal levels required for the wavefront analysis remain very reasonable and allow to consider high signal-to-noise ratios (see Section 3.2.1.1.2).

3.3.6.1 GEO-to-ground link

3.3.6.1.1 Probability Distribution

Firstly, in order to validate Eq. (3.67), let us consider the case of a full and perfect correction of the turbulent wavefront or in another words neglect phase fluctuations. In that case, the coupled flux attenuation is given by Eq. (3.68) with the sum of the modal coefficients in the last term equal to zero and follow therefore a log-normal distribution. Figure 3.15a shows the corresponding analytic density and the simulated (end-to-end and SAOST) distributions.

In order to ensure stochastic convergence temporal series of 8000 samples with a correlation time of 7.3 ms over a time horizon of 8 s were generated. For the end-to-end simulation, 26 phase screens of 3.3 m and 512 pixels were simulated. This corresponds to a 6.4 mm pixel size small enough to appropriately sample the Fried parameter.

The absolute difference between the end-to-end simulated and theoretical average coupled flux attenuation is less than 0.1%. Furthermore, Kolmogorov-Smirnov (KS) goodness-of-fit tests [Stephens, 1970, Wall, 2012] performed between the analytic and empirical CDFs yielded statistically conclusive results hence confirming the relevance of the approach regarding the treatment of the log-amplitude fluctuations' effect on the coupled flux in that case.

The distributions corresponding to both the effect of scintillation and phase fluctuations on the coupled flux are presented in Figure 3.15b.

The analytic model, statistically validated anew by goodness-of-fit tests, yields fairly accurate results. While there are differences of the order of 0.5% and 3% when comparing respectively the first two moments of the analytic and end-to-end distributions, these differences are

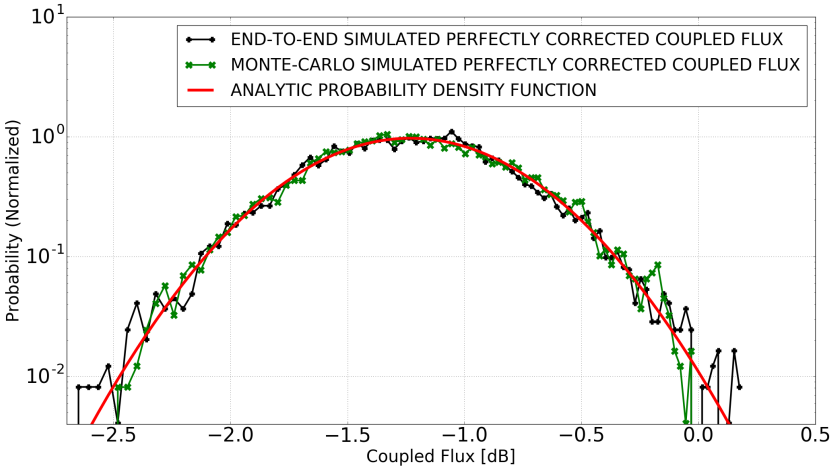

(a)

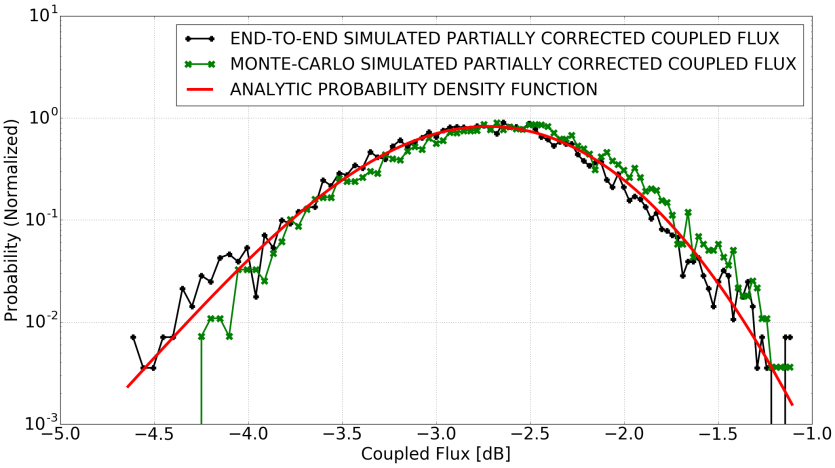

(b)

Figure 3.15: Comparison of the analytic PDF to end-to-end as well as Monte-Carlo (SAOST) simulations histograms of (A) coupled flux without phase fluctuations (fully compensated turbulent wavefront) (B) partially corrected coupled flux for the GEO scenario

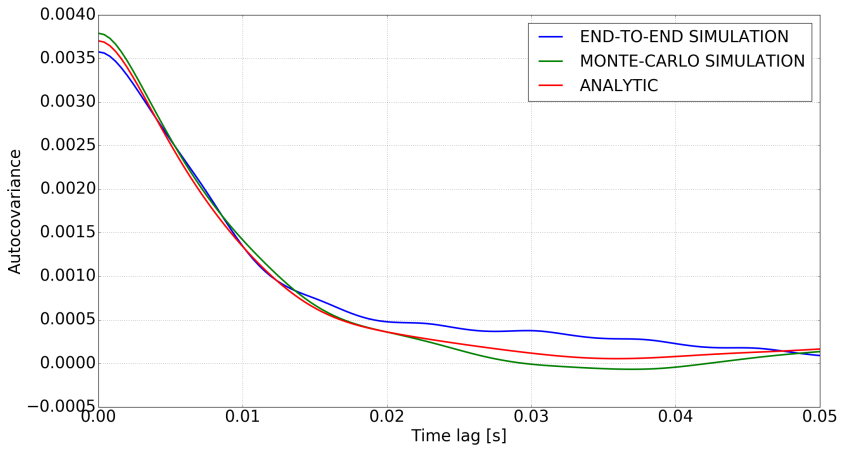

Figure 3.16: Auto-covariance of the partially corrected coupled flux given by the analytic approximation as well as the end-to-end and Monte-Carlo (SAOST) simulations for the GEO scenario

comprised in the standard errors related to the accuracy and convergence of such statistical estimators [Priestley, 1989, Broersen, 1998] for correlated time series. Consequently, for the GEO-to-ground scenario considered here where partial AO as well as scintillation effects are considered, our analytic model adequately captures the statistical behavior of the transmission channel.

3.3.6.1.2 Temporal properties

As presented in Section 3.3.5.3, an important parameter for the analytic computation of the AFD and AIFD is the value of the second time derivative of the auto-covariance (i.e. a measure of its concavity) at zero time lag, $\ddot{R}_{f_{SMF}}(\tau)|_{\tau=0}$. Hereinafter, the evolution of the auto-covariance of the coupled flux against time-lag obtained by both SAOST and end-to-end simulations as well as the analytic approximation given by Eq. (3.79) is presented in Figure 3.16. The overall good agreement between our analytic results and simulations models regarding the auto-covariance as well as the probability distribution of the coupled flux allow for a fairly precise prediction of the evolution of the AFD and AIFD with respect to the fading/inter-fading threshold as presented in Figures 3.17a and 3.17b.

From an overall system point-of-view, relevant fading levels depend on the link budget as well as the detection and modulation and coding schemes considered that will be studied in details in the next Chapter. Nevertheless, it is interesting to note to what extent varying the average required power impacts the AFD for the GEO-to-ground scenario presented here. One can see that the AFD corresponding to the mean level fading threshold (-2.73 dB) is about 10 ms (it is roughly equal to the AIFD for this threshold as expected) and that it is divided by a factor 3 when the mean level fading threshold is roughly -4.5 dB.

Figures 3.18a and 3.18b show respectively the end-to-end FDD and IFDD for the mean level

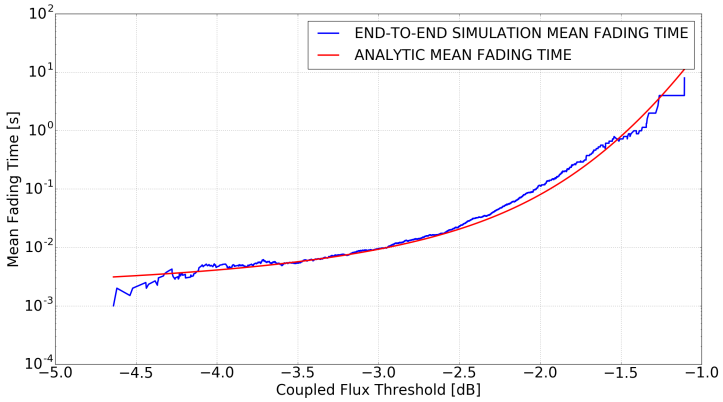

(a)

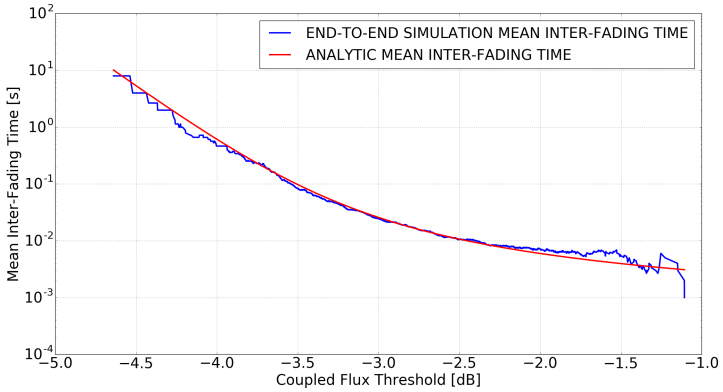

(b)

Figure 3.17: Comparison of the evolution against the fading threshold of analytic and end-to-end (A) average fade duration (B) average inter-fade duration for the GEO scenario

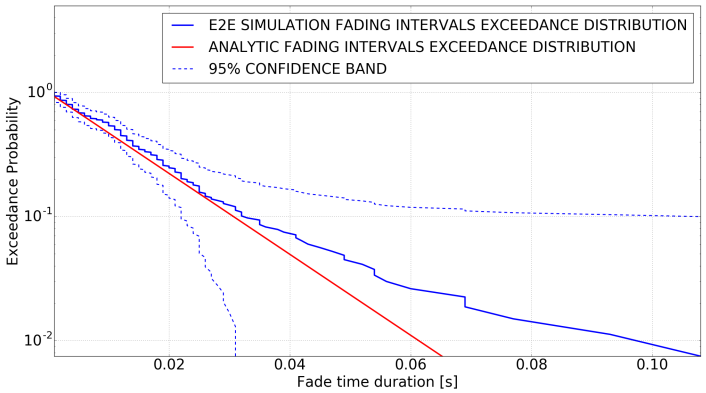

(a)

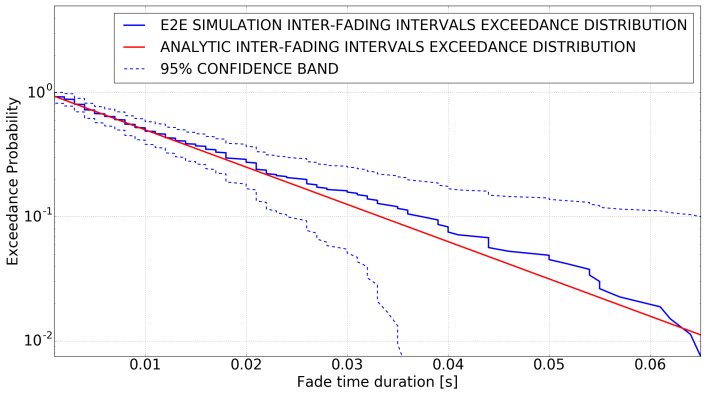

(b)

Figure 3.18: Comparison of the analytic and end-to-end exceedance distributions of (A) fade duration (B) inter-fade duration for a fading threshold corresponding the average coupled flux attenuation for the GEO scenario

fading threshold. A fine agreement between these distributions and the analytic geometric law described by Eq. (3.85) can be observed. KS goodness-of-fit tests have been performed, and the geometric densities are well inside the 95% confidence bands. Combined with the experimental results presented in [Henniger, 2012], this tends to corroborate the hypothesis that two-state Markov channels could emulate the correlated burst-like fades induced by turbulence over the free-space optical channel. Our results extend the relevance of such modeling options to the case of AO corrected SMF coupled signals for the GEO downlinks and will therefore permit an accurate and rigorous joint optimization of AO systems and digital mitigation techniques of interest.

3.3.6.2 LEO-to-ground link

3.3.6.2.1 Probability Distribution

A similar analysis is done in the LEO scenario for which temporal series 2 s long, with 8000 occurrences and a correlation time of 0.6 ms were generated. For the end-to-end simulation, 36 phase screens of 2.13 m and 256 pixels were simulated. This corresponds to a 8.3 mm pixel size small enough to appropriately sample the Fried parameter. Figure 3.19a shows the distribution of the coupled flux when phase fluctuations are completely compensated. The absolute relative difference between the end-to-end simulated and predicted theoretical average attenuation is around 0.3%.

The distributions of the partially corrected attenuation are presented in Figure 3.19b. The analytic results were statistically validated by KS tests at a 95% confidence level. The difference in terms of average coupled flux is less than 1%.

However, one can deduce from the auto-covariances presented in Figure 3.20 that the absolute difference between the analytically and end-to-end computed variances is about 8%. This discrepancy is statistically relevant since the standard error related to the accuracy of the sample variance is only about 5%. This exposes a certain inaccuracy in our analytic model that stems from the underlying treatment of the log-amplitude fluctuations' impact on the coupling efficiency. The latter is taken into account by averaging the log-amplitude spatial structures smaller than the pupil through the derivation of $\mu_{f_{\mathrm{SMF}}^{\mathrm{Scint}}}$ (see Section 3.3.3). In doing so, the effect of these log-amplitude fluctuations on the variations of the coupling efficiency is neglected. The fact that such an assumption has a noticeable impact in the LEO rather than in the GEO scenario is not surprising since that neglecting log-amplitude fluctuations in the LEO case is fundamentally a worse approximation owing to less aperture averaging (smaller pupil diameter) combined to more challenging turbulence conditions (lower elevation).

3.3.6.2.2 Temporal properties

In spite of the discrepancies described above, the value of the second time derivative in the vicinity of zero predicted by the analytic model is quite close to both end-to-end and SAOST results (less than 5% of difference). This yields analytic predictions of the evolution of the AFD and AIFD with respect to the fading threshold, presented respectively in Figures 3.21a and 3.21b, that are in good agreement with the simulated fading durations. The AFD and AIFD corresponding to the mean level fading threshold (-3.2 dB) are about 2 ms. Like for the GEO downlink, the end-to-end results reveal a departure from the analytic calculation as the threshold get closer to extreme values due to lower numbers of simulated fading events in these regions.

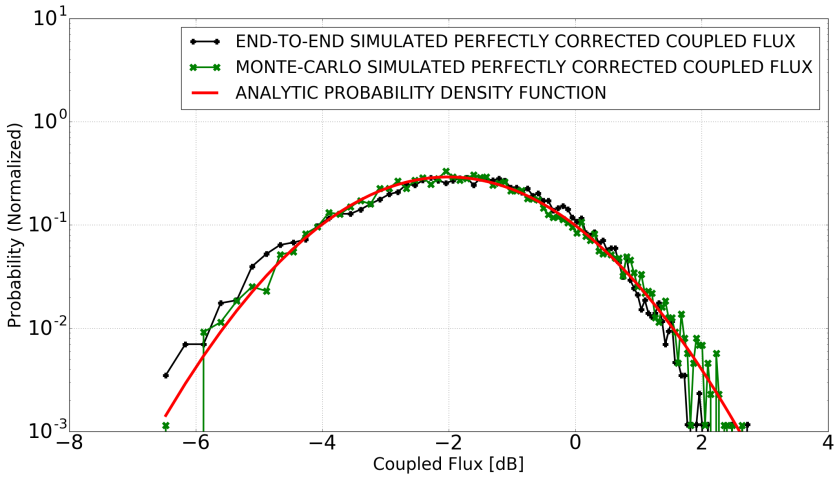

(a)

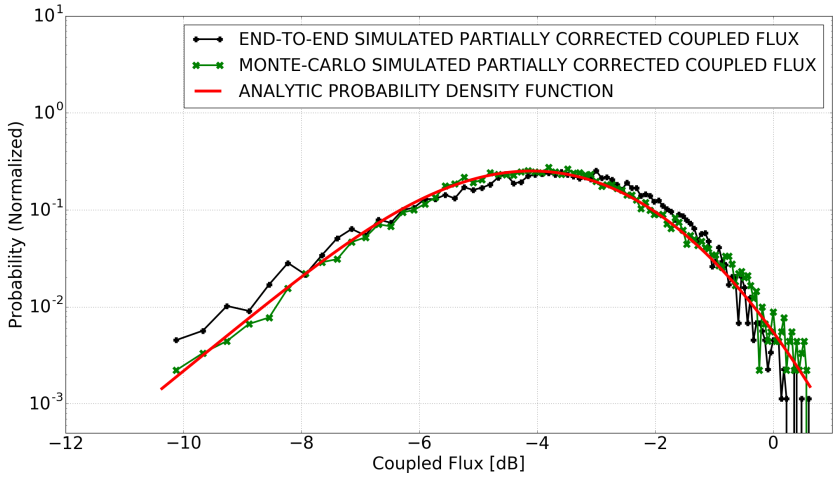

(b)

Figure 3.19: Comparison of the analytic PDF to end-to-end as well as Monte-Carlo (SAOST) simulations histograms of (A) coupled flux without phase fluctuations (fully compensated turbulent wavefront) (B) partially corrected coupled flux for the LEO scenario

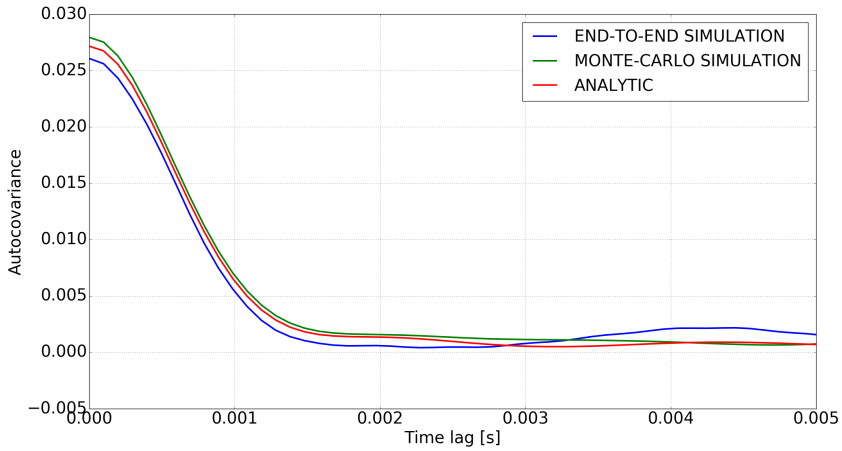

Figure 3.20: Auto-covariance of the partially corrected coupled flux given by the analytic approximation as well as the end-to-end and Monte-Carlo (SAOST) simulations for the LEO scenario

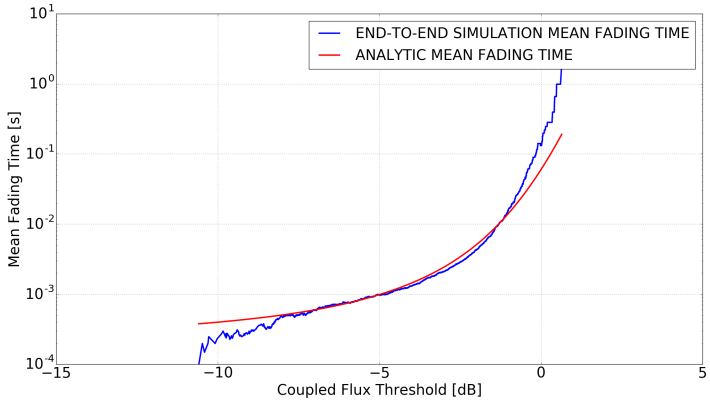

(a)

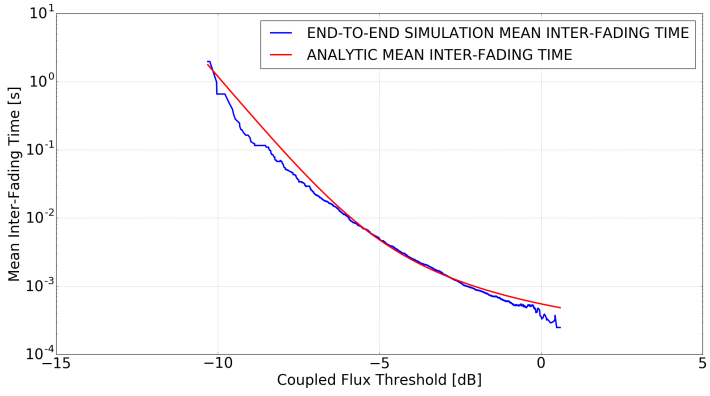

(b)

Figure 3.21: Comparison of the evolution against the fading threshold of analytic and end-to-end (A) average fade duration (B) average inter-fade duration for the LEO scenario

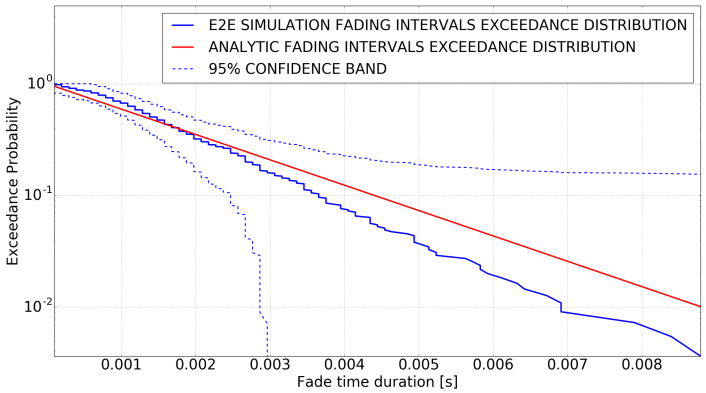

(a)

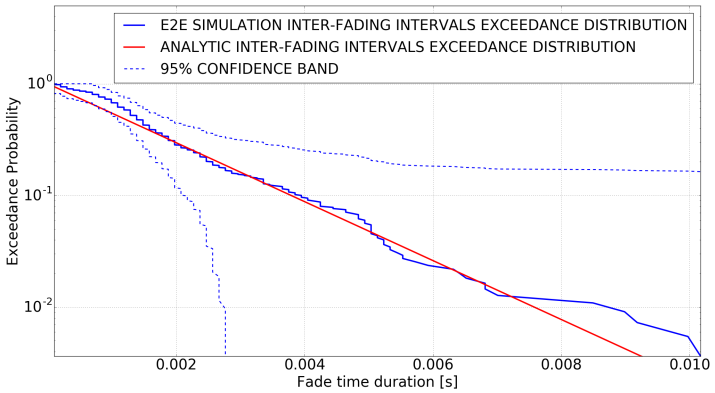

(b)

Figure 3.22: Comparison of the analytic and end-to-end exceedance distributions of (A) fade duration (B) inter-fade duration for a fading threshold corresponding the average coupled flux attenuation for the LEO scenario

Figures 3.22a and 3.22b show respectively the end-to-end FDD and IFDD for the average coupled flux threshold. The analytic geometric law still gives fairly close results for average to long fading durations. For the shorter durations the analytic distribution is less precise as it does not capture a clear inflection in the empirical distribution and slightly crosses the 95% confidence bands. Such a bump in the exceedance probability of very short fade duration events means that the latter are statistically underrepresented in the end-to-end results and therefore, in the contrary, incorrectly overrepresented by the geometric law. Although still allowing for predictions in terms of orders of magnitude, the precise origin of such a feature should be investigated further as it may, in this scenario, question the accuracy of modeling options based on such an underlying Markovian assumption.

3.3.7 AO performance impact on fades temporal characteristics

In this section, for both the formerly discussed GEO and LEO scenarios, an analysis of the influence of three distinct AO system performances denoted high (HP), medium (MP) and low performance (LP), on the analytic FDD and IFDD is presented. The specifications of the AO systems studied are reported in Table 3.2. The turbulence parameters, link parameters as well as pupil diameters are unchanged with respect to those given in Table 3.1.

For respectively the GEO and LEO downlinks, Figure 3.23a and Figure 3.23b show the analytic exceedance probability distributions of fading durations as well as inter-fading durations (dashed lines) for the mean-normalized coupled flux attenuation corresponding to the different AO systems. This normalization is adopted in order to emphasize on AO systems' ability to mitigate the coupled signal fluctuations only therefore neglecting the impact of distinct AO systems on the average coupled flux. The AFD and AIFD corresponding to each case are directly reported on the graph by thin vertical lines.

Table 3.2: AO system parameters corresponding to the three performance levels of both GEO and LEO scenarios

		N_r	f_s	σ^2_{res}	$\mu_{f_{SMF}}$
GEO	High Perf.	9	1.0 kHz	0.4 rad^2	-2.7 dB
	Medium Perf.	5	0.4 kHz	1.3 rad^2	-5.2 dB
	Low Perf.	4	0.3 kHz	1.9 rad^2	-6.7 dB
LEO	High Perf.	6	2.0 kHz	0.5 rad^2	-3.2 dB
	Medium Perf.	3	0.8 kHz	1.3 rad^2	-5.2 dB
	Low Perf.	2	0.5 kHz	2.0 rad^2	-6.7 dB

The fading thresholds chosen for computing these probability distributions are selected in order to ensure a fractional fade duration (FFD), defined as the overall proportion (in percent) of time spent below the threshold, of 0.5% for the LEO as well as GEO highest performance systems. These thresholds correspond to -1.5 dB in GEO and -5 dB in LEO for the highest performance systems. For the lower performance systems, thresholds of -1.5 dB in GEO and -5 dB in LEO yield drastically increased FFD for the less performing systems: 14% and 25% respectively for the MP an LP systems in the GEO case and 4% and 14% in the LEO case.

Is considering lower order residuals relevant?

It is interesting to infer on the importance of considering the impact of lower order residuals instead of an ideal AO model -characterized by its fitting error only- on the temporal characteristics of the coupled flux by considering the LP systems. Indeed, for these systems the coupled flux fluctuations are globally dominated by the injection efficiency fluctuations. The AFDs

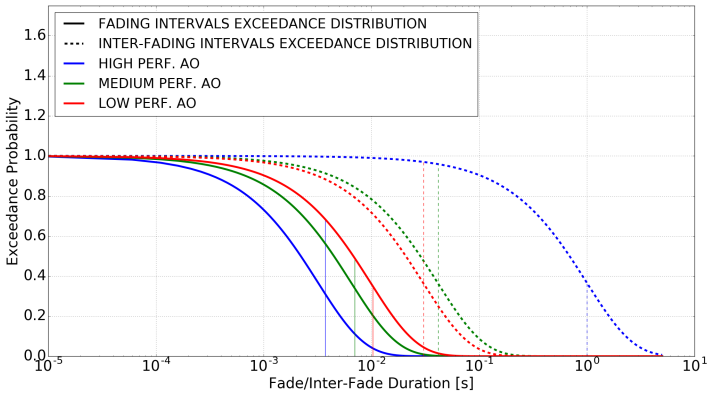

(a)

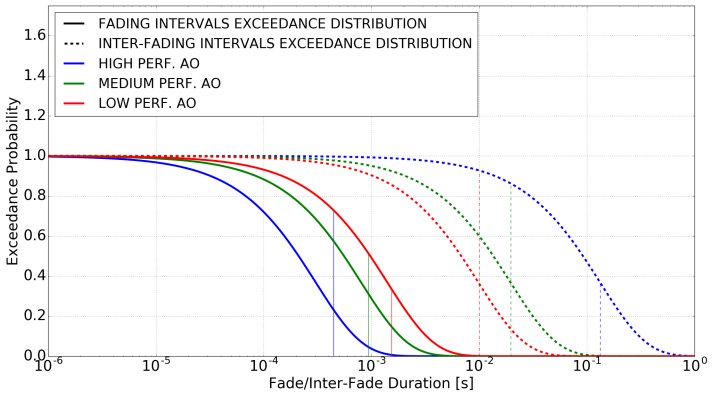

(b)

Figure 3.23: Fade duration (plain lines) and inter-fade duration (dashed lines) analytic exceedance distributions for each AO performance levels and for (A) GEO-to-ground downlink scenario (B) LEO-to-ground downlink scenario

-reported on Figure 3.23a and Figure 3.23b- resulting from the partial AO model are roughly 10 ms in GEO and 1.5 ms in LEO. It was found that for an equivalent average level of correction and the same thresholds, neglecting the lower order residuals yields AFDs approximately 50% smaller. The AIFDs are 10 ms in LEO and 30 ms in GEO when considering the partial AO correction whereas they are respectively 150% and 75% larger when using an ideal AO model. These differences are not negligible when assessing data reliability mechanisms options and specifications (e.g. allowed latencies or required memory for time interleavers), especially given the very high data rates envisioned for satellite-to-ground optical communication.

How distinct partial AO performances affect the fading duration distribution?

On one hand, from the transmission system overall-design point of view, these FFDs can

be compensated by increasing the average coupled power. Not including the average loss specific to each AO correction, it would require for the MP and LP systems additional 3 and 5 dB in GEO, 5 and 9 dB in LEO, in order to reach a 0.5% FFD. The average loss specific to each AO system can be taken into account using the values of $\mu_{f_{SMF}}$ reported in Table 3.2. For instance in the GEO scenario, when compared to the HP correction, the MP correction requires $5.2+3-2.7=5.5$ dB of additional mean optical power in order to guarantee a 0.5% FDD.

On the other hand, while limiting such a recourse to increasing the average coupled power, numerical interleaving combined with FEC coding can overcome the information loss related to the decrease in AO correction by taking advantage of the channel correlation and adding redundancy in the transmitted data. The FFD as a metric does not capture the temporal distribution of fading events and therefore, by itself does not allow for an assessment of interleaved and coded transmissions' reliability. For the latter, parameters such as average, maximum and minimum fade/inter-fade durations are needed as well. For the three AO performance levels presented here, Tables 3.3 and 3.4 synthesize the characteristic fade and inter-fade durations corresponding to 99% and 1% exceedance probabilities for respectively the GEO and LEO scenarios.

Table 3.3: Characteristic fade and inter-fade durations for the three performance levels in the GEO scenario

		Fading Duration [ms]	Inter-fading Duration [ms]
$\Pr(\tau_{\text{fade}}>\tau^0_{\text{fade}})=.99$	High Perf.	0.032	10
	Med. Perf.	0.065	0.4
	Low Perf.	0.098	0.3
$\Pr(\tau_{\text{fade}}>\tau^0_{\text{fade}})=.01$	High Perf.	15	4500
	Med. Perf.	30	190
	Low Perf.	45	140

For the GEO-to-ground link, dividing the total residual variance σ^2_{res} of the high performance system by a factor 3 or 5 respectively increases the minimum, maximum and average fading durations by a factor 2 or 3. This may seem a notably small improvement in light of the specifications required by the high performance system for instance. However, the gain with respect to the inter-fading durations is remarkably significant as the HP system outperforms by several orders of magnitude the other AO corrections hence not only making fading events shorter to some extent but drastically spreading them further apart. Regarding the LEO downlink, reducing the total residual phase variance of the HP system in roughly the same

proportions than for the GEO case leads to similar observations in terms of fading durations and their distribution. The impact of AO performance on inter-fading durations is again striking, since that downgrading from the HP to the MP and LP systems yields respectively maximum, minimum and average inter-fading durations roughly 10 times smaller.

Table 3.4: Characteristic fade and inter-fade durations for the three performance levels in the LEO scenario

		Fading Duration [ms]	Inter-fading Duration [ms]
$\Pr(\tau_{\text{fade}}>\tau^0_{\text{fade}})=.99$	High Perf.	0.003	1.3
	Med. Perf.	0.008	0.2
	Low Perf.	0.014	0.1
$\Pr(\tau_{\text{fade}}>\tau^0_{\text{fade}})=.01$	High Perf.	1.4	611
	Med. Perf.	3.7	90
	Low Perf.	6.4	45

Finally, in each scenario the MP and LP AO systems present close performances in terms of temporal characteristics that are relevant for the optimization of digital mitigation techniques. The HP AO systems, on the contrary, seem to mitigate fading events more acutely at the cost of only roughly twice the control-loop frequency and 4 times the number of actuators of the medium correction.

3.4 Summary and conclusion

After some generalities about adaptive optics, the first part of this chapter was intended to rigorously detail a simplified model of partial adaptive optics based on prior analytic developments. The advantages and limitations of such a model were clearly exposed.

The objectives of the second part of this chapter and the principal conclusions drawn from it were threefold.

Firstly, relying on the aforementioned model of partial adaptive optics, another analytic model was presented for the computation of the partially corrected coupled flux into single-mode fibers. Such a model relied on two main assumptions: the absence of correlation between the phase and log-amplitude fluctuations; and the fact that the log-amplitude fluctuations' impact on the coupling efficiency is taken into account by averaging the log-amplitude spatial structures smaller than the pupil.

Secondly, the development of analytic expressions for the statistical (probability and cumulative distribution functions) and temporal properties (autocovariance, average fading time and fading time distribution) of the coupled flux were presented. These analytic results were compared to end-to-end simulations. This comparison emphasized the interest in the developed analytic model. The latter provides relevant order of magnitudes, if not accurate results, while avoiding time consuming and complex simulations.

Finally, using these analytic developments a short analysis on the impact of distinct AO performance systems on the temporal characteristics of the coupled flux was provided. Typically these temporal characteristics are required for the computation of packet error rates while considering an imperfect interleaving of the channel [Yee and Weldon, 1995, Wilhelmsson and Milstein, 1999]. Therefore, constituting here only a precursory work, similar studies will allow to efficiently and accurately design data reliability techniques for AO corrected optical donwlinks. The importance of considering the lower residuals instead of a perfect correction in similar studies was underlined. The results presented in this last section highlighted as well the importance of not solely considering average AO performance parameters such as the residual variance or average attenuation, originally used in the context of astronomy or imagery applications.

4 DATA RELIABILITY MECHANISMS FOR OPTICAL SATELLITE-TO-GROUND COMMUNICATION

Contents

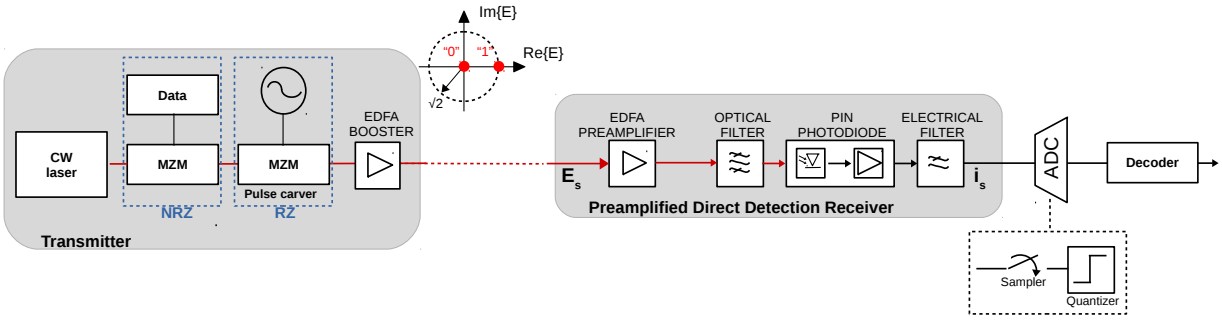

Figure 4.1: Transceiver design for NRZ- and RZ-OOK signal generation and detection (constellation diagram shown for normalized to unity average optical power)

4.1 Introduction

Free-space optical communication being a relatively recent field of research, finding the optimal coding strategies for satellite laser downlinks is currently actively investigated. Generally, data reliability mechanisms are mostly efficient when appropriately tailored to the transmission channel. In this chapter, the coding scheme studied during this thesis is detailed.

Firstly, the modeling of the OOK and DBPSK communication subsystems as well as the physical layer interleaving and error correcting code is described. Higher layers interleaving and erasure code are then introduced in the context of a communication cross-layer approach. The relevance in the framework of free-space optical communication of the latter is given.

The last part of this chapter details the overall system optimization in a particular case study that highlights the interest of the distinct models developed during this thesis. It illustrates the refined trade-offs that can potentially be considered.

4.2 Optical communication subsystem

This section emphasizes the optical detection techniques studied in the framework of this thesis, namely direct (square-law) detection and balanced (delayed) detection. In addition to the principles of such techniques, their associated modulation formats as well as their performance modeling are presented.

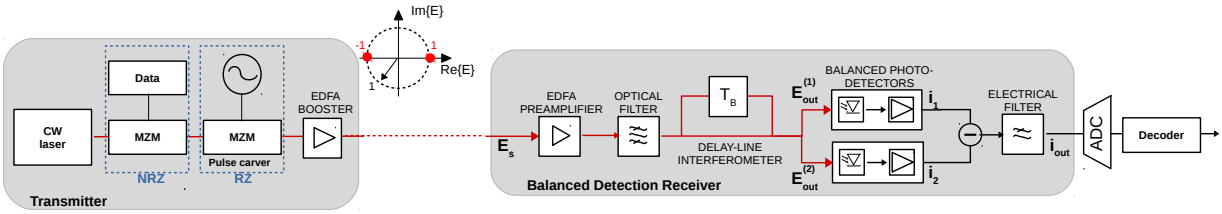

Figure 4.2: Transceiver design for NRZ- and RZ-DBPSK signal generation and detection (constellation diagram shown for normalized to unity average optical power)

4.2.1 General principle of direct and interferometric detection

4.2.1.1 Direct detection: On-Off Keying

By employing a photodiode as a square-law device one can generate an electrical signal proportional to the power of the incident optical signal. In other words the optical signal power is directly measured and such a system detects the envelope of the optical signal [Winzer, 2002]. The simplest direct detection receiver is therefore constituted of a single-ended photo-detector, as shown in Fig. 4.1. The output photo-current $i_{\text{out}}(t)$ is proportional to the responsivity of the photo-diode and given by:

$$\begin{aligned} i_{\text{out}}(t) &\propto E_s(t)E_s^*(t) \\ &\propto \left(A_s(t)\exp(j\phi_s)\right)\left(A_s^*(t)\exp(-j\phi_s)\right) \\ &\propto |A_s(t)|^2, \end{aligned} \tag{4.1}$$

where $E_s(t)$ denotes the signal optical field, $A_s(t)$ the complex amplitude of the optical signal, and $\phi_s(t)$ represents its phase. Hence, any optical phase or polarization information is lost.

At the transmitter end, a single bit of information is modulated onto the amplitude (intensity) of the optical carrier by switching it on and off. Most commonly, this is be done by externally modulating the laser signal thanks to a Mach-Zehnder Modulator (MZM). A second MZM can be used in order to generate return-to-zero formats (RZ). This is explained in further details in Section 4.2.2. Following detection, the electrical analog signal is converted into a digital signal by an analog-to-digital converter (ADC).

4.2.1.2 Interferometric detection: Differential Binary Phase Shift Keying

In a differential encoding scheme, each bit behaves as a phase reference for the subsequent bits. At the receiver end, balanced photo-detectors are combined with a DLI as shown in Fig. 4.2. The incoming optical $E_s(t)$ signal after amplification is split into two branches using a 3 dB

coupler. The latter couples the incident signal $E_s(t)$ with its delayed version $E_s(t-T_s)$, where T_s represents the symbol period (in the case of DBPSK it is the bit period). This induces either a constructive or destructive interference between two adjacent bits so that the preceding bit in the stream can be used as a phase reference. Mathematically the coupler output is given by:

$$\begin{bmatrix} E_{out}^{(1)} \\ E_{out}^{(2)} \end{bmatrix} = \begin{bmatrix} 1 & j \\ j & 1 \end{bmatrix} \begin{bmatrix} E_{in}^{(1)} \\ E_{in}^{(2)} \end{bmatrix} = \begin{bmatrix} 1 & j \\ j & 1 \end{bmatrix} \begin{bmatrix} E_s(t) \\ E_s(t-T_s) \end{bmatrix} = \begin{bmatrix} E_s(t) + jE_s(t-T_s) \\ jE_s(t) + E_s(t-T_s) \end{bmatrix} \tag{4.2}$$

The output photo-current $i_{out}(t)$ is given by the difference of two photo-currents $i_1(t)$ and $i_2(t)$ as follows:

$$\begin{aligned} i_{out}(t) &= i_1(t) - i_2(t) \\ &\propto |E_{out}^{(1)}|^2 - |E_{out}^{(2)}|^2 \\ &\propto \left(\left[E_s(t) + jE_s(t-T_s) \right] \left[E_s(t) + jE_s(t-T_s) \right]^* \right) - \left(\left[jE_s(t) + E_s(t-T_s) \right] \left[jE_s(t) + E_s(t-T_s) \right]^* \right). \end{aligned} \tag{4.3}$$

It is worth mentioning that in theory, a single-ended photo-detector is sufficient to detect a DBPSK signals [Winzer, 2002, Jacobsen, 1994]. However, the use of a couple of balanced photo-detectors yields roughly a 3 dB optical signal-to-noise ratio (OSNR) gain over direct-detected OOK at the same bit error rate (BER) thanks to the increased symbol spacing [Humblet and Azizoglu, 1991].

At the transmitter, the data is encoded on the binary phase changes between adjacent bits using differential precoding where usually a 1-bit is encoded onto a π phase change whereas a 0-bit corresponds to no phase change. Compared to the OOK modulation, the symbol spacing for DBPSK increases by a factor of $\sqrt{2}$ at a fixed average optical power. An architecture similar to the OOK one can be used in order to generate either NRZ or RZ pulses.

The performances of both the OOK and DBPSK architectures, briefly introduced in the previous paragraphs, are affected by several phenomena inherent to their components. The following two subsections, 4.2.2 and 4.2.3, respectively details the modeling (from a system-level point of view) of the transmitter and receiver ends in the framework of this thesis.

4.2.2 Transmitter

4.2.2.1 CW laser

Generating an ideal, perfect light-wave with constant amplitude, frequency and phase is in practice impossible. Due to spontaneous emission, photons with random phase are added to the coherent output field which is generated by stimulated emission inside the laser. This phenomenon induces slight perturbations of the amplitude and phase of the output field. Ran-

dom variations of the laser intensity limit the maximum achievable optical SNR while random variations of the phase lead to an increased spectral linewidth of the laser [Agrawal, 2011].

Relative intensity noise. Intensity noise whose coefficient denoted RIN [dB/Hz] is defined as the ratio of the mean-squared fluctuations in the observed (measured) power spectral density and the average output power of the laser [Derickson, 1998]. Assuming that the instantaneous intensity (power) of the optical field emitted by a laser source under continuous wave condition is a stationary random process denoted by $P_{\mathrm{CW}}(t)$ whose ensemble average is P_0, one can use a simple system-level modeling approach [Bottacchi, 2009]. It allows one to write the intensity field as the sum of the average intensity (deterministic) and the random process defined as the difference between the instantaneous intensity of the optical field and its ensemble average:

$$P_{\mathrm{CW}}(t) = P_0\left(1 + \frac{P_{\mathrm{CW}}(t) - P_0}{P_0}\right). \tag{4.4}$$

Furthermore, assuming that the relative intensity noise is white and Gaussian, the power of the fluctuations corresponding to $\frac{P_{\mathrm{CW}}(t)-P_0}{P_0}$ are related to its coefficient (RIN) as:

$$\sigma^2_{\mathrm{RIN}} = P_0^2 \mathrm{RIN} B_{\mathrm{noise}}, \tag{4.5}$$

where B_{noise} denotes the noise bandwidth and unit responsivity is assumed. Such a modeling can only be used to emulate the worst-case impact of relative intensity noise as a first order approximation. Indeed, it is well known that the latter is not a white noise process since it follows the intrinsic frequency response of the laser [Bottacchi, 2009, Petermann, 1988].

Phase noise. It depends on the spectral linewidth of a laser, denoted Δf_L in the following, which is defined as the full-width at half-maximum of the CW spectrum. The latter can be approximated by a Lorentzian shape [Agrawal, 2011] assuming that the correlation between intensity and phase fluctuations is neglected and relaxation oscillations are ignored. The instantaneous phase of a laser is a random walk or Brownian motion. It can be modeled as Wiener process with a variance given by [Ho, 2005]:

$$\sigma^2_{\phi_L} = 2\pi\Delta f_L, \tag{4.6}$$

and two-sided power spectral density given by:

$$S_{\dot{\phi}_L}(f) = \frac{\Delta f_L}{2\pi f^2}. \tag{4.7}$$

Furthermore, in this work only single-mode lasers and external modulation as detailed in the following are considered. External modulation has the advantage of avoiding an additional

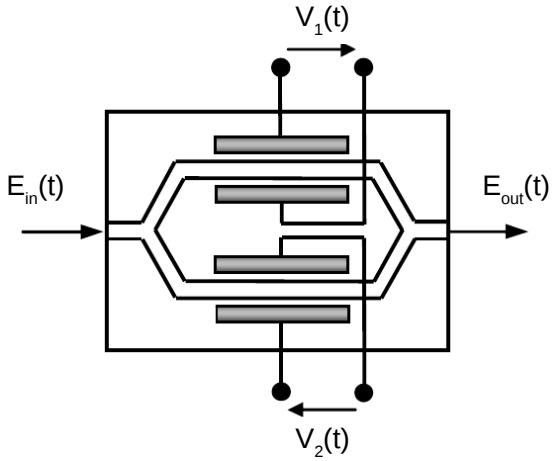

Figure 4.3: Simplified diagram of a dual-drive Mach-Zehnder modulator

impairment called chirp (variations in the carrier frequency of the laser when it is directly modulated [Petermann, 1988]. The latter can have deleterious effects when implementing dense WDM channel packing and can lead to increased signal distortions caused by the interaction with fiber chromatic dispersion [Koch, 1997, Ackerman et al., 2002]. Although WDM is not studied in the framework of this thesis, one has to keep in mind its significance in drastically increasing the capacity of future satellite-to-ground systems. Accordingly, despite the fact that the work presented here emphasizes on a single WDM channel, system-level trade-offs were made considering its potential implementation. Using an external modulator, the laser acts simply as a continuous wave (CW) source.

4.2.2.2 External Modulator

Electro-optic MZMs are widely used as external modulators thanks to their wide-band characteristics, their capability of modulating both intensity and phase at rates exceeding 40 Gbps [Caplan, 2007]. MZMs rely upon the principle of interference, controlled by modulating the optical phase. A simplified diagram representing its principle is given in Fig. 4.3. The input optical signal is split into two paths at an input coupler. One (or both) paths are equipped with phase modulators that induce a phase difference between the two fields. The phase difference is controlled by the applied phase modulation voltages, also called driving voltages and denoted as $V_1(t)$ and $V_2(t)$ in the following. Eventually, the two fields interfere at an output coupler. Depending on the applied electrical voltage, the interference varies from destructive to constructive hence producing intensity modulation.

The MZM is characterized by its optical field transfer function that can be expressed as

[Conradi, 2002]:

$$\begin{aligned} T_{\text{Field}}(V_1, V_2) &= \frac{E_{\text{out}}(t)}{E_{\text{in}}(t)} \\ &= \frac{1}{2}\left(\exp\left[j\phi(V_1)\right] + \gamma \exp\left[j\phi(V_2) + j\psi\right]\right), \end{aligned} \tag{4.8}$$

where $\phi(V_1)$ and $\phi(V_2)$ are the voltage-modulated optical phases in each arm, ψ is an additional, temporally constant phase shift in one of the arms, referred to as the modulator bias. The parameter γ is related to extinction ratio δ of the modulator by:

$$\gamma = \frac{\sqrt{\delta} - 1}{\sqrt{\delta} + 1}. \tag{4.9}$$

The phases are usually linearly related to the driving voltages as:

$$\phi_1(t) = \phi(V_1) = \frac{V_1(t)}{V_{\pi 1}}\pi, \quad \phi_2(t) = \phi(V_2) = \frac{V_2(t)}{V_{\pi 2}}\pi. \tag{4.10}$$

$V_{\pi 1}$ and $V_{\pi 2}$ are the voltages required in order to obtain a phase shift of π in each arm, thereby letting the MZM switch from full transmission to full extinction. Therefore, by driving the two arms in such a way that $V_1(t) = -V_2(t)$ as well as imposing $V_{\pi 1} = V_{\pi 2} = V_\pi$ one can modulate the input signal free from chirp as the phase term in Eq. (4.8) vanishes. This driving condition is known as push–pull operation.

By considering different bias and driving voltages, different operational principles can be implemented. For instance, in order to generate a modulation in intensity such as NRZ-OOK, the MZM can be operated with a DC bias voltage of $-V_\pi/2$ and a peak-to-peak modulation of V_π. This is illustrated in Fig. 4.4a where in addition to field transfer function T_{Field}, the optical power transfer function given by $|T_{\text{Field}}|^2$ (also called the MZM transmission) has been plotted. When the MZM is operated at the minimum transmission point with a DC bias of $-V_\pi$ and a peak-to-peak modulation of $2V_\pi$, a phase skip of π occurs when crossing the minimum transmission point. This is shown in Fig. 4.4b and becomes apparent from the field transfer function. In doing so, the MZM can therefore be used for binary phase modulation such as NRZ-DBPSK.

4.2.2.3 Pulse-carver

The MZM can also be used as a pulse-carver in order to generate RZ formats. In that case, two MZMs are typically required at the transmitter as depicted in Figures 4.1 and 4.2. Pulse carving is implemented by sinusoidally driving the second MZM as depicted in Fig. 4.5. Three carving methods are usually available [Winzer and Essiambre, 2006]:

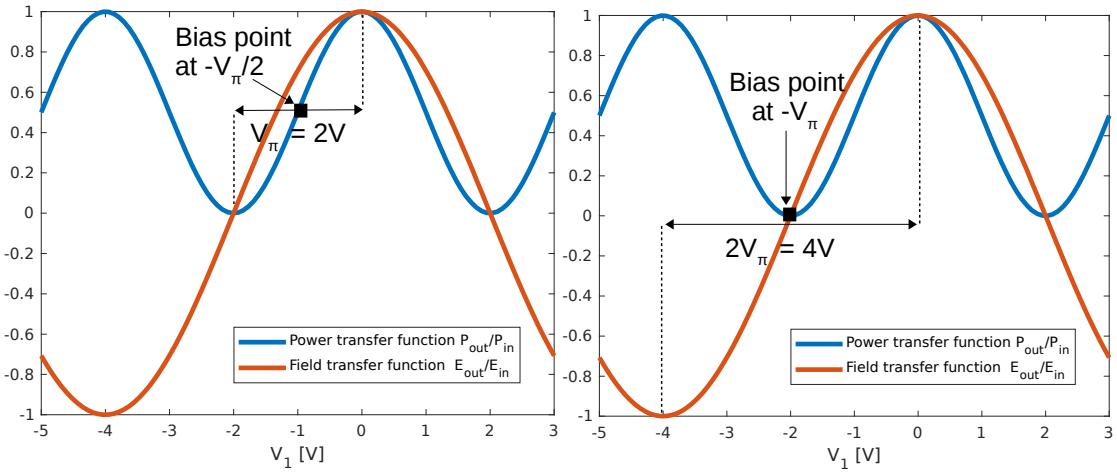

Figure 4.4: Mach-Zehnder transfer function for intensity (blue) and field (orange). (A) Bias point and peak-to-peak voltage sing required for OOK modulation. (B) Bias point and peak-to-peak voltage sing required for DBPSK modulation.

- Sinusoidally driving the second MZM at the data rate between minimum and maximum transmission yields optical pulses with a full-width at half-maximum of 50% of the bit period (i.e. a duty cycle of 50%).

- Sinusoidally driving the second MZM at half the data rate between two transmission minima yields a pulse whenever the drive voltage passes a transmission maximum. This way, duty cycles of 33% are achieved.

- Sinusoidally driving the second MZM at half the data rate between two transmission maxima results in pulses with 67% duty cycle and with alternating phase.

While NRZ formats require a simpler implementation, they are less robust to inter-symbol interference (ISI) caused by imperfections in the frequency response and the limited bandwidth of opto-electronic transmitter and receiver components. Hence, it is well-known that the use of RZ pulses yields in an improved sensitivity of some 2 to 3 dB over NRZ [Boivin and Pendock, 1999, Winzer and Kalmar, 1999, Winzer et al., 2001]. Theoretical and experimental contributions have shown for instance that for optically preamplified direct detection receivers, RZ formats can be as close as 0.5 dB from the theoretical quantum limit (aiming at a BER of 10^{-9}) while NRZ are within 2.2 dB [Caplan and Atia, 2001, Pfennigbauer et al., 2002]. This advantage in terms of sensitivity comes nevertheless at the expense of a broader optical spectrum and slightly more complicated transmitter structures [Winzer, 2002].

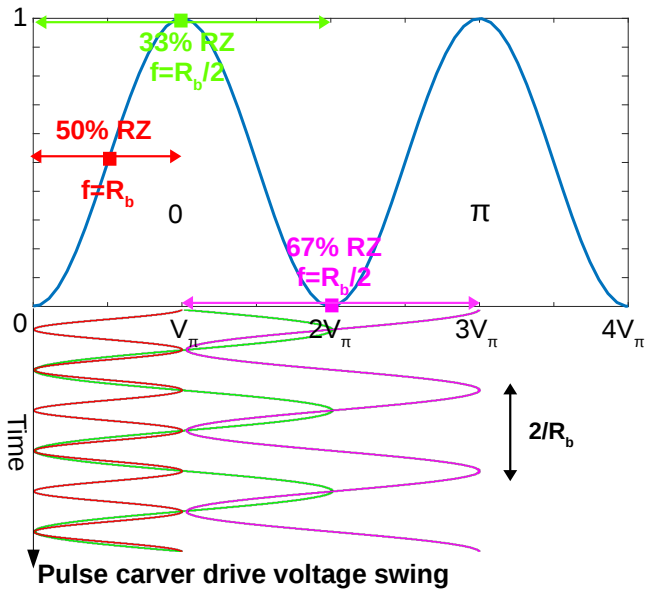

Figure 4.5: Overview of the different ways to drive the secondary MZM in order to generate RZ formats.

4.2.2.4 Booster Amplifier

A booster amplifier is used at the transmitter in order to drastically scale up the average output optical power. As for the receiver it consists of an EDFA. Typically, up to 40 dBm of average transmit power can be achieved at the output of such an amplifier [Wysocki et al., 2006]. The latter present mainly one drawback that is the introduction of amplified spontaneous emission (ASE) noise along with amplification. Hence, it is sometimes beneficial to use an optical filter in order to mitigate the impact of ASE.

The power spectral density of ASE generated by the booster amplifier at high level of pump power is given by [Agrawal, 2011]:

$$N_{\text{boost}} = 2n_{\text{sp}_{\text{tx}}}(G_{\text{boost}} - 1)h\nu, \tag{4.11}$$

where ν is the transmission (optical carrier) frequency (roughly 193 THz), h Planck's constant, G_{boost} the booster gain and n_{sp} the spontaneous-emission factor. At high gain, the latter is approximately equal to half the amplifier's noise figure. The factor 2 accounts for the two polarization modes or in other words the use of polarization filters is not considered here.

ASE noise is modeled as a circularly symmetric complex Gaussian noise process [Agrawal, 2011, Desurvire, 1994]. The output optical field from the transmitter is given by:

$$E_{\text{Tx}}(t) = \sqrt{G_{\text{boost}}}E_s(t) + E_{\text{ASE}_{\text{Tx}}}(t), \tag{4.12}$$

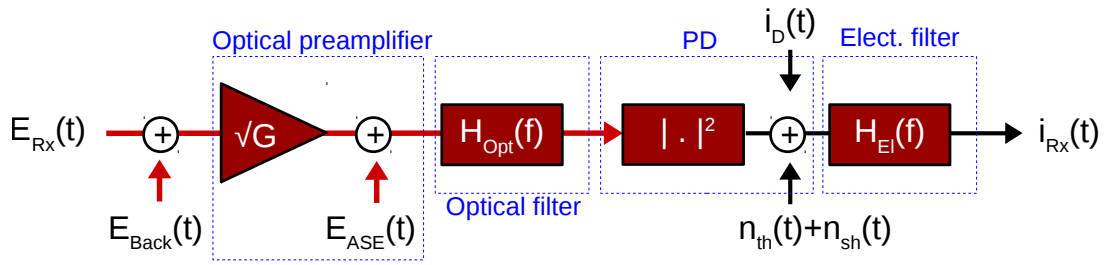

Figure 4.6: Baseband equivalent model of the OOK system.

where $E_s(t)$ is the modulated signal and $E_{\mathrm{ASE_{Tx}}}(t)$ represents the ASE noise field at the booster's output.

4.2.3 Receiver

4.2.3.1 Pre-amplified OOK Receiver

The general principle of an OOK pre-amplified receiver was described in 4.2.1.1. In the present section the emphasis is put on the modeling of such a receiver in the context of FSO communication. Figure. 4.6 represents its baseband equivalent model.

4.2.3.1.1 Input optical signal

At the input of EDFA, after propagation through the atmosphere the transmitted signal, $E_{\mathrm{Tx}}(t)$ is attenuated by a factor $\sqrt{a_{\mathrm{SMF}}}$. The signal coupled into the fiber at the receiver is therefore given by:

$$E_{\mathrm{Rx}}(t) = (E_{\mathrm{Tx}}(t) + E_{\mathrm{back}}(t))\sqrt{a_{\mathrm{SMF}}(t)}. \tag{4.13}$$

The parameter $a_{\mathrm{SMF}(t)}$ corresponds to the coupled flux fluctuations into the fiber after partial AO correction, as described in 3.3. The mean of $a_{\mathrm{SMF}}(t)$ depends on the distinct (average) losses described in 2.4.3.8. $E_{\mathrm{back}}(t)$ represents the parasitic field due to background light sources such as the sun or the atmosphere itself. Typical values for its power spectral density (per spatial mode) are given for instance in [Leeb, 1989]. As for ASE, it can be modeled as a zero-mean Gaussian process.

4.2.3.1.2 Pre-amplification

As for the optical booster, the EDFA pre-amplifier amplifies the coupled signal while introducing ASE noise. The pre-amplifier ASE noise is characterized by its power spectral density:

$$N_{\text{pre-amp}} = 2n_{\mathrm{sp_{rx}}}(G_{\text{pre-amp}} - 1)h\nu. \tag{4.14}$$

4.2.3.1.3 Optical filtering

An optical filter (bandpass) is necessary in order to suppress to some extent the potential accumulation of background and ASE noises before detection by the photo-detector. Several types of optical filter are available in practice. They are based on interference, diffraction, or absorption, and can be used as fixed and tunable filters (e.g. Fabry-Perot interferometer, Bragg reflector, Dielectric thin-film interference, acousto-optic tunable filter, absorption filter, hybrid filter) [Kartalopoulos and Society, 2000]. The selection of the appropriate filter type depends on the end-application and services the system is designed for. For instance, in applications with a large number of channels but relatively slow switching speeds (e.g., video broadcasting), the Fabry-Perot filter (FPF) is considered to be well suited. Bragg gratings photo-imprinted in optical fibers (FBG) in combination with a circulator to convert the FBG's bandstop characteristics into bandpass characteristics [Kashyap, 2010] have as well advantageous properties in the filed of optical communications. They allow the flattening of the gain of amplifiers, have low insertion loss, very low polarization and are thus attractive candidates for applications of complex filtering or precise chromatic dispersion compensation [Riant, 2003]. Therefore these two types of optical bandpass filters were considered in the framework of this thesis.

In Fig. 4.6, $H_{\text{Opt}}(f)$ represents the equivalent low-pass transfer function of the optical bandpass filter. Under the Lorentzian approximation the transfer function of the FPF is given by [Saleh and Teich, 2007]:

$$H_{\text{Opt}}(f) = \frac{1}{1+\frac{j2f}{B_o}}, \tag{4.15}$$

where B_o is the 3-dB bandwidth (FWHM) of the optical filter. The FBG filter transfer function is given by [Kashyap, 2010]:

$$H_{\text{Opt}}(f) = \frac{-j\kappa \sin\left[\beta(f)L_g\right]}{\tanh(\kappa L_g)\beta(f)\cos\left[\beta(f)L_g\right] - j2\pi\left(\frac{f}{v_g}\right)\sin\left(\beta(f)L_g\right)}, \tag{4.16}$$

where $\beta(f) = \sqrt{(2\pi f/v_g)^2 - \kappa^2}$ is the grating coupling coefficient, and L_g is the grating length. Fixing κ and L_g one can adjust v_g to obtain the desired bandwidth.

4.2.3.1.4 Photo-detection

In pre-amplified receivers photo-detection is done using PIN diodes. Ideally, this PD can be modeled as a simple square-law device, characterized by its responsivity R_{PIN}. In practice however, the photo-diode is not a perfect squarer and has to be modeled in consequence. The dark current i_D, resulting from the leakage current generated by the bias voltage applied to the PIN diode, has to be taken into account. Moreover, a semi-classical description of its

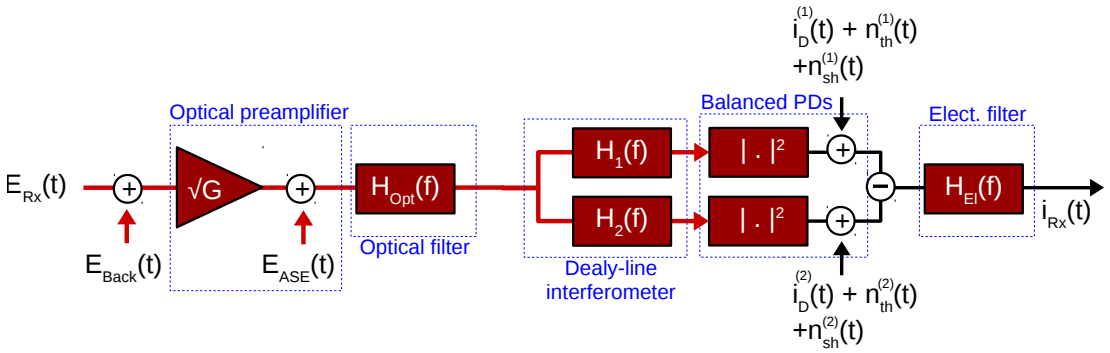

Figure 4.7: Baseband equivalent model of the DBPSK system.

behavior is assumed where, conditioned on the envelope of the input field, the photo-diode generates electrons following a non-homogeneous Poisson process with rate equal to the square of the field envelope [Humblet and Azizoglu, 1991] in order to include the effect of shot noise. Note that, in that regard Fig. 4.6 is misleading since this noise contribution has not been "simply added" at the output of the squarer. Although not explicitly represented, the PD is usually followed by a transimpedance amplifier that converts the photo-current to a measurable voltage. In addition to shot noise the PD module circuitry generates thermal noise that can be modeled as zero-mean signal-independent Gaussian noise of variance:

$$\sigma^2_{\text{therm}} = \frac{4k_B T}{R_{\text{load}}} \tag{4.17}$$

where k_B is Boltzmann constant, T the PD temperature (in Kelvin) and R_{load} corresponds to the load resistor of the module.

4.2.3.1.5 Electrical filtering

Following photo-detection, the electrical signal is filtered by a low-pass filter assumed to have a fifth-order Bessel characteristic [Johnson et al., 1980]:

$$H_{\text{El}}(f) = \frac{945}{jF^5 + 15F^4 - 105jF^3 - 420F^2 + 945jF + 945}, \tag{4.18}$$

where $F = 2.43f/B_e$, and B_e is the filter's 3-dB cutoff frequency.

4.2.3.2 Pre-amplified DPSK Receiver

Figure 4.6 presents the baseband equivalent model of the pre-amplified balanced detector introduce in 4.2.1.2. Individual block and components described in the case of the pre-amplified OOK receiver are obviously modeled identically in the present case. The DLI modeling is described subsequently. Specific limitations inherent to balanced detection are also highlighted.

4.2.3.2.1 Delay-line interferometer

The principles of the coupler and the DLI were explained in 4.2.1.2. From the perspective of a base-band representation the DLI can be described in terms of a transfer function for each arm as in [Wang and Kahn, 2004]. When one arm has a delay equal to the bit duration T_b these transfer functions are given by:

$$H_1(f) = \frac{\exp(-j2\pi f T_b) + 1}{2} \tag{4.19}$$

$$H_2(f) = \frac{\exp(-j2\pi f T_b) - 1}{2} \tag{4.20}$$

4.2.3.2.2 Degradation in balanced detectors

As pointed out in [Winzer and Kim, 2003] the sensitivity gain of DPSK receivers over OOK receivers can be impacted by imperfections related to the constituting components of the former. The authors of [Winzer and Kim, 2003] clearly highlight the influence of important receiver parameters on system performance as they discussed the relevant design criteria of such systems for either RZ- or NRZ-DPSK formats (assuming ASE dominated noise). Five main contributors to the potential degradation in sensitivity are briefly described hereafter.

Amplitude imbalance. An amplitude imbalance between the two arms may occur when for instance the two diodes have unequal responsivities, when there is unequal coupling losses or unequal electronics losses before the two complementary signals are combined. From a system-level implementation, such an amplitude imbalance can simply be taken into account by introducing the amplitude imbalance factor β defined as:

$$i_{\mathrm{Rx}}(t) = (1+\beta)i^{(1)}(t) - (1-\beta)i^{(2)}(t), \tag{4.21}$$

where $i^{(1)}(t)$ and $i^{(2)}(t)$ are the two complementary electrical signals. Balanced detection is achieved when $\beta = 0$. When one branch completely fails or single-ended detection is considered -that is when $\beta = -1$ (constructive detection) or $\beta = 1$ (destructive detection)- a sensitivity penalty canceling the gain that balanced detection NRZ-DPSK presents over NRZ-OOK occurs. In practice as pointed out in [Winzer and Kim, 2003] balanced detectors are somewhat robust to such a degradation. For an imbalance factor $\beta = 0.1$ (corresponding to an amplitude mismatch as high as 22%) less than 0.1 dB excess optical SNR penalty at BER=10^{-10} was found experimentally. However, amplitude imbalance can enable additional performance deterioration when considering the impact of the DLI's finite extinction ratio.

Phase imbalance. A phase imbalance can originate from a difference in the propagation delays between the output ports of the DLI and the combiner. This difference may occur when the path lengths are not perfectly equal or when some electronic delays occur after detection.

Roughly, a sensitivity penalty between 0.5 to 1 dB can be expected for a delay difference of a quarter of a bit duration.

Delay-to-Bit Rate Mismatch. Imperfections inherent to the DLI manufacturing can cause a mismatch between its delay and the symbol time. Generally a 10% may lead to roughly a 0.5 dB sensitivity penalty.

Finite extinction ratio of DLI. An imperfect optical splitter within the DLI module induces an non-ideal extinction ratio yielding to imperfect constructive or destructive interference at the two output ports. In [Winzer and Kim, 2003], it was found experimentally that this degradation impacts performance solely when amplitude imbalance is present. When an imperfect detector amplitude balancing with $\beta = 0.1$ is considered, a degradation due to a finite DLI extinction ratio of 10 dB induces a sensitivity penalty of only 0.2 dB.

Laser frequency offset. A DPSK receiver relies on the interference of two optical fields. It is therefore sensitive to potential offsets between the transmit laser frequency and the frequency at which the DLI shows optimum extinction set by the interferometer's phase difference. A frequency offset of only 5% can lead to a sensitivity penalty of 1 dB. In practice however, such an offset can be completely compensated by properly tuning the path length difference within the DLI itself using a phase shifter in one of the arms.

4.2.3.3 Additional limitations

For both the modeling of OOK and DPSK receivers previously described, it is assumed that the bandwidths of the modulator and PIN photo-detectors are infinite. Inter-symbol interference (ISI) is therefore caused only by optical and electrical filtering in such a model. The results presented in the remainder were obtained for 10 Gbps links which justifies such an assumption since typical MZMs and PIN diodes nowadays have significantly larger bandwidths. For substantially lager data rates, bandwidth limitations of every component of the transmission chain should be taken into account.

Other significant degradation occurring in practice stem from the different insertion and coupling losses of optical components such as the EDFAs and optical filters. These can readily be accounted for by considering for instance an effective optical amplifier gain including the insertion loss.

Finally, any potentially deleterious effects related to the propagation into the fiber has been neglected. In addition to optical or electrical filtering, fiber dispersion can increase ISI thus degrading performance. For instance the authors of [Wang and Kahn, 2004] have analyzed the impact of chromatic dispersion and polarization-mode dispersion on DPSK receivers. Furthermore, the latter is known to induce slow fading in WDM systems [Liu et al., 2004,

Kaminow et al., 2013] supplementing to turbulence-induced fading in the case of FSO systems. A detailed joint analysis of these phenomena in the framework of satellite-to-ground links is beyond the scope of the work presented in this document and constitute future prospect of research.

4.2.4 Monte-Carlo modeling of the physical layer performances

The simplest model, based upon an enumeration of the distinct detection noise sources and an overall Gaussian assumption has been proven to be inaccurate in predicting either decision thresholds or log-likelihood ratios for preamplified systems [Gnauck and Winzer, 2005, Winzer, 2001, Benedetto and Bosco, 2005].

Closed-form expressions yielding the exact signal and noise probability distribution exist only when considering unrealistically simplified systems where the electrical filter is an ideal integrator of period $T_{\text{int}} = 1/(2B_e)$, the optical filter has a periodic impulse response with exactly $M = T_{\text{int}}B_o$ non-vanishing, equal Fourier coefficients and the optical filter does not influence the signal field [Humblet and Azizoglu, 1991, Marcuse, 1991, Marcuse, 1990]. In that case the probability density functions of the detected signal are known to be χ-square like. Although such closed-form expressions are convenient due to their simplicity, they do not provide accurate PHY modeling options as soon as non-negligible ISI degrades performance in real systems.

A third analytic option relies on a method employing Karhunen-Loeve series expansion. It was first described in [Forestieri, 2000] for OOK and extended to DBPSK formats in [Wang and Kahn, 2004]. This method can evaluate the BER or log-likelihood ratios while accounting for pulse shaping, optical and electrical filtering. However it does not present a simple closed-form expression. It relies on numerically computing the moment-generating function of the decision sample, the inverse Laplace transform of the latter as well as a saddle-point integration approximation for estimating the BER. It may therefore become excessively complex to implement when even more realistic features need to be considered (e.g. realistic optical signals produced by a MZM whose drive signals have been filtered [Wang and Kahn, 2004]).

At the expense of computational time, while providing accurate results -in the frame of the simplifications and assumptions detailed in the previous sections- an end-to-end simulation tool does not suffer such limitations.

An end-to-end physical layer (PHY) simulator of the transmission system (SIMCOP introduced in 1.2.5) has been developed by ISAE on behalf of CNES. In the framework of this thesis, in order to accurately compute the mutual information at the output of PHY, it has been enhanced by the transmitter and receivers' models described in the previous sections. It allows to take

into account the effects of ISI, as well as the exact statistical properties of detection noise. SIMCOP has been used in a project unconnected to this thesis -conducted by CNES, ISAE and Airbus Defense and Space- and compared to simulation results obtained by Synopsys's OptSim software. Sensitivity results provided by SIMCOP and OptSIm showed a difference inferior to 0.2 dB overall. SIMCOP has been used for computing the results presented in the remainder of this chapter.

4.3 Physical Layer Data reliability Mechanisms

The purpose of data reliability mechanisms (interleaving and coding) and how they are relevant to the FSO channel has been introduced in Section 1.2.4. Moreover, Sections 2.4.3.4, 2.4.3.5 and 2.4.3.6 explained how channel capacity -or equivalently mutual information (MI)-, thanks to Shannon's noisy coding theorem, represents a powerful measure of information for inferring on the performance of error-correcting codes (ECC).

4.3.1 Error-correcting code

SIMCOP, whose modeling assumptions are described in the previous sections of the present chapter, takes as input time series of instantaneous coupled flux fluctuations into the EDFA after partial AO correction (see Eq. (4.13) and the definition of the parameter $a_{\mathrm{SMF}(t)}$). For the results presneted later in Section 4.5, such time series were obtained using SAOST.

The purpose of SIMCOP, is therefore to convert these coupled flux times series into instantaneous MI times series characterized by the proper statistical and temporal properties. The motivation behind the computation of MI resides in the fact that it allows to precisely characterize the behavior of the error correction decoder without actually realizing the decoding [Chauvet et al., 2010, Chauvet et al., 2012].

In practice, for each value of an input time series of coupled flux attenuation, SIMCOP computes histograms of the simulated detected signal for either a 0 or 1-bit as shown solely in Fig. 4.8 for the purpose of illustration. Assuming that a sufficient number of bits are simulated, it provides accurate estimates of the received signal probability distributions that can in turn be used to compute either instantaneous BER or MI.

Section 2.4.3.7 detailed how, on slow fading channel, the notion of an instantaneous mutual information was relevant. It also highlighted the channel outage probability as a proper measure for the performance of the error-correcting code on PHY. For the sake of convenience the latter is recalled hereafter:

$$P_{\mathrm{Outage}}\left(R_0^{\mathrm{PHY}}\right) = \Pr\left(\mathrm{MI}(t) < R_0^{\mathrm{PHY}}\right), \tag{4.22}$$

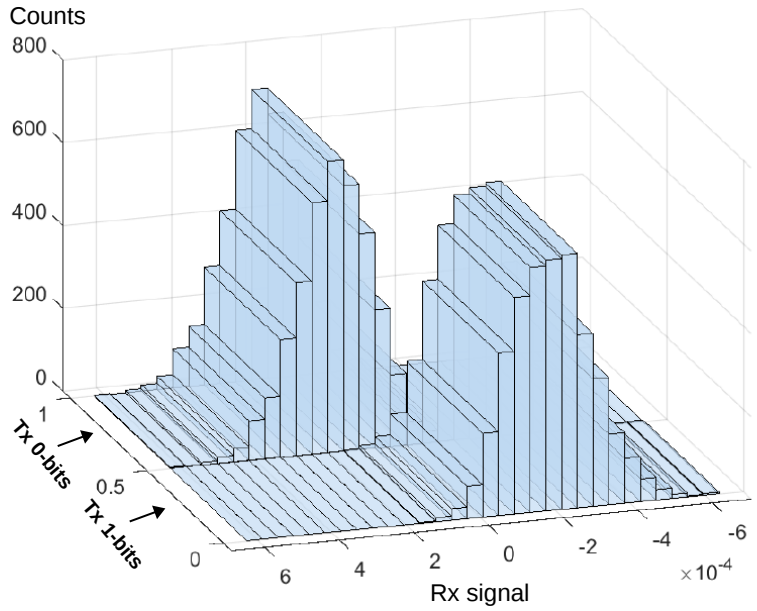

Figure 4.8: Illustration of simulated histograms of received signals corresponding to the transmitted bits.

where R_0^{PHY} is the coding rate of the error-correcting code (i.e. the proportion of the data-stream that is useful i.e. non-redundant).

4.3.2 Time-interleaving

4.3.2.1 Uniform convolutional interleaver

In essence, time interleaving spreads successive transmitted symbols in different time slots in order to overcome the bursty distribution of errors encountered over slow fading channel. Time interleaving comes at the cost of increasing memory space, system complexity and time-delay (latency). In the class of periodic interleaving exist two main techniques: block interleaving and convolutional interleaving.

In the case of the former, the transmitted sequence is fed into a rectangular array (also called block) of dimensions B-by-N (B rows and N columns). The input sequence is fed into such an array row-by-row and read-out (shifted) column-by-column in order to get symbols, initially successive, that appear in time $B-1$ symbols apart over the channel. At the receiver, the transmitted sequence is restored by applying a B-by-N array as a deinterleaver. Hence, the interleaving-deinterleaving process necessitates in that case the equivalent memory of $2BN$ symbols and induces the same amount of latency (in time).

Figure 4.9 illustrates the principle of a convolutional interleaver. Such an interleaver can

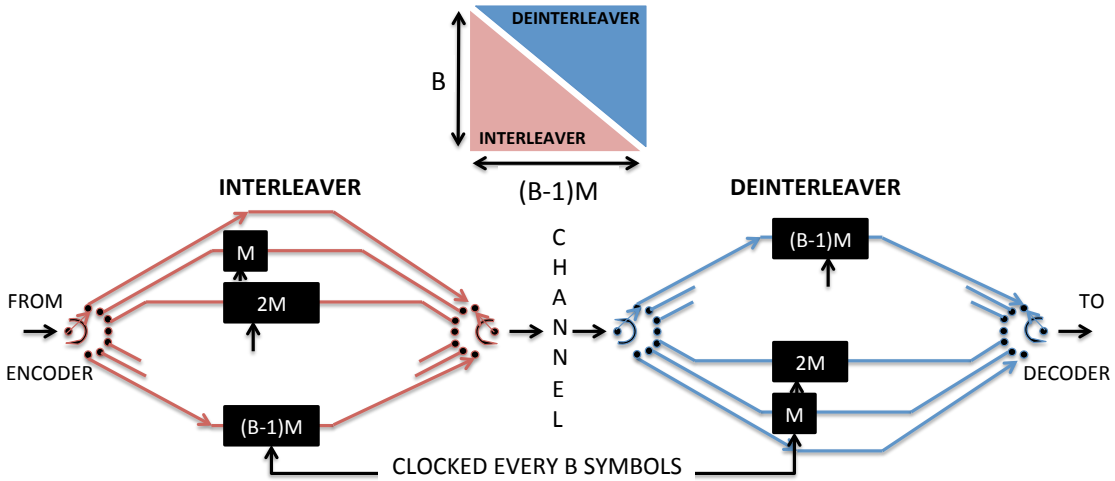

Figure 4.9: Diagram of the realization of a B-by-N convolutional interleaver. Adapted from [Hanna, 1993].

be created by splitting diagonally the B-by-N array of a block interleaver. The first half corresponds to the interleaver and the second to the deinterleaver.

At the transmitter, the coded sequence is fed into a B-by-N triangular array of shift- registers. Defining $M = N/B$, the i^{th} shift-register has a length of $(i-1)M$. At the receiver, the original sequence is restored using an inverse structure of such shift-registers. The clocking of the registers every B symbols is required as the oldest symbols are shifted out to the channel at the transmitter. Symbols that are delayed by $(i-1)M$ stages at the transmitter are delayed by $(B-i)M$ stages at the receiver.

Convolutional interleaving has two main advantages over the block interleaver [Hanna, 1993, Clark and Cain, 1981]:

- **Decrease in required memory:** The total memory space requirements is $N(B-1)$ symbols. Therefore it is less than half of the memory required by a B-by-N block interleaver.
- **Decrease in latency:** All symbols receive a total delay of $(B-1)M$ stages. For a clocking rate equal to B, this results in $B(B-1)M$ or $N(B-1)$ symbol times. This delay is therefore less than half the delay required in a B-by-N block interleaver.

The main drawback of convolutional interleavers with respect to simpler block interleavers is obviously their increased implementation complexity. For instance, in the case of a block interleaver the memory read and write is explicit but a convolutional interleaver needs to write and read at the same time. In general, the practical implementation of interleavers and thus their real performance, depend on an aggregate of features. For instance, many of the interleaver algorithms used in practice require some pre-processing before starting

actual interleaving processes [Asghar and Liu, 2010]. The precise hardware implementation and mechanisms study pertaining to such considerations goes beyond the scope of this thesis. Therefore, it was chosen to emphasize on the benefits provided by typical convolutional interleavers due to their theoretical advantages over simpler block interleavers, as stated above.

4.3.2.2 Required Memory and induced latency

To emulate the effect of an uniform convolutional interleaver at the transmitter and the associated de-interleaver at the receiver, the instantaneous channel capacity is uniformly averaged over a sliding window of size denoted PHY_interleaver_Length (given in unit of time) in the following. It is assumed here that the interleaving process is perfect in the sense that the interleaved codeword experiences every fading state comprised in PHY_interleaver_Length.

At the transmitter (i.e. satellite), the PHY memory needed in order to store the corresponding data is simply given by the product of the interleaver size in seconds and the data rate:

$$\text{Tx\_PHY\_memory} = \text{PHY\_interleaver\_Length} \times \text{bit\_Rate}. \tag{4.23}$$

The memory required at the receiver is equal to the transmitter's memory times the number of bits (quantization bits) required for representing the log-likelihood ratio (LLR) needed by the soft decoder:

$$\text{Rx\_PHY\_memory} = \text{PHY\_interleaver\_Length} \times \text{bit\_Rate} \times \text{length\_LLR} \tag{4.24}$$

Finding the optimal number of such quantization bits cannot be achieved using the MI computation approach used here. Simulation of actual coding and decoding processes must be conducted in that case. However, for the optical channel and in the case of pre-amplified systems this number is considered to be optimally situated between 4 and 6 bits [Djordjevic et al., 2014].

By neglecting the actual processing time of the interleaving-deinterleaving hardware operation as a first order approximation, PHY_interleaver_Length corresponds to the latency induced on PHY.

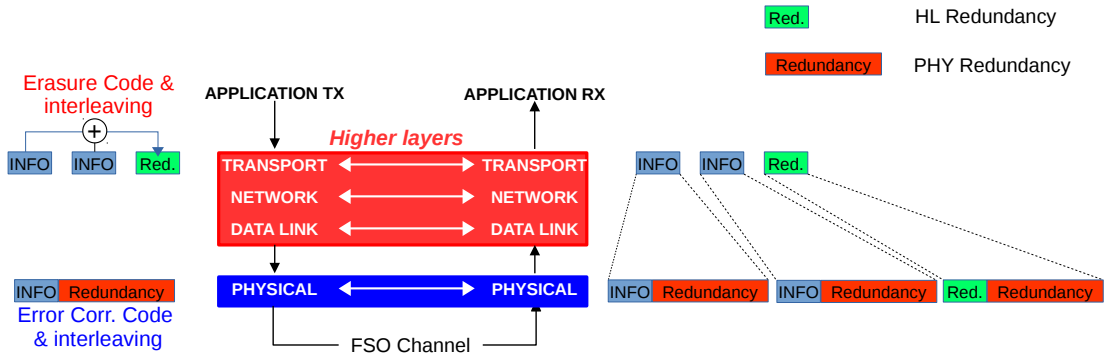

Figure 4.10: Overview of the layered coding strategy.

4.4 Cross-layer approach

4.4.1 Motivation

Symbol-wise error correction coding at PHY has a limited performance against burst errors that can often be longer that the codewords [Henniger et al., 2003]. As introduced in Sections 1.2.4 and 1.2.5, this is due to the very high data rates aimed and very slow coherence times of the FSO channel. Associating with the PHY coding time interleavers (operating on symbols) can increase the robustness of the system to the bursty nature of the channel. For instance, in [Cazaubiel et al., 2006], where the feasibility of a link between a geostationary satellite (ARTEMIS) and an airplane was demonstrated, a long PHY coding scheme (DVB-S2 with datagram of up to 64800 bits) was used. Combined with the fact that relatively low data-rates were considered (2 Mbps and 50 Mbps), a good spreading of errors as well as correction of corrupted bits over a codeword were achieved. At the data rates investigated during this thesis (tens of Gbps), the feasibility of similar coding strategies is challenged. This problem was raised for example in [Henniger and Gonzalez, 2006, Henniger, 2006, Fuchs et al., 2007, Henniger, 2007], where it was proposed to consider alternative strategies such as including higher layers (HL) coding for which longer codewords can be implemented.

In a framework akin to the one cited in the aforementioned publications, a similar approach was investigated during this thesis. By exploiting the interactions between the PHY and HL, the objective was to study a layered coding approach that uses:

- **On PHY**, error-correction coding combined with bit-interleaving within each packet
- **On HL**, erasure-correction coding across the packets combined with packet-interleaving

The principle of this layered approach is schematically represented in Fig. 4.10. Such a strategy has been studied for instance in the case of radio-frequency wireless links in [Berger et al., 2008,

Courtade and Wesel, 2011], however without considering an important factor that is the time-correlation of the channel at hand. In the present case, an accurate description of the AO corrected satellite-to-ground optical channel has been developed including such a correlation that cannot be neglected in practice. In that regard, the last simulation tool developed, introduced in Section 1.2.5 as DREAM (Data Reliability EvAluation Module), allowed the investigation of the optimal combination of the strengths of error and erasure-correction coding and the depths of interleavers. From a system-level design, it permits the optimization of the overall performance while considering a given resource constraint. Given a prescribed performance level, it may also optimize the resource utilization efficiency. Section 4.3 described the PHY interleaving and coding. The following subsections describe how the modeling of the HL data reliability mechanisms has been done. For the sake of clarifying the implementation of this layered operation of data reliability mechanisms, Figure 4.11 illustrates how the effect of interleaving and decoding over the PHY and HL has been emulated in DREAM.

4.4.2 Higher layers erasure channel

4.4.2.1 Instantaneous packet error rate at the higher layers

At the PHY the transmitter sends information at a fixed coding rate of R_0^{PHY} bits/channel use. When an outage event occurs (i.e. when $\text{MI}(t) < R_0^{\text{PHY}}$), the PHY ECC in use does not allow for an "error-free" decoding of the codeword(s) sent at the instant t. From the HL perspective, the erroneous packets corresponding to these outages are erased. This, in essence, describes the behavior of the so-called erasure channel at the HL.

The HL work on an input stream of instantaneous packet-error rates, denoted $\text{PER}(t)$, that is the output of the PHY. In practice, the instantaneous $\text{PER}(t)$ at the output of the PHY is obtained by thresholding the time series of instantaneous MI to either a state of complete erasure (i.e. $\text{PER}(t) = 1$) when $\text{MI}(t)$ is in outage or to an error-free ECC decoding state (i.e. $\text{PER}(t) = 0$) otherwise.

4.4.2.2 Erasure coding

As for the PHY ECC, the HL erasure code (EC) can be characterized by a given coding rate denoted R_0^{HL}. ECs are able to correct the erased data if and only if the amount of missing data is less than the amount of the EC redundancy. This means that the decoding is successful as soon as $1 - \text{PER}(t)$ is greater than R_0^{HL}. When that happens, the instantaneous decoded PER at the HL output, denoted $\text{PER}^{\text{dec.}}(t)$, is equal to zero. Conversely, when $\text{PER}(t)$ is lower than the EC rate, the decoder fails and $\text{PER}^{\text{dec.}}(t) = \text{PER}(t)$, i.e. the PER is unchanged. The statistical average of the decoded PER, denoted $\left\langle \text{PER}_{\text{HL}}^{\text{dec.}}(t) \right\rangle$, constitutes the most relevant performance

measure described thus far, since it characterizes the system performance at the input of the application layer.

The advantage of using such erasure coding is that this kind of decoding is done in software. Related data can be stored on memories that are not necessarily dedicated to it. This is obviously interesting when considering HL interleavers that would otherwise require significant memory resources on the PHY.

However, the drawback of such techniques is that the decoding is done on an erasing channel where one only considers the data correctly corrected by the PHY. The PHY codewords that are not decoded by the ECC are simply deleted, which might possibly represent a significant amount of "useful bits". HL erasure decoding is therefore less effective than an ECC decoding which makes the best use of all the information received.

4.4.2.3 Time-interleaving

At reception, prior to erasure decoding, the effect of packet convolutional interleaving/deinterleaving at the HL can be emulated again by a uniform sliding average window that slides over the time series of PER(t), thus yielding a time series of interleaved HL PER. In doing so it is assumed that the coded packet of a given erasure codeword are perfectly spread over the interleaver length. The HL memory needed at the transmitter in order to store the corresponding data is given by the product of the HL sliding window's length (in seconds) and the physical layer code rate R_0^{PHY} (as only the non-erased packets are considered):

$$\text{Tx\_HL\_memory} = \text{HL\_interleaver\_Length} \times \text{bit\_Rate} \times R_0^{\text{PHY}}. \tag{4.25}$$

Since erasure decoding is considered the HL memory needed at the receiver is simply equal to the HL transmitter's memory (no quantization bits have to be taken into account in contrary to ECC):

$$\text{Rx\_HL\_memory} = \text{HL\_interleaver\_Length} \times \text{bit\_Rate} \times R_0^{\text{PHY}}. \tag{4.26}$$

Similarly to the case of PHY interleaving, by neglecting the actual processing time of the interleaving-deinterleaving operation as a first order approximation, HL_interleaver_Length corresponds to the latency induced on HL.

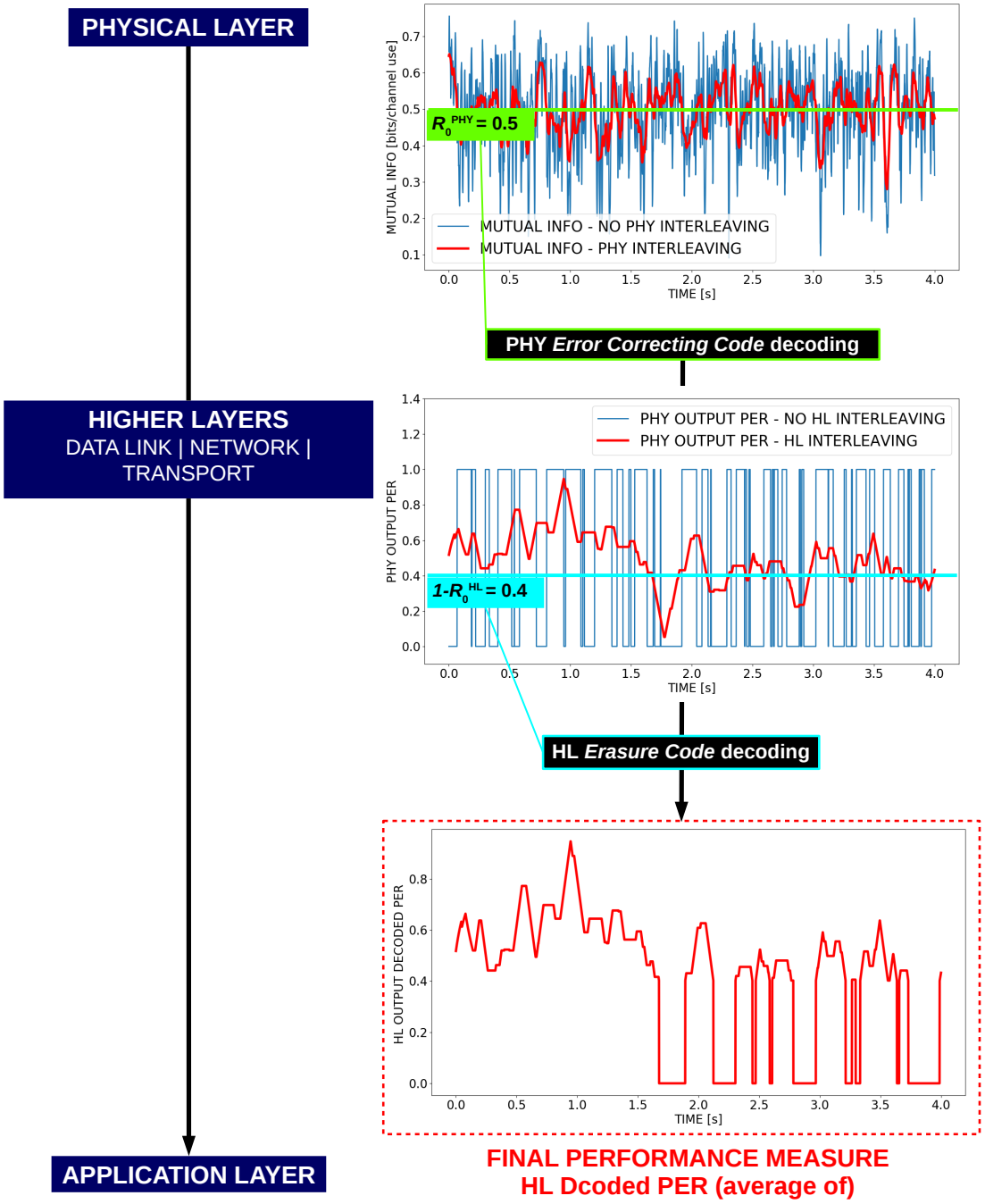

Figure 4.11: Illustration of the emulation of interleaving and decoding over the PHY and HL as implemented in DREAM. Uniform convolutional interleaving/deinterleaving on PHY is implemented by performing a sliding average on the instantaneous mutual information time series. The decoding of the ECC of a given code rate R_0^{PHY} is emulated by thresholding the interleaved times series. It yields times series of instantaneous PER. The interleaving and decoding of the EC on the HL is done similarly. The instantaneous PER is set to zero when it is less than $1 - R_0^{\mathrm{HL}}$.

4.5 Overall system optimization

This section provides an example of the system-level performance trade-offs that can be considered using the ensemble of modeling tools previously described. As an application case, a LEO-to-ground link scenario is considered. Although, obviously not the case for the quantitative analyses made in the following, the general trends and conclusions highlighted at the end of the present section are valid for the GEO-to-ground scenario. When considering data reliability mechanisms and their optimization, the transmitter's end (satellite) will be emphasized since it is, in the downlink case, the transmission's end that usually present highly constrained and limited resources. The results presented in the following were obtained assuming ideal thresholding in the case of the OOK architecture. The DBPSK receiver is assumed ideal as none of the limitations described in 4.2.3.2 were considered.

The LEO-to-ground scenario parameters correspond to those used in Section 3.3.6. The impact of the three levels of AO performance studied in Section 3.3.7 for this scenario are also analyzed hereafter. For the reader's convenience, the parameters related to the latter are recalled in Tables 4.1 and 4.2. In the link budget calculation, only the transmit, receive gains and link losses were accounted for.

Table 4.1: Characteristic link, turbulent and AO parameters for the LEO-to-ground downlink scenario

Downlink Scenario	LEO
Elevation	20 deg
Range	1584 km
Orbital Velocity	7.5 km s^{-1}
Rx Aperture Diameter	25 cm
Tx Aperture Diameter	13.5 cm
Fried Parameter r_0	0.056 m
Log-amplitude Variance σ_χ^2	0.135
Link loss	262 dB
Transmit gain	108 dB
Receive gain	114 dB

4.5.1 Physical layer performance assessment

4.5.1.1 Filter bandwidth optimization

Prior to optimizing the PHY system in the presence of fading due atmospheric turbulence, trade-offs must be made without considering the impact of the latter. For both OOK and

Table 4.2: AO system parameters corresponding to the three performance levels of the LEO scenario

	Radial orders	Frequency	Residual variance	Normalized average coupled flux attenuation
High Perf.	6	2.0 kHz	0.5 rad^2	-3.2 dB
Medium Perf.	3	0.8 kHz	1.3 rad^2	-5.2 dB
Low Perf.	2	0.5 kHz	2.0 rad^2	-6.7 dB

DBPSK formats receiver sensitivity can be improved by optimizing jointly the optical and electrical filters bandwidth. Parameters given in Table 4.3 are representative of preamplified direct detection systems using COTS [Caplan and Atia, 2001] for FSO links.

In the case of an OOK system, Figs. 4.12a and 4.12b present, respectively for a NRZ and a 33% duty cycle RZ format, the sensitivity (in dBm) at a targeted BER of 10^{-3} in function of both the electrical and optical filters 3-dB bandwidths, $[B_e, B_o]$ normalized by the bit rate R_b. The optima can be seen to be around $[0.4R_b, 1.5R_b]$ for NRZ and $[0.6R_b, 1.5R_b]$ for RZ. An enhancement of about 1 dB is offered by considring RZ instead of NRZ pulses. Note that pulses for both RZ and NRZ coding have been raised-cosine filtered at the transmitter. This fundamentally reduce the gain of RZ over NRZ (compared to the case where perfect rectangular pulses are considered).

In addition, it is observed that RZ coding is significantly more tolerant to unoptimized receiver bandwidths. Physical explanations for such a behavior were given in [Winzer et al., 2001]. It is related to trade-offs with respect to the amount of noise filtered -optical in the case of ASE from booster and preamplifier and background light as well as electrical detection noise- versus the amount of ISI introduced as well as the amount of signal energy rejected in the process. Generally, for NRZ, the optimal optical bandwidth is found by trading optical noise with optical-filter-induced ISI. For RZ there is less optically induced ISI, and an optimum between signal energy rejection and collected ASE needs to be established. Filtering the pulses (raised-cosine) slightly broadens the signal spectrum and causes the optimum bandwidths to shrink in the NRZ case due to less ISI. However, it leads to broader optimal bandwidths for RZ in order not to reject too much signal energy.

Figures 4.12c and 4.12d present similar results in the case of a DBPSK modulation using an ideally balanced detector. In that case every potential degradation discussed in Section 4.2.3.2 has been ignored in the simulations. Hence when compared to OOK a gain of roughly 3 dB is obtained as expected. The optima can be seen to be around $[0.6R_b, 1.5R_b]$ for NRZ and $[0.8R_b, 1.5R_b]$ for RZ. Trends similar to the OOK results, in terms of tolerance to unoptimized filter bandwidths, can be observed when comparing NRZ and RZ coding. Furthermore, globally DBPSK seems to be even more tolerent than OOK (note that contour lines are separated

Table 4.3: Main transceiver parameters common to both OOK and DBPSK systems.

TRANSMITTER	
Communication wavelength	1550 nm
Gross bit rate	10 Gbps
Number of polarization modes	2
CW laser	
RIN	-145 dB/Hz
linewidth	10^6 Hz
NRZ coder	
Type	Raised-cosine
Roll-off	0.5
Span	6 symbols
MZM	
Extinction ratio	20 dB
Polarization Voltage V_π	2 V
EDFA Booster	
Gain	20 dB
Noise figure	6 dB
Background noise power density	10^{-27} W/Hz

RECEIVER	
EDFA Preamplifier	
Gain	40 dB
Noise figure	6 dB
PIN photo-detector(s)	
Responsivity	0.8 A/W
Load resistor	100 Ω
Temperature	300 K
Dark current	1 nA
Electrical filter	
Type	Bessel 5th order
Bandwidth	Optimized
Optical filter	
Type	Fabry-Perot
Bandwidth	Optimized

SIMULATION PARAMETERS	
Samples per symbol	19
Number of simulated bits	2^{16}

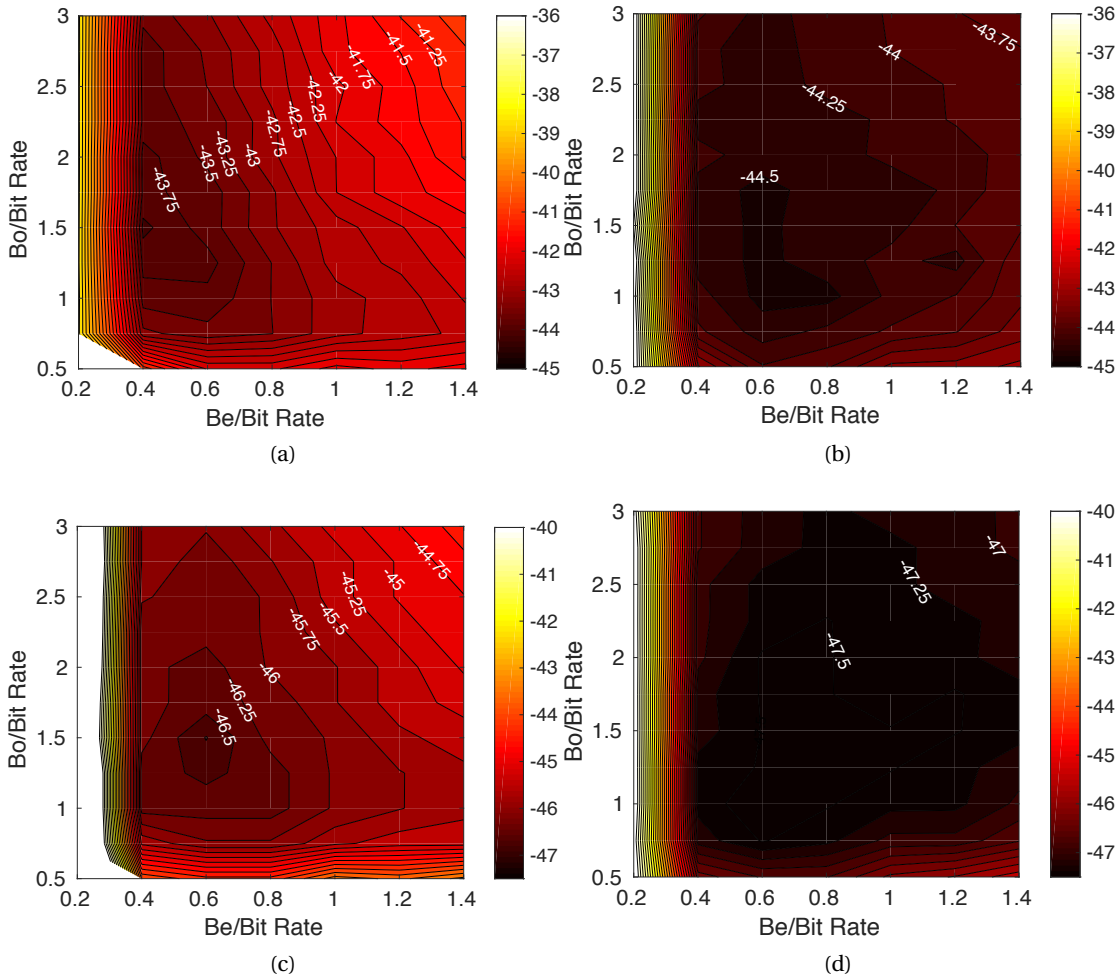

Figure 4.12: Evolution of the sensitivity against the optical and electrical filter bandwidths at a BER of 10^{-3} for a 10 Gbps transmission for (A) OOK-NRZ, (B) DBPSK-NRZ, (C) OOK-RZ and (D) DBPSK-RZ.

by 0.25 dB for both OOK and DBPSK results) due to its increased robustness to both ISI and noise [Winzer et al., 2003].

In terms of sensitivity, due to the advantage of RZ-33% coding over its NRZ counterpart, the former is favored as it comes at the expense of a manageable increase in complexity at the transmitter end. In terms of complexity, the relevant trade-off to be made is considering either an OOK or DBPSK system. In the following subsections we will therefore analyze such a compromise while considering as well the joint impact of AO and data reliability techniques. In order to progressively illustrate the distinct mechanisms at play, the analysis will be carried out first on PHY only and subsequently considering the cross-layered approach described in Section 4.4.

4.5.1.2 Outage probability

4.5.1.2.1 Ergodic mutual information

Aiming at finding global performance trends while jointly comparing in a straightforward manner the impact of interleaving and AO can prove to be difficult. In that regard, it is useful to consider first a performance metric that allows for a simple understanding and characterization of their benefits. The reasoning is to use the non-fading channel as a reference. The losses introduced by the fading process are then characterized in terms of average power differences with respect to this unfaded baseline.

The simplest performance metric consists in the difference between the power required to sustain a given channel capacity (i.e. mutual information) in the case of an unfaded AWGN channel and the power required to sustain fading capacity. The latter, also called ergodic mutual information, is in fact the instantaneous mutual information averaged over all the fading events. Hence it corresponds in theory to the case of an “infinite" PHY interleaver. The fading capacity loss is therefore non-recoverable by means of digital mitigation techniques such as interleavers. However, it is equal to what has been called so far the average level of performance (average normalized coupled flux attenuation, roughly equal to either -3dB, -5dB and -7dB; see Table 4.2) of a given AO system.

This can intuitively be understood by considering the qualitative effects of an AO system and interleaving on the channel fading. With respect to the non-corrected case, a given AO system permits a decrease in averaged coupling losses as well as the mitigation of the fluctuation of the latter. In comparison, interleaving allows only the mitigation of such fluctuations and does not affect the average mutual information level.

This is illustrated in Figures 4.13a and 4.13b for a prescribed code rate $R_0^{\mathrm{PHY}} = 0.55$. These graphs show respectively the ergodic mutual information obtained for the RZ-OOK and RZ-DBPSK systems discussed in 4.5.1.1. In both cases, the evolution of the ergodic mutual information is given against the required **unfaded** receiver power for the three distinct levels of AO performances reported in Table 4.2. Therefore, when considering sufficiently long interlaving, the influence of the channel can be reduced to a loss in terms of average power. Ideally, the latter can be compensated by an increase of the transmitted power.

4.5.1.2.2 Joint impact of AO and interleaving

For $R_0^{\mathrm{PHY}} = 0.55$, the results presented in Figure 4.14 show the outage probability evolution against the required unfaded receiver power for the OOK system while considering the impact

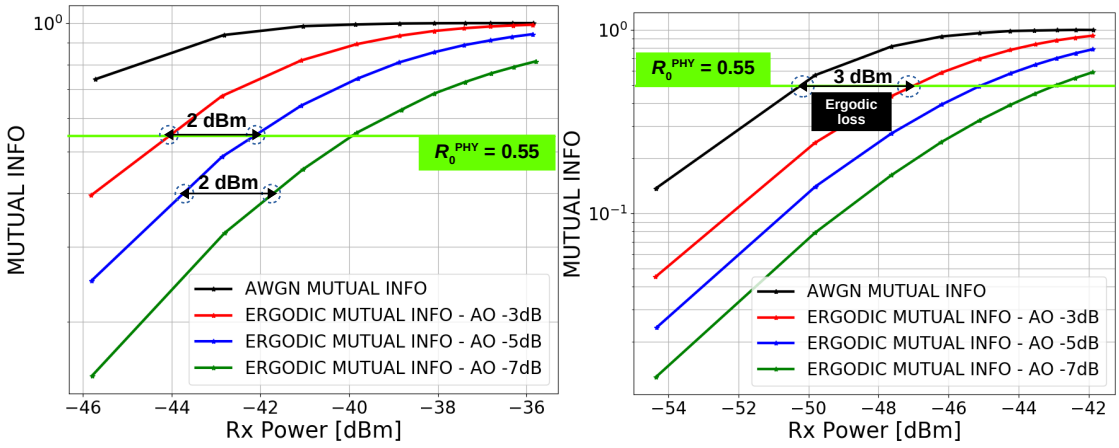

Figure 4.13: Ergodic mutual information evolution against the required unfaded receiver power for pure AWGN and for the three AO corrections in the case of (A) OOK transceiver and (B) DBPSK transceiver

of the medium and low performance AO systems. In each case, two interleaving depths are considered: 7.5 ms (dot-dashed curves) and 30 ms (dashed curves). The case corresponding to no interleaving at all are the plain curves. The vertical curves correspond to the ergodic mutual information (infinite interleaver).

Such results highlight mainly two general features concerning the joint optimization of AO and interleaving:

- **Impact of AO:** Increasing the **average** performance level of an AO system does not have a straightforward or constant effect on the outage probability. For instance, the gap between the two non-interleaved curves widens as the outage probability decreases. As discussed in 3.3.7, this is related to the impact that can have distinct AO systems on the fading as well as inter-fading duration distributions. Moreover, as AO tends to reduce the fading durations distribution, the gain provided by the same increase in power is greater in the presence of a better correction.
- **Impact of interleaving:** Increasing the size of the interleavers contribute to reducing the aforementioned gap. The theoretical limit of infinite interleaving yield a constant difference that corresponds to the difference in average performance of the AO systems. In essence, interleaving tends to alter the slope of the outage probability curves. The latter progressively become parallel as the interleaver size increases.

In practice, the infinite interleaving case permit the definition of another convenient performance metric called the finite interleaver loss [Barron and Boroson, 2006]. For a given

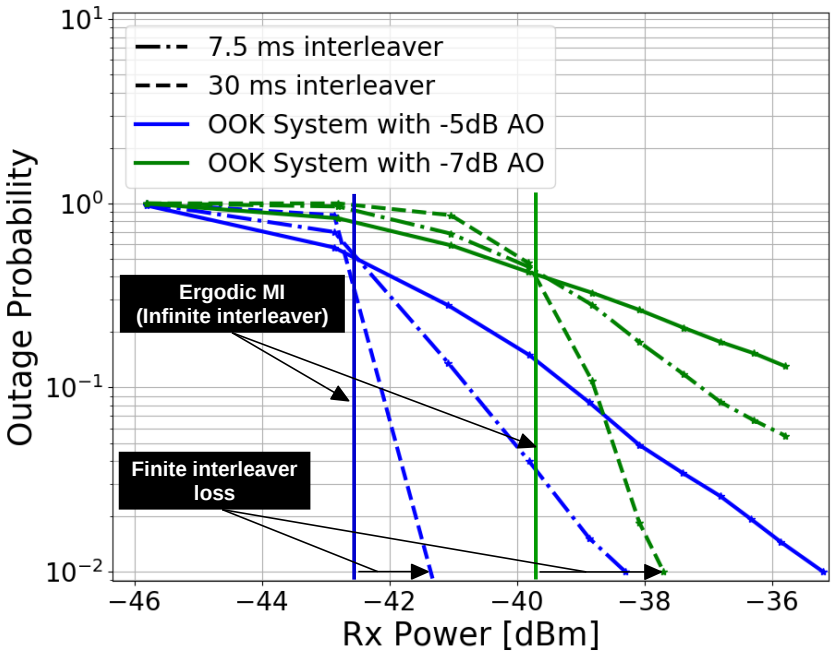

Figure 4.14: Outage probabilities evolution against the required unfaded receiver power for a code rate of R0=0.55, for the high performance and low performance AO systems and, for a 7.5 as well a 30 ms interleaver.

prescribed code rate, it is the difference between the power corresponding to a given outage probability and the power related to the corresponding ergodic mutual information. Therefore, at a targeted outage probability and for a given interleaving length, the finite interleaver loss characterizes how the latter performs compared to the ideal infinite interleaving case. It provides an information that can be used to infer on the trade-offs between the limited average power and interleaving memory for a given AO system.

As an example, consider the finite interleaving loss at a targeted outage probability of 10^{-2}. In the case of a 30 ms interleaver it is approximately 1 dBm for the medium performance AO system and 2 dBm for the low performance AO system. Whereas, In the case of a 7.5 ms interleaver it is approximately 4 dBm for the medium performance AO system and more than 6 dBm for the low performance AO system.

4.5.1.2.3 Joint impact of AO, detection system and interleaving

It is interesting to consider how the combination of a DBPSK tranceiver, a low performance AO system and some interleaving perform against a high performance AO system with a simpler OOK tranceiver. For $R_0^{\text{PHY}} = 0.55$, Fig. 4.15 presents the outage probabilities for the OOK system equipped with high performance AO, the DBPSK system equipped with either medium or low performance AO. The gain related to using a 30 ms interleaver is also shown for the DBPSK

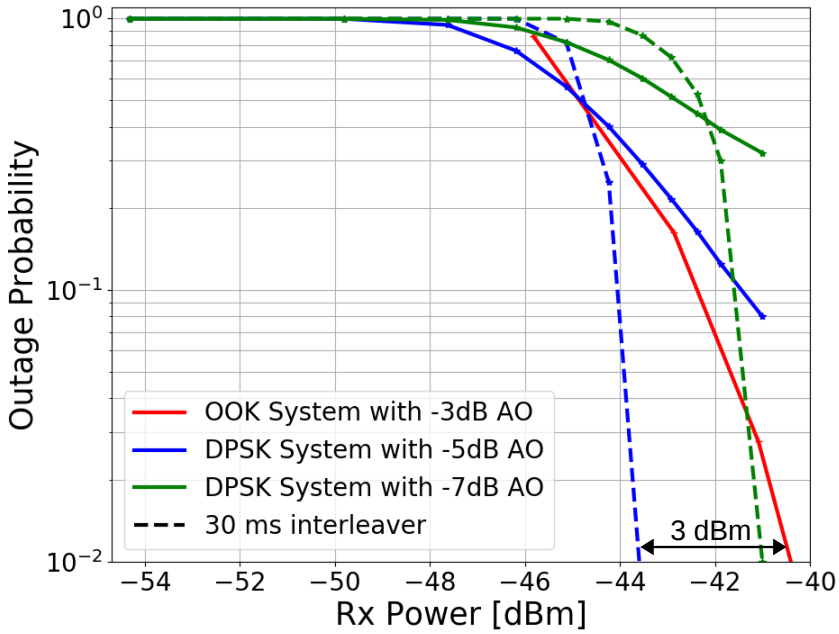

Figure 4.15: Outage probabilities evolution against the required unfaded receiver power for a code rate of R0=0.55 for the OOK transceiver equipped with a high performance AO system and the DBPSK transceiver equipped with either a medium or a low performance AO system as well a 30 ms interleaver.

system.

Consider a targeted outage probability of 10^{-2}. Without interleaving, the OOK system although penalized by its inherent roughly 3 dB disadvantage over the DBPSK system performs better thanks to the high performance AO. Drastically decreasing the complexity of the AO system by considering the low performance system combined with a 30 ms interleaver achieve a slightly better performance. The best overall performance is achieved by the medium performance system combined to the same amount of interleaving. Such performance trade-offs have to be weighted by the acceptable complexity and cost of the distinct subsystems. On the other hand, as discussed in Sections 1.2.2 and 4.2.3.2, the increased performance of DBPSK comes as well at the price of a non negligible increase in complexity that might be challenging for space based systems. It is worth noting however that a DBPSK system is considered for both NASA's LCRD and JAXA's JDRS optical terminals [Edwards and Fletcher, 2013, Yamakawa et al., 2015].

4.5.2 Cross-layer optimization

In the previous analysis, for the purpose of illustrating the impact of several mechanisms at PHY, the coding rate was kept constant. The interleaving duration was not optimized. In the following sections, the data reliability techniques i.e. coding rates and interleaving memories

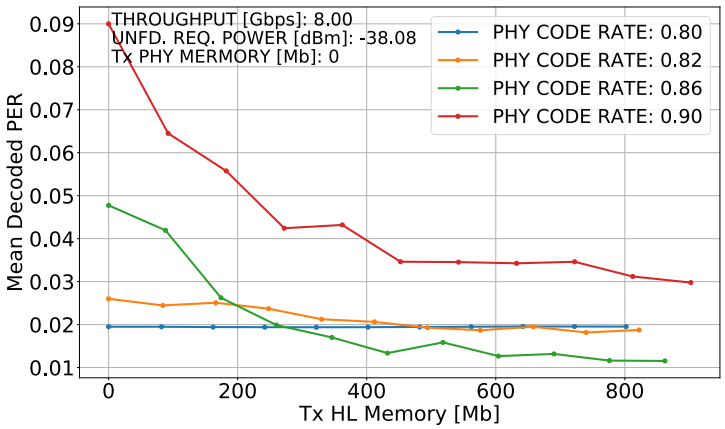

Figure 4.16: Evolution of the average decoded PER against the size of the HL interleaver memory in function of the PHY ECC code rate for the OOK architecture equipped with the high performance AO, and for a 8 Gbps throughput ($R_0^{\text{GLOBAL}} = 0.8$ and 10 Gbps gross bit rate), a 38 dBm unfaded Rx power and no interleaving on the PHY layer

are optimized while considering the layered approach described in Section 4.4. The analysis is carried out for both the OOK and DBPSK architectures and for the three same AO systems.

4.5.2.1 Global code rate

The product of the PHY and HL code rates defines the global rate of the system:

$$R_0^{\text{GLOBAL}} = R_0^{\text{PHY}} R_0^{\text{HL}}. \tag{4.27}$$

This global code rate sets the throughput (i.e. the useful information rate or the data transfer efficiency) of the transmission when it is multiplied by the gross data rate (constant and fixed to 10 Gbps here, see Table 4.3). Note that the definition of such a global code rate sets an inherent constraint of the systems as the physical layer's code rate cannot be lower than the global code rate. The overall resources optimization is done at constant throughput.

4.5.2.2 Targeted transmission performance

As explained in Section 4.4.2.2, from the application layer point of view, the most relevant performance metric one should consider is the average of the instantaneous decoded PER at the output of the HL, denoted $\left\langle \text{PER}_{\text{HL}}^{\text{dec.}}(t) \right\rangle$. Hereafter, we will consider that a transmission is successful as soon as the condition $\left\langle \text{PER}_{\text{HL}}^{\text{dec.}}(t) \right\rangle \leq 10^{-4}$ is met.

4.5.2.3 Impact of HL interleaving

For the high performance AO system and the OOK architecture, Fig. 4.16 shows the evolution of $\langle \mathrm{PER}_{\mathrm{HL}}^{\mathrm{dec.}}(t) \rangle$ against the size of the HL memory allocated at the transmitter side for a transmission's throughput set to 8 Gbps (i.e. a global code rate of $R_0^{\mathrm{GLOBAL}} = 0.8$), no PHY memory and, for an average unfaded power of 38 dBm.

Given the definition of $R_0^{\mathrm{GLOBAL}} = 0.8$ (see Eq. (4.27)), the distinct curves characterize different proportions of PHY vs HL redundancy. One can note that the horizontal curve corresponds to the case where $R_0^{\mathrm{PHY}} = R_0^{\mathrm{GLOBAL}}$ and therefore $R_0^{\mathrm{HL}} = 1$ i.e. no HL erasure coding is implemented and the global redundancy is fully allocated to the PHY ECC. In that case it is obvious that the HL interleaving cannot have an impact on the fading mitigation, hence the horizontal curve. While $\langle \mathrm{PER}_{\mathrm{HL}}^{\mathrm{dec.}}(t) \rangle$ is seen to decrease when the HL interleaver memory size increases, an optimum allocation of coding rates can be found. Here, the curve corresponding to $R_0^{\mathrm{PHY}} = 0.86$ decreases faster than the curve corresponding to $R_0^{\mathrm{PHY}} = 0.82$. Further increasing R_0^{PHY} (i.e. decreasing R_0^{HL}) to 0.90 worsens things. Such optima will be found in the following where the overall system optimization will be presented.

4.5.2.4 Minimum memory for successful transmission

The overall system presents numerous objective variables that can potentially be optimized over constrained ranges of several distinct parameters. Available memory and power on board the satellite are two critical resources. Therefore it is relevant to investigate to what extent AO and optimized coding techniques influence their utilization efficiency. For a given AO performance and system architecture, in the following the emphasis is put on minimizing the required total memory at the transmitter, denoted $\left(\mathrm{Tx\_memory}\right)^{\mathrm{Total}}$, as well as the unfaded power required at the receiver, $\mathrm{P_{Rx}}$, for an successful downlink. Such a minimization depends on the allocation of coding rates and interleaving lengths on both PHY and HL, the performance level of AO and the targeted throughput:

$$\underset{\mathrm{P_{Rx}}, R_0^{\mathrm{PHY}}, R_0^{\mathrm{HL}}}{\text{minimize}} \left[\left(\mathrm{Tx\_memory}\right)^{\mathrm{Total}} = \mathrm{Tx\_HL\_memory} + \mathrm{Tx\_PHY\_memory} \right]$$

$$\text{subject to} \begin{cases} \langle \mathrm{PER}_{\mathrm{HL}}^{\mathrm{dec.}}(t) \rangle \leq 10^{-4} \\ \\ R_0^{\mathrm{PHY}} R_0^{\mathrm{HL}} = R_0^{\mathrm{GLOBAL}} \end{cases}$$

Figure 4.17 presents the results of such an optimization for the OOK architecture equipped with a high performance AO system. Note that Figures 4.17a and 4.17b are identical results,

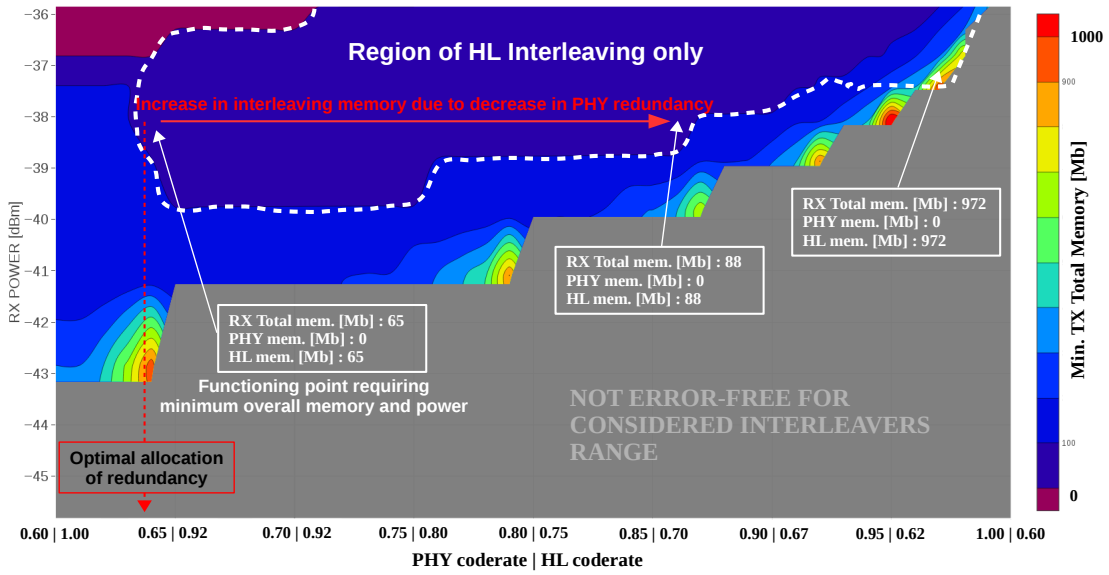

(a)

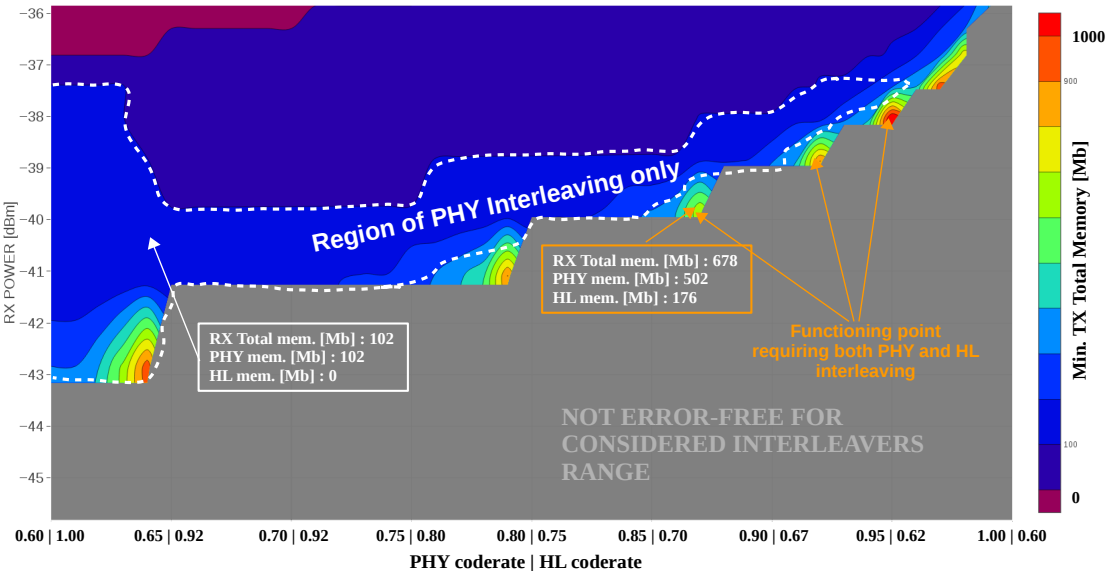

(b)

Figure 4.17: Evolution of the minimum memory for a successful transmission (average decoded HL PER of 10^{-4}), against the PHY and HL code rates (x-axis) and the unfaded receiver power (y-axis) required by an OOK transceiver equipped with a high performance AO system. These results are obtained for a targeted throughput of 6 Gbps (i.e. a global code rate $R_0^{\text{GLOBAL}} = 0.6$). Note that (A) and (B) are identical and presented here for the sake of clarifying the various conclusions that can be drawn by analyzing the figure.

duplicated here solely for the sake of clarifying the various conclusions that can be drawn by analyzing the figure.

For a fixed $R_0^{\text{GLOBAL}} = 0.6$ (i.e. a 6 Gbps throughput), this map shows the evolution of the calculated minimum required total memory against P_{Rx} on the y-axis, and the allocation of PHY and HL coding rates on the x-axis. The maximum interleaving length allowed during the optimization computation was set to 0.22 s equally split between the PHY and HL (i.e. maximum of 0.11 s allowed for HL_interleaver_Length and for PHY_interleaver_Length separately). Note that at 10 Gbps, this allows a maximum of 1100 Mb for PHY interleaving independently of R_0^{PHY}, whereas for HL interleaving the allowed memory depends by definition on the PHY coding rate (see Eq. (4.25)). It is less than 1100 Mb expect when $R_0^{\text{PHY}} = 1$ (i.e. $R_0^{\text{HL}} = R_0^{\text{GLOBAL}} = 0.6$, the overall redundancy is completely allocated to the HL).

One discerns four main regions on this map:

- The grayed area corresponds to a region for which no successful transmission is possible for the given set of chosen parameters.
- At high unfaded powers the dark blue zone corresponds to a region where an successful transmission is achievable when interleaving is optimally done on the HL exclusively. This region is highlighted in Fig. 4.17a.
- At lower unfaded powers the light blue zone corresponds to a region where an successful transmission is achievable when interleaving is optimally done on PHY exclusively. This region is highlighted in Fig. 4.17b.
- At high unfaded powers and low PHY coding rates, the purple zone delimits a region where successful transmission is possible without requiring any form of interleaving.

As shown in Fig. 4.17a, the global minimum in terms of total memory is found in the region of the exclusively HL interleaving and is equal to 65 Mb. It is found when an optmimum allocation of PHY and HL redundancy allocation is met: $R_0^{\text{PHY}} = 0.64$ and $R_0^{\text{HL}} \simeq 0.94$.

Globally, for a fixed unfaded power, as the strength of the overall layered coding is progressively transferred from the PHY error-correcting code to the HL erasure code (i.e. by looking at an horizontal line from the left to the right of the map as depicted by the red arrow in Fig. 4.17a) the total required memory increases. That fact highlights the overall better efficiency of the PHY error-correcting code as expected since as explained in 4.4.2.2. The erasure code only makes use of the information that has been anteriorly decoded by the PHY. Therefore, for a fixed throughput, the following general conclusions regarding the trends observed in Figure 4.17 are drawn:

- When considering low power levels, the PHY ECC is inherently more efficient and hence so is PHY interleaving. The HL coding and interleaving act as a supplementary level of reliability as soon as the PHY mechanisms are insufficient. Or in other words when the latter are limited by the maximum allowed interleaving and/or when high R_0^{PHY} are considered. That behavior is emphasized in Fig. 4.17b where, at the right-end of the PHY interleaving region exist functioning points requiring both PHY and HL interleaving.

- When greater required power levels are allowed, a combination of optimal PHY and HL coding can lead to a drastic decrease in required interleaving memory. Furthermore, in that case the latter is completely allocated to the HL.

These conclusions were drawn for a fixed global code rate $R_0^{\text{GLOBAL}} = 0.6$. Increasing the latter while keeping the constraints imposed on the maximum allowed interleaving sizes unchanged, exacerbates the behavior previously described. Fig. 4.18 shows the evolution of similar optimizations carried out for distinct throughputs. Increasing the latter progressively induces the reduction of the optimal HL interleaving area (dark blue) until only PHY interleaving remains (light blue). Recall that increasing the throughput inherently reduces both the PHY and HL coding strengths, see Section 4.5.2.1. In general, for the considered layered approach consisting of a combination of ECC and EC, HL interleaving is advantageous (in terms of required memory) only in favorable conditions: in higher allowed power regimes and lower throughputs.

4.5.2.5 Optimized systems

The conclusions made in the previous section concerned a single AO system and the OOK architecture. The impact of different AO performance levels and the potential benefits offered by the DBPSK receiver are investigated hereafter. In order to have an overview of how the overall resources scale with an increasing throughput, Fig. 4.19 presents the evolution of the global minimums of the required memory allowing an successful transmission against said throughput. Hence, each point on these graphs represents an operating point of the overall system that is optimal with respect to memory and power utilization as the latter have been minimized. The constrained range of interleaver lengths used is unchanged: from no interleaving to 0.22 s equally split between PHY and HL was allowed during the calculations. The unfaded required power at the receiver ranged from -52 to -38 dBm for both architectures.

Figures 4.19a and 4.19b shows the results respectively corresponding to the OOK and DBPSK receivers. For some points of interest on these curves, are reported the optimal required power, distribution of PHY and HL code rates, PHY and HL memories, as well as latency. Unsurprisingly, targeting higher throughputs requires larger interleaving memory as well as power. Overall, the benefits of increasing the performance of the AO system is threefold:

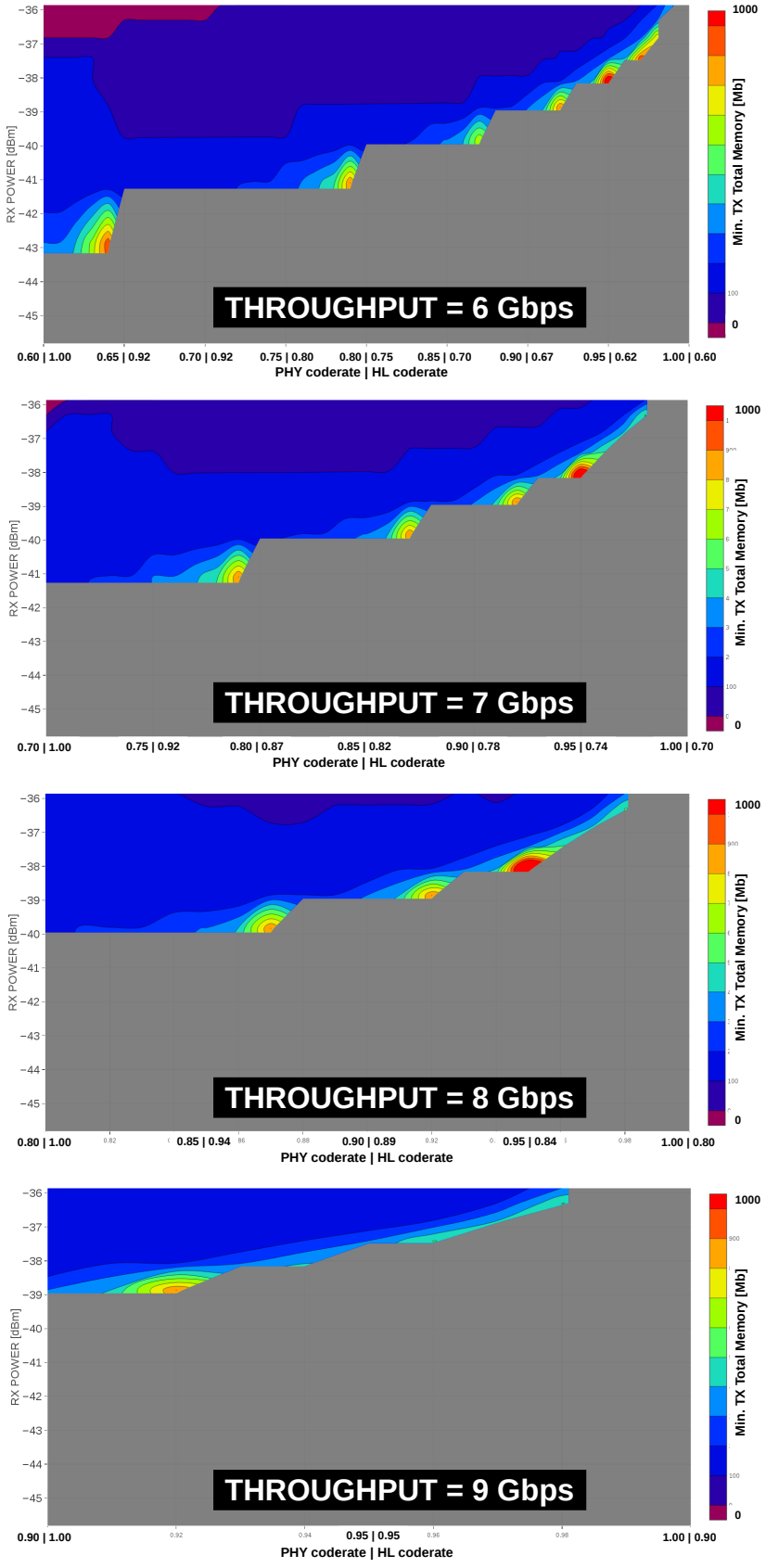

Figure 4.18: Evolution of the required minimum memory for a successful transmission $\left(\left\langle \mathrm{PER}_{\mathrm{HL}}^{\mathrm{dec.}}(t)\right\rangle \leq 10^{-4}\right)$ when progressively increasing the throughput. The other system parameters are identical to those presented in 4.17.

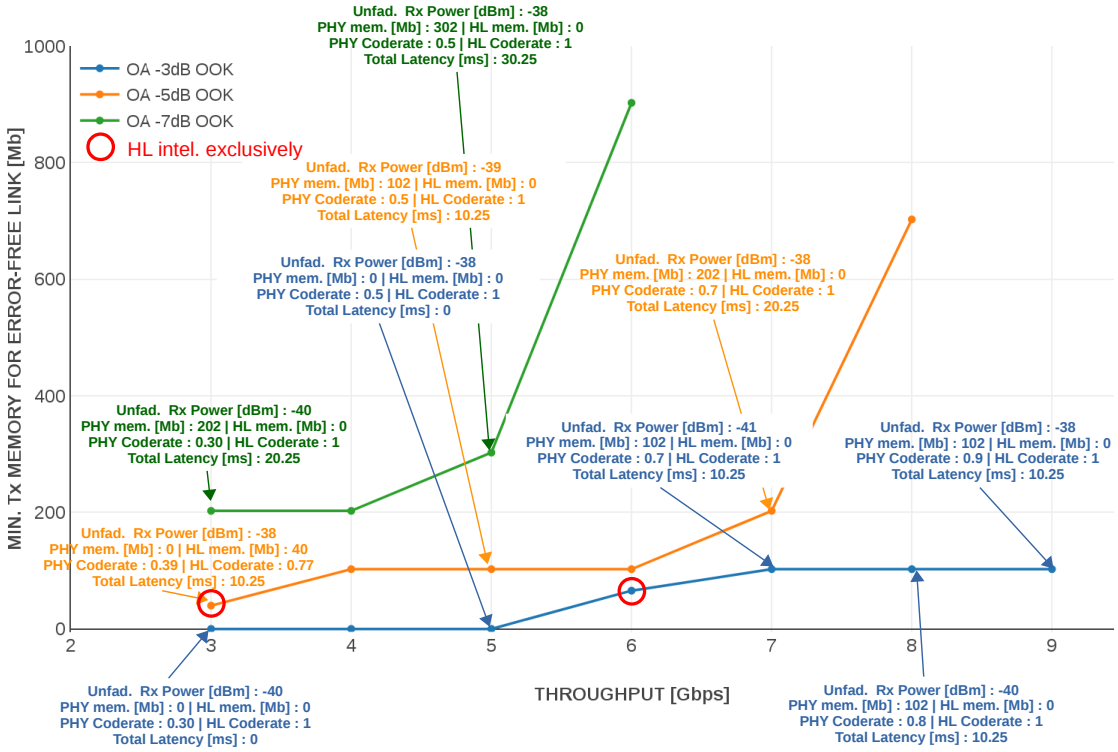

(a)

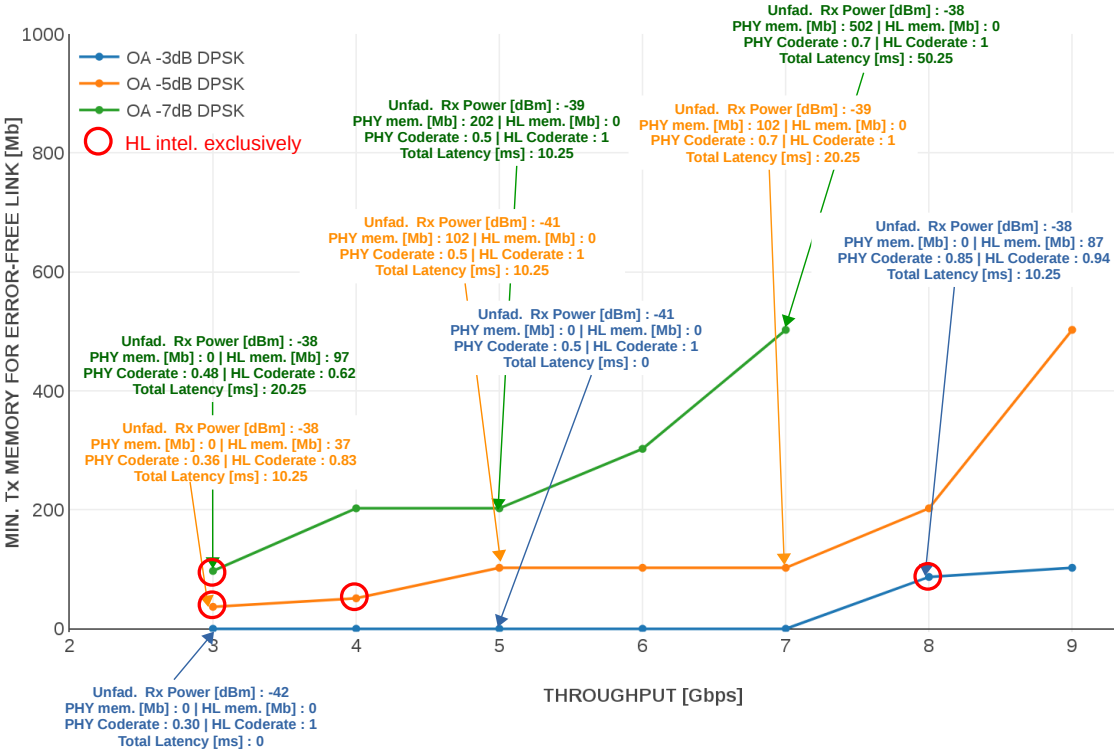

(b)

Figure 4.19: Evolution of the global minimum total memory required by the transmitter in order to ensure a successful transmission $\left(\left\langle \mathrm{PER}_{\mathrm{HL}}^{\mathrm{dec.}}(t)\right\rangle \leq 10^{-4}\right)$ against the targeted throughput. Every point on these curves represents an operating point of the overall system that is optimal with respect to memory and power utilization. The case of an OOK transceiver is presented in (A) while the DPBSK is presented in (B). In both case, each curve characterizes a given AO performance level. The optimal allocation of interleaving and coding between PHY and HL are reported for several points of interest.

- **Decrease in total memory:** Globally, averaged over all the throughputs, the high performance system allows a decrease of roughly 80% with respect to the medium performance system and a 95% decrease with respect to the low performance system. As the throughput increases, the high performance systems ensure reasonable interleaving lengths as only 100 Mb are required at 9 Gbps.
- **Decrease in required power:** At low throughput, this impact is less striking as interleaving and required power have jointly been minimized. Consider for instance the 3 Gbps operating points corresponding to the OOK architecture. The low performance system has an advantage of 2 dB over the medium performance system. However the latter comes at the cost of 5 times more interleaving memory. On the other hand, examining operating points at higher throughput, where the data reliability mechanisms efficiencies are expected to be limited, a better AO system yields a clear advantage.
- **Favoring HL interleaving:** Operating points where interleaving is optimally, exclusively performed at the HL are circled in red. As previously explained, the inherent features of the adopted layered approach advantage the HL interleaving at lower throughput. However, understandably such a behavior depends on the channel fluctuations. Therefore, increasing the AO performance expands the possibility of optimally implementing HL interleaving at higher throughputs.

The benefits of using a DBPSK architecture might have been expected to be an overall constant advantage of approximately 2 to 3 dB in required power as it is the case in terms of sensitivity, ergodic capacity or outage probability. Analyzing equivalent operating points on both architectures one notices that DBPSK indeed provides almost always at least a 1 dB advantage. However, further comparing figures 4.19a and 4.19b the enhancement provided by the DBPSK architecture is not solely related to the required power. Up to approximately 5 Gbps, DBPSK does not seem to provide a striking advantage with respect to the required interleaving memory. At higher throughput and for identical level of AO performance, DBPSK permits to roughly decrease by a factor 3 the required total memory. This behavior is explained once more by considering the expected limited overall efficiency of both PHY and HL coding and interleaving in this regime. In that case, the 3 dB advantage of DBPSK over OOK results in an alleviation of these intrinsic limitations. Consequently, combined with the high performance AO system HL interleaving can be envisaged at throughput as high as 8 Gbps.

4.6 Summary and conclusion

The first part of this chapter detailed the modeling of the communication subsystem. The improvements made to SIMCOP allowed us to account for an accurate description of the typical impairments (noises, ISI) encountered in such systems.

The second part of this chapter was dedicated to the description of data reliability techniques. The motivations behind the investigation of a cross-layer strategy and their relevance in the framework of free-space optical communication were clearly stated. The modeling assumptions underlying DREAM were also presented.

The last part of the present chapter presented how, using the range of developed models and simulation tools, the overall system optimization could be carried out. The emphasis was put on a data transfer scenario from a LEO satellite. This case study analysis highlighted the potential impact of jointly investigating physical mitigation techniques such as AO and digital mitigation techniques such as interleaving in a layered approach.

The relevance of such studies lies in the refined trade-offs that are made accessible as the latter can have an important impact on the overall design at a system level. For instance, as already mentioned, in contrary to PHY ECC and interleaving, HL data reliability mechanisms, although less efficient, are attractive because implementable in software. This implies that they may be designed using resources that are not not exclusively meant for that purpose (for instance the satellite's random-access memory) whereas PHY techniques usually requires additional, dedicated hardware (such as ASICs). Therefore, HL data reliability mechanisms can potentially lead to a decrease in implementation complexity that is of interest especially at the satellite's end. On the other hand, their lower performances must be compensated on ground by considering AO systems that possibly require non commercially available components.

5 CONCLUSIONS

5.1 Summary and main findings

The development of satellite optical downlinks is driven by the demand in very high rate transmission from Earth orbiting satellites to ground stations in the near future for either communication or data transfer applications. While those future satellite-to-ground laser communication systems promise extremely high data-rates, reasonable costs of implementation in the short term will be attainable only by leveraging the benefits of existing single mode components developed for fiber telecommunication. Among other major impairments, optical downlinks are highly affected by atmospheric turbulence as it severely degrades the coupling efficiency of the incoming optical wave into single-mode components.

To mitigate the signal fading induced by atmospheric turbulence several mitigation techniques are commonly considered. As demonstrated by several recent experiments, the use of adaptive optics at the ground station end should contribute to reduce substantially the criticality of such fading by partially compensating turbulence-induced phase fluctuations. Nevertheless, when very high injection stability is needed, complex and expensive adaptive optics systems have to be considered. In that case, the use of digital data reliability techniques such as interleaving and coding could scale down the specifications and cost of adaptive optics systems. These digital techniques are however limited by the satellite resources (in terms of buffer memory and power) and constrained by the targeted applications (in terms of latency and throughput). Hence, the investigation of trade-offs characterizing the overall system performance is required.

In this framework, the general objective of this thesis was to jointly study adaptive optics and data reliability techniques. It led to the development of various simulation tools as well as analytic models that will be exploited in future system-level optimizations. Moreover, an in-depth study of the specific characteristics and various trade-offs of reliable satellite optical

donwlinks corrected by adaptive optics has been conducted.

The first part of this thesis dealt with the study and characterization of the impact of partial adaptive optics on the coupled flux into single-mode fibers. It relied on a simplified model accounting for the most important errors characterizing an adaptive optics system in the framework of satellite downlinks. Taking into account both the impact of scintillation and phase distortions on the coupling efficiency, this model has been proved to be accurate for both GEO and LEO scenarios, at elevations greater than 20 deg for which it has been validated by end-to-end wave optics simulations.

Furthermore, relying on such an underlying simplified model, original analytic expressions characterizing the statistics (probability distribution) and temporal properties (autocovariance) of the partially corrected coupled flux have been derived. They allow to easily compute relevant temporal properties (e.g. mean, maximum and minimum duration of fade) of the channel. Those are useful for the optimization of digital fading mitigation techniques. These expression have been compared and validated as well by end-to-end simulations. This comparison emphasized the interest in the developed analytic model. The latter provides relevant order of magnitudes, if not accurate results, while avoiding time consuming and complex simulations. Finally, while considering both GEO and LEO downlinks, the aforementioned results have been used to infer on the impact of distinct AO performances on such temporal characteristics. By dosing so, the importance of considering the lower AO residuals instead of a perfect correction was underlined. This analysis highlighted as well the importance of not solely considering average AO performance parameters such as the residual variance or average attenuation, originally used in the context of astronomy or imagery applications.

The second part of this thesis concerned the study of the benefits and limitations of both interleaving and coding at the physical as well as the higher layers of the communication stack. In order to provide accurate results in that regard, the enhancement of an end-to-end physical layer simulator was undertaken. The emphasis was put on the investigation of pre-amplified direct detection (using OOK) and differentially coherent detection systems (using DBPSK).

Due to the nature of the satellite-to-ground optical channel, bursty errors occur during the transmission. These errors can hardly be corrected by conventional error-correcting codes on the physical layer. They have to be associated with time interleavers that potentially increase system complexity as they usually require additional dedicated hardware. To alleviate such drawbacks, this thesis investigated the performances of a layered strategy. In order to investigate the performance of a cross-layer coding scheme a dedicated simulator was developed. It permits to optimize the overall system's resources utilization efficiency with respect to a targeted performance level. Furthermore, combining such developments with the work previously dedicated to adaptive optics, yielded prospective and original conclusions.

Specifically presented in this manuscript, a data transfer scenario from a LEO satellite whose memory is considered as a constrained resource was minimized while ensuring successful transmission. This case study lent itself well into illustrating the benefits of jointly investigating physical mitigation techniques such as adaptive optics and digital mitigation techniques such as interleaving in a layered approach. In particular it was noted that even at high throughput, the complexity and cost related to physical layer interleaving could be replaced by higher layer interleaving by increasing the ground based adaptive optics performance.

5.2 Limitations and scope for future work

Despite the refined trade-offs that can be explored by the various developments carried out throughout this work, several limitations that demand future improvements should be underlined. They reside, at first, in some important assumptions made regarding the modeling of the simplified adaptive optics simulation tool and its analytic framework. In that regard, the following points constitute interesting prospects and should be further investigated:

- **The impact of log-amplitude spatial structures smaller than the pupil on the coupled flux fluctuations.**
  In strong turbulence conditions, averaging out the effect of those log-amplitude fluctuations has an impact particularly noticeable in LEO-to-ground scenarios characterized by less aperture averaging (smaller pupil diameter) combined to more challenging turbulence conditions (lower elevation). Considering potential improvements or new developments in that direction are mandatory for extending the domain of validity of SAOST.

- **The modeling of the wave-front sensing in more challenging turbulent conditions.**
  The impact of scintillation on wave-front-sensing was not taken into account during the development of the simplified AO model. This may therefore limit its validity in the case of very low elevation downlinks that are typical of LEO scenarios. Incorporating analytic developments in that regard and further investigating the accuracy of SAOST by end-to-end comparison (or experimental results) in these regimes seems advisable. To fine-tune the analysis, consideration could be given to the limited dynamics of the sensor, the flux allocated to the wavefront analyzer, the sensitivity of the sensors used, as well as the slope calculation algorithms.

  In a second step, it seems relevant to look into wave-front sensing concepts that may enhance the robustness of a conventional Shack-Hartmann WFS in challenging turbulent conditions. The limitations of the Shack-Hartmann sensor reside primarily in the required homogeneity of the flux distribution over the sub-pupil (see Sections 3.2.3.7 and 3.2.1.1). Thus, investigating the possibility of dynamically taking into account

such an intensity distribution in the phase estimation process -by adapting the data formation model (e.g. filtering out the measurements that do not present a satisfactory SNR)- could be a promising enhancement. Other types of wave-front sensors could of course be investigated as well. For instance, looking into the benefits of focal plane analyzers, that couple phase and amplitude in their measurement principle could be a solution to these limitations at the expense however of a high computation cost. Hence, today the practical implementation of such analyzers require that those computational constraints be lifted.

Furthermore, although adaptive optics were emphasized here, other systems based on multi-apertures receivers -exploiting receive diversity- have been widely considered as well. Such receivers conventionally require the combination of the signals detected by the distinct subapertures. The optical signals corresponding to each subaperture are then downconverted separately and can be processed digitally. The main drawback of such systems lies in their potential complexity as the number of required amplifiers, detectors and processing chains scales up when very high data rates are aimed. Minimizing the complexity of any signal processing method employed in order to mitigate the impact of turbulence in this framework constitue an interesting perspective. Recently, Belmonte and Kahn, [Belmonte and Kahn, 2018] determined optimal beams (stochastic eigenmodes) that might allow in the near future the implementation of adaptive multi-input multi-output signal processing. This would enable the compensation of fast fluctuations of both phase (and amplitude) in a potentially more efficient fashion than adaptive optics while drastically reducing the complexity of such systems.

- **A refinement of the simplified model based on experimental results.** Such an experimental confrontation would allow the enhancement of the channel model by taking into account phenomena not modeled in this work: the influence of continuous misalignments, possible vibrations, as well as the evolution of the conditions of turbulence along the line of sight. In that prospects, measurements campaigns are planned in the coming months involving LISA (the AO bench developed by ONERA) and OSIRIS (DLR's LEO satellite (see the introductory Section 1.2). The outcomes of such campaigns -for the models presented in this thesis- reside in the potential representativeness improvements regarding the aforementioned points. Eventually, such refinements will yield a channel model that covers all time scales (from the duration of the link -typically a few minutes- to the shortest time of the perturbations likely to be encountered (a few fractions of milliseconds)).

- Concerning the data reliability modeling as implemented in DREAM, one main feature merits further investigation: **the modeling of the convolutional time interleaver.** The effect of an uniform convolutional interleaver at the transmitter and the associated deinterleaver at the receiver has been emulated by uniformly averaging the instantaneous

mutual information over a sliding window whose size corresponds to the depth of the simulated interleaver. The term uniform presumes that the interleaving process is perfect: the interleaved codeword experiences every fading state comprised in the sliding window. In practice this condition is not always ensured when considering very large interleaving depths. To remedy to such a limitation, non-uniform averaging sliding window should be implemented and its effect carefully analyzed.

- Finally, using the collection of models presented in this manuscript, the work undertaken in the framework of **jointly optimizing adaptive optics and coding techniques could be deepened and pursued by considering the impact of distinct allocations of the AO error budget.** Throughout the results detailed in this thesis, an equal proportion of spatial (fitting plus aliasing) and temporal error was assumed. At a fixed total residual variance and from the overall system-level, it might be interesting to investigate the potential benefits of optimizing the AO error budget with respect to relevant performance and quality of service metrics such as those identified in this thesis (Mutual information, PER, throughput). The prospects of such an optimization are for instance the possible relaxation of the load imposed upon the AO real-time computer, hence making it available for updating the command matrix according to a dynamical model of the turbulence in a Kalman filtering approach [Petit et al., 2004] that is fundamentally more efficient than the classical minimum mean square error solution (see 3.2.2.5).

6 SYNTHÈSE EN FRANÇAIS

Contents

6.1 Introduction et contexte

Au cours des dernières décennies, les technologies de l'information et des télécommunications ont connu une expansion considérable. En conséquence, les besoins en capacité et en bande passante des utilisateurs finaux des systèmes sans fil ont considérablement augmenté. Les systèmes sans fil conventionnels basés sur des technologies radiofréquence (RF) sembleront bientôt atteindre leurs limites fondamentales. Ainsi, le désir de passer des fréquences RF aux fréquences optiques s'est naturellement manifesté il y a plusieurs années.

De nos jours, les transmissions optique sans fil sont considérées comme une technologie viable pour la prochaine génération de systèmes de télécommunication à large bande. En raison de plusieurs de leurs avantages inhérents sur les systèmes de télécommunication RF, les liens optiques sont envisagés pour une variété d'applications et dans le cadre de divers scénarios comme le montre la figure 1.1. Théoriquement, plusieurs réseaux optiques sans fil impliquant des liaisons satellites, terrestres et même intérieures pourraient être intégrés et exploités dans leur ensemble en les connectant par exemple au réseau fibré. Ce faisant, les liaisons optiques sans fil pourraient géographiquement étendre les caractéristiques de haute capacité de ce dernier à des zones géographiques autrement difficiles à atteindre.

Dans le cadre de transmissions de données à partir de charges utiles de satellites scientifiques ou de défense, les liaisons optiques constituent une alternative tout aussi prometteuse. Comme le montre la figure 1.2, les plates-formes spatiales équipées de capteurs d'observation de la Terre font face à une croissance exponentielle de la quantité de données qu'elles peuvent rassembler et qui ont besoin être transmis aux stations au sol souvent dans un délai court. Le tableau 1.1 montre l'évolution attendue de la quantité d'informations générées par les systèmes d'imagerie tels que les radars à synthèse d'ouverture (SAR) et les imageurs hyperspectraux en 2020. Il met donc en évidence la demande de transmission à très haut débit depuis des satellites en orbite terrestre vers des stations terrestres dans un proche avenir.

Enfin, un troisième type de scénario qui devrait bénéficier de tels liens optiques concerne l'exploration de l'espace lointain ("Deep Space"). Les engins spatiaux, ou sondes, impliqués dans de telles missions d'exploration ont généralement des ressources très limitées car la taille, le poids et la puissance ("SWaP" en anglais) des équipements embarqués sont sévèrement restreints. Les transmissions optiques depuis ces sondes pourraient réduire considérablement les SWaP de leurs systèmes de communication. En outre, il est intéressant de noter qu'aux États-Unis, l'utilisation potentielle de liaisons optiques dans le cadre de l'exploration de l'espace lointain a été l'un des principaux supports financiers pour le développement de liaisons optiques par satellite [Boroson and Robinson, 2015, Cesarone et al., 2011].

6.1.1 Avantages des liens optiques en espace libre

Les avantages offerts par de tels liens optiques découlent essentiellement de la grande directivité du faisceau émis et de la très haute fréquence de la porteuse. Parmi ces avantages, dont certains on déjà été cités, on trouve:

- **Réduction globale des SWaP**: environ la moitié de la masse et de la consommation d'énergie des systèmes RF typiques, ainsi que près du dixième du diamètre d'une antenne RF typique.
- **Bande passante élevée**: la quantité d'information transmise par un système de communication est directement liée à la bande passante de la porteuse modulée. C'est habituellement une fraction de la fréquence de la porteuse. Dans la bande C, la fréquence de la porteuse est d'environ 192 THz [Yoichi Maeda, 2009]
- **Spectre non régulé**: pour éviter des interférences néfastes entre distinctes porteuses adjacentes les liaisons RF sont régulées et contrôlées par des agences internationales (ITU), régionales (CEPT en Europe) et nationales (ANFR et Arcep en France). La directivité accrue des transmissions optiques réduit de telles interférences. Par conséquent, il n'y a pas de restrictions réglementaires pour l'utilisation des bandes optiques.
- **Sécurité accrue**: compte tenu de leur directivité élevée et de leur immunité aux interférences électromagnétiques, les liaisons optiques ont une faible probabilité d'être interceptées ou bloquées.

6.1.2 Défis liés à la mise en œuvre des liens optiques en espace libre

Afin de bénéficier des avantages précédemment décrits, les liaisons optiques descendantes (Satellite vers le sol) doivent surmonter plusieurs inconvénients. La fréquence élevée de la porteuse induit plusieurs obstacles qui peuvent affecter la fiabilité et la disponibilité de ces liaisons. Trois problèmes majeurs consistent en:

- L'impact de **phénomènes atmosphériques**, tels que le brouillard, le brouillard et la turbulence atmosphérique qui affectent grandement la propagation de l'onde optique à travers l'atmosphère
- La haute directivité du faisceau transmis qui complique **l'acquisition et le pointage**
- L'indisponibilité potentielle du système causée par **la couverture nuageuse**

Pour contrer les indisponibilités liées à la couverture nuageuse, certaines données météorologiques peuvent être exploitées pour mettre en œuvre de la diversité de site (réseau géographique

optimisé de plusieurs stations terrestres optiques [Lacoste et al., 2011, Poulenard et al., 2014, Fuchs et al., 2017, Poulenard et al., 2017]). L'utilisation de mémoires tampons à bord du satellite, en conjonction avec certains protocoles de transmission de données [Clare and Miles, 2016] permettent également d'améliorer la disponibilité du système.

L'atténuation des erreurs dynamiques liées à un pointage imparfait requiert généralement la stabilisation de la ligne de visée nécessitant une référence de pointage appropriée (balise) à l'emplacement du récepteur ainsi que certains systèmes d'asservissement de manière à, par exemple, détecter et corriger les effets liés aux vibration du terminal de vol [Kaushal et al., 2017].

Les phénomènes atmosphériques limitent quant à eux les performances du système en provoquant des distorsions du faisceau transmis. Les gaz et les particules constitutifs de l'atmosphère provoquent une absorption et une diffusion qui induisent principalement l'atténuation de l'onde optique (voir section 2.2.1.1). Les variations de température et d'humidité le long de la ligne de visée provoquent des variations spatio-temporelles de l'indice de réfraction de l'air communément appelées turbulence optique atmosphérique. De telles fluctuations de l'indice de réfraction sont à l'origine des fluctuations de l'amplitude et de la phase du faisceau incident (voir section 2.2.2).

Afin d'atteindre les très haut débits visés, les futures systèmes de communications optiques en espace libre se devront de tirer partie des technologies développées pour les communications fibrées telles que les amplificateurs à fibre dopée à l'erbium (EDFA). Comme mentioné plus haut un intérêt supplémentaire réside également dans l'objectif d'intégrer à terme les liens sans fils aux réseaux terrestres fibrés [Arimoto et al., 2012]. Dans ce cas, la turbulence optique provoquera l'évanouissement du signal reçu en raison des fluctuations affectant à la fois la puissance collectée par le télescope de réception et l'efficacité de couplage du faisceau incident dans de telles composants fibres (voir section 2.4). Pour atténuer ces évanouissements, les systèmes en cours de développement envisagent généralement deux types de techniques de compensation:

- Des techniques de compensation physique telles que l'optique adaptative agissant sur le faisceau optique reçu
- Un ensemble de techniques numériques comprenant des entrelaceurs et un codage canal qui agit sur le signal télécom numérisé.

Dans cette thèse, l'accent est mis sur l'étude des effets délétères liés à la turbulence atmosphérique et à la compensation de ces derniers au travers de l'analyse conjointe de deux types de techniques: optique adaptative (OA) et mécanismes de fiabilité numériques (codage et entrelacement).

6.2 Compensation des effets de la turbulence sur la fiabilité des liens optiques

6.2.1 Compensation physiques des évanouissements: optique adaptative

Les évanouissements du signal détecté liés à la dégradation de l'efficacité d'injection du flux incident dans une fibre optique mono-mode (FOM) peuvent être spécifiquement atténués en utilisant un système d'OA. Le principe de fonctionnement de l'OA est détaillé dans la Section 3.2. Celle-ci permet de compenser en temps réel les fluctuations de phase de l'onde incidente dues à la turbulence atmosphérique.

Cependant, les liaisons satellite-sol, en particulier à partir des satellites LEO, représentent un cadre d'application difficile pour l'OA en raison de conditions opérationnelles compliquées (évolution rapide de la turbulence et régime de forte turbulence à basse élévation). Par conséquent, ce n'est que récemment que les premières démonstrations d'OA pour les liaisons descendantes optiques ont été rapportées (voir la section 1.2.1 et la table 1.3 pour plus de détails). D'un point de vue expérimental, il reste encore beaucoup à faire pour comprendre les limites des performances de l'OA en pratique, et en particulier son impact sur l'efficacité du couplage dans les FOM.

En plus des distorsions de phase, la turbulence atmosphérique provoque des fluctuations du log-amplitude de l'onde perturbée communément appelés scintillation. L'impact de la scintillation est plus important à mesure que la distance de propagation dans l'atmosphère augmente (voir par exemple Eq. (2.38)). Par conséquent, elle affecte potentiellement gravement les liaisons descendantes des satellites LEO notamment à très basse élévation. En pratique, l'effet lié à la scintillation peut être atténuée en augmentant l'ouverture du télescope récepteur (effet communément appelé "aperture averaging" dans la littérature anglophone). Cependant, puisque la variance du front d'onde turbulent augmente comme $\left(\frac{D_{Rx}}{r_0}\right)^{5/3}$, avec r_0 indiquant le paramètre Fried (voir Eq. (2.16)) et D_{Rx} le diamètre du télescope, augmenter ce dernier sans améliorer le système d'OA peut intensifier les pertes d'injection. A l'inverse, en supposant une ouverture de diamètre fixe, la scintillation résiduelle peut-être vue comme imposée au récepteur et le niveau de performance de l'OA conduit à deux cas limites:

- Une mauvaise correction entraîne des évanouissements principalement causés par des pertes d'injection
- A l'inverse, un très bon système d'OA permet des évanouissements limités par la scintillation

Ceci est illustré par la Fig. 1.3. A noter que le second cas limite pourrait ne pas être réalisable pour une grande ouverture - telle que requise par les liaisons GEO-sol - si ce n'est au prix d'un système d'OA plus complexe comprenant des composants potentiellement non-disponibles sur étagère.

L'évaluation simple de tels compromis est rendue possible grâce aux outils analytiques développés et validés au cours de cette thèse.

6.2.2 Techniques de compensation numériques des évanouissements: entrelacement et codage

Les mécanismes de fiabilité de données que constituent l'entrelacement et le codage canal peuvent permettre d'assouplir les spécifications et le coût des systèmes d'OA lorsqu'une stabilité d'injection très élevée est requise. Pour être efficace, ces techniques doivent néanmoins être adaptées aux particularités du canal atmosphérique optique. Ce dernier est caractérisé par des fluctuations qui sont lentes comparées à la période symbole correspondant aux débits visés. Des erreurs par paquets ("burst") qui limitent les performances des codes correcteurs d'erreurs sont donc caractéristiques du canal optique en espace libre. Pour surmonter cette distribution d'erreurs par paquet on a typiquement recourt à l'émission l'entrelacement préalable des symboles. Ces entrelaceurs, après avoir désassemblé chaque mot de code, étalent leurs éléments individuels avec un intervalle temporel comparable à une durée caractéristique du canal à évanouissement, comme illustré sur la figure 1.4.

Néanmoins, en plus de la latence intrinsèquement introduite, un tel processus d'entrelacement peut tout simplement conduire à des tailles de mémoire potentiellement très élevées en raison du temps de cohérence du canal (voir Section 2.4.1). Ainsi, pour pallier les inconvénients induits par les entrelaceurs, des mécanismes de fiabilité aux différentes couches de la pile de communication doivent être envisagés. Sur n'importe quel canal corrélé, en étudiant les interactions entre ces mécanismes de fiabilité au niveau de différentes couches, on peut trouver des stratégies de codage qui permettent de meilleures performances globales. Dans le cadre des transmissions optiques par satellite, une telle approche a été envisagée dans [Henniger and Gonzalez, 2006, Henniger, 2006, Fuchs et al., 2007, Henniger, 2007].

Dans cette thèse, un schéma de codage similaire est proposé. Un code correcteur d'erreur combiné à de l'entrelacement symboles au niveau de la couche physique sont associés à un code à effacement combiné à un entrelacement paquets au niveau des couches supérieures.

Les avantages liés à une telle stratégie sont discutés en détail dans la section 4.4.

6.2.3 Problématique liée au dimensionnement conjoint

L'objectif global de cette thèse est l'étude de la fiabilité des liaisons de communication optique satellite-sol en considérant l'apport conjoint d'une correction par OA partielle et le schéma de codage décrit plus haut.

Pour être efficace, codage et entrelacement doivent être adaptés au canal. L'optimisation du système global requiert donc une connaissance précise des propriétés statistiques et temporelles des évanouissements du signal détecté qui sont évidemment liés aux variations instantanées du flux couplé dans la FOM après correction par OA. Si ce n'est expérimentalement, ces propriétés statistiques peuvent généralement être obtenues au moyen de simulations bout-en-bout qui sont néanmoins très longues ou complexes à mettre en œuvre lorsqu'une bonne représentation des phénomènes physiques impliqués est requise. De plus, comme illustré par la figure 1.6 un large éventail de paramètres d'entrée définissant plusieurs cas d'application d'intérêt doivent être considérés. L'optimisation future et efficace du système global constitue donc un problème complexe.

Au cours de cette thèse, plusieurs outils de modélisation simplifiés et développements analytiques spécifiques ont donc été validés et utilisés. Ils visent à rendre une telle optimisation des futures systèmes pratique tout en permettant l'étude approfondies des interactions entre OA et codage de part leur précision.

La figure 1.5 présente un aperçu des différents modules de simulation implémentés, améliorés et utilisés à cette fin. Ils sont regroupés en quatre catégories:

- la modélisation de la propagation optique dans l'atmosphère
- la modélisation de la correction partielle par optique adaptative
- la modélisation du sous-système de communication (couche physique)
- la modélisation des mécanismes de fiabilité de données (entrelacement et codage au niveau couche physique et couches hautes)

6.3 Contributions principales de la thèse

La première partie de cette thèse a porté sur l'étude et la caractérisation du flux couplé dans une FOM après correction par OA partielle. Cette étude s'est appuyé sur un modèle simplifié tenant compte des erreurs intrinsèques prédominantes caractérisant un système d'OA partielle dans le cadre des liaisons descendantes (SAOST). Prenant en compte à la fois l'effet de la scintillation et des distorsions de phase sur l'efficacité du couplage, ce modèle a été

validé par simulations bout-en-bout pour des scénarios GEO et LEO (élévations supérieures à 20 deg).

S'appuyant sur les hypothèses sous-adjacentes à ce modèle simplifié, des expressions analytiques originales caractérisant les propriétés statistiques (distribution de probabilité) et temporelles (autocovariance) du flux couplé partiellement corrigé ont été développées. Elles permettent de facilement calculer des caractéristiques temporelles pertinentes telles que durées moyenne, maximale et minimale des évanouissements du signal. Celles-ci sont nécessaire à l'optimisation de la profondeur des entrelaceurs. Ces expressions ont été comparées et validées par des simulations de bout-en-bout. Cette comparaison a souligné l'intérêt pour le modèle analytique développé. Ce dernier fournit des résultats précis tout en évitant les longues et complexes simulations. Enfin, ces résultats ont permis d'inférer sur l'impact de différentes performances d'OA sur de telles caractéristiques temporelles.

Cette étude de cas menée pour un scénario GEO et LEO a mis en lumière l'importance de considérer les résidus de correction aux bas ordres. Elle a également mis en évidence l'importance de ne pas tenir compte uniquement de métriques de performance moyenne, tels que la variance résiduelle ou l'atténuation du flux couplé moyen, communément utilisés dans le cadre d'applications d'astronomie ou d'imagerie.

La seconde partie de cette thèse a porté sur l'étude des avantages et des limites de l'entrelacement et du codage aussi bien sur les couches physiques que sur les couches hautes. Afin de fournir des résultats précis, l'amélioration d'un simulateur couche physique (SIMCOP) a été entreprise. L'accent a été mis sur l'étude de systèmes à détection directe pré-amplifiée (modulation OOK) et à détection différentiellement cohérente (modulation DBPSK).

L'utilisation d'entrelaceurs pour lutter contre les paquets d'erreur augmente la complexité du système, car ils nécessitent généralement l'utilisation d'un matériel dédié. Afin d'étudier les performances d'un système de codage multicouche permettant de potentiellement réduire une telle contrainte, un simulateur dédié a été développé (DREAM). Il permet d'optimiser l'utilisation des ressources du système global (mémoire, puissance, redondance) en tenant compte d'un niveau de performance ciblé.

A titre d'exemple d'utilisation de ce simulateur, un scénario propre au transfert de données depuis un satellite LEO dont la mémoire est considérée comme une ressource limitée a été présenté. L'analyse qui en a découlé a mis en évidence les bénéfices potentiels liés à l'étude conjointe de l'OA, de l'entrelacement et du codage dans une approche multicouche. Contrairement aux codes correcteur d'erreurs et à l'entrelacement implémentés sur la couche physique, les code à effacement et entrelaceurs couches hautes, bien que moins efficaces, peuvent être implémentés en logiciel. Cela implique qu'ils peuvent être conçus en utilisant des ressources qui ne sont pas exclusivement destinées à cet effet (par exemple en utilisant la

RAM du satellite) tandis que les techniques couche physique nécessitent généralement un matériel supplémentaire dédié (e.g. ASIC). Par conséquent, les mécanismes de fiabilité des données au niveau des couches hautes contribuent à réduire la complexité du terminal bord au prix néanmoins d'un système d'OA plus performant. L'ensemble des modèles développés au cours de la thèse permettent de trancher de tels compromis.

6.4 Perspectives

Malgré la précision avérée des divers développements réalisés tout au long de ce travail, certaines hypothèses méritent d'être soulignées en ce qui concerne notamment la modélisation des fluctuations du flux couplé après correction par OA. À cet égard, les points suivants constituent des perspectives intéressantes et méritent d'être approfondis:

- **L'impact des structures spatiales du log-amplitude plus petites que la pupille sur les fluctuations du flux couplé.** Dans des conditions de forte turbulence, la moyenne des fluctuations du log-amplitude a un impact particulièrement perceptible dans les scénarios LEO-sol caractérisés par un moyennage des effets de la scintillation moindre (diamètre pupillaire plus petit) combiné à des conditions de turbulence plus difficiles (basse élévation). Considérer des améliorations potentielles ou de nouveaux développements dans cette direction est nécessaire pour étendre le domaine de validité de SAOST aux très faibles élévations.

- **La modélisation de la détection du front d'onde dans des conditions de forte turbulence.** L'impact de la scintillation sur la détection du front d'onde n'a pas été pris en compte lors du développement du modèle d'OA simplifié. Cela peut donc également limiter sa validité dans le cas de liaisons descendantes à très basse élévation. L'intégration de développements analytiques à cet égard et l'étude plus approfondie de la précision de SAOST par une comparaison au modèle bout-en-bout (ou des résultats expérimentaux) dans ces régimes semble souhaitable. Pour affiner l'analyse, on pourrait considérer la dynamique limitée du capteur, le flux alloué à l'analyseur de front d'onde, la sensibilité des capteurs utilisés, ainsi que les algorithmes de calcul de pente.

  Dans un deuxième temps, il semble pertinent de se pencher sur des concepts de détection de front d'onde qui pourraient améliorer la robustesse d'un Shack-Hartmann classique dans des conditions turbulentes difficiles. Les limites du Shack-Hartmann résident principalement dans l'homogénéité requise de la distribution du flux sur la sous-pupille (voir les sections 3.2.3.7 et 3.2.1.1). Ainsi, étudier la possibilité de prendre en compte dynamiquement une telle distribution d'intensité dans le processus d'estimation de phase -en adaptant le modèle de formation de données (par exemple filtrer les mesures qui ne présentent pas un SNR satisfaisant)- pourrait constituer

une amélioration prometteuse. D'autres types de capteurs de front d'onde pourraient également être étudiés. Par exemple, en examinant les avantages des analyseurs plan focal, qui couplent phase et amplitude dans leur principe de mesure pourraient être une solution à ces limitations au détriment toutefois d'un coût de calcul élevé. Par conséquent, aujourd'hui, la mise en œuvre pratique de tels analyseurs nécessite que ces contraintes de calcul soient levées.

- **Un affinement du modèle simplifié basé sur des résultats expérimentaux.** Une telle confrontation expérimentale permettrait d'enrichir le modèle de canal de propagation caractérisant les système incluant un OA partielle en prenant en compte des phénomènes non modélisés dans ce travail: l'influence de désalignements continus, de possibles vibrations, ainsi que l'évolution des conditions de turbulence le long de la ligne de visée au cours du défilement. Dans ce cadre, des campagnes de mesures sont prévues dans les mois à venir impliquant LISA (le banc développé par l'ONERA) et OSIRIS (le satellite LEO du DLR (voir la section introductive 1.2). Les résultats issus de ces campagnes permettront d'accroître représentativité de SAOST en couvrant toutes les échelles de temps (de la durée du lien (typiquement quelques minutes) aux plus courtes perturbations susceptibles d'être rencontrées (quelques fractions de millisecondes)).

- Concernant la modélisation des mécanismes de fiabilité des données tels que ceux implémentés dans DREAM, une fonctionnalité principale mérite d'être explorée: **la modélisation de l'entrelaceur convolutif**. L'effet d'un entrelaceur convolutif uniforme et du désentrelaceur associé à la réception a été émulé en calculant une moyenne uniforme de l'information mutuelle instantanée sur une fenêtre glissante dont la taille correspond à la profondeur de l'entrelaceur simulé. Le terme uniforme présume que le processus d'entrelacement est parfait: le mot de code entrelacé subit tous les états d'évanouissement compris dans la fenêtre glissante. En pratique, cette condition n'est pas toujours assurée lorsqu'on considère de très grandes profondeurs d'entrelacement. Pour remédier à une telle limitation, une fenêtre glissante pondérée doit être considérée et son effet soigneusement analysé. Notons que cette implémentation servira aussi à simuler certains schémas d'entrelacement qui consistent à diviser un mot de code en plusieurs parties et à envoyer ces différentes parties avec des retards différents.

- Enfin, en utilisant l'ensemble des modèles présentés dans ce manuscrit, le travail entrepris dans le cadre de **l'optimisant conjointe d'OA et des techniques de codage pourrait être approfondi en considérant l'impact d'une allocation non équitable du budget d'erreur de l'OA**. L'ensemble des résultats présentés dans cette thèse sont caractéristiques d'une proportion égale d'erreur spatiale (fitting plus aliasing) et temporelle a été supposée. À variance résiduelle totale fixe, il pourrait être intéressant d'étudier les avantages potentiels de l'optimisation du budget d'erreur d'OA. Les perspectives d'une telle optimisation sont par exemple de pouvoir décontraindre la charge du calculateur

temps réel, le rendant ainsi disponible pour mettre à jour la matrice de commande selon un modèle dynamique de la turbulence dans une approche de filtrage de Kalman [Petit et al., 2004] considérée plus efficace que la solution plus commune détaillée dans 3.2.2.5.

List of publications

Peer-reviewed article

Canuet, L., Védrenne, N., Conan, J.-M., Petit, C., Artaud, G., Rissons, A., and Lacan, J. (2018). Statistical properties of single-mode fiber coupling of satellite-to-ground laser links partially corrected by adaptive optics. *J. Opt. Soc. Am. A*, 35(1):148–162.

International conference proceedings

Canuet, L., Vedrenne, N., Conan, J.-M., Artaud, G., Rissons, A., and Lacan, J. (October 2016). Evaluation of communication performance for adaptive optics corrected geo-to-ground laser links. *In International Conference on Space Optics*, volume 7685.

Canuet Lucien, Lacan Jérôme, Védrenne Nicolas, Géraldine Artaud, and Rissons Angélique,"Performance Evaluation of Coded Transmission for Adaptive-Optics Corrected Satellite-To-Ground Laser Links", in *proceedings of ICSOS (IEEE International Conference on Space Optical Systems and Applications)*, November 2017 – Naha, Okinawa, Japan

Canuet Lucien, Lacan Jérôme, Védrenne Nicolas, Géraldine Artaud, and Rissons Angélique, "Cross-layer optimization for adaptive-optics corrected satellite-to-ground laser links", in *proceedings of the 8th international symposium – OPTRO 2018 optronics in defense and security*, 6-8 February 2018, Paris

Bibliography

[Aalo et al., 2005] Aalo, V. A., Piboongungon, T., and Efthymoglou, G. P. (2005). Another look at the performance of mrc schemes in Nakagami-m fading channels with arbitrary parameters. *IEEE Transactions on Communications*, 53(12):2002–2005.

[Abahamid et al., 2004] Abahamid, A., Vernin, J., Benkhaldoun, Z., Jabiri, A., Azouit, M., and Agabi, A. (2004). Seeing, outer scale of optical turbulence, and coherence outer scale at different astronomical sites using instruments on meteorological balloons. *Astronomical Society of the Pacific*, 422:1123–1127.

[Ackerman et al., 2002] Ackerman, D., Johnson, J., Ketelsen, L., Eng, L., Kiely, P., and Mason, T. (2002). Chapter 12 - telecommunication lasers. In Kaminow, I. P., , and Li, T., editors, *Optical Fiber Telecommunications IV-A (Fourth Edition)*, Optics and Photonics, pages 587 – 665. Academic Press, Burlington, fourth edition edition.

[Adoul, 1974] Adoul, J. P. (1974). Error intervals and cluster density in channel modeling (corresp.). *IEEE Transactions on Information Theory*, 20(1):125–129.

[Aghajanzadeh and Uysal, 2010] Aghajanzadeh, S. and Uysal, M. (2010). Diversity-multiplexing trade-off in coherent free-space optical systems with multiple receivers. *IEEE/OSA Journal of Optical Communications and Networking*, 2(12):1087–1094.

[Agrawal, 2011] Agrawal, G. P. (2011). *Fiber-Optic Communication Systems*. John Wiley & Sons, Inc.

[Alexander, 1997] Alexander, S. B. (1997). *Optical communication receiver design / Stephen B. Alexander*. SPIE Optical Engineering Press ; Institution of Electrical Engineers Bellingham, Wash., USA : London, UK.

[Alonso et al., 2004] Alonso, A., Reyes, M., and Sodnik, Z. (2004). Performance of satellite-to-ground communications link between artemis and the optical ground station. *Proc.SPIE*, 5572:5572 – 5572 – 12.

[Andrews and Phillips, 2005] Andrews, L. and Phillips, R. (2005). *Laser Beam Propagation through Random Media*. SPIE Optical Engineering Press, Wash.

[Andrews et al., 1999] Andrews, L. C., Phillips, R. L., Hopen, C. Y., and Alhabash, M. A. (1999). Theory of optical scintillation. *J. Opt. Soc. Am. A*, 16(7):1417–1429.

[Ansari et al., 2012] Ansari, I. S., Yilmaz, F., Alouini, M. S., and Kucur, O. (2012). On the sum of gamma random variates with application to the performance of maximal ratio combining over Nakagami-m fading channels. In *2012 IEEE 13th International Workshop on Signal Processing Advances in Wireless Communications (SPAWC)*, pages 394–398.

[Arimoto et al., 2012] Arimoto, Y., Chiuchiarelli, A., Corsini, R., Presi, M., and Ciaramella, E. (2012). Carrier class availability in a transparent 1.25 gb/s free space optical communication link over 320 m. In *2012 International Workshop on Optical Wireless Communications (IWOW)*, pages 1–3.

[Arimoto et al., 1995] Arimoto, Y., Toyoshima, M., Toyoda, M., Takahashi, T., Shikatani, M., and Araki, K. (1995). Preliminary result on laser communication experiment using (ets-vi). *Proc.SPIE*, 2381:2381 – 2381 – 8.

[Arnold, 2014] Arnold, F. (2014). Ground receiver unit for optical communication between ladee spacecraft and esa ground station. *Proc. of SPIE*, 8971.

[Arnold et al., 2014] Arnold, F., Buchheim, K., and Kudielka, K. (Zurich March 14 2014). Ccsds sls-opt ruag space-to-ground link. *RUAG Space*.

[Arnon et al., 2012] Arnon, S., Barry, J., Karagiannidis, G., Schober, R., and Uysal, M. (2012). *Advanced Optical Wireless Communication Systems*. Cambridge University Press, New York, NY, USA, first edition edition.

[Asghar and Liu, 2010] Asghar, R. and Liu, D. (2010). Multimode flex-interleaver core for baseband processor platform. 2010.

[Babcock, 1953] Babcock, H. W. (1953). The possibility of compensating astronomical seeing. *The Publications of the Astronomical Society of the Pacific*, 65:229.

[Barron and Boroson, 2006] Barron, R. J. and Boroson, D. M. (2006). Analysis of capacity and probability of outage for free-space optical channels with fading due to pointing and tracking error. *Proc.SPIE*, 6105:6105 – 6105 – 12.

[Bartlett, 1946] Bartlett, M. S. (1946). On the theoretical specification and sampling properties of autocorrelated time-series. *Supplement to the Journal of the Royal Statistical Society*, 8(1):27–41.

[Belmonte and Kahn, 2011] Belmonte, A. and Kahn, J. (2011). Field conjugation adaptive arrays in free-space coherent laser communications. *IEEE/OSA Journal of Optical Communications and Networking*, 3(11):830–838.

[Belmonte and Kahn, 2016] Belmonte, A. and Kahn, J. M. (2016). *Satellite Downlink Coherent Laser Communications*, pages 325–343. Springer International Publishing, Cham.

[Belmonte and Kahn, 2018] Belmonte, A. and Kahn, J. M. (2018). Approaching fundamental limits to free-space communication through atmospheric turbulence. volume 10559, pages 10559 – 10559 – 7.

[Bendat and Piersol, 2012] Bendat, J. S. and Piersol, A. G. (2012). *Stationary Random Processes*, pages 109–171. John Wiley & Sons, Inc.

[Benedetto and Bosco, 2005] Benedetto, S. and Bosco, G. (2005). *Channel Coding for Optical Communications*, pages 63–78. Springer US, Boston, MA.

[Berger et al., 2008] Berger, C. R., Zhou, S., Wen, Y., Willett, P., and Pattipati, K. (2008). Optimizing joint erasure- and error-correction coding for wireless packet transmissions. *IEEE Transactions on Wireless Communications*, 7(11):4586–4595.

[Bohmer et al., 2012] Bohmer, K., Gregory, M., Heine, F., Kämpfner, H., Lange, R., Lutzer, M., and Meyer, R. (2012). Laser communication terminals for the european data relay system. *Proc.SPIE*, 8246:8246 – 8246 – 7.

[Boivin and Pendock, 1999] Boivin, L. and Pendock, G. J. (1999). Receiver sensitivity for optically amplified rz signals with arbitrary duty circle. In *Optical Amplifiers and their Applications*, page ThB4. Optical Society of America.

[Boroson and Robinson, 2015] Boroson, D. M. and Robinson, B. S. (2015). *The Lunar Laser Communication Demonstration: NASA's First Step Toward Very High Data Rate Support of Science and Exploration Missions*, pages 115–128. Springer International Publishing, Cham.

[Boroson et al., 2014] Boroson, D. M., Robinson, B. S., and et. al., D. V. M. (2014). Overview and results of the lunar laser communicaiton demonstration. *Proc. of SPIE*, 8971.

[Boroson et al., 2009] Boroson, D. M., Scozzafava, J. J., Murphy, D. V., Robinson, B. S., and Lincoln, M. I. T. (2009). The lunar laser communications demonstration (LLCD). In *2009 Third IEEE International Conference on Space Mission Challenges for Information Technology*, pages 23–28.

[Bottacchi, 2009] Bottacchi, S. (2009). *Noise Principles in Optical Fiber Communication*, pages 31–116. John Wiley & Sons, Ltd.

[Broersen, 1998] Broersen, P. M. T. (1998). Estimation of the accuracy of mean and variance of correlated data. In *IMTC/98 Conference Proceedings. IEEE Instrumentation and Measurement Technology Conference. Where Instrumentation is Going (Cat. No.98CH36222)*, volume 1, pages 36–41 vol.1.

[Brown, 1997] Brown, W. C. (1997). Optimum thresholds for optical on-off keying receivers operating in the turbulent atmosphere. *Proc.SPIE*, 2990.

[Brown, 1966] Brown, Jr., W. P. (1966). Validity of the Rytov Approximation in Optical Propagation Calculations. *J. Opt. Soc. Am. A*, 56:1045–+.

[Bufton, 1973] Bufton, J. L. (1973). Comparison of vertical profile turbulence structure with stellar observations. *Appl. Opt.*, 12:1785–1793.

[Canuet et al., 2016] Canuet, L., Vedrenne, N., Conan, J.-M., Artaud, G., Rissons, A., and Lacan, J. (October 2016). Evaluation of communication performance for adaptive optics corrected geo-to-ground laser links. In *International Conference on Space Optics*, volume 7685.

[Canuet et al., 2018] Canuet, L., Védrenne, N., Conan, J.-M., Petit, C., Artaud, G., Rissons, A., and Lacan, J. (2018). Statistical properties of single-mode fiber coupling of satellite-to-ground laser links partially corrected by adaptive optics. *J. Opt. Soc. Am. A*, 35(1):148–162.

[Caplan, 2007] Caplan, D. O. (2007). Laser communication transmitter and receiver design. *Journal of Optical and Fiber Communications Reports*, 4(4):225–362.

[Caplan and Atia, 2001] Caplan, D. O. and Atia, W. A. (2001). A quantum-limited optically-matched communication link. In *OFC 2001. Optical Fiber Communication Conference and Exhibit. Technical Digest Postconference Edition (IEEE Cat. 01CH37171)*, volume 1, pages MM2–MM2.

[Cazaubiel et al., 2006] Cazaubiel, V., Planche, G., Chorvalli, V., Le Hors, L., Roy, B., Giraud, E., Vaillon, L., Carré, F., and Decourbey, E. (2006). Lola: A 40000 km optical link between an aircraft and a geostationary satellite. 621:87.

[CCSDS, 2002] CCSDS (2002). Recommendation for space data system standards telemetry channel coding ccsds 101.0-b-6. *Blue Book*.

[CCSDS, 2011] CCSDS (2011). Recommendation for space data system standards tm synchronization and channel coding ccsds 131.0-b-2. *Blue Book*.

[Cesarone et al., 2011] Cesarone, R. J., Abraham, D. S., Shambayati, S., and Rush, J. (2011). Deep-space optical communications. In *2011 International Conference on Space Optical Systems and Applications (ICSOS)*, pages 410–423.

[Cha, 2007] Cha, S. (2007). Comprehensive survey on distance/similarity measures between probability density functions. *International Journal of Mathematical Models and Methods in Applied Sciences*, 1(4):300–307.

[Chan and Conradi, 1997] Chan, B. and Conradi, J. (1997). On the non-gaussian noise in erbium-doped fiber amplifiers. *Journal of Lightwave Technology*, 15(4):680–687.

[Chauvet et al., 2010] Chauvet, W., Amiot-Bazile, C., and Lacan, J. (2010). Prediction of performance of the dvb-sh system relying on mutual information. In *2010 5th Advanced Satellite Multimedia Systems Conference and the 11th Signal Processing for Space Communications Workshop*, pages 413–420.

[Chauvet et al., 2012] Chauvet, W., Lacan, J., Amiot-Bazile, C., Lacoste, F., and Ros, B. (2012). Physical layer dvb-sh performance prediction based on mutual information. *International Journal of Satellite Communications and Networking*, 30(5):193–211.

[Churnside and Clifford, 1987] Churnside, J. H. and Clifford, S. F. (1987). Log-normal Rician probability-density function of optical scintillations in the turbulent atmosphere. *J. Opt. Soc. Am. A*, 4:1923–1930.

[Clare and Miles, 2016] Clare, L. and Miles, G. (2016). Deep space optical link arq performance analysis. In *2016 IEEE Aerospace Conference*, pages 1–11.

[Clark and Cain, 1981] Clark, G. C. and Cain, J. B. (1981). *Error-Correction Coding for Digital Communications*. Perseus Publishing.

[Clifford,] Clifford, S.-F. *The classical theory of wave propagation in a turbulent medium*, pages 9–43.

[Clifford et al., 1974] Clifford, S. F., Ochs, G. R., and Lawrence, R. S. (1974). Saturation of optical scintillation by strong turbulence. *J. Opt. Soc. Am. A*, 64:148–154.

[Conan, 1994] Conan, J.-M. (1994). *Etude de la correction partielle en optique adaptative*. PhD thesis, Universite Paris XI Orsay.

[Conan et al., 1995] Conan, J.-M., Rousset, G., and Madec, P.-Y. (1995). Wave-front temporal spectra in high-resolution imaging through turbulence. *J. Opt. Soc. Am. A*, 12.

[Conradi, 2002] Conradi, J. (2002). Chapter 16 - bandwidth-efficient modulation formats for digital fiber transmission systems. In Kaminow, I. P. and Li, T., editors, *Optical Fiber Telecommunications IV-B (Fourth Edition)*, Optics and Photonics, pages 862 – 901. Academic Press, Burlington, fourth edition edition.

[Corrsin, 1951] Corrsin, S. (1951). On the spectrum of isotropic temperature fluctuations in an isotropic turbulence. *Journal of Applied Physics*, 22(4):469–473.

[Couch, 2000] Couch, II, L. W. (2000). *Digital and Analog Communication Systems*. Prentice Hall PTR, Upper Saddle River, NJ, USA, 6th edition.

[Courtade and Wesel, 2011] Courtade, T. A. and Wesel, R. D. (2011). Optimal allocation of redundancy between packet-level erasure coding and physical-layer channel coding in fading channels. *IEEE Transactions on Communications*, 59(8):2101–2109.

[Cover and Thomas, 2006] Cover, T. M. and Thomas, J. A. (2006). *Elements of Information Theory (Wiley Series in Telecommunications and Signal Processing)*. Wiley-Interscience.

[Dai and Mahajan, 2007] Dai, G. and Mahajan, V. N. (2007). Nonrecursive determination of orthonormal polynomials with matrix formulation. *Optics Letters*, 32(1):74–76.

[Dai and Mahajan, 2008] Dai, G. and Mahajan, V. N. (2008). Orthonormal polynomials in wavefront analysis: error analysis. *Applied Optics*, 40(19):3433–3445.

[Derickson, 1998] Derickson, D. (1998). *Fiber Optic Test and Measurement*. Hewlett-Packard professional books. Prentice Hall PTR.

[Dessenne, 1998] Dessenne, C. (1998). *Commande modale et prédictive en Optique Adaptative*. PhD thesis, Université de Paris VII.

[Dessenne et al., 1998] Dessenne, C., Madec, P. Y., and Rousset, G. (1998). Optimization of a predictive controller for closed-loop adaptive optics. *Appl. Opt.*, 37:4623–4633.

[Desurvire, 1994] Desurvire, E. (1994). *Erbium-doped fiber amplifiers : principles and applications / Emmanuel Desurvire*. Wiley New York.

[Djordjevic et al., 2014] Djordjevic, I., Ryan, W., and Vasic, B. (2014). *Optical Channel Capacity*. Springer Publishing Company, Incorporated.

[Dreischer et al., 2014] Dreischer, T., Thieme, B., and Buchheim, K. (2014). Functional system verification of the optel laser downlink system for small satellites in leo. *Proc. International Conference on Space Optical Systems and Applications (ICSOS) 2014*.

[Drobinski et al., 1998] Drobinski, P., Brown, R. A., Flamant, P. H., and et al. (1998). Evidence of Organized Large Eddies by Ground-Based Doppler Lidar, Sonic Anemometer and Sodar. *Boundary-Layer Meteorology*, 88:343–361.

[Edwards and Fletcher, 2013] Edwards, B. L. and Fletcher, A. (2013). Nasa's laser communications relay demonstration project. In *Advanced Solid-State Lasers Congress*, page LM3B.4. Optical Society of America.

[Edwards et al., 2012] Edwards, B. L., Israel, D., Wilson, K., Moores, J., and Fletcher, A. (2012). Overview of the laser communications relay demonstraiton project. *Proc. International Conference on Space Optical Systems and Applications (ICSOS) 2012*.

[Efthymoglou and Aalo, 2008] Efthymoglou, G. and Aalo, V. (2008). Performance of rake receivers in Nakagami fading channel with arbitrary fading parameters. *Electronics letters*, 31(18):1610–1612.

[Epple, 2010] Epple, B. (2010). Simplified channel model for simulation of free-space optical communications. *J. Opt. Commun. Netw.*, 2(5):293–304.

[Esposito et al., 2000] Esposito, S., Feeney, O., and Riccardi, A. (2000). Laboratory test of a pyramid wavefront sensor. *Proc.SPIE*, 4007.

[Fante, 1975] Fante, R. (1975). Electromagnetic beam propagation in turbulent media. *Proc. of the IEEE*, 63(12):1669–1692.

[Fidler et al., 2010] Fidler, F., Knapek, M., Horwath, J., and Leeb, W. R. (2010). Optical communications for high-altitude plat-forms. *Journal of Selected Topics in Quantum Electronics*, 16(5).

[Fischer et al., 2017a] Fischer, E., Berkefeld, T., Feriencik, M., Feriencik, M., Kaltenbach, V., Soltau, D., Adolph, P., Czichy, R., Kunde, J., Heine, F., Saucke, K., Meyer, R., Richter, I., and Sodnik, Z. (2017a). Use of adaptive optics in ground stations for high data rate satellite-to-ground links. *Proc.SPIE*, 10562.

[Fischer et al., 2017b] Fischer, E., Feriencik, M., Kudielka, K., Dreischer, T., Soltau, D., Kunde, J., Czichy, R., Armengol, J. M. P., and Sodnik, Z. (2017b). (invited) upgrade of esa optical ground station with adaptive optics for high data rate satellite-to-ground links. In *2017 IEEE International Conference on Space Optical Systems and Applications (ICSOS)*.

[Flatté et al., 1994] Flatté, S. M., Bracher, C., and Wang, G. (1994). Probability-density functions of irradiance for waves in atmospheric turbulence calculated by numerical simulation. *J. Opt. Soc. Am. A*, 11:2080–2092.

[Flatté et al., 1993] Flatté, S. M., Wang, G., and Martin, J. (1993). Irradiance variance of optical waves through atmospheric turbulence by numerical simulation and comparison with experiment. *J. Opt. Soc. Am. A*, 10:2363–2370.

[Forestieri, 2000] Forestieri, E. (2000). Evaluating the error probability in lightwave systems with chromatic dispersion, arbitrary pulse shape and pre- and postdetection filtering. *Journal of Lightwave Technology*, 18(11):1493–1503.

[Fried, 1966] Fried, D. L. (1966). Optical resolution through a randomly inhomogeneous medium for very long and very short exposures. *J. Opt. Soc. Am.*, 56(10):1372–1379.

[Fried, 2001] Fried, D. L. (2001). Adaptive optics wave function reconstruction and phase unwrapping when branch points are present. *Optics Communications*, 200:43–72.

[Fried and Vaughn, 1992] Fried, D. L. and Vaughn, J. L. (1992). Branch cuts in the phase function. *Appl. Opt.*, 31:2865–2882.

[Friis, 1946] Friis, H. T. (1946). A note on a simple transmission formula. *Proceedings of the IRE*, 34(5):254–256.

[Fuchs et al., 2007] Fuchs, C., Henniger, H., Epple, B., Giggenbach, D., Amirfeiz, M., Jentile, M., Nepi, G. D., Mazzi, F., and Martini, G. (2007). Broadband communications for aeronautical networks: The atenaa outer optical link validation. In *1st CEAS European Air and Space Conference*.

[Fuchs et al., 2017] Fuchs, C., Poulenard, S., Perlot, N., Riedi, J., and Perdigues, J. (2017). Optimization and throughput estimation of optical ground networks for leo-downlinks, geo-feeder links and geo-relays. *Proc.SPIE*, 10096:10096 – 10096 – 10.

[Fusco et al., 2006] Fusco, T., Petit, C., Rousset, G., Sauvage, J.-F., Dohlen, K., D. Mouillet, J. C., Baudoz, P., Kasper, M., Fedrigo, E., Rabou, P., Feautrier, P., Downing, M., Gigan, P., Conan, J.-M., Beuzit, J.-L., Hubin, N., Wildi, F., and Puget, P. (2006). Design of the extreme ao system for sphere, the planet finder instrument of the vlt. *Proc.SPIE*, 6272:6272 – 6272 – 11.

[Fusco et al., 2004] Fusco, T., Rousset, G., Rabaud, D., Gendron, E., Mouillet, D., Lacombe, F., Zins, G., Madec, P.-Y., Lagrange, A.-M., Charton, J., Rouan, D., Hubin, N., and Ageorges, N. (2004). NAOS on-line characterization of turbulence parameters and adaptive optics performance. *Journal of Optics A: Pure and Applied Optics*, 6:585–596.

[Fusco et al., 2004] Fusco, T., Rousset, G., Rabaud, D., Gendron, E., Mouillet, D., Lacombe, F., Zins, G., Madec, P.-Y., Lagrange, A.-M., Charton, J., Rouan, D., Hubin, N., and Ageorges, N. (2004). Naos on-line characterization of turbulence parameters and adaptive optics performance. *Journal of Optics A: Pure and Applied Optics*, 6(6):585.

[Gagliardi and Karp, 1995] Gagliardi, R. and Karp, S. (1995). *Optical Communications*. Wiley Series in Telecommunications and Signal Processing. Wiley.

[Gazzi et al., 1976] Gazzi, M., Vicentini, V., Pantani, L., Radicati, B., Stefanutti, L., and Werner, C., editors (1976). *Log-normal probability distribution of strong irradiance fluctuations: An asymptotic analysis*.

[Geisler et al., 2016] Geisler, D. J., Yarnall, T. M., Stevens, M. L., Schieler, C. M., Robinson, B. S., and Hamilton, S. A. (2016). Multi-aperture digital coherent combining for free-space optical communication receivers. *Opt. Express*, 24(12):12661–12671.

[Gendron and Lena, 1994] Gendron, E. and Lena, P. (1994). Astronomical adaptive optics. 1: Modal control optimization. *Astronomical Society of the Pacific*, 291:337–347.

[Gendron and Lena, 1995] Gendron, E. and Lena, P. (1995). Astronomical adaptive optics. II. Experimental results of an optimized modal control. *Astron. Astrophys. Suppl.*, 111:153–+.

[Giggenbach et al., 2009] Giggenbach, D., Horwath, J., and Knapek, M. (2009). Optical data downlinks from earth observation platforms. *Proc.SPIE*, 7199:7199 – 7199 – 14.

[Gil-Pelaez, 1951] Gil-Pelaez, J. (1951). Note on the inversion theorem. *Biometrika*, (38):481–482.

[Gnauck et al., 2002] Gnauck, A. H., Raybon, G., Chandrasekhar, S., Leuthold, J., Doerr, C., Stulz, L., Agarwal, A., Banerjee, S., Grosz, D., Hunsche, S., Kung, A., Marhelyuk, A., Maywar, D., Movassaghi, M., Liu, X., Xu, C., Wei, X., and Gill, D. M. (2002). 2.5 tb/s (64x42.7 gb/s) transmission over 40x100 km nzdsf using rz-dpsk formatand all-raman-amplified spans. In *Optical Fiber Communications Conference*, page FC2. Optical Society of America.

[Gnauck and Winzer, 2005] Gnauck, A. H. and Winzer, P. J. (2005). Optical phase-shift-keyed transmission. *Journal of Lightwave Technology*, 23(1):115–130.

[Gochelashvily and Shishov, 1971] Gochelashvily, K. S. and Shishov, V. I. (1971). Laser Beam Scintillation Beyond a Turbulent Layer. *Journal of Modern Optics*, 18:313–320.

[Goodman, 1985] Goodman, J. W. (1985). *Statistical Optics*. Wiley-Interscience.

[Gousset, 2015] Gousset, S. (2015). *Optimization of an adaptive optics system for space observation and implementation of an innovative near infra-red detector in wave-front sensing*. Theses, Université Paris Diderot (Paris 7).

[Gracheva and Gurvich, 1965] Gracheva, M. E. and Gurvich, A. S. (1965). Strong fluctuations in the intensity of light propagated through the atmosphere close to earth. *Soviet Radiophysics*, 8(4):511–515.

[Greenwood, 1977] Greenwood, D. P. (1977). Bandwidth specification for adaptive optics systems∗. *J. Opt. Soc. Am.*, 67(3):390–393.

[Gregory et al., 2017] Gregory, M., Heine, F., Kämpfner, H., Meyer, R., Fields, R., and Lunde, C. (2017). Tesat laser communication terminal performance results on 5.6gbit coherent inter satellite and satellite to ground links. *Proc.SPIE*, 10565:10565 – 10565 – 6.

[Grigoryev et al., 2014] Grigoryev, V., Kovalev, V., Shargorodskiy, V., and Sumerin, V. (October 2014). High-bit-rate laser space communication technology and results of on-board experiment. In *International Conference on Space Optics*, volume 7685.

[Guo et al., 2005] Guo, D., Shamai, S., and Verdu, S. (2005). Mutual information and minimum mean-square error in gaussian channels. *IEEE Transactions on Information Theory*, 51(4):1261–1282.

[Hanna, 1993] Hanna, S. A. (1993). Convolutional interleaving for digital radio communications. In *Proceedings of 2nd IEEE International Conference on Universal Personal Communications*, volume 1, pages 443–447 vol.1.

[Heine et al., 2018] Heine, F., Pimentel, P. M., Rochow, C., Saucke, K., Tröndle, D., Lutzer, M., Meyer, R., Bischl, H., and Matuz, B. (2018). The european data relay system and alphasat to t-aogs space to ground links, status, and achievements in 2017. *Proc.SPIE*, 10524:10524 – 10524 – 6.

[Hemmati, 2009a] Hemmati, H. (2009a). *Near-Earth Laser Communications*. Optical Science and Engineering. CRC Press.

[Hemmati, 2009b] Hemmati, H. (2009b). *Near-Earth Laser Communications, Chapter 2*. Optical Science and Engineering. CRC Press.

[Hemmati and Caplan, 2013] Hemmati, H. and Caplan, D. (2013). Chapter 4 - optical satellite communications. In Kaminow, I. P., , Li, T., , and Willner, A. E., editors, *Optical Fiber Telecommunications (Sixth Edition)*, Optics and Photonics, pages 121 – 162. Academic Press, Boston, sixth edition edition.

[Henniger, 2006] Henniger, H. (2006). Packet-layer forward error correction coding for fading mitigation. *Proc.SPIE*, 6304.

[Henniger, 2007] Henniger, H. (2007). Link performance of mobile optical links. *Proc.SPIE*, 6709.

[Henniger, 2012] Henniger, H. (2012). Transmission performance analysis of free-space optical communications using Gilbert-erasure channel. *IEEE Transactions on Communications*, 60(1):55–61.

[Henniger et al., 2003] Henniger, H., Giggenbach, D., David, F., and Rapp, C. (2003). Evaluation of fec for the atmospheric optical im/dd channel. 4975.

[Henniger and Gonzalez, 2006] Henniger, H. and Gonzalez, A. (2006). Transmission scheme and error protection for simplex long-distance atmospheric fso systems. *The Mediterranean Journal of Electronics and Communications*, 2(3):118–126.

[Herrmann, 1980] Herrmann, J. (1980). Least-squares wave front errors of minimum norm. *J. Opt. Soc. Am.*, 70(1):28–35.

[Hill and Frehlich, 1997] Hill, R. J. and Frehlich, R. G. (1997). Probability distribution of irradiance for the onset of strong scintillation. *J. Opt. Soc. Am. A*, 14:1530–1540.

[Ho, 2005] Ho, K.-P. (2005). *Phase-modulated optical communication systems*. New York : Springer. Includes bibliographical references (p. [385]-422) and index.

[Humblet and Azizoglu, 1991] Humblet, P. A. and Azizoglu, M. (1991). On the bit error rate of lightwave systems with optical amplifiers. *Journal of Lightwave Technology*, 9(11):1576–1582.

[Inoue et al., 2014] Inoue, H., Okamoto, E., Shoji, Y., and et. al., Y. T. (2014). Comparative study on low-rate forward error correction codes in downlink satellite-to-ground laser communications. *Proc. International Conference on Space Optical Systems and Applications (ICSOS) 2014*.

[Isserlis, 1916] Isserlis, L. (1916). On certain probable errors and correlation coefficients of multiple frequency distributions with skew regression. *Biometrika*, 11(3):185–190.

[Isserlis, 1918] Isserlis, L. (1918). On a formula for the product-moment coefficient of any order of a normal frequency distribution in any number of variables. *Biometrika*, 12(1/2):134–139.

[Jacobsen, 1994] Jacobsen, G. (1994). *Noise in digital optical transmission systems*. Artech House Boston.

[Jennifer C. Ricklin and Lachinova, 2008] Jennifer C. Ricklin, Stephen M. Hammel, F. D. E. and Lachinova, S. L. (2008). Atmospheric channel effects on free-space laser communication. In *Free-Space Laser Communications Principles and Advances*. Springer.

[Johnson et al., 1980] Johnson, D., Johnson, J., and Moore, H. (1980). *A handbook of active filters*. Prentice-Hall.

[Jolissaint et al., 2006] Jolissaint, L., Véran, J.-P., and Conan, R. (2006). Analytical modeling of adaptive optics: foundations of the phase spatial power spectrum approach. *J. Opt. Soc. Am. A*, 23(2):382–394.

[Jono et al., 2007] Jono, T., Takayama, Y., Shiratama, K., Mase, I., Demelenne, B., Sodnik, Z., Bird, A., Toyoshima, M., Kunimori, H., Giggenbach, D., Perlot, N., Knapek, M., and Arai, K. (2007). Overview of the inter-orbit and the orbit-to-ground laser communication demonstration by oicets. *Proc.SPIE*, 6457:6457 – 6457 – 10.

[Kahn, 2006] Kahn, J. (2006). Modulation and detection techniques for optical communication systems. In *Optical Amplifiers and Their Applications/Coherent Optical Technologies and Applications*, page CThC1. Optical Society of America.

[Kaminow et al., 2013] Kaminow, I. P., , Li, T., , and Willner, A. E. (2013). *Optical Fiber Telecommunications*. Academic Press, sixth edition edition.

[Kartalopoulos and Society, 2000] Kartalopoulos, S. and Society, I. C. (2000). *Optical Spectral Filters and Gratings*, pages 71–89. IEEE Press understanding science and technology series. SPIE Optical Engineering Press.

[Kashyap, 2010] Kashyap, R. (2010). Chapter 6 - fiber grating band-pass filters. In Kashyap, R., editor, *Fiber Bragg Gratings (Second Edition)*, pages 217 – 300. Academic Press, Boston, second edition edition.

[Kaushal et al., 2017] Kaushal, H., Jain, V. K., and Kar, S. (2017). *Acquisition, Tracking, and Pointing*, pages 119–137. Springer India, New Delhi.

[Khalighi and Uysal, 2014] Khalighi, M. A. and Uysal, M. (2014). Survey on free space optical communication: A communication theory perspective. *IEEE Communications Surveys Tutorials*, 16(4):2231–2258.

[Klein and Degnan, 1974] Klein, B. J. and Degnan, J. J. (1974). Optical antenna gain. 1: Transmitting antennas. *Appl. Opt.*, 13(9):2134–2141.

[Koch, 1997] Koch, T. L. (1997). Chapter 4 - laser sources for amplified and {WDM} lightwave systems. In KAMINOW, I. P. and KOCH, T. L., editors, *Optical Fiber Telecommunications {IIIB}*, pages 115 – 162. Academic Press, Boston.

[Lacoste et al., 2011] Lacoste, F., Guérin, A., Laurens, A., Azema, G., Periard, C., and Grimal, D. (2011). FSO ground network optimization and analysis considering the influence of clouds. In *Proceedings of the 5th European Conference on Antennas and Propagation (EUCAP)*, pages 2746–2750.

[Lansing et al., 2002] Lansing, F., Lemmerman, L., Walton, A., Bothwell, G., Bhasin, K., and Prescott, G. (2002). Needs for communications and onboard processing in the vision era. In *IEEE International Geoscience and Remote Sensing Symposium*, volume 1, pages 375–377 vol.1.

[Lee and Chan, 2005] Lee, E. J. and Chan, V. W. S. (2005). Performance of the transport layer protocol for diversity communication over the clear turbulent atmospheric optical channel. In *IEEE International Conference on Communications, 2005. ICC 2005. 2005*, volume 1, pages 333–339 Vol. 1.

[Lee and Harp, 1969] Lee, R. and Harp, J. (1969). Weak scattering in random media, with applications to remote probing. In *Proceedings of the IEEE*, volume 57, pages 375–406.

[Leeb, 1989] Leeb, W. R. (1989). Degradation of signal to noise ratio in optical free space data links due to background illumination. *Appl. Opt.*, 28(16):3443–3449.

[Li, 2003] Li, J. (2003). On the achievable information rate of asymmetric optical fiber channels with amplifier spontaneous emission noise. In *IEEE Military Communications Conference, 2003. MILCOM 2003.*, volume 1, pages 124–129 Vol.1.

[Liu et al., 2004] Liu, X., Xie, C., and van Wijngaarden, A. J. (2004). Multichannel pmd mitigation and outage reduction through fec with sub-burst-error-correction period pmd scrambling. *IEEE Photonics Technology Letters*, 16(9):2183–2185.

[Liva et al., 2009] Liva, G., Matuz, B., Katona, Z., Paolini, E., and Chiani, M. (2009). On construction of moderate-length ldpc codes over correlated erasure channels. In *2009 IEEE International Conference on Communications*, pages 1–5.

[Madec, 2012] Madec, P.-Y. (2012). Overview of deformable mirror technologies for adaptive optics and astronomy. *Proc.SPIE*, 8447.

[Mahajan, 2013] Mahajan, V. N., editor (2013). *Optical imaging and aberrations, Part III: wavefront analysis*. SPIE Press.

[Mahdiraji and Zahedi, 2006] Mahdiraji, G. A. and Zahedi, E. (2006). Comparison of selected digital modulation schemes (ook, ppm and dpim) for wireless optical communications. In *2006 4th Student Conference on Research and Development*, pages 5–10.

[Mahé, 2000] Mahé, F. (2000). *Application d'un modèle atmosphérique à l'étude des fluctuations d'indice de réfraction dans la couche limite. Influence de la scintillation sur l'analyse de front d'onde*. PhD thesis, Université de Nice-Sophia Antipolis, Nice France.

[Maire et al., 2007] Maire, J., Ziad, A., Borgnino, J., and Martin, F. (2007). Measurements of profiles of the wavefront outer scale using observations of the limb of the Moon. *Mon. Not. R. Astr. Soc.*, 377:1236–1244.

[Maire et al., 2006] Maire, J., Ziad, A., Borgnino, J., Mourard, D., Martin, F., Jankov, S., Bonneau, D., and Patru, F. (2006). Wavefront outer scale deduced from interferometric dispersed fringes. *Astronomical Society of the Pacific*, 448:1225–1234.

[Marcuse, 1990] Marcuse, D. (1990). Derivation of analytical expressions for the bit-error probability in lightwave systems with optical amplifiers. *Journal of Lightwave Technology*, 8(12):1816–1823.

[Marcuse, 1991] Marcuse, D. (1991). Calculation of bit-error probability for a lightwave system with optical amplifiers and post-detection gaussian noise. *Journal of Lightwave Technology*, 9(4):505–513.

[Martin et al., 1994] Martin, F., Tokovinin, A., Agabi, A., Borgnino, J., and Ziad, A. (1994). G.S.M.: a Grating Scale Monitor for atmospheric turbulence measurements. I. The instrument and first results of angle of arrival measurements. *Astron. Astrophys. Suppl.*, 108:173–180.

[Martin and Flatté, 1988] Martin, J. M. and Flatté, S. M. (1988). Intensity images and statistics from numerical simulation of wave propagation in 3-d random media. *Appl. Opt.*, 27(11):2111–2126.

[Maréchal, 1947] Maréchal, A. (1947). Étude des effets combinés de la diffraction etdes aberrations géometriques sur l'image d'un point lumineux. *Rev. Opt. Theor. Instrum.*, (26):257–277.

[McGlamery, 1976] McGlamery, B. L. (1976). Computer simulation studies of compensation of turbulence degraded images. *Proc.SPIE*, 0074:0074 – 0074 – 9.

[Meimon et al., 2013] Meimon, S., Cassaing, F., and Prévôt, G. (2013). Experimental study of distorted beams coupling in a single mode waveguide. *Journal of Optics*, 15(3):035707.

[Miller et al., 2001] Miller, J. E., Eaton, F. D., and Stokes, S. D. (2001). Correlation of weather parameters with sodar-derived Cn2 profiles. In Thompson, W. E. and Merritt, P. H., editors, *Proc. SPIE, Laser Weapons Technology II*, volume 4376 of *Presented at the Society of Photo-Optical Instrumentation Engineers (SPIE) Conference*, pages 116–123.

[Moision and Hamkins, 2005] Moision, B. and Hamkins, J. (2005). Coded modulation for the deep-space optical channel: Serially concatenated pulse-position modulation. *IPN Progress Report 42-161*.

[Neichel, 2008] Neichel, B. (2008). *Study of distant galaxies and tomographic adaptive optics for the ELTs.* PhD thesis, Universite Paris-Diderot - Paris VII.

[Noll, 1976] Noll, R. J. (1976). Zernike polynomials and atmospheric turbulence. *J. Opt. Soc. Am.*, 66(3):207–211.

[Oaida et al., 2014] Oaida, G. V., Wu, W., and et. al., B. I. E. (2014). Optical link design and validation testing of the optical payload for lasercomm science (opals) system. *Proc. of SPIE*, 8971.

[Obukhov, 1949] Obukhov, A. M. (1949). Structure of the temperature field in a turbulent current. *Izvestiya Akademia Nauk SSSR, Series Goegraficheskaya i Geograficheskaya*, 13(6):58–69.

[Owens, 1967] Owens, J. C. (1967). Optical refractive index of air: Dependence on pressure, temperature and composition. *Appl. Opt.*, 6(1):51–59.

[Perlot, 2007] Perlot, N. (2007). Turbulence-induced fading probability in coherent optical communication through the atmosphere. *Appl. Opt.*, 46(29):7218–7226.

[Personick, 1973] Personick, S. D. (1973). Receiver design for digital fiber optic communication systems, i and ii. *The Bell System Technical Journal*, 52(6):843–874.

[Petermann, 1988] Petermann, K. (1988). *Laser Diode Modulation and Noise*. Advances in Opto-Electronics. Springer Netherlands.

[Petit, 2006] Petit, C. (2006). *Etude de la commande optimale en Optique Adaptative et Optique Adaptative MultiConjuguée, validation numérique et expérimentale*. PhD thesis, Paris 13.

[Petit et al., 2009] Petit, C., Conan, J.-M., Kulcsár, C., and Raynaud, H.-F. (2009). Linear quadratic gaussian control for adaptive optics and multiconjugate adaptive optics: experimental and numerical analysis. *J. Opt. Soc. Am. A*, 26(6):1307–1325.

[Petit et al., 2008] Petit, C., Conan, J.-M., Kulcsár, C., Raynaud, H.-F., and Fusco, T. (2008). First laboratory validation of vibration filtering with lqg control law for adaptive optics. *Opt. Express*, 16(1):87–97.

[Petit et al., 2004] Petit, C., Quiros-Pacheco, F., Conan, J.-M., Kulcsar, C., Raynaud, H.-F., Fusco, T., and Rousset, G. (2004). Kalman-filter-based control for adaptive optics. *Proc.SPIE*, 5490.

[Petit et al., 2016] Petit, C., Védrenne, N., Velluet, M.-T., Michau, V., Artaud, G., Samain, E., and Toyoshima, M. (2016). Investigation on adaptive optics performance from propagation channel characterization with the small optical transponder. *Optical Engineering*, 55:55 – 55 – 17.

[Pfennigbauer et al., 2002] Pfennigbauer, M., Strasser, M. M., Pauer, M., and Winzer, P. J. (2002). Dependence of optically preamplified receiver sensitivity on optical and electrical filter bandwidths-measurement and simulation. *IEEE Photonics Technology Letters*, 14(6):831–833.

[Poulenard et al., 2017] Poulenard, S., Mège, A., Fuchs, C., Perlot, N., Riedi, J., and Perdigues, J. (2017). Digital optical feeder links system for broadband geostationary satellite. *Proc.SPIE*, 10096:10096 – 10096 – 8.

[Poulenard et al., 2014] Poulenard, S., Ruellan, M., Roy, B., Riédi, J., Parol, F., and Rissons, A. (2014). High altitude clouds impacts on the design of optical feeder link and optical ground station network for future broadband satellite services. *Proc. SPIE*, 8971.

[Priestley, 1989] Priestley, M. (1989). *Spectral Analysis and Time Series*. Probability and Mathematical Statistics : a serie of monographs and textbooks. Academic Press.

[Puryear et al., 2011] Puryear, A., Jin, R., Lee, E., and Chan, V. W. S. (2011). Experimental analysis of the time dynamics of coherent communication through turbulence: Markovianity and channel prediction. In *2011 International Conference on Space Optical Systems and Applications (ICSOS)*, pages 28–37.

[Ragazzoni, 1996] Ragazzoni, R. (1996). Pupil plane wavefront sensing with an oscillating prism. *Journal of Modern Optics*, 43:289–293.

[R.E Good and Dewan, 1988] R.E Good, R.R. Beland, E. M. J. B. and Dewan, E. (1988). Atmospheric models of optical turbulence. *SPIE*.

[Riant, 2003] Riant, I. (2003). Fiber bragg gratings for optical telecommunications. *Comptes Rendus Physique*, 4(1):41 – 49.

[Richardson and Lynch, 2007] Richardson, L. F. and Lynch, P. (2007). *Weather Prediction by Numerical Process*. Cambridge Mathematical Library. Cambridge University Press, 2 edition.

[Rigaut et al., 1991] Rigaut, F., Rousset, G., Kern, P., Fontanella, J. C., Gaffard, J. P., Merkle, F., and Léna, P. (1991). Adaptive optics on a 3.6-m telescope - Results and performance. *Astronomical Society of the Pacific*, 250:280–290.

[Rigaut et al., 1998] Rigaut, F. J., Veran, J., and Lai, O. (1998). Analytical model for Shack-Hartmann-based adaptive optics systems. In *Proc. SPIE Vol. 3353, p. 1038-1048, Adaptive Optical System Technologies, Domenico Bonaccini; Robert K. Tyson; Eds.*, pages 1038–1048.

[Robert et al., 2008] Robert, C., Conan, J.-M., Michau, V., Renard, J.-B., Robert, C., and Dalaudier, F. (2008). Retrieving parameters of the anisotropic refractive index fluctuations spectrum in the stratosphere from balloon-borne observations of stellar scintillation. *J. Opt. Soc. Am. A*, 25(2):379–393.

[Roberts et al., 2016] Roberts, W. T., Antsos, D., Croonquist, A., Piazzolla, S., Roberts, L. C., Garkanian, V., Trinh, T., Wright, M. W., Rogalin, R., Wu, J., and Clare, L. (2016). Overview of ground station 1 of the nasa space communications and navigation program. *Proc.SPIE*, 9739.

[Roddier, 1981] Roddier, F. (1981). V the effects of atmospheric turbulence in optical astronomy. volume 19 of *Progress in Optics*, pages 281 – 376. Elsevier.

[Roddier, 1988] Roddier, F. (1988). Curvature sensing and compensation: a new concept in adaptive optics. *Appl. Opt.*, 27:1223–1225.

[Roddier, 1990] Roddier, N. A. (1990). Atmospheric wavefront simulation using Zernike polynomials. *Optical Engineering*, 10(29).

[Roggemann and Koivunen, 2000a] Roggemann, M. C. and Koivunen, A. C. (2000a). Branch-point reconstruction in laser beam projection through turbulence with finite-degree-of-freedom phase-only wave-front correction. *J. Opt. Soc. Am. A*, 17:53–62.

[Roggemann and Koivunen, 2000b] Roggemann, M. C. and Koivunen, A. C. (2000b). Wave-front sensing and deformable-mirror control in strong scintillation. *J. Opt. Soc. Am. A*, 17:911–919.

[Roth, 2013] Roth, C. (2013). High-throughput hardware decoder implementation for optical deep-space communications. *TTC 2013 6th ESA International Workshop on Tracking, Telemetry and Command Systems for Space Applications*.

[Rousset, 1993] Rousset, G. (1993). Wavefront sensing. In Alloin, D. and Mariotti, J.-M., editors, *Adaptive Optics for Astronomy*, volume 243, pages 115–137, Cargèse, France. ASI, Kluwer Academic Publisher.

[Rousset et al., 1990] Rousset, G., Fontanella, J., Kern, P., Gigan, P., and Rigaut, F. (1990). First diffraction-limited astronomical images with adaptive optics. *aap*, 230:L29–L32.

[Rousset et al., 1998] Rousset, G., Lacombe, F., Puget, P., Hubin, N. N., Gendron, E., Conan, J.-M., Kern, P. Y., Madec, P.-Y., Rabaud, D., Mouillet, D., Lagrange, A.-M., and Rigaut, F. J. (1998). Design of the nasmyth adaptive optics system (naos) of the vlt. *Proc.SPIE*, 3353:3353 – 3353 – 9.

[Ruilier, 1998] Ruilier, C. (1998). A study of degraded light coupling into single-mode fibers. volume 3350, pages 319–329. SPIE.

[Ruilier and Cassaing, 2001] Ruilier, C. and Cassaing, F. (2001). Coupling of large telescopes and single-mode waveguides: application to stellar interferometry. *Opt. Soc. Am.*, 18(1):143–149.

[Sacek,] Sacek, V. http://www.telescope-optics.net/zernike_expansion_schemes.htm.

[Saleh and Teich, 2007] Saleh, B. and Teich, M. (2007). *Fundamentals of Photonics*. Wiley Series in Pure and Applied Optics. Wiley.

[Sasiela, 1994] Sasiela, R. (1994). *Electromagnetic wave propagation in turbulence*. Springer-Verlag.

[Sasiela and Mooney, 1986] Sasiela, R. J. and Mooney, J. G. . (1986). An optical phase reconstructor based on using a multiplier-accumulator approach. *Proc.SPIE*, 0551:0551 – 0551 – 7.

[Saucke et al., 2017] Saucke, K., Heine, F., Tröndle, D., Pimentel, P. M., Fischer, E., Berkefeld, T., Feriencik, M., Richter, I., Lutzer, M., and Meyer, R. (2017). The tesat transportable adaptive optical ground station and the operational experiences. *Proc.SPIE*, 10562:10562 – 10562 – 8.

[Shack and Platt, 1971] Shack, R. B. and Platt, B. C. (1971). Production and use of a lenticular hartmann screen. 61:656.

[Shaklan and Roddier, 1988] Shaklan, S. and Roddier, F. (1988). Coupling starlight into single-mode fiber optics. *Applied Optics*, 27(11).

[Shannon, 1948] Shannon, C. E. (1948). A mathematical theory of communication. *Bell system technical journal*, 27.

[Simon and Alouini, 2005] Simon, M. K. and Alouini, M. S. (2005). *Digital Communication over Fading Channels; 2nd ed.* Wiley, Newark, NJ.

[Sinsky et al., 2004] Sinsky, J. H., Adamiecki, A., Gnauck, A., Burrus, C. A., Leuthold, J., Wohlgemuth, O., Chandrasekhar, S., and Umbach, A. (2004). Rz-dpsk transmission using a 42.7-gb/s integrated balanced optical front end with record sensitivity. *Journal of Lightwave Technology*, 22(1):180–185.

[Sklar, 1997] Sklar, B. (1997). A primer on turbo code concepts. *IEEE Communications Magazine*, 35(12):94–102.

[Smith, 1993] Smith, F., editor (1993). *Atmospheric propagation of radiation*. Number 2 in The Infrared and Electro-Optical Systems Handbook. SPIE Optical Engineering Press and ERIM.

[Stephens, 1970] Stephens, M. A. (1970). Use of the Kolmogorov-Smirnov, Cramer-Von Mises and related statistics without extensive tables. *Journal of the Royal Statistical Society. Series B (Methodological)*, 32(1):115–122.

[Strohbehn, 1978] Strohbehn, J. W. (1978). *Modern theories in the propagation of optical waves in a turbulent medium*, pages 45–106. Springer Berlin Heidelberg, Berlin, Heidelberg.

[Tatarski, 1961] Tatarski, V. (1961). *Wave Propagation In a Turbulent Medium*. Dover Publications,Inc. New York.

[Tatarskii, 1971] Tatarskii, V. I. (1971). *The effects of the turbulent atmosphere on wave propagation*.

[Tonguz and Wagner, 1991] Tonguz, O. K. and Wagner, R. E. (1991). Equivalence between preamplified direct detection and heterodyne receivers. *IEEE Photonics Technology Letters*, 3(9):835–837.

[Toyoshima, 2006] Toyoshima, M. (2006). Trends of research and development on optical space communications technology. In *IEICE General Conference*.

[Toyoshima et al., 2015] Toyoshima, M., Fuse, T., Kolev, D. R., Takenaka, H., Munemasa, Y., Iwakiri, N., Suzuki, K., Koyama, Y., Kubooka, T., Akioka, M., and Kunimori, H. (2015). Current status of research and development on space laser communications technologies and future plans in nict. In *2015 IEEE International Conference on Space Optical Systems and Applications (ICSOS)*, pages 1–5.

[Tse and Viswanath, 2005] Tse, D. and Viswanath, P. (2005). *Fundamentals of Wireless Communication*. Cambridge University Press, New York, NY, USA.

[Tyson and Frazier, 2012] Tyson, R. and Frazier, B. (2012). *Field Guide to Adaptive Optics*. SPIE field guides. Society of Photo Optical.

[Valley, 1980] Valley, G. C. (1980). Isoplanatic degradation of tilt correction and short-term imaging systems. *Appl. Opt.*, 19(4):574–577.

[Vedrenne et al., 2016] Vedrenne, N., Conan, J.-M., Petit, C., and Michau, V. (2016). Adaptive optics for high data rate satellite to ground laser link. *Proc. SPIE 9739, Free-Space Laser Communication and Atmospheric Propagation XXVIII, 97390E*, 9739.

[Védrenne et al., 2012] Védrenne, N., Conan, J.-M., Velluet, M.-T., Séchaud, M., Toyoshima, M., Takenaka, H., Guérin, A., and Lacoste, F. (2012). Turbulence effects on bi-directional ground-to-satellite laser communication systems. In *ICSOS proceedings*. International Conference on Space Optical Systems and Applications (ICSOS). September 9–12, Ajaccio (France).

[Véran, 1998] Véran, J. (1998). *Estimation de la réponse impulsionnelle et restauration d'image en optique adaptative. Application au système d'optique adapative du Télescope Canada-France-Hawaii.* PhD thesis, ENST Paris.

[Voitsekhovich et al., 1998] Voitsekhovich, V. V., Kouznetsov, D., and Morozov, D. K. (1998). Density of turbulence-induced phase dislocations. *Appl. Opt.*, 37:4525–4535.

[Voitsekhovich, V. V. et al., 2001] Voitsekhovich, V. V., Orlov, V. G., and Sanchez, L. J. (2001). Influence of scintillations on the performance of adaptive astronomical systems with Hartmann-like wavefront sensors. *A & A*, 368(3):1133–1136.

[Wall, 2012] Wall, J. V., C. J. (2012). *Practical statistics for astronomers*, volume Cambridge observing handbooks for research astronomers. Cambridge University Press, 2nd ed edition.

[Walters and Kunkel, 1981] Walters, D. L. and Kunkel, K. E. (1981). Atmospheric modulation transfer function for desert and mountain locations: the atmospheric effects on r_0. *J. Opt. Soc. Am.*, (71):397–405.

[Wang and Kahn, 2004] Wang, J. and Kahn, J. M. (2004). Impact of chromatic and polarization-mode dispersions on dpsk systems using interferometric demodulation and direct detection. *Journal of Lightwave Technology*, 22(2):362–371.

[Wang et al., 1978] Wang, T., Ochs, G. R., and Clifford, S. F. (1978). A saturation-resistant optical scintillometer to measure C_n^2. *J. Opt. Soc. Am. A*, 68:334–+.

[Wang and Strohbehn, 1974] Wang, T.-I. and Strohbehn, J. W. (1974). Perturbed log-normal distribution of irradiance fluctuations. *J. Opt. Soc. Am. A*, 64:994–+.

[Webb and Marino, 1975] Webb, W. E. and Marino, J. T. (1975). Threshold detection in an on–off binary communications channel with atmospheric scintillation. *Appl. Opt.*, 14(6):1413–1417.

[Wecker, 1978] Wecker, W. E. (1978). A note on the time series which is the product of two stationary time series. *Stochastic Processes and their Applications*, 8(2):153 – 157.

[Whiteley et al., 1998] Whiteley, M. R., Roggemann, M. C., and Welsh, B. M. (1998). Temporal properties of the Zernike expansion coefficients of turbulence-induced phase aberrations for aperture and source motion. *J. Opt. Soc. Am. A*, 15(4):993–1005.

[Wilhelmsson and Milstein, 1999] Wilhelmsson, L. and Milstein, L. B. (1999). On the effect of imperfect interleaving for the Gilbert-Elliott channel. *IEEE Transactions on Communications*, 47(5):681–688.

[Wilson, 2002] Wilson, R. W. (2002). SLODAR: measuring optical turbulence altitude with a Shack-Hartmann wavefront sensor. *Mon. Not. R. Astr. Soc.*, 337:103–108.

[Wilson et al., 2003] Wilson, R. W., Wooder, N. J., Rigal, F., and Dainty, J. C. (2003). Estimation of anisoplanatism in adaptive optics by generalized SCIDAR profiling. *Mon. Not. R. Astr. Soc.*, 339:491–494.

[Wilson et al., 2005] Wilson, S. G., Brandt-Pearce, M., Cao, Q., and Baedke, M. (2005). Optical repetition mimo transmission with multipulse ppm. *IEEE Journal on Selected Areas in Communications*, 23(9):1901–1910.

[Winzer, 2001] Winzer, P. (2001). Performance estimation of receivers corrupted by optical noise. In *Optical Amplifiers and Their Applications*, page OTuE16. Optical Society of America.

[Winzer, 2002] Winzer, P. J. (2002). Optical transmitters, receivers, and noise. In J.G.Proakis, editor, *Wiley Encyclopedia of Telecommunications*, page 1824–1840.

[Winzer et al., 2003] Winzer, P. J., Chandrasekhar, S., and Kim, H. (2003). Impact of filtering on rz-dpsk reception. *IEEE Photonics Technology Letters*, 15(6):840–842.

[Winzer and Essiambre, 2006] Winzer, P. J. and Essiambre, R. J. (2006). Advanced optical modulation formats. *Proceedings of the IEEE*, 94(5):952–985.

[Winzer and Kalmar, 1999] Winzer, P. J. and Kalmar, A. (1999). Sensitivity enhancement of optical receivers by impulsive coding. *Journal of Lightwave Technology*, 17(2):171–177.

[Winzer and Kim, 2003] Winzer, P. J. and Kim, H. (2003). Degradations in balanced dpsk receivers. *IEEE Photonics Technology Letters*, 15(9):1282–1284.

[Winzer et al., 2001] Winzer, P. J., Pfennigbauer, M., Strasser, M. M., and Leeb, W. R. (2001). Optimum filter bandwidths for optically preamplified nrz receivers. *J. Lightwave Technol.*, 19(9):1263.

[Wright et al., 2015] Wright, M. W., Morris, J. F., Kovalik, J. M., Andrews, K. S., Abrahamson, M. J., and Biswas, A. (2015). Adaptive optics correction into single mode fiber for a low earth orbiting space to ground optical communication link using the OPALS downlink. *Opt. Express*, 23(26):33705–33712.

[Wysocki et al., 2006] Wysocki, P., Wood, T., Grant, A., Holcomb, D., Chang, K., Santo, M., Braun, L., and Johnson, G. (2006). High reliability 49 db gain, 13w pm fiber amplifier at 1550 nm with 30 db per and record efficiency. In *2006 Optical Fiber Communication Conference and the National Fiber Optic Engineers Conference*, pages 1–3.

[Xiaoming Zhu, 2002] Xiaoming Zhu, J. M. K. (2002). Pilot-symbol assisted modulation for correlated turbulent free-space optical channels. *Proc.SPIE*, 4489.

[Xu et al., 2009] Xu, F., Khalighi, A., Caussé, P., and Bourennane, S. (2009). Channel coding and time-diversity for optical wireless links. *Opt. Express*, 17(2):872–887.

[Yamakawa et al., 2015] Yamakawa, S., Chishiki, Y., Sasaki, Y., Miyamoto, Y., and Kohata, H. (2015). Jaxa's optical data relay satellite programme. In *2015 IEEE International Conference on Space Optical Systems and Applications (ICSOS)*, pages 1–3.

[Yee and Weldon, 1995] Yee, J. R. and Weldon, E. J. (1995). Evaluation of the performance of error-correcting codes on a Gilbert channel. *IEEE Transactions on Communications*, 43(8):2316–2323.

[Yoichi Maeda, 2009] Yoichi Maeda, Francesco Montalti, G. B. (2009). *Optical Fibres, Cables and Systems ITU-T Manual*. ITU.

[Yura and Hanson, 2010] Yura, H. T. and Hanson, S. G. (2010). Mean level signal crossing rate for an arbitrary stochastic process. *J. Opt. Soc. Am. A*, 27(4):797–807.

[Ziad et al., 2004] Ziad, A., Schöck, M., Chanan, G. A., Troy, M., Dekany, R., Lane, B. F., Borgnino, J., and Martin, F. (2004). Comparison of Measurements of the Outer Scale of Turbulence by Three Different Techniques. *Appl. Opt.*, 43:2316–2324.